

Drone-based Integration of Hyperspectral Imaging and Magnetism for Mineral Exploration.

Von der Fakultät für Geowissenschaften, Geotechnik und Bergbau
der Technischen Universität Bergakademie Freiberg
genehmigte

Dissertation

Zur Erlangung des akademischen Grades

Doctor rerum naturalium

(Dr. rer. nat.)

vorgelegt

von **M.Sc. Robert Jackisch**

geboren am 17.05.1986 in Görlitz, Deutschland

Gutachter: Prof. Dr. Jens Gutzmer, Freiberg, Deutschland
Prof. Dr. Steven Micklethwaite, Queensland, Australien

Tag der Verleihung: 21.01.2022



Versicherung

Hiermit versichere ich, dass ich die vorliegende Arbeit ohne unzulässige Hilfe Dritter und ohne Benutzung anderer als der angegebenen Hilfsmittel angefertigt habe; die aus fremden Quellen direkt oder indirekt übernommenen Gedanken sind als solche kenntlich gemacht.

Bei der Auswahl und Auswertung des Materials sowie bei der Herstellung des Manuskripts habe ich Unterstützungsleistungen von folgenden Personen erhalten:

- Jens Gutzmer (Supervisor)
- Richard Gloaguen (Supervisor, Koautor von Artikel 1–3)
- Robert Zimmermann (Koautor von Artikel 1–3)
- Markku Pirttijärvi (Koautor von Artikel 1–3)
- Moritz Kirsch (Koautor von Artikel 2, 3)
- Björn H. Heincke (Koautor von Artikel 1, 3)
- Heikki Salmirinne (Koautor von Artikel 1, 3)
- Ari Saartenoja (Koautor von Artikel 1, 2)
- Yuleika Madriz (Koautor von Artikel 1)
- Sandra Lorenz (Koautor von Artikel 2)
- Laura Tusa (Koautor von Artikel 2)
- Hernan Ugalde (Koautor von Artikel 2)
- Erik Vest-Sørensen (Koautor von Artikel 3)
- Mikko Savolainen (Koautor von Artikel 2)
- Jukka-Pekka Kujasalo (Koautor von Artikel 1)
- Stefanie Lode (Koautor von Artikel 3)

Weitere Personen waren an der Abfassung der vorliegenden Arbeit nicht beteiligt. Die Hilfe eines Promotionsberaters habe ich nicht in Anspruch genommen. Weitere Personen haben von mir keine geldwerten Leistungen für Arbeiten erhalten, die nicht als solche kenntlich gemacht worden sind.

Die Arbeit wurde bisher weder im Inland noch im Ausland in gleicher oder ähnlicher Form einer anderen Prüfungsbehörde vorgelegt.

Ort, Datum

Unterschrift

Plagiarism declaration

I hereby declare that I completed this work without any improper help from a third party and without using any aids other than those cited. All ideas derived directly or indirectly from other sources are identified as such.

In the selection and in the use of materials and in the writing of the manuscript I received support from the following persons:

- Jens Gutzmer (supervisor)
- Richard Gloaguen (supervisor, co-author of articles 1–3)
- Robert Zimmermann (co-author of articles 1–3)
- Markku Pirttijärvi (co-author of articles 1–3)
- Moritz Kirsch (co-author of articles 2, 3)
- Björn H. Heincke (co-author of articles 1, 3)
- Heikki Salmirinne (co-author of articles 1, 3)
- Ari Saartenoja (co-author of articles 1, 2)
- Yuleika Madriz (co-author of article 1)
- Sandra Lorenz (co-author of article 2)
- Laura Tusa (co-author of article 2)
- Hernan Ugalde (co-author of article 2)
- Erik Vest-Sørensen (co-author of article 3)
- Mikko Savolainen (co-author of article 2)
- Jukka-Pekka Kujasalo (co-author of article 1)
- Stefanie Lode (co-author of article 3)

Persons other than those above did not contribute to the writing of this thesis. I did not seek advice from a professional doctorate consultant. No persons received payment for assistance rendered to me in the writing of this thesis.

This thesis has not previously been submitted to another examination authority in the same or similar form in Germany or abroad.

Place, Date

Signature

Acknowledgements

This thesis was written at the Helmholtz-Zentrum Dresden-Rossendorf (HZDR), Helmholtz Institute Freiberg for Resource Technology (HIF). The interdisciplinary work results from the project MULSEDRO (MultiSensorDrones) which was financed by the EIT RawMaterials and the European Union (grant ID 16193).

First, I want to thank my supervisors Jens Gutzmer and Richard Gloaguen for your support, motivation, and guidance. I am deeply thankful to Moritz Kirsch for his enthusiastic encouragement, trust, asking the right questions, and the motivational 5k's. Further, Sandra Lorenz, Robert Zimmermann and Erik Herrmann for the most productive creation and exchange of ideas, the tremendous conduction of field works and software solutions. I gratefully thank all other colleagues of the Division of Exploration and HIF which contributed to the uniquely positive scientific and working atmosphere. Cecilia Contreras, Lucas Pereira, Peter Seidel, Laura Tusa, Kasra Shahi, Sam Thiele, Junaidh Fareedh, Ethan Barnes, Yuleika Madriz, Maggi Fuchs, Louis Andreani, Raimon Tolosana-Delgado, Robert Möckel, Anett Begenau, Vanessa Weitzel, the administration and technical personnel, the people at Erzlabor (Roland, Kai, Micha, Dirk) and to the many others, thank you a lot.

I would like to thank all involved project partners, the Geological Survey of Denmark and Greenland (GEUS), the Geological Survey of Finland, Radaí Oy, DMT, LTU, Yara Suomi and Bluejay Mining. I thank GEUS Björn Heincke for restlessly driving MULSEDRO, and Erik Vest-Sørensen for untangling Disko Islands geology. Also I thank Heikki Salmirinne and Maarit Middleton from GTK. A big thanks goes to the Radaí Oy, Ari Saartenoija, Markku Pirttijärvi, Lauri Maalissma, Arto Saarinen, Jani Väyrynen, for your hospitality at Oulu and outstanding mag data. I thank Jouku Jylänki and Aleksi Salo for guidance in Finland. Urpo Kuronen and Hans Jensen is thanked for logistical and geological backup on Disko. For inspirational conversations I sincerely thank Martin Sonntag, Jan Lampke, Jan Mahling, Hernan Ugalde and Bill Morris.

Lastly, I wish to express my deepest gratitude to my family, my parents Dagmar und Markus, my sister Laura, my friends in Freiberg and elsewhere, and my dearest Nikita. Without you I could not have completed this journey.

List of publications

First authored publications and manuscript as part of this thesis

- Jackisch, R.**; Madriz, Y.; Zimmermann, R.; Pirttijärvi, M.; Saartenoja, A.; Heincke, B.H.; Salmirinne, H.; Kujasalo, J.-P.; Andreani, L.; Gloaguen, R. Drone-Borne Hyperspectral and Magnetic Data Integration: Otanmäki Fe-Ti-V Deposit in Finland. *Remote Sensing* 2019, 11, 2084.
- Jackisch, R.**; Lorenz, S.; Kirsch, M.; Zimmermann, R.; Tusa, L.; Pirttijärvi, M.; Saartenoja, A.; Ugalde, H.; Madriz, Y.; Savolainen, M.; Gloaguen, R. Integrated Geological and Geophysical Mapping of a Carbonatite-Hosting Outcrop in Siilinjärvi, Finland, Using Unmanned Aerial Systems. *Remote Sensing* 2020, 12, 2998.
- Jackisch, R.**, Heincke, B. H., Zimmermann, R., Sørensen, E. V., Pirttijärvi, M., Kirsch, M., Salmirinne, H., Lode, S., Kuronen, U., & Gloaguen, R. (2021). Drone-based magnetic and multispectral surveys to develop a 3D model for mineral exploration at Qullissat, Disko Island, Greenland. *Solid Earth Discussions*, 2021, 1–51.

Co-authored peer-reviewed publications in direct relation to this thesis

- Heincke, B., **Jackisch, R.**, Saartenoja, A., Salmirinne, H., Rapp, S., Zimmermann, R., Pirttijärvi, M., Sørensen, E.V., Gloaguen, R., Ek, L., Bergström, J., Karinen, A., Salehi, S., Madriz, Y. & Middleton, M. 2019: Developing multi-sensor drones for geological mapping and mineral exploration: setup and first results from the MULSEDRO project. Geological Survey of Denmark and Greenland Bulletin 43.
- Booyesen, R., **Jackisch, R.**, Lorenz, S., Zimmermann, R., Kirsch, M., Nex, P.A.M., and Gloaguen, R., 2020, Detection of REEs with lightweight UAV-based hyperspectral imaging: Scientific Reports, v. 10, p. 17450.
- Duan, P.; Lai, J.; Ghamisi, P.; Kang, X.; **Jackisch, R.**; Kang, J.; Gloaguen, R. Component Decomposition-Based Hyperspectral Resolution Enhancement for Mineral Mapping. *Remote Sens.* 2020, 12, 2903.
- Flores, H.; Lorenz, S.; **Jackisch, R.**; Tusa, L.; Contreras, I.C.; Zimmermann, R.; Gloaguen, R. UAS-Based Hyperspectral Environmental Monitoring of Acid Mine Drainage Affected Waters. *Minerals* 2021, 11, 182.
- Lorenz, S., Ghamisi, P., Kirsch, M., **Jackisch, R.**, Rasti, B., and Gloaguen, R., 2021, Feature extraction for hyperspectral mineral domain mapping: A test of conventional and innovative methods: *Remote Sensing of Environment*, v. 252, p. 112129.

Co-authored technical reports and extended conference abstracts

- Herrmann, E., **Jackisch, R.**, Lorenz, S., Zimmermann, R., Gloaguen, R., and Günther, L., 2018, Machbarkeitsstudie zur Nutzung multi-und hyperspektraler Verfahren für Kippenzustandsbeschreibung und Tagebaurestseemonitoring: Landesamt fuer Umwelt Landwirtschaft und Geologie Sachsen. p. 67.
- Jackisch, R.**, Pirttijärvi, M., Salmirinne, H., Kärenlampi, K., Heincke, B., Jylänki, J., Zimmermann, R., Sørensen, E.-V., Middleton, M., and Madriz, Y., 2019, Acquisition and Processing Report of the MULSEDRO EIT RM Project from the Otanmäki Fe–Ti–V Deposit, Finland: GTK Open File Research Report, p. 124.

Jackisch, R., 2020, Drone-based surveys of mineral deposits: *Nature Reviews Earth & Environment*, v. 1, p. 187, doi:10.1038/s43017-020-0042-1.

Shahi, K.R., Ghamisi, P., **Jackisch, R.**, Khodadadzadeh, M., Lorenz, S., and Gloaguen, R., 2020, A New Spectral-Spatial Subspace Clustering Algorithm for Hyperspectral Image Analysis: *ISPRS Annals of the Photogrammetry, Remote Sensing and Spatial Information Sciences*, v. 3, p. 185–191.

Conference abstracts and non-peer reviewed publications

Jackisch, R., Zimmermann, R., Lorenz, S., Saartenoja, A., Pirttijärvi, M., and Gloaguen, R., 2018, Integration of drone-borne hyperspectral and geomagnetic data. A combined approach in geologic remote sensing. A test from the Siilinjärvi carbonatite, Finland., in *EGU General Assembly Conference Abstracts*, Vienna, Austria, p. 17812.

Jackisch, R., Zimmermann, R., Lorenz, S., Saartenoja, A., Pirttijärvi, M., and Gloaguen, R., 2018, A novel approach combining geomagnetic and hyperspectral drone-borne data. Advances in remote sensing based mineral exploration and environmental monitoring., in *Resources for Future Generations*, Vancouver, BC, Canada, Vancouver, Canada, p. 226.

Jackisch, R., Madriz, Y., Zimmermann, R., Pirttijärvi, M., Saartenoja, A., Salmirinne, H., Henning Heincke, B., and Gloaguen, R., 2019, Integration of UAS-borne hyperspectral remote-sensing and geophysics in mineral exploration under sub-polar conditions in Finland., in *EGU General Assembly Conference Abstracts*, Vienna, Austria, *EGU General Assembly Conference Abstracts*, p. 14613.

Jackisch, R., Zimmermann, R., Heincke, B.H., Karinen, A., Salmirinne, H., Pirttijärvi, M., Lorenz, S., Madriz, Y., and Gloaguen, R., 2020, UAS-based hyperspectral and magnetic mineral exploration targeting Ni-PGE mineralization on Northern Disko Island, West Greenland., in *EGU General Assembly Conference Abstracts*, Vienna, Austria, *EGU General Assembly Conference Abstracts*, p. 20765.

Salmirinne, H., Heincke, B., **Jackisch, R.**, Saartenoja, A., 2020, Science Blog: Game of drones – unmanned aerial vehicles in mineral exploration and geological mapping: *GTK Science Blog*, <https://www.gtk.fi/en/science-blog-game-of-drones-unmanned-aerial-vehicles-in-mineral-exploration-and-geological-mapping/> (last accessed November 2020).

Abstract

The advent of unoccupied aerial systems (UAS) as disruptive technology has a lasting impact on remote sensing, geophysics and most geosciences. Small, lightweight, and low-cost UAS enable researchers and surveyors to acquire earth observation data in higher spatial and spectral resolution as compared to airborne and satellite data. UAS-based applications range from rapid topographic mapping using photogrammetric techniques to hyperspectral and geophysical measurements of surface and subsurface geology. UAS surveys contribute to identifying metal deposits, monitoring of mine sites and can reveal arising environmental issues associated with mining. Further, affordable UAS technology will boost exploration data availability and expertise in the global south.

This thesis investigates the application of UAS-based multi-sensor data for mineral exploration, in particular the integration of hyperspectral imagers, magnetometers and digital cameras (covering the visible red, green, blue light spectrum). UAS-based research is maturing, however the aforementioned methods are not unified effectively. RGB-based photogrammetry is used to investigate topography and surface texture. Image spectrometers measure mineral-specific surface signatures. Magnetometers detect geomagnetic field changes caused by magnetic minerals at surface and depth. The integration of such UAS sensor-based methods in this thesis augments exploration potential with non-invasive, high-resolution, safe, rapid and practical survey methods.

UAS-based surveying acquired, processed and integrated data from three distinct test sites. The sites are located in Finland (Fe-Ti-V at Otanmäki; apatite at Siilinjärvi) and Greenland (Ni-Cu-PGE at Qullissat, Disko Island) and were chosen as geologically diverse areas in subarctic to arctic environments. Restricted accessibility, unfavourable atmospheric conditions, dark rocks, debris and vegetation cover and low solar illumination were common features. While the topography in Finland was moderately flat, a steep landscape challenged the Greenland field work. These restraints meant that acquisitions varied from site to site and how data was integrated and interpreted is dependent on the commodity of interest.

Iron-based spectral absorption and magnetic mineral response were detected using hyperspectral and magnetic surveying in Otanmäki. Multi-sensor-based image feature detection and classification combined with magnetic forward modelling enabled seamless geologic mapping in Siilinjärvi. Detailed magnetic inversion and multispectral photogrammetry led to the construction of a comprehensive 3D model of magmatic exploration targets in Greenland.

Ground truth at different intensity was employed to verify UAS-based data interpretations during all case studies.

Laboratory analysis was applied when deemed necessary to acquire geologic-mineralogic validation (e.g., X-ray diffraction and optical microscopy for mineral identification to establish lithologic domains, magnetic susceptibility measurements for subsurface modelling), for example for trace amounts of magnetite in carbonatite (Siilinjärvi) and native iron occurrence in basalt (Qullissat). Technical achievements were the integration of a multicopter-based prototype fluxgate-magnetometer data from different survey altitudes with ground truth, and a feasibility study with a high-speed multispectral image system for fixed-wing UAS.

The employed case studies transfer the experiences made towards general recommendations for UAS application-based multi-sensor integration. This thesis highlights the feasibility of UAS-based surveying at target scale (1–50 km²) and solidifies versatile survey approaches for multi-sensor integration.

Table of Contents

Acknowledgements	i
Abstract.....	iv
Table of Contents	vi
List of Figures	xi
List of Tables	xiii
1 Chapter 1 – Introduction	1
<i>1.1 Introduction and Motivation.....</i>	<i>2</i>
1.1.1 Framing mineral exploration.....	2
1.1.2 Technological progress and sustainability in mining.....	3
<i>1.2 Benefits of drones in mineral exploration</i>	<i>5</i>
1.2.1 The integrated UAS-based multi-sensor workflow.....	7
1.2.2 Literature review of UAS technology use in mineral exploration	10
<i>1.3 Research objective and structure of the thesis.....</i>	<i>14</i>
<i>References.....</i>	<i>17</i>
2 Chapter 2 – General methods	22
<i>2.1 UAS types, data acquisition and the case study.....</i>	<i>23</i>
2.1.1 Terminology addressing UAS.....	24
2.1.2 Introducing the deployed UAS.....	24
2.1.3 Acquired and integrated data types — optical and magnetics	28
2.1.4 Case study approach	29
<i>2.2 Optical remote sensing.....</i>	<i>31</i>
2.2.1 Multispectral- and hyperspectral imaging.....	32
2.2.2 Image spectroscopy for geologic application	35
2.2.3 Development of a fixed-wing-based multispectral camera	39
<i>2.3 Magnetic sensing.....</i>	<i>40</i>
2.3.1 Basics regarding the magnetic field.....	40
2.3.2 Magnetic sensors used on UAS.....	43
2.3.3 Fluxgate magnetometer used in this study	44
2.3.4 Magnetic surveying used	46
3 Chapter 3 — A first test of UAS in Finland.....	59

<i>Drone Borne Hyperspectral and Magnetic Data Integration: Otanmäki Fe Ti V Deposit in Finland</i>	60
<i>Abstract</i>	60
3.1 <i>Introduction</i>	61
3.2 <i>Location and Geology</i>	64
3.2.1 Regional Setting and Description of the Study Area	64
3.2.2 Geologic Setting	66
3.3 <i>Methods and Survey Strategies</i>	67
3.3.1 Survey Outline.....	67
3.3.2 Multispectral UAS Imaging	68
3.3.3 Hyperspectral UAS Imaging	68
3.3.4 Structure-from-Motion Multi-Vision Stereo Photogrammetry	70
3.3.5 Copter-Borne Magnetic Measurements	71
3.3.6 Fixed Wing Magnetic Measurements	73
3.3.7 Ground Truth—Magnetic Survey.....	75
3.3.8 Ground Truth—pXRF, Spectroscopy, Susceptibility, Sampling	75
3.4 <i>Results</i>	76
3.4.1 UAS Multispectral Imagery	76
3.4.2 UAS Hyperspectral Imagery	77
3.4.3 Handheld Spectroscopy	79
3.4.4 UAS-HSI Accuracy Assessment	81
3.4.5 Magnetism—Ground and UAS Borne	81
3.4.6 Geochemistry	83
3.4.7 Integration of Ground Truth and Multicopter Data.....	84
3.4.8 Data Integration.....	85
3.4.9 Geologic Interpretation and Ore Class Estimation.....	86
3.5 <i>Discussion</i>	88
3.5.1 Consequences of UAS Imaging.....	88
3.5.2 Consequences of UAS Magnetic Measurements.....	89
3.5.3 Can Drone Borne Analysis Compete with Airborne Survey and Outperform Ground Based Acquisition?.....	90
3.6 <i>Conclusions</i>	91
<i>References</i>	92
4 Chapter 4 – Innovative methods in an extended workflow.	98
<i>Integrated Geological and Geophysical Mapping of a Carbonatite-Hosting Outcrop in Siilinjärvi, Finland, Using Unmanned Aerial Systems</i>	99
<i>Abstract</i>	99
4.1 <i>Introduction</i>	100

4.2	<i>Materials and Methods</i>	102
4.2.1	UAS Data Acquisition Method	102
4.2.2	Data Products: Feature Extraction, Supervised Image Classification and Magnetic Forward Modelling	103
4.2.3	The Adapted Workflow Conducted for this Survey	104
4.2.4	Ground Truthing and Laboratory Validation	106
4.3	<i>Case Study: The Siilinjärvi Carbonatite Complex</i>	107
4.3.1	Local Geology and Study Area	107
4.3.2	The Jaakonlampi Test Area	109
4.4	<i>Results</i>	111
4.4.1	Ground Spectroscopy and Principal Lithologic Representation	111
4.4.2	UAS-Based Optical Remote Sensing Observations	113
4.4.3	UAS-based Magnetic Observations	115
4.4.4	Geologic Modelling and Ground Magnetic Susceptibility	118
4.5	<i>Data Integration and Validation</i>	119
4.5.1	Geologic Mapping and Interpretation	120
4.5.2	Mineralogic Validation and Additional Observation	123
4.5.3	Validation of Structural Observations	124
4.6	<i>Discussion</i>	125
4.6.1	Assessing the General UAS Survey Workflow with Focus on Image Data	125
4.6.2	Further Implications of UAS Magnetic Surveys and Added Understanding of the Local Geology	128
4.7	<i>Conclusion</i>	129
	<i>References</i>	130
5	<i>Chapter 5 – The final field test on Disko Island</i>	136
	<i>UAS-based surveying and 3D modelling for exploration of the Qullissat area on Disko Island, West Greenland</i>	137
	<i>Abstract</i>	137
5.1	<i>Introduction</i>	138
5.1.1	Regional geological settings	140
5.1.2	Mineral potential	141
5.1.3	Geochronology and magnetic polarity of basalt members	142
5.1.4	Qullissat study area	143
5.1.5	Data from former exploration	145
5.2	<i>Methods and materials</i>	146
5.2.1	Acquisition and processing of UAS-based magnetic data	146
5.2.2	Acquisition and processing of fixed-wing multispectral and photogrammetric data	147

5.2.3	Ground-based and laboratory measurements.....	149
5.2.4	Ground magnetic surveys.....	149
5.2.5	Magnetic susceptibility measurements, handheld spectroscopy and grab sampling	150
5.2.6	Petrophysical measurements on core samples from drill core FP94-4-5.....	151
5.3	<i>Results</i>	151
5.3.1	Magnetic analysis	151
5.3.2	Magnetic modelling — 3-D magnetic inversion	154
5.3.3	Observations from UAS multispectral and photogrammetric data	159
5.3.4	Ground-based spectroscopy and magnetic susceptibility	160
5.3.5	Petrophysical properties of drilling FP94-4-5	162
5.3.6	Photomicrographs and SEM images.....	163
5.4	<i>Discussion & Interpretation</i>	165
5.4.1	Surface investigation	165
5.4.2	Joint interpretation.....	166
5.4.3	Linking landslide features to the exploration target.....	170
5.4.4	Evaluation and recommendation	172
5.5	<i>Conclusion</i>	172
	<i>References</i>	173
6	Chapter 6 – Discussion	180
	<i>Discussion</i>	181
6.1	<i>Acquisition</i>	181
6.1.1	Spatial footprints and survey efficiency.....	181
6.1.2	Ground sampling	184
6.1.3	Solar elevation and survey window	186
6.1.4	Magnetic data acquisition recommendation.....	188
6.1.5	Image acquisition recommendation	189
6.2	<i>Processing</i>	190
6.2.1	Hyperspectral fidelity	190
6.2.2	Narrow spectral absorption features	193
6.2.3	Processing suggestions.....	194
6.2.4	Improving degraded image data	195
6.3	<i>Integration</i>	195
6.3.1	Integrating magnetics.....	195
6.3.2	Spatial and spectral integration.....	199
6.3.3	The value of integrated public geologic and satellite data.....	202
6.3.4	Recommendations for integration.....	204
	<i>References</i>	205

7	Chapter 7 – Conclusions and Outlook	209
7.1	<i>Summary and general recommendations</i>	<i>210</i>
7.2	<i>Further research directions for UAS-based sensors.....</i>	<i>212</i>
	<i>References.....</i>	<i>214</i>
8	Appendix.....	217
	<i>Appendix A.....</i>	<i>217</i>
	<i>Appendix B.....</i>	<i>221</i>
	<i>Appendix C</i>	<i>222</i>
	<i>Appendix D</i>	<i>223</i>
	<i>Appendix E.....</i>	<i>229</i>
	<i>Appendix F.....</i>	<i>230</i>
	<i>Appendix G</i>	<i>235</i>

List of Figures

Figure 1.1 Branches of sampling and analytic methods in mineral exploration.....	3
Figure 1.2 Impact of non-invasive, small-scale drone technology on the exploration & mining.....	4
Figure 1.3 Advantages and disadvantages of survey categories.	6
Figure 1.4 Generalized top-down data-integration workflow using UAS-based sensors.	10
Figure 1.5 Screened body of literature retrieved from SCOPUS.	11
Figure 1.6 Co-occurrence literature network.....	12
Figure 2.1 UAS types used during field research.....	25
Figure 2.2 Tholeg multicopter with main sensors.	26
Figure 2.3 Comparison of three image types.	34
Figure 2.4 Spectral transmission for the solar radiation.	35
Figure 2.5 Reflectance spectrum for Goethite	37
Figure 2.6 Integrated msCam components.	39
Figure 2.7 General magnetic dipole models.	40
Figure 2.8 Geomagnetic field components.....	41
Figure 2.9 Sankey flow diagram showing UAS and magnetic sensor combinations	44
Figure 2.10 Examples of magnetic interference measured during Tholeg UAS take-off.....	46
Figure 2.11 Synthetic, buried 3D geologic bodies	49
Figure 2.12 Upward continuation and derivative of magnetic survey data conducted in this work.	51
Figure 3.1 Hill-shaded total magnetic intensity (TMI) map of the Otanmäki area	64
Figure 3.2 Location of the study area at Otanmäki	65
Figure 3.3 Aibot UAS equipped with the HSI camera Rikola	67
Figure 3.4 Principal magnetic processing workflows for UAS surveys.	72
Figure 3.5 Acquisition patterns of the different magnetic surveys across the mapped ore zones	73
Figure 3.6 Results of multispectral fixed-wing survey.....	76
Figure 3.7 Results from hyperspectral data collected from the multicopter.	78
Figure 3.8 Result of SAM mapping using input spectra from the USGS spectral library	79
Figure 3.9 Plots from exemplary spectra that are extracted from the UAS borne hyperspectral datasets.....	79
Figure 3.10 Results of the acquired handheld spectra	80
Figure 3.11 TMI plots from all magnetic surveys.....	82
Figure 3.12 The total magnetic intensity extracted from the ground magnetic survey and multi-copter UAS	83
Figure 3.13 Boxplot distribution of pXRF measurements of the major compounds.....	84
Figure 3.14 Comparison of ground-based measurements and multi copter magnetic data.....	85
Figure 3.15 Scatter plots showing the relationships of different scanning methods from the outcrop	86
Figure 3.16 SfM-MVS DSM clipped to the outcrop surface.	87

Figure 4.1. Detailed chart of proposed data-driven UAS based integration and modelling workflow.	106
Figure 4.2. Official geologic map; bedrock of Finland	108
Figure 4.3. Photographic illustrations of the applied field methods.....	110
Figure 4.4. Representative hyperspectral image drone-based spectra	112
Figure 4.5. Six selected handheld scans, representative for the mapped lithologies	113
Figure 4.6. Overview of image-based data products showing the three trenches.....	114
Figure 4.7. Display of feature extractions and supervised classification maps.....	115
Figure 4.8. Total magnetic intensity data plotted with shaded relief and UAS flight paths.....	116
Figure 4.9. Comparison of magnetic data at different scales	118
Figure 4.10. Structural and geological information is synthesized.....	121
Figure 4.11. Enlarged maps of the interpreted geology from the three surveyed trenches	122
Figure 4.12. Enlarged view on an orthographically projected point cloud of trench 3.....	123
Figure 4.13. Compilation of structural data from field work and point cloud analysis	125
Figure 5.1 General overview of the study area on northern Disko in West Greenland.	145
Figure 5.2 Primary data of the multispectral UAS-based surveys after basic processing.....	148
Figure 5.3 Overview of legacy airborne geophysical, ground-based magnetics and UAS-based magnetics.....	150
Figure 5.4 Magnetic attribute maps from the UAS-based magnetic data in the Qullissat area.	153
Figure 5.5 3-D voxel-based model for the magnetic inversion.	156
Figure 5.6 Results from the MVI tests	157
Figure 5.7 Three depth slices through the resulting inversion model.....	158
Figure 5.8 Data products derived from the UAS multispectral and photogrammetry data.....	160
Figure 5.9 Spectral measurements taken on a typical basaltic outcrop.....	162
Figure 5.10 Ground-based susceptibility measurements and petrophysical logs from drill hole FP94-4-5.....	163
Figure 5.11 Photographs of a polished thin section of a fine crystalline basalt sample.....	164
Figure 5.12 Integration of UAS-based data.	167
Figure 5.13 Integrated interpretation.....	168
Figure 5.14 Combined plots of surface topography	169
Figure 6.1 Distribution of survey area that was retrieved from available literature	181
Figure 6.2 Spatial footprints of magnetic and hyperspectral UAS-based surveys	182
Figure 6.3 Plots of UAS performance	184
Figure 6.4 Displayed is a time series of Terra MODIS satellite images.....	188
Figure 6.5 Radiance distribution of each calibration panel per HSI campaign.....	192
Figure 6.6 Comparison of two Rikola HSI scenes	193
Figure 6.7 Example for detectable, narrow spectral absorptions caused by REE minerals	194
Figure 6.8 Sampling points, magnetics, and geology at Jaakonlampi.	198

Figure 6.9 Spectral comparison of a PSR3500-handheld spectrum	200
Figure 6.10 High-contrast resolution comparison for different sensors illustrates target resolution	201
Figure 6.11 Comparison of legacy ground magnetic mapping and fixed-wing UAS survey.....	203
Figure 6.12 Two publicly available PlanetScope satellite images at 3 m.....	204
Figure A8.1 Co-occurrence network based on abstract and title keywords.....	219
Figure A8.2 An overview of reported UAS types, research topics and the documented UAS-type.....	220
Figure C8.3 Photograph of an apatite-bearing carbonatite sample from Siilinjärvi	222
Figure D8.4 Training and validation for support vector machine classifications.....	224
Figure D8.5 Cross-section profile plots across the DSM	226
Figure D8.6 Optical microscopy conducted for thin sections.....	227
Figure D8.7. X-ray diffraction pattern for the carbonatite sample.....	228
Figure D8.8. X-ray diffraction pattern for the dolerite sample.....	228
Figure E8.9 Flight lines and error points logged by DJI Mavic.....	229
Figure F8.10 Results from the inversion model.....	233
Figure F8.11 X-components of the magnetization 50 m below the surface.....	234
Figure G8.12 Field test of hyperspectral image acquisition	236
Figure G8.13 Different views depicting the msCam system	238
Figure G8.14 Ground imaging performance test of msCam.....	240
Figure G8.15 Setup for field test scans with the msCam.....	241
Figure G8.16 Geologic test samples	241
Figure G8.17 Examples of recovered flight lines and image positions	242
Figure G8.18 Comparing the commercial UAS eBee Sequoia with msCam.....	244
Figure G8.19 Comparison of reference DSM with msCam DSM.....	245
Figure G8.20 msCam VIS-NIR mosaic image and product from a combination of two flights	246

List of Tables

Table 2.1 Typical technical and application-specific properties of multicopter and fixed-wing UAS.	25
Table 2.2. Comparison of UAS types used in this work.....	27
Table 2.3 General and specific aspects of the data acquisition, processing and integration workflow.....	30
Table 3-1 Technical details of the used UAS	68
Table 3-2 Technical data and settings of the Rikola camera during flight operation.	69
Table 3-3 Acquisition parameters of the created orthophoto and DSM from two cameras.	71
Table 3-4 Parameters of SenSys MagDrone R1 UAS-borne fluxgate magnetometer	71
Table 3-5 Parameters of the magnetic surveys. Survey time includes take-off and landing	73
Table 3-6 Comparison of TMI grid values	82

Table 4-1. Sensors with technical specifications and platforms used during this study.	104
Table 4-2. Value range for magnetic susceptibilities based on reference literature and own measurements.....	119
Table 5.1 Magnetic features identified in the residual magnetic anomaly and in its attribute maps	153
Table D2 Properties of test trenches, information for the UAS surveys.....	223
Table D3. Technical specifications of used cameras.....	223
Table D4 Confusion matrix trench 1.....	225
Table D5 Confusion matrix trench 2.....	225
Table D6 Confusion matrix trench 3.....	225
Table D7 Mineral abundance from a carbonatite–glimmerite zone and a dolerite dyke sample.....	228
Table G8.8. Technical parameters of msCam system.	237
Table G8.9 Processing metrics as generated from Agisoft Photoscan and error statistics for msCam.....	246

I

Chapter 1 – Introduction

The first chapter introduces mineral exploration, the benefits of drone-based surveying and the motivation for the following research. It outlines the main concepts and research objectives that link each chapter. A literature review spanning the last fifteen years maps drone-based research in mineral exploration. The geoscientific potential of drones was shown over a decade ago, when military-grade unoccupied aerial systems were used to measure magnetic phenomena on the seafloor.

However, a lack of guidelines for data processing and workflows, case studies and ease-of-use decelerated the early integration of drones in geoscientific research. Recently, considerable progress in terms of available case studies and technology adoption by the mining industry is observed. An overview regarding drone-based mineral exploration was published in *Nature Reviews Earth & Environment*¹ in the section ‘Tools of the Trade’.

¹ Jackisch, R., 2020, Drone-based surveys of mineral deposits: *Nature Reviews Earth & Environment*, v. 1, p. 187, doi:10.1038/s43017-020-0042-1.

1.1 Introduction and Motivation

1.1.1 Framing mineral exploration

Minerals are vital components for a sustainable growth of modern societies and an increasingly important part for the technologies needed to enable the transfer to a circular and low-carbon economy. Minerals and metals are concentrated only rarely in abundances sufficient to allow economic extraction (Haldar, 2018).

Mineral deposits are not infinite, and so new discoveries are required to satisfy an increasing raw material demand. Furthermore, most of the obvious deposits have been discovered already, requiring exploration efforts to focus on remote and inaccessible areas (e.g., Greenland) or where surface cover obstructs the detection using surficial methods (Dixey, 1949).

At the same time, some metals (e.g., lithium, REEs) have quickly become a critical part of our technology-driven civilization, resulting in exponential growth in demand and associated increases in value. These economic influences provide unique exploration opportunities, as previously uneconomic metal concentrations can become viable deposits. Such volatile market dynamics require quickly deployable and non-invasive exploration techniques.

Additionally, deposits of established commodities (e.g., copper, nickel, cobalt) are becoming harder to find because effortlessly accessible deposits are depleted. Thus, exploration is required in new areas and at greater depths. This increases exploration costs and exacerbates the social challenges surrounding the minerals industry by aggregating the societal footprint of exploration activity (Sánchez and Hartlieb, 2020).

An example technology to increase mineral explorations social acceptance are unoccupied aerial vehicles, or drones, used for non-invasive surveying. Drones are beneficial in most areas where accessibility, climate, and topography could restrict traditional ground exploration. A multi-sensor drone platform can cover various survey methods to capture surface and subsurface information in order to support mineral exploration.

1.1.2 Technological progress and sustainability in mining

Correctly outlining deposit footprints is a problem of differing resolution, scale and dimension, which is also demonstrated by the multitude of current exploration technologies that are available (Figure 1.1). The goal is to identify a deposit footprint by using imperfect sampling strategy at minimal cost. For validation of the subsurface, drilling is most often the single alternative and the highest cost factor in mineral exploration (Dentith and Mudge, 2014).

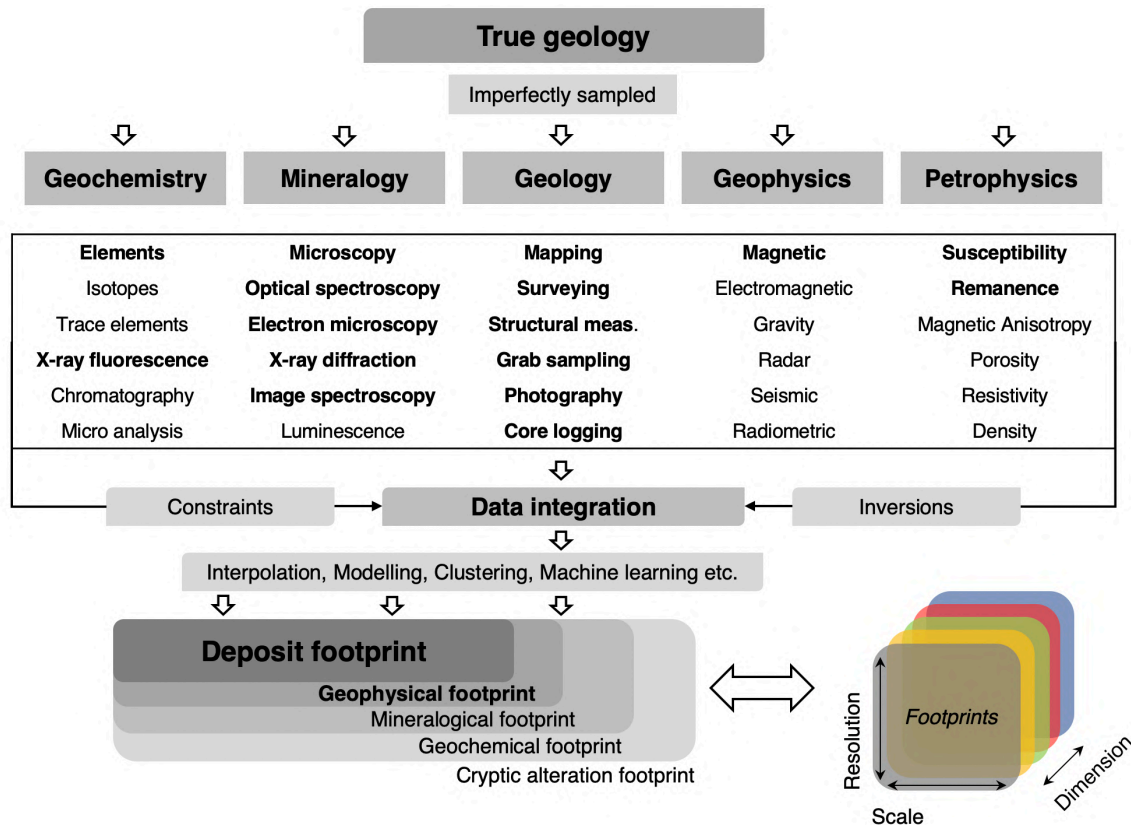


Figure 1.1 Branches of sampling and analytic methods in mineral exploration. The sampling data is integrated and used to define a deposit footprint of variable size. Deposit footprints are a function of scale, resolution, and data dimension. Bold font indicates application in this thesis. Modified with additions, after Leshner et al., 2017.

Mineral exploration as part of mining falls under the sustainable development goals (SDG) of the United Nations and the Paris Agreement. Reaching the SDGs requires modern technologies and transfer of knowledge (United Nations, 2015; Stafford-Smith et al., 2017). Technological progression and material recycling are expected to contribute towards the SDG and will supply a sustainable energy-material transition because mining will continue and grow to assure a mineral availability for an economy driven by change (Ali et al., 2017).

Mineral exploration and the subsequent mineral extraction are associated irrevocably with issues in sustainable development (Thorsteinsdottir et al., 2020). It is apparent that, in order to achieve sustainable growth, non-invasive exploration methods are preferred, for example

airborne geophysics, passive seismic, and remotely controlled machines (Kesselring et al., 2020; Malehmir et al., 2020; Sánchez and Hartlieb, 2020).

Drones, as part of a strategy to provide innovative technologies in exploration, can directly contribute to many of the SDGs. From the 17 formulated SDGs of 2015, I identify ten goals where multi-sensor drones have or could have an impact (Figure 1.2). The figure illustrates where drones have potential impact on some of the problems defined in the SDGs.

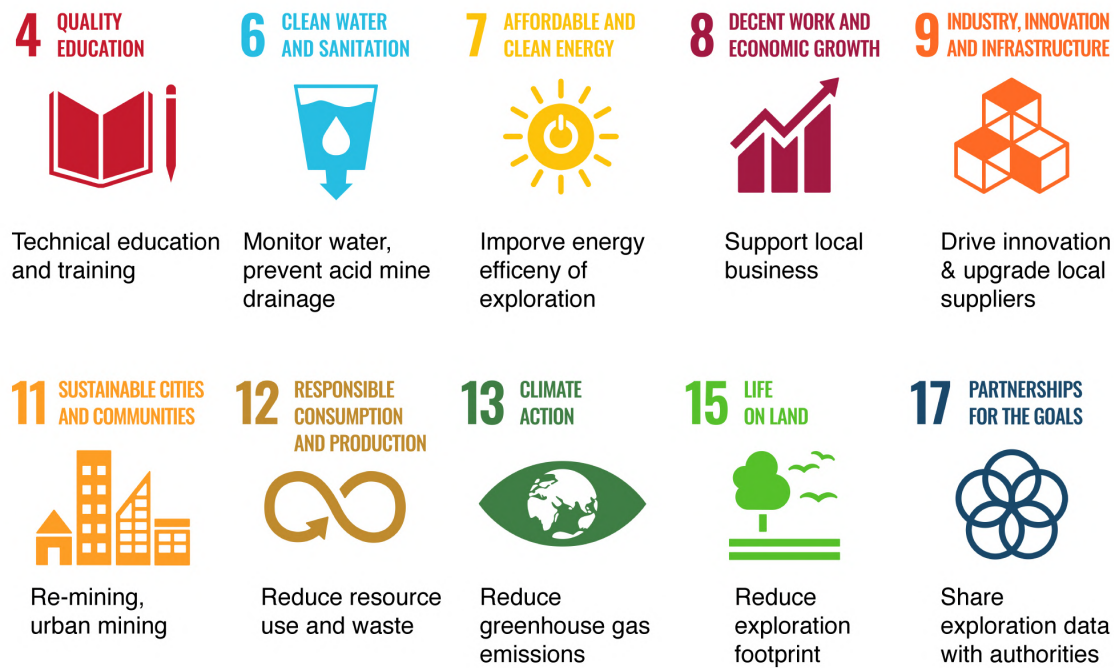


Figure 1.2 Good impact of non-invasive, small-scale drone technology on the exploration & mining industry in the framework of the UN sustainable development goals. Modified after Responsible Mining Foundation (2020).

New exploration technologies can impact the resource estimations for individual ore deposits, driven by innovation in commercial and academic research (Upstill and Hall, 2006). With an increasing or dynamic mineral demand and higher commodity revenue, a re-exploration of matured mineral provinces is possible. That can happen when certain metal supply chains become critical. Criticality can be induced by numerous factors, including social, economic, political as well as actual abundance shortage in the crust (Lusty and Gunn, 2014). Social factors could be the license-to-operate and a lack of risk affection in the local communities. Economic and political aspects could be a distrust in innovation with an uncertain return of invest, and insufficient or lacking legal frameworks that support mineral exploration activities. Nonetheless, due to economic pressure, new frontiers of minerals exploration will be reached in the near future such as deep-sea beds and the arctic regions (Lusty and Gunn, 2014), which are highly susceptible to environmental impacts. Scientific UAS-based magnetic surveys were conducted over deep-sea regions (Gee et al., 2008), and doing so is quicker and more cost-

effective than vessel-towed sensor survey. While sea-bed mining is facing extreme knowledge and legislative gaps, the incentive of reserve raw materials for future generations in ocean-accessing less developed countries is crucial in sustainable development (Levin et al., 2020).

On the other hand, arctic exploration, for example Northern Canada, Siberia, and Greenland is in steady progress. Government and industry are proactive to create frameworks for social sustainability to grow skill, employment and economic security, but the factual contribution of mining to Greenland's economy was reported as modest despite the expectations (Tiainen, 2016). This might change rapidly due to global warming (Shepherd et al., 2020) which will open new sea routes, thaw permafrost soil and reduce inland ice which will uncover new land. Yet, knowledge about impacts on climate change, sustainable development, economic evaluation and social acceptance of mining in the arctic is incomplete and requires further research (Tolvanen et al., 2019).

1.2 Benefits of UAS in mineral exploration

UAS have the potential to support mine activities during a project's mine life cycle (exploration, exploitation, to closure and remediation (Park and Choi, 2020)). UAS present a compromise between coverage and observation scope, and are indispensable when land access is impossible, dangerous or logistically complex (Figure 1.3), showing also the interoperability of UAS and their sensors to contribute in most different fields. UAS-based data is suitable to seamlessly close the data space between groundwork and airborne-based surveying. A UAS can carry lightweight sensors (e.g., ~10 kg) that detect, for example, changes in the geomagnetic field and measure a continuous spectrum of reflected electromagnetic radiation in the visible and near infrared wavelength range.

UAS close exploration survey gaps, where established airborne or helicopter methods cannot be applied, due to flight safety concerns. In areas where ground survey is not feasible or dangerous, and for repetitive or monotonous tasks, UAS surveying can replace ground surveying (Lane and Stoll, 2017).

On the African continent, where high temperatures, strong winds and vast areas with minimal infrastructure defy field work, UAS-based exploration is employed and the benefits surpass the challenges by providing high-resolution data in greenfield and brownfield areas (Booyesen et al., 2019).

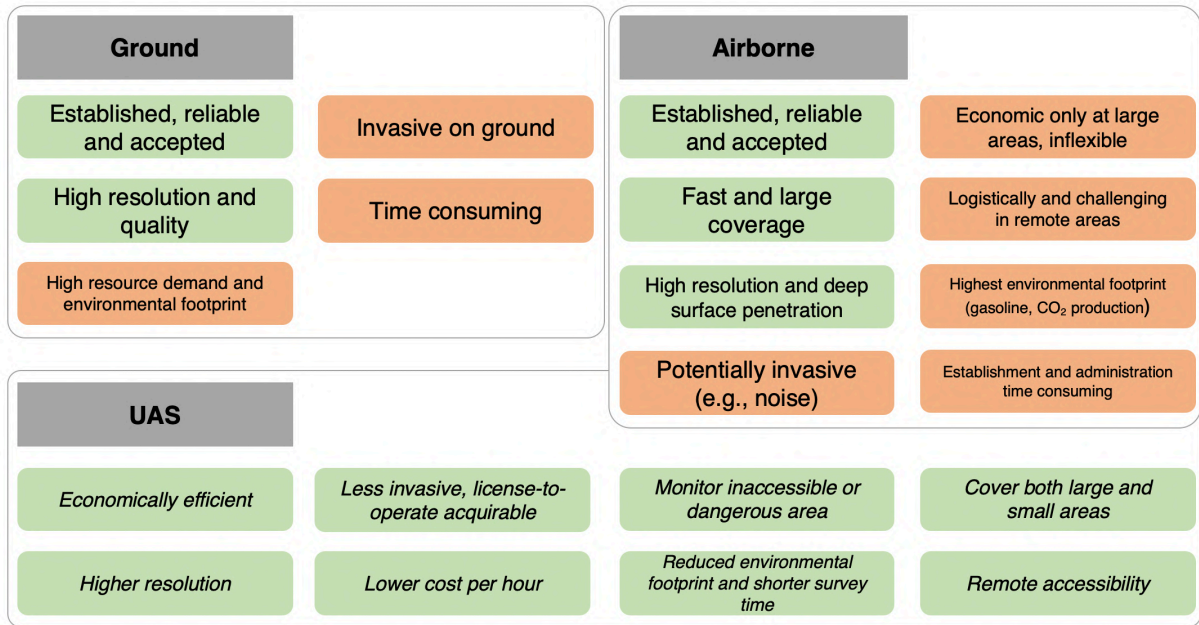


Figure 1.3 Advantages and disadvantages of survey categories: ground, airborne or UAS-borne methods. UAS and manned aircraft-based methods share common traits but differ in their survey capability, resolution and coverage. Green colour shows advantage, orange colour indicates challenges or problems.

Flexible surveying technologies (UAS) would positively impact invasive actions such as drilling and sampling campaigns. UAS surveys have the potential to provide more cost effective geophysical and remote sensing data and high resolution field mapping data. UAS help to increase outcrop coverage and data density that can direct drilling and ground-sampling campaigns towards new targets, among others (see Gloaguen et al., 2018). Conventional ground surveys (e.g., soil and rock sampling) are highly-detailed but can only cover some tens of kilometres per day. Ground survey also cannot capture the regional-local surface patterns visible in orthoimages. Regional-scale reconnaissance and mapping by aircraft, helicopter and satellite does not provide sufficient resolution to effectively map geological features on a small scale, e.g., at 1 km² (Jackisch, 2020).

UAS can potentially

1. present an economical alternative to airborne survey and optimize ground survey with more area per unit cost,
2. provide straightforward aerial access to small or inaccessible targets,
3. reduce risk for personnel and investment,
4. be more environmentally friendly.

Referring to point 1.), economic alternatives reduced costs and the feasibility to conduct smaller surveys as alternative to airborne or ground surveying.

Regarding 2.), exploration surveys are time consuming, costly and traditional airborne surveying using airplane and helicopter begins to be feasible at larger (> kilometre) scale. It requires extended planning, administrative labour and proximity to an airport or helipad. Ground survey demands human workforce, produces a large environmental footprint and is slower.

Different types of data are often needed to identify mineral resources, and success connects directly to data quality and interpretation. Successful exploration using UAS should deliver a similar data quality, when compared to the alternatives. Additionally, the UAS must be robust to fly and measure data regardless of most weather conditions and with a guaranteed return-to-home capability. Regarding data quality, a UAS multi-sensor system should prove that noise disturbance from motors, wires, electronics and vibrations are addressed and mitigated. Therefore, a universal quality assurance/quality control (QA/QC) is demanded similar to established geophysical surveying (Teskey et al., 1991; Reeves, 2006).

Further referring to point 2.), one challenge for UAS surveying arises from diverse air traffic regulations in each country, e.g., survey altitude and take-off weight regulations differ (Stöcker et al., 2017). Investment risk also involves that a multi-sensor-UAS system is knowledge intensive, requires state-of-the-art sensor technologies and must be flexible to technical improvements (e.g., battery lifetime, motor replacement, modularization). A large benefit of UAS is the reduced logistics for equipment during transport in remote areas, and has been demonstrated even in harsh arctic environments (Parshin et al., 2018; Gaffey and Bhardwaj, 2020).

1.2.1 The integrated UAS-based multi-sensor workflow

A high benefit of UAS-based methods is multilayer data integration. An integration of multiple sensors creates comprehensive data that is more than the sum of its parts, and results in a significant advantage over a single data source. (Chung and Fabbri, 1993; Hall and Llinas,

1997; Khaleghi et al., 2013). Information layers from multiple sensors can be overlapped or merged, increasing the detection probability and reliability of exploration targeting with a more accurate survey of the environment. Sensor integration fuses the data from each sensor type and uses different processing algorithms to provide a model, for example from the geology. Mapping is improved by correlating data from external sources such as legacy maps, ground control points as well as satellite and airborne data that exploit overlapping fields of view. The resulting resource or structural model balances the strengths of the different survey methods.

Mapping-based predictions can subsequently use the information provided by sensor integration to support more meaningful interpretations and refine relationships between measured parameters (Torppa et al., 2019). Integrated hyperspectral and magnetic airborne- and helicopter studies are applied, for example in geology, volcanology (Slavinski et al., 2010; Miller et al., 2020) and mineral mapping.

Active instruments, for example light detection and ranging (Lidar) sensors scan the surface topography using lasers (Kaňuk et al., 2018). Experimental electromagnetic (EM) sensors measure electromagnetic conductivity of the subsurface (Götze et al., 2014; Bastani et al., 2020) and ground penetrating radars acquire subsurface images (García-Fernández et al., 2020).

However, the aforementioned sensor systems share a high payload, significant power consumption and noise susceptibility resulting in technical barriers towards an integrated system beyond the demonstrator stage. Furthermore, processing routines are delicate and increase the development period for each system. Passive hyperspectral, multispectral and magnetic instruments reduced their size and power consumption significantly during recent years. Carried by UAS in conjunction with high-resolution visible true colour (RGB) cameras, the combination of hyper and multispectral cameras with magnetic sensors offers a promising solution with decreased data ambiguity, high increased signature confidence and data consistency.

RGB cameras acquire colour, texture and shading in high-resolution images to create topographic models, for example of geology (Madjid et al., 2018). Hyper- and multispectral cameras measure surficial spectral absorption properties that, for example, indicate the presence of an iron alteration associated with a local mineralisation or environmental contamination (Jackisch et al., 2018). Hyperspectral image spectroscopy can precisely identify surface materials and provide high resolution in the visible and near-infrared electromagnetic wavelengths. It also adds structural or topological feature information in otherwise indistinguishable surface domains (Lorenz et al., 2021). UAS-based spectroscopic imaging reached a maturity over the last years, accelerated from agriculture research (Aasen et al., 2018).

Subtle anomalies measured by magnetic sensors identify variations in rock properties. The joint data can be used to determine the frequency and composition of minerals for direct and indirect targeting. In this way, mineral deposit footprints can be described more accurately (Cunningham et al., 2018).

Each sensor type has inherent strengths and weaknesses in geologic scenarios. Multispectral cameras are robust at accurately mapping large or inaccessible areas in multiple discrete colour channels (Turner et al., 2020) but in general, image spectroscopy and RGB mapping requires sufficient daylight and is susceptible to non-geologic covering agents, such as water, snow, vegetation and shadow. Magnetometers can detect subsurface structures and susceptibility contrast accurately, but the nature of geophysical signals is ambivalent and profits highly from auxiliary data. Magnetic systems do not measure between survey lines, making interpretations based on interpolated grids ambiguous (Dentith and Mudge, 2014). Therefore, UAS-based magnetic data processing routines are researched increasingly (Gavazzi et al., 2019).

Magnetic surveying is a primary exploration tool in geophysics and applicable for most deposit types. Ore deposits that were discovered and explored using magnetics are plenty, e.g., massive sulphides, porphyry-Cu, skarns, paleo-drainage placers, carbonatites, and obviously iron ores to name a few (Dentith and Gunn, 1997). UAS-based multi-sensor data integration provides a basis, from which to assess impacts of exploration and post-mining activities, for example bench failure, soil erosion and acid mine drainage (Flores et al., 2021).

Built on case studies, this thesis explores the advantages and disadvantages of image spectroscopy and magnetic sensing in UAS-based exploration scenarios. All aforementioned factors resulted in the choice of those sensors. The UAS as a platform links geology, remote sensing and magnetics. A schematic workflow lays out the used data integration framework of this thesis (Figure 1.4). The three data-source pillars of this work are image spectroscopy, magnetics and photogrammetry.

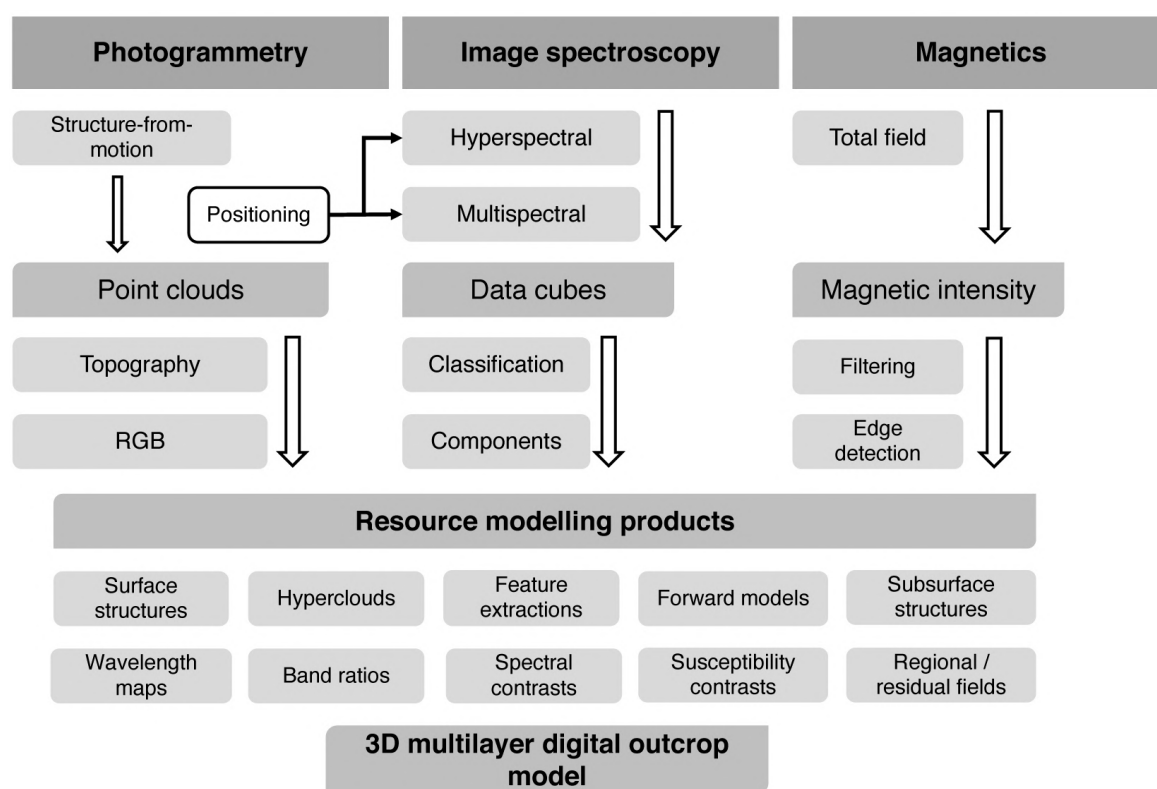


Figure 1.4 Generalized top-down data-integration workflow using UAS-based sensors to model a digital multi-layer outcrop. Data products shown are described in the subsequent chapters.

1.2.2 Body of literature regarding UAS technology in mineral exploration

A semantic text analysis using keywords that cover magnetic and spectroscopic UAS-based surveying in mineral exploration and geology was conducted. Available literature of the years 2005–2020 was reviewed. Preliminary search approaches showed only a small number of reported peer-reviewed research articles, therefore a review of extended abstracts and conference papers was included to provide a more complete body of literature.

In general, the application of UAS is growing in various geosciences, including exploration and mining (Park and Choi, 2020). The literature data base SCOPUS (www.scopus.com, last accessed 06.11.2020) was used in title-abstract-keyword-based search (Appendix A). A screening of the manuscripts reveals a near-even distribution between primary research articles (52 %) and conference papers (45 %), and the remaining texts are either reviews or books.

The United States of America is leading publishing country and followed by China and Italy. Six of the ten leading countries are in Europe. A nearly exponential growth for UAS use is observed at around 2012, while the trend to use magnetics started later (end 2017, Figure 1.5). As reported in 2014 (Colomina and Molina, 2014), the majority of early UAS applications employed small unoccupied aerial vehicles (UAV) and off-the-shelf camera systems. A driver in the use of hyperspectral image analysis and processing is precision farming, but those

publications were excluded here. The number of published applications of UAS-based hyperspectral methods in geology or exploration is less than twenty contributions only, at the time.

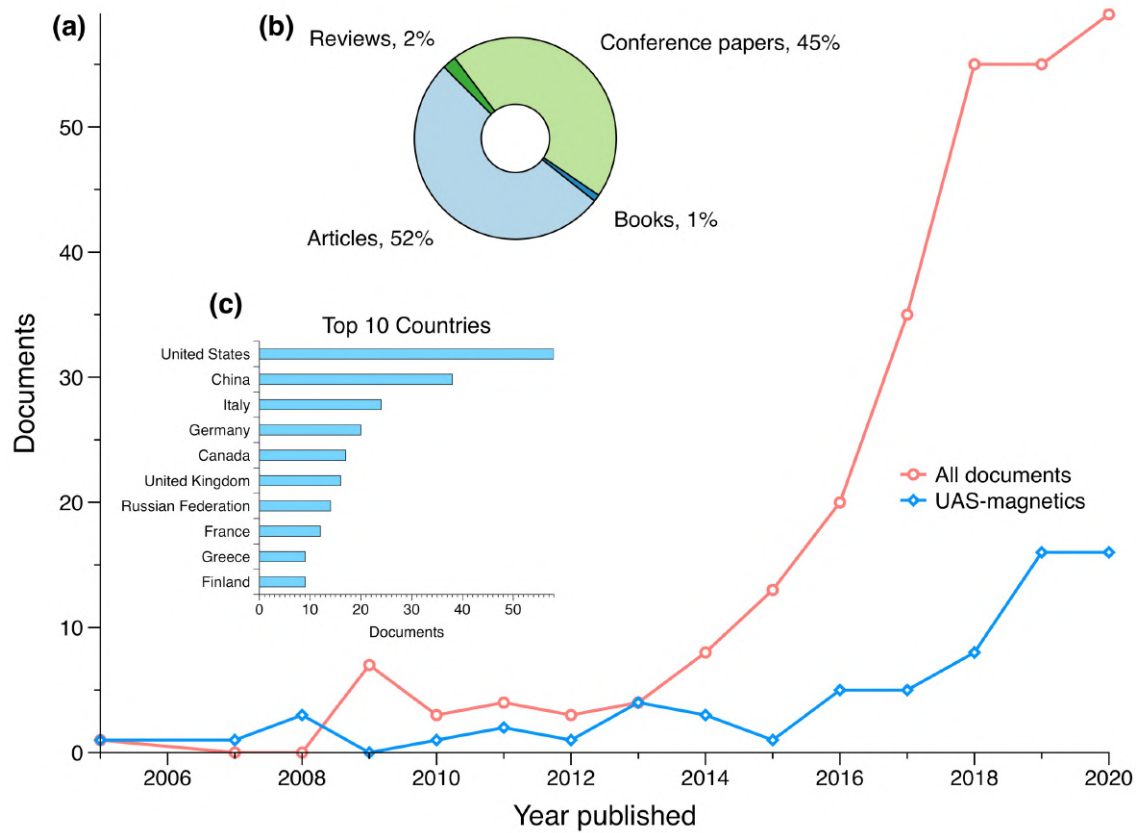


Figure 1.5 Screened body of literature retrieved from SCOPUS. (a) Development of literature comparing all selected documents ($n = 277$) with the selection especially regarding UAS-based magnetic research ($n = 67$). (b) Composition of literature classified for full articles, conference abstracts, books or book chapters, and reviews. (c) The ten leading countries in terms of publication origin.

Magnetic surveying is the largest field and represents 29 % of the studies (Figure 1.5a; Appendix A). UAS type, sensor or study parameters such as surveyed surface area and total survey line length are the most important parameters. Not all texts contain information on those parameters. The principal differentiations of UAS types found are multicopter, fixed-wing, helidrone, airship or multiple types.

Magnetic sensors are differentiated between scalar (e.g., proton or optically pumped) and vector (Fluxgate or Förster-sensor) magnetometers (Telford et al., 1990; Kearey and Brooks, 1991; Hinze et al., 2013). About half of the reviewed articles employ multicopter using scalar magnetometers, and often the GEM Systems Dronemag (GSMP-35U/25U, optically pumped magnetometer) is used. This relates presumably to its early market introduction off-the-shelf UAS solution (EEGS, 2016). Some studies did not provide the type of magnetometer, but the

‘UAV’ (cluster 1) connects to all other keywords in the network. Unsurprisingly, it reflects the literature search target for drone-based applications. It is practical to view location and distance between clusters and keywords. ‘Geologic mapping’ (cluster 4) builds an intermediate cluster between ‘geophysics’ (cluster 3) and ‘UAV’ (cluster 1). Interestingly, ‘Structure-from-motion’ (SfM; cluster 2) and ‘photogrammetry’ (cluster 1) do not fall under one cluster. It appears that SfM is used mainly as a term in aerial photography, mapping and elevation modelling, while photogrammetry is an umbrella term that connects to ‘cameras’, ‘GPS positioning’, light-detection and ranging (‘Lidar’) and ‘3D model’. ‘Mineral exploration’ (cluster 4) stands separated from ‘UAV’ (cluster 1), but also to ‘geophysics’ (cluster 3) and ‘hyperspectral mapping’. The network indicates that UAS-based geophysics and image spectroscopy are insufficiently connected. This analysis suggests there is a research gap with respect to the integration of spectroscopy and magnetic technologies.

I apply the same VOS methods to create a text co-occurrence network, based on abstract and title text (~67,900 words, Appendix A), therefore contextually driven by the authors without automatically provided keywords from the library database system. There appear two main clusters: cluster 1 contains generally the concepts evolving around UAS, sensor payload and time, mining, magnetics, weight and survey. The second cluster involves geotechnical-geotechnical applications (e.g., Rauhala et al., 2017) of UAS, including terms such as ‘digital elevation model’, ‘photogrammetry’, ‘topography’, ‘fault’, ‘fracture’, ‘high resolution’ among others. This seems to reinstate the earlier appearance and use of light-weight RGB cameras on consumer drones (Niethammer et al., 2010; Bemis et al., 2014), for example the DJI Phantom series.

Furthermore, the abstract-title based analysis draws a similar semantic landscape as the database-keyword analysis. The thematic zones of magnetics and spectroscopy show little overlap, as being due to a lack of integration of the two sensor types. Nonetheless, UAS are used in exploration workflows and already provide information for mineral exploration in early prospects, brownfield mapping and remediation (e.g., waste dumps, tailings). For example, UAS-based magnetic surveys are used in exploration project areas in Canada. Data from international press releases (www.skyharbourltd.com/news-media/news/news-display/index.php?content_id=597, last accessed 17.11.2020 and www.newsfilecorp.com/release/48390, last accessed 17.11.2020), report 402 km and ~500 km of drone-based flight lines at 20 m and 40 m line distance. Both surveys cover different geological targets, and the target is to define prospective drill sites.

In Australia, drone-based magnetics are used for hard-to-access targets in the vast outback, with plenty of dense bushes and shrubland vegetation. The vegetation inhibits ground-based surveying by human operators, but drones can measure faster and with data resolution nearly similar to ground magnetics (according to Chris Wijns, exploration geophysicist, personal communication to Moritz Kirsch, 10.11.2020).

In Finland, an important provider of drone-based geophysical services (Radai Oy, Oulu, Finland) with focus on pure magnetics surveyed 15,000-line kilometres in 40–50 field days during 2019, including the non-survey days where wind, precipitation and harsh temperatures delay operations. The UAS-based magnetic system is cost-effective between 200–10,000-line kilometres, but it does not replace ground or manned aircraft survey (Ari Saartenoja, CEO Radai Oy, personal communication, 17.11.2020).

It appears that UAS-based magnetics fills a specific niche according to the required survey parameters, linked to terrain, area and target type. The outstanding question that remains is why are UAS-based image spectroscopy and magnetics not integrated sufficiently? Data handling, processing and evaluation routines do exist. The routines are often developed in satellite and airborne applications, in aviation, robotics, machine vision, remote sensing or military use. For example, an often cited numeric calibration for vector magnetometers was applied for the Ørsted or CHAMP magnetic mapping satellite missions (Merayo et al., 2000). Magnetic airborne data acquisition routines have been developed for decades (Leliak, 1961) and the magnetic method used in mineral exploration has itself developed into a primary exploration tool (Nabighian et al., 2005a).

Similar trends do exist in hyperspectral mineral exploration, where image processing routines and geologic remote sensing methods are adapted from satellite data protocols (Goetz et al., 1985; van der Meer et al., 2012a). To date, most methods lack a direct transferability for UAS-based application and require adaptations. Specifically, for UAS-based hyperspectral and magnetic surveying in mineral exploration (Jakob et al., 2017; Jackisch et al., 2020).

1.3 Research objective and structure of the thesis

The overarching contribution of this thesis is the investigation of UAS-based multi-sensor data acquisition, processing and integration provided through case studies, conducted in mining environments. I apply and adapt concepts from geologic satellite remote sensing (van der Meer et al., 2012b), airborne magnetic surveying (Nabighian et al., 2005b) and photogrammetric modelling (Bemis et al., 2014) in UAS-based applications. Thus, the work in this thesis focuses

on evaluating and advancing necessary acquisition and integration workflows. I define the main objectives as following:

1. A first objective is to examine data acquisition strategies for UAS-based magnetics and image spectroscopy. Data from multicopter and fixed-wing UAS-borne magnetics, and multicopter-borne hyperspectral images provide the main data basis. Feasible data resolution, time or effort per survey line/image and external conditions of the experimental UAS surveys require a discussion. The acquisition of ground truth data (e.g., samples, spectra, magnetic susceptibility) is part of each case study. Magnetic ground survey data is included to verify UAS-based magnetics. Fixed-wing UAS-based multispectral image acquisition is a secondary objective. The development, testing and optimization of a prototype multispectral camera system, which will be designed for high-velocity imaging with a fixed-wing UAS, is a side objective.
2. Secondly, the evaluation of UAS-based data processing is necessary to produce exploitable data products. Challenges such as poor imaging conditions, proxy targeting and high data dimensionality are inherent processing issues and require examination. Conditions that hamper optical data processing involve sensor-related noise, steep terrain, low solar angles and dark or inhomogeneous surface material. Those conditions are addressed by using approved topographic-radiometric corrections (Jakob et al., 2017b) and testing of novel image processing routines for dimensionality reduction, feature extraction and filtering. Magnetic processing includes the application of standard airborne methods, levelling and grinding workflows. Proper data processing is crucial, because fixed-wing and multicopter UAS-based data inherit platform specific issues which could impede data integration.
3. The third objective of this thesis is the assessment of UAS-based data-driven modelling in data integration. Integrated data products provide the basis for further data analysis, image classification and geologic mapping. Important for evaluation are spectral comparisons, classification accuracy assessment and magnetic survey line analysis. Magnetic data integration includes magnetic gridding and forward modelling. Spectral indices calculation, supervised and unsupervised image classification, structural mapping, resource modelling and topographic analysis are follow-up objectives for interpretations in each case study.

This thesis is structured in the following:

In **Chapter 2**, the UAS are introduced and described. An overview is provided of the workflow, and the application of optical and magnetic sensors to the case studies. The chapter also contains a brief overview of techniques used in remote sensing and magnetics.

Chapters 3–5 present the results of the three case studies, whereof **chapter 3** and **4** have been published as primary research articles, and **chapter 5** is in preparation for journal submission.

Chapter 3 (paper 1) presents data acquisition as proof-of-concept based on the field work results in the Finnish Otanmäki Fe-Ti-V brownfield area. The focus is on high-resolution direct targeting of iron oxides (hematite, magnetite) using multicopter UAS-based magnetics and multicopter hyperspectral imaging. Data integration is shown for an outcrop from which ground magnetic susceptibility and ground spectroscopy was acquired for validation. We show how UAS-based magnetic surveying can reach a detail close to ground-based magnetics at a fraction of time.

Chapter 4 (paper 2) builds around the study outcrops at the Finnish Siilinjärvi phosphate mine site. We apply UAS-based methods with a focus on processing for data-driven integration and modelling. For direct surface and indirect subsurface targeting, we use mainly fixed-wing magnetics, multicopter-based hyperspectral images and structural mapping from photogrammetric point clouds. Field conditions such as topography, illumination and area size were similar in the first two studies. The main goal of this study is a comprehensive integration workflow to simplify geologic mapping with drones.

The third study is presented in **Chapter 5** (paper 3) and provides a demonstration of the multi-sensor UAS-system used on a large, structurally complex area in Qullissat, Greenland. We adopted the formerly introduced methods and included selected data from legacy exploration campaigns. Arctic field conditions challenge our multispectral image acquisition and require adapted magnetic flight lines to maintain good data quality. Nonetheless, the study illustrates how regional geologic information synergizes with UAS-based data integration and interpretation.

Chapter 6 addresses recurring issues and the added value of our multi-sensor solution. Topics discussed are scale and resolution of the acquired data during this thesis.

Chapter 7 provides a perspective on different and future sensor generations, an outlook on the high-velocity multispectral camera system in development and the conclusion of this thesis.

References

- Aasen, H., Honkavaara, E., Lucieer, A., and Zarco-Tejada, P.J., 2018, Quantitative remote sensing at ultra-high resolution with UAV spectroscopy: A review of sensor technology, measurement procedures, and data correction workflows: *Remote Sensing*, v. 10, p. 1–42, doi:10.3390/rs10071091.
- Ali, S.H. et al., 2017, Mineral supply for sustainable development requires resource governance: *Nature*, v. 543, p. 367–372, doi:10.1038/nature21359.
- Bemis, S.P., Micklethwaite, S., Turner, D., James, M.R., Akciz, S., Thiele, S.T., and Bangash, H.A., 2014, Ground-based and UAV-Based photogrammetry: A multi-scale, high-resolution mapping tool for structural geology and paleoseismology: *Journal of Structural Geology*, v. 69, p. 163–178, doi:10.1016/J.JSG.2014.10.007.
- Booyesen, R., Zimmermann, R., Lorenz, S., Gloaguen, R., Nex, P.A.M., Andreani, L., and Möckel, R., 2019, Towards multiscale and multisource remote sensing mineral exploration using RPAS: A case study in the Lofdal Carbonatite-Hosted REE Deposit, Namibia: *Remote Sensing*, v. 11, doi:10.3390/rs11212500.
- Burkin, J.N., Lindsay, M.D., Occhipinti, S.A., and Holden, E.J., 2019, Incorporating conceptual and interpretation uncertainty to mineral prospectivity modelling: *Geoscience Frontiers*, v. 10, p. 1383–1396, doi:10.1016/j.gsf.2019.01.009.
- Chung, C.-J.F., and Fabbri, A.G., 1993, The representation of geoscience information for data integration: *Nonrenewable Resources*, v. 2, p. 122–139.
- Colomina, I., and Molina, P., 2014, Unmanned aerial systems for photogrammetry and remote sensing: A review: *ISPRS Journal of Photogrammetry and Remote Sensing*, v. 92, p. 79–97, doi:10.1016/j.isprsjprs.2014.02.013.
- Cunningham, M., Samson, C., Wood, A., and Cook, I., 2018, Aeromagnetic Surveying with a Rotary-Wing Unmanned Aircraft System: A Case Study from a Zinc Deposit in Nash Creek, New Brunswick, Canada: *Pure and Applied Geophysics*, doi:10.1007/s00024-017-1736-2.
- Gunn, P.J., and Dentith, M., and, 1997, Magnetic responses associated with mineral deposits: *AGSO journal of Australian geology & geophysics*, v. 17, p. 145–158.
- Dentith, M., and Mudge, S.T., 2014, *Geophysics for the Mineral Exploration Geoscientist*. (Ed.) Cambridge University Press:, doi:10.1007/s00126-014-0557-9.
- Dixey, F., 1949, Modern Methods of Mineral Exploration: *Nature*, v. 164, p. 171–174, doi:10.1038/164171a0.
- van Eck, N.J., and Waltman, L., 2014, Measuring Scholarly Impact: 285–320 p., doi:10.1007/978-3-319-10377-8.
- van Eck, N.J., and Waltman, L., 2010, Software survey: VOSviewer, a computer program for bibliometric mapping: *Scientometrics*, v. 84, p. 523–538, doi:10.1007/s11192-009-0146-3.
- Van Eck, N.J., and Waltman, L., 2019, VOSviewer Manual version 1.6.10: CWTS Meaningful metrics, www.vosviewer.com/documentation/Manual_VOSviewer_1.6.10.pdf (last access 28.01.2022).
- EEGS, 2016, Special Issue on the Application of Drone Technology for Geophysics.: *FastTIMES*, p. 66.

- Flores, H., Lorenz, S., Jackisch, R., Tusa, L., Contreras, I.C., Zimmermann, R., and Gloaguen, R., 2021, UAS-Based Hyperspectral Environmental Monitoring of Acid Mine Drainage Affected Waters: Minerals, v. 11, doi:10.3390/min11020182.
- Gaffey, C., and Bhardwaj, A., 2020, Applications of Unmanned Aerial Vehicles in Cryosphere: Latest Advances and Prospects: Remote Sensing, v. 12, doi:10.3390/rs12060948.
- García-Fernández, M., Álvarez López, Y., De Mitri, A., Castrillo Martínez, D., Álvarez-Narciandi, G., and Las-Heras Andrés, F., 2020, Portable and Easily-Deployable Air-Launched GPR Scanner: Remote Sensing, v. 12, p. 1833.
- Gavazzi, B., Le Maire, P., Mercier de Lépinay, J., Calou, P., and Munsch, M., 2019, Fluxgate three-component magnetometers for cost-effective ground, UAV and airborne magnetic surveys for industrial and academic geoscience applications and comparison with current industrial standards through case studies: Geomechanics for Energy and the Environment, v. 20, p. 100117, doi:10.1016/j.gete.2019.03.002.
- Gee, J.S., Cande, S.C., Kent, D. V., Partner, R., and Heckman, K., 2008, Mapping geomagnetic field variations with unmanned airborne vehicles: Eos Transactions American Geophysical Union, v. 89, p. 178–179, doi:10.1029/2008EO190002.
- Gloaguen, R. et al., 2018, The need for multi-source, multi-scale hyperspectral imaging to boost non-invasive mineral exploration., in International Geoscience and Remote Sensing Symposium (IGARSS), v. 2018- July, doi:10.1109/IGARSS.2018.8518742.
- Goetz, A.F.H., Vane, G., Solomon, J.E., and Rock, B.N., 1985, Imaging Spectrometry for Earth Remote Sensing: Science, v. 228, p. 1147–1153, doi:10.1126/science.228.4704.1147.
- Götze, H.-J., Afanasjew, M., Alvers, M., Barrio-Alvers, L., Börner, R.-U., Brandes, C., Eröss, R., Menzel, P., Meyer, U., and Scheunert, M., 2014, Towards an integrative inversion and interpretation of airborne and terrestrial data, in Tomography of the earth's crust: From geophysical sounding to real-time monitoring, Springer, p. 21–41.
- Haldar, S., 2018, Mineral Exploration Principles and Applications: Amsterdam, Elsevier, 360 p.
- Hall, D.L., and Llinas, J., 1997, An introduction to multisensor data fusion: Proceedings of the IEEE, v. 85, p. 6–23, doi:10.1109/5.554205.
- Hinze, W.J., von Frese, R.R.B., and Saad, A.H., 2013, Gravity and Magnetic Exploration: Cambridge, Cambridge University Press, doi:10.1017/CBO9780511843129.
- Jackisch, R., 2020, Drone-based surveys of mineral deposits: Nature Reviews Earth & Environment, v. 1, p. 187, doi:10.1038/s43017-020-0042-1.
- Jackisch, R., Lorenz, S., Kirsch, M., Zimmermann, R., Tusa, L., Pirttijärvi, M., Saartenoja, A., Ugalde, H., Madriz, Y., Savolainen, M. and Gloaguen, R., 2020, Integrated geological and geophysical mapping of a carbonatite-hosting outcrop in Siilinjärvi, Finland, using unmanned aerial systems: Remote Sensing, v. 12, doi:10.3390/RS12182998.
- Jackisch, R., Lorenz, S., Zimmermann, R., Möckel, R., and Gloaguen, R., 2018, Drone-Borne Hyperspectral Monitoring of Acid Mine Drainage: An Example from the Sokolov Lignite District: Remote Sensing 2018, Vol. 10, Page 385, v. 10, p. 385, doi:10.3390/RS10030385.
- Jakob, S., Zimmermann, R., and Gloaguen, R., 2017, The Need for Accurate Geometric and Radiometric Corrections of Drone-Borne Hyperspectral Data for Mineral Exploration: MEPHySTo-A Toolbox for Pre-Processing Drone-Borne Hyperspectral Data: Remote Sensing, v. 9, doi:10.3390/rs9010088.

- Kaňuk, J., Gallay, M., Eck, C., Zraggen, C., and Dvorný, E., 2018, Technical Report: Unmanned Helicopter Solution for Survey-Grade Lidar and Hyperspectral Mapping: Pure and Applied Geophysics, v. 175, p. 3357–3373, doi:10.1007/s00024-018-1873-2.
- Kearey, P., and Brooks, M., 1991, An introduction to geophysical exploration. 2nd edition: Blackwell Scientific Publications, 263 p.
- Kesselring, M., Wagner, F., Kirsch, M., Ajjabou, L., and Gloaguen, R., 2020, Development of sustainable test sites for mineral exploration and knowledge spillover for industry: Sustainability (Switzerland), v. 12, p. 1–17, doi:10.3390/su12052016.
- Khaleghi, B., Khamis, A., Karray, F.O., and Razavi, S.N., 2013, Multisensor data fusion: A review of the state-of-the-art: Information Fusion, v. 14, p. 28–44, doi:10.1016/j.inffus.2011.08.001.
- Lane, J.W., and Stoll, J.B., 2017, Introduction to this special section: Unmanned autonomous vehicles: The Leading Edge, v. 36, p. 550.
- Leliak, P., 1961, Identification and Evaluation of Magnetic- Field Sources of Magnetic Airborne Detector Equipped Aircraft: , p. 95–105.
- Leshner, M. et al., 2017, Integrated Multi-Parameter Exploration Footprints of the Canadian Malartic Disseminated Au, McArthur River-Millennium Unconformity U, and Highland Valley Porphyry Cu Deposits: Preliminary Results from the NSERC-CMIC Mineral Exploration Footprints Research: Proceedings of Exploration, v. 17, p. 8–12.
- Levin, L.A., Amon, D.J., and Lily, H., 2020, Challenges to the sustainability of deep-seabed mining: Nature Sustainability, v. 3, p. 784–794, doi:10.1038/s41893-020-0558-x.
- Lorenz, S., Ghamisi, P., Kirsch, M., Jackisch, R., Rasti, B., and Gloaguen, R., 2021, Feature extraction for hyperspectral mineral domain mapping: A test of conventional and innovative methods: Remote Sensing of Environment, v. 252, doi:10.1016/j.rse.2020.112129.
- Lusty, P.A.J., and Gunn, A.G., 2014, Challenges to global mineral resource security and options for future supply: Geological Society Special Publication, v. 393, p. 265–276, doi:10.1144/SP393.13.
- Madjid, M.Y.A., Vandeginste, V., Hampson, G., Jordan, C.J., and Booth, A.D., 2018, Drones in carbonate geology: Opportunities and challenges, and application in diagenetic dolomite geobody mapping: Marine and Petroleum Geology, v. 91, p. 723–734, doi:10.1016/j.marpetgeo.2018.02.002.
- Malehmir, A., Gisselø, P., Socco, V.L., Carvalho, J., Marsden, P., Onar-Verboon, A., and Loska, M., 2020, New ways of exploring subsurface with Smart Exploration Solutions: First Break, v. 38, p. 77–89.
- Marjoribanks, R., 2010, Geological methods in mineral exploration and mining: Berlin-Heidelberg, Springer-Verlag, 238 p., doi:10.1007/978-3-540-74375-0.
- van der Meer, F.D., van der Werff, H.M.A., van Ruitenbeek, F.J.A., Hecker, C.A., Bakker, W.H., Noomen, M.F., van der Meijde, M., Carranza, E.J.M., de Smeth, J.B., and Woldai, T., 2012a, Multi- and hyperspectral geologic remote sensing: A review: International Journal of Applied Earth Observation and Geoinformation, v. 14, p. 112–128, doi:10.1016/j.jag.2011.08.002.

- van der Meer, F.D., van der Werff, H.M.A., van Ruitenbeek, F.J.A., Hecker, C.A., Bakker, W.H., Noomen, M.F., van der Meijde, M., Carranza, E.J.M., de Smeth, J.B., and Woldai, T., 2012b, Multi- and hyperspectral geologic remote sensing: A review: *International Journal of Applied Earth Observation and Geoinformation*, v. 14, p. 112–128, doi:10.1016/j.jag.2011.08.002.
- Bastani, M., Johansson, H., Paulusson, A., Paulusson, K., and Dynesius, L., 2020, Unmanned Aerial Vehicles (UAV) and ground-based electromagnetic (EM) systems: *First Break*, v. 38, p. 4.
- Merayo, J.M.G., Brauer, P., Primdahl, F., Petersen, J.R., and Nielsen, O. V, 2000, Scalar calibration of vector magnetometers: *Measurement science and technology*, v. 11, p. 120.
- Miller, C.A., Schaefer, L.N., Kereszturi, G., and Fournier, D., 2020, Three-Dimensional Mapping of Mt. Ruapehu Volcano, New Zealand, From Aeromagnetic Data Inversion and Hyperspectral Imaging: *Journal of Geophysical Research: Solid Earth*, v. 125, p. 1–24, doi:10.1029/2019JB018247.
- Nabighian, M.N., Grauch, V.J.S., Hansen, R.O., LaFehr, T.R., Li, Y., Peirce, J.W., Phillips, J.D., and Ruder, M.E., 2005a, The historical development of the magnetic method in exploration: *Geophysics*, v. 70, doi:10.1190/1.2133784.
- Nabighian, M.N., Grauch, V.J.S., Hansen, R.O., LaFehr, T.R., Li, Y., Peirce, J.W., Phillips, J.D., and Ruder, M.E., 2005b, The historical development of the magnetic method in exploration: *Geophysics*, v. 70, doi:10.1190/1.2133784.
- Niethammer, U., Rothmund, S., James, M.R., Travelletti, J., and Joswig, M., 2010, Uav-based remote sensing of landslides: *International Archives of the Photogrammetry, Remote Sensing and Spatial Information Sciences - ISPRS Archives*, v. 38, p. 496–501.
- Park, S., and Choi, Y., 2020, Applications of unmanned aerial vehicles in mining from exploration to reclamation: A review: *Minerals*, v. 10, p. 1–32, doi:10.3390/min10080663.
- Parshin, A. V, Morozov, V.A., Blinov, A. V, Kosterev, A.N., and Budyak, A.E., 2018, Low-altitude geophysical magnetic prospecting based on multirotor UAV as a promising replacement for traditional ground survey Low-altitude geophysical magnetic prospecting based on multirotor UAV as a promising replacement for traditional ground survey: *Geospatial Information Science*, p. 1–8, doi:10.1080/10095020.2017.1420508.
- Rauhala, A., Tuomela, A., Davids, C., and Rossi, P.M., 2017, UAV remote sensing surveillance of a mine tailings impoundment in Sub-Arctic conditions: *Remote Sensing*, v. 9, p. 1–14.
- Reeves, C., 2006, *Aeromagnetic Surveys. Principles, Practice & Interpretation*: Earthworks, p. 155, doi:10.1007/BF01465543.
- Responsible Mining Foundation, 2020, *Mining and the SDGs: a 2020 status update*: Responsible Mining Foundation, p. 46.
- Sánchez, F., and Hartlieb, P., 2020, Innovation in the Mining Industry: Technological Trends and a Case Study of the Challenges of Disruptive Innovation: *Mining, Metallurgy & Exploration*, v. 37, p. 1385–1399, doi:10.1007/s42461-020-00262-1.
- Shepherd, A. et al., 2020, Mass balance of the Greenland Ice Sheet from 1992 to 2018: *Nature*, v. 579, p. 233–239, doi:10.1038/s41586-019-1855-2.
- Slavinski, H., Morris, B., Ugalde, H., Spicer, B., Skulski, T., and Rogers, N., 2010, Integration of lithological, geophysical, and remote sensing information: A basis for remote predictive geological mapping of the Baie Verte Peninsula, Newfoundland: *Canadian Journal of Remote Sensing*.

- Stafford-Smith, M., Griggs, D., Gaffney, O., Ullah, F., Reyers, B., Kanie, N., Stigson, B., Shrivastava, P., Leach, M., and O’Connell, D., 2017, Integration: the key to implementing the Sustainable Development Goals: *Sustainability Science*, v. 12, p. 911–919, doi:10.1007/s11625-016-0383-3.
- Stöcker, C., Bennett, R., Nex, F., Gerke, M., and Zevenbergen, J., 2017, Review of the Current State of UAV Regulations: *Remote Sensing*, v. 9, doi:10.3390/rs9050459.
- Telford, W.M., Geldart, L.P., and Sheriff, R.E., 1990, *Applied Geophysics*: 770 p.
- Teskey, D., Barlow, R., Hood, P.J., Lefebvre, D., Paterson, N., Reford, M., and Watson, D., 1991, Guide to aeromagnetic specifications and contracts: Geological Survey of Canada, open file, v. 2349, p. 73.
- Thorsteinsdottir, H., Chalmers, B., Waldmeier, C., Yrjö-Koskinen, E., Turley, L., Larrea, C., Marques, I.S., Tolochko, O., Katz, B., and Venuti, S., 2020, Sustainability Reporting in the Mining Sector: Current Status and Future Trends: *United Nations Environment Programme*, 114 pp.
- Tiainen, H., 2016, Contemplating governance for social sustainability in mining in Greenland: *Resources Policy*, v. 49, p. 282–289, doi:10.1016/j.resourpol.2016.06.009.
- Tolvanen, A., Eilu, P., Juutinen, A., Kangas, K., Kivinen, M., Markovaara-Koivisto, M., Naskali, A., Salokannel, V., Tuulentie, S., and Similä, J., 2019, Mining in the Arctic environment – A review from ecological, socioeconomic and legal perspectives: *Journal of Environmental Management*, v. 233, p. 832–844, doi:10.1016/j.jenvman.2018.11.124.
- Torppa, J., Nykänen, V., and Molnár, F., 2019, Unsupervised clustering and empirical fuzzy memberships for mineral prospectivity modelling: *Ore Geology Reviews*, v. 107, p. 58–71, doi:10.1016/j.oregeorev.2019.02.007.
- Turner, R.M., MacLaughlin, M.M., and Iverson, S.R., 2020, Identifying and mapping potentially adverse discontinuities in underground excavations using thermal and multispectral UAV imagery: *Engineering Geology*, v. 266, doi:10.1016/j.enggeo.2019.105470.
- United Nations, 2015, Transforming our world: the 2030 Agenda for Sustainable Development: Division for Sustainable Development Goals: New York, NY, USA, [https://sustainabledevelopment.un.org/content/documents/21252030 Agenda for Sustainable Development web.pdf](https://sustainabledevelopment.un.org/content/documents/21252030%20Agenda%20for%20Sustainable%20Development%20web.pdf).
- Upstill, G., and Hall, P., 2006, Innovation in the minerals industry: Australia in a global context: *Resources Policy*, v. 31, p. 137–145, doi:10.1016/j.resourpol.2006.12.002.

II

Chapter 2 – General methods

This chapter supports the respective research papers of this thesis by introducing theoretical aspects of multi- and hyperspectral imaging and magnetics. An overview of the UAS as the main sensor platform in this thesis is given. An introduction to spectroscopy and the magnetic method provides background information and outlines methodological aspects, especially for detection of mineralogic signatures.

2.1 UAS types, data acquisition and the case study

UAS-based outcrop mapping is supported by a growing set of available sensors and possibilities to map different lithologies. The most common application is RGB-based photogrammetry, from which detailed natural colour orthoimages, high-resolution digital elevation models and 3D point clouds are created (Dering et al., 2019). The developments in sensor technology, spectral filters, and miniaturisation introduced multispectral and hyperspectral cameras as an innovative optical instrument. An extended spectral range of a camera has the means to analyse surface materials, minerals and element proxies. Nevertheless, well-exposed mineralized rock outcrops can be rare, increasing the need to obtain data from the subsurface as an additional data source. The capability to sense below the surface increases the data dimension from 2D (surface) over 2.5D (photogrammetry) to 3D, and adds new possibilities to capture, visualise, interpret and model structural and geologic data.

The UAS is regarded as novel and disrupting technology with the potential to enhance the geologic field toolbox. Indeed, numerous review articles focusing on UAS-based applications were published in the last decade. Relevant for this thesis are mainly contributions that address UAS practices in geology, geomorphology and mining (Lee and Choi, 2016; Ren et al., 2019; Dering et al., 2019; James et al., 2020; Park and Choi, 2020; Said et al., 2020). Most of those reviews and studies include mainly RGB-sensor applications in structural mapping and mine monitoring. Hyperspectral, multispectral and non-magnetic geophysical UAS application in geology and exploration are not always available (Chapter 2). However, UAS-based magnetics were reviewed recently (Kim, 2020), which illustrates a growing maturity of that specific sensor-platform combination. Regarding multi- and hyperspectral imaging, a growing knowledge base exists for UAS usage in agriculture, biodiversity and vegetation mapping (Adão et al., 2017; Aasen et al., 2018; Zhong et al., 2018; Yao et al., 2019; Gaffey and Bhardwaj, 2020). Having said that, many of the imaging methods focusing on vegetation cannot be transferred to geology. Nonetheless, processing and technical or aerodynamic aspects and issues (flight height, endurance, legislation) are similar.

In this work, referring to the introduced sensor integration, I used several UAS platforms to acquire the case study data on field campaigns. All acquired data are geolocated by using information from global navigational satellite systems (e.g., the global positioning systems GPS, GALILEO, GLONASS) and integrated in geographic information systems (GIS). Each data point has a geographic position in a coordinate reference system and obtained an elevation in meters above sea level (asl) or ground level (agl).

2.1.1 Terminology addressing UAS

In this thesis, I focus on small unoccupied aerial vehicles (UAV) below 10 kg of take-off weight. The common term ‘UAV’ is applied in cases where the UAV itself is meant. The definitions for drone systems or UAV differ, according to each user group (Colomina and Molina, 2014). A common UAS definition implies that the overall layout of the system-specific gear includes the UAV, a ground control station, a remote control and position antennas, using GNSS. As in the abbreviation UAS, the term unoccupied/unmanned implies the absence of a human operator (Hassanalian and Abdelkefi, 2017). An autopilot is not mandatory for operation, and UAS surveys have to be monitored by a human operator with the constant ability to interfere and provide control inputs.

2.1.2 Introducing the deployed UAS

Two types of UAS were employed in this work, which are the multicopter (multiple rotors) and the fixed-wing UAS (Figure 2.1). The principal difference between the two platforms is the method of uplift creation. A multicopter generates uplift only through its motor thrust. For fixed-wing UAS, human force (or a catapult) accelerates the UAV till take-off (Figure 2.1a–b), propelled with a small thrust-creating motor, usually situated at the tail or nose. Its wing surface creates uplift by airflow. Therefore, the fixed-wing has longer flight durations relative to multicopter UAS. Payloads for fixed-wing UAS instruments are more limited but the payload depends also on the wing surface area. Also, fixed-wing UAS maintain a permanent velocity, which influences the way data is obtained efficiently during flight. A constant measurement or data stream are preferable. Terrain conditions determine the start and landing points, the lowest flight height and the manoeuvrability near trees, cliffs and other obstacles. Multicopter provide full control over their absolute spatial position, and they can hold their position over or in front of a target to acquire data as needed.

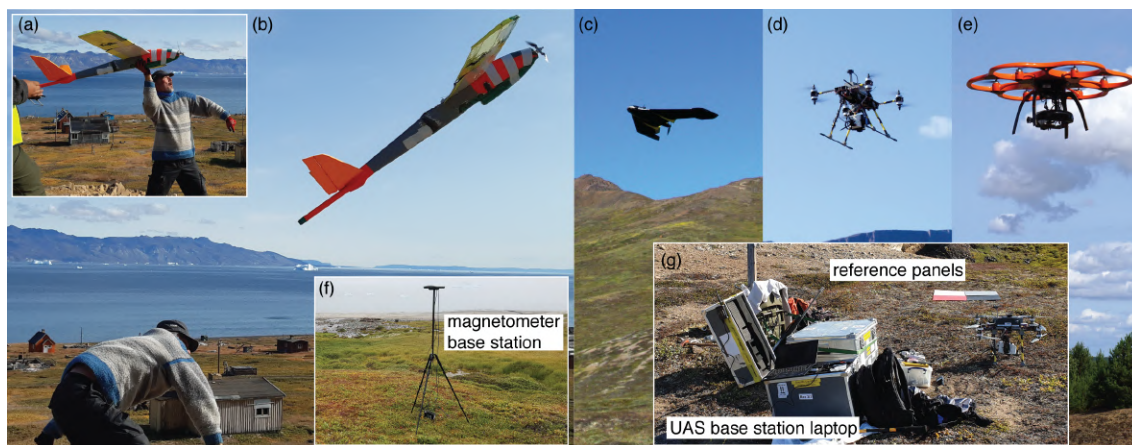


Figure 2.1 UAS types used during field research. (a) Lifting the fixed-wing magnetic survey Albatros UAS under the supervision of the pilot who controls motor thrust during take-off in b. (c) Fixed-wing eBee UAS used for multispectral and high-resolution RGB imaging. (d) Quadcopter Tholeg conducts a hyperspectral survey. (e) Hexacopter Aibot X6v2 conducts a hyperspectral survey. (f) A magnetometer base station records diurnal magnetic field changes. (g) Set-up of a typical UAS base station during flight operations, including field computer and calibration panels (Photo courtesy by Björn Heincke & Robert Zimmermann).

UAS are available in different dimensions, ranging from hand-size to meter-wide of wingspans. Multicopters (Figure 2.1d–e) can be as small as remote-controlled model planes and are controlled remotely and with high precision. For geologic applications in remote or hard-to-access areas, a size that can still be transported by a small ground team provides greater flexibility and is preferable, bearing in mind that batteries, controllers, base stations, reference materials, field computers and further hardware require transportation.

UAS payload is particularly dependent on propulsion system and battery power. Multicopter UAS by are equipped with multiple rotors (Figure 2.1d, e), where pairs of 4, 6, 8, 10 or 12 are common. Accordingly, more motors provide higher trust to transport passive and active sensor systems (usually heavier), and provide higher system redundancy, therefore more safety in the event of a motor failure. Maximum take-off weight (MTOW) of UAS is usually restricted by a legal framework and air traffic regulations. Most sovereign states employ strict air traffic rules, imposing some limitations on a potential UAS-based research (Stöcker et al., 2017). For example, a MTOW > 0.25 kg already requires some form of regulatory procedure in Germany (www.bmvi.de/drohnen, last accessed 04.02.2021). Safety distance to critical infrastructures needs to be maintained at all times or requires special permissions as well as flying over private property or in restricted airspace. Nevertheless, a UAS survey in populated areas involves less risk than a manned flight mission at low altitudes, due to smaller UAV weight, which would create less impact energy in case of a failure (Kroll, 2013).

Table 2.1 Typical technical and application-specific properties of multicopter and fixed-wing UAS.

Characteristics	Multicopter	Fixed-wing
	Technical	
Flexibility	High	medium
Dimension	cm–m	m–dm
Weight range	1–25 kg	1–15 kg
Usual payload	> 10 kg (upper limit)	> 2 kg (upper limit)
Usual flight time	15–45 min battery; >1 h gasoline	1–3 h
Flight altitude	Legally restricted 100–120 m, otherwise 1000–5000 m	
Maneuverability	Excellent, stop-go, direct obstacle evasion possible	poor, predefined flight path preferably, stall, curves
Start/land area	1–2 m ²	30–100 m ²
Connection	radio-telemetry in different frequency bands	

Failure midair safety	emergency landing on spot, return-to-base, parachute, motor redundancy	gliding, parachute, return-to-base
Application		
Typical use	Photography, inspection, photogrammetry, lateral applications, rescue and maintenance, transport, inner-city, animal detection, outcrop scanning	Land survey, land-line and pipe-line inspection, land-use, agriculture, reconnaissance
Sensors (examples)	RGB, multispectral, hyperspectral, infrared, magnetic, electric, gravimetric, Lidar, laser-altimeter, chemical, temperature, thermal, radar, radiometric	RGB, multispectral, infrared, magnetic, electric, Lidar, laser-altimeter, chemical, temperature
Stability	side wind-resistant, vibrations, GPS-glitching possible	front-wind stable, moving
Take-off	stationary	In-run and acceleration, catapult

For this work, the main multicopter UAS (THO-R-PX-8-12) was built by Tholeg, (Glauchau, Germany) and used with different sensors (Figure 2.2). The system can carry up to 5 kg of payload at a MTOW of ~10 kg. The frame is made of rigid, non-magnetic carbon fibre and can be fixed mechanically during field work. The Tholeg UAS is powered by two 7500 mAh Li-polymer batteries enabling a flight time of about 12 min (~2.5 kg payload) to 20 min (with ~800 g payload, e.g., a fluxgate magnetometer with data logger). Flights are controlled by predefined plans with GPS points, and flown in Visual Line of Sight (VLOS). The performance is monitored by software via a radio link, using a 433 MHz telemetry module with up to 5 km range.

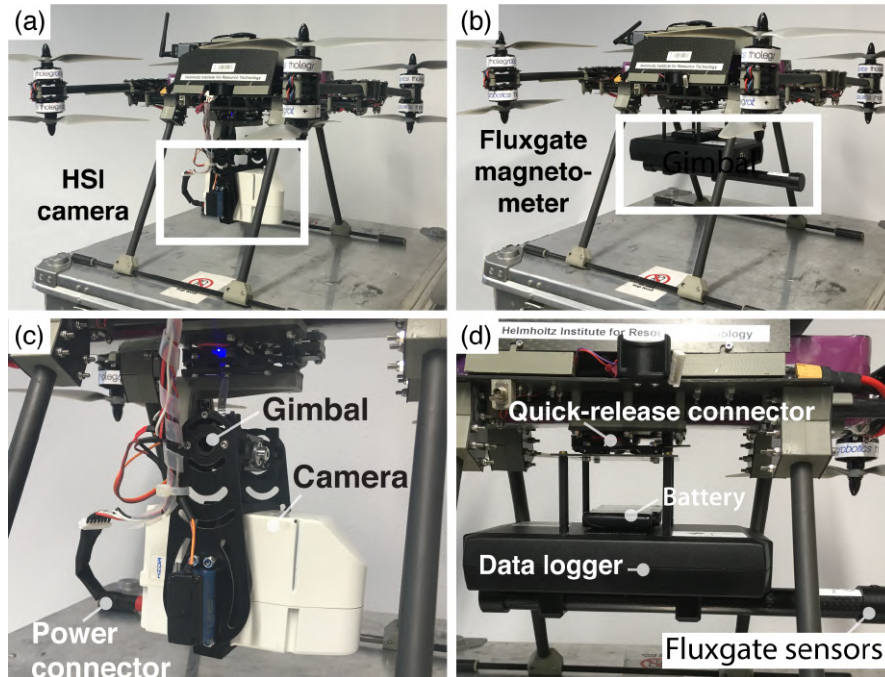







Figure 2.2 Tholeg multicopter with main sensors. (a) HSI camera. (b) With fluxgate magnetometer Magdrone R1. (c) Close-up of HSI camera on a two-axis servo gimbal. (d) Close-up on fluxgate magnetometer.

UAS flight altitude defines image resolution and geophysical signal characteristics. Surveying closer to ground can provide a higher signal resolution. Legal maximum flight altitudes ranges from 100 to 120 m in most countries. An increase in magnetic survey altitude could be advantageous in areas of cemented iron-oxyhydroxide soil layers (ferricrete) to reduce their magnetic influence. A further advantage of UAS for geophysical survey is the high line production rate per time unit. Feasible ranges for fixed-wing magnetics are around 10,000 km per contract (Ari Saartenoja, personal communication, 17.10.2020). Target areas under 5,000–10,000 m² are often covered with multicopter that can offer higher resolutions and precise flight line control.

Table 2.2 summarizes the UAS models used in this work and gives technical parameters.

Table 2.2. Comparison of UAS types used in this work.

UAS model	Tholeg Tho-R-PX8-12	Aibotix Aibot x6v2	Sensefly eBee/eBee Plus	Radai Albatros	DJI Mavic 1 Pro
Type	Multicopter	Multicopter	Fixed-wing	Fixed-wing	Multicopter
Image					
Motors	8	6	1	1	4
Weight (g)	3,500	3,400	700/1,100	5,000	734
Size	70×70×35 cm	105×05×45 cm	96/110 cm wingspan	2.5–2.8 m wingspan	33.5 cm diam.
Flight time ² (min)	12–20	12–15	50	59	27
Speed (m·s ⁻¹)	0–12	0–8	11–30	10–30	0–19
Usual payload (g)	2,000–10,000	2,000	~ 500	2,000	~250
Sensors tested	Rikola HSI camera, digicam, fluxgate mag	Rikola HSI camera, digicam, fluxgate mag	SODA RGB, Sequoia MSI camera	Fluxgate mag, MSI camera msCam	DJI-RGB camera
Fail-safe	Redundant motor	Redundant motor	Glide near home point	Glide near home point	Redundant motor
Durability	High, spare parts abundant	medium, carbon-fibre can break easily, hard to replace	High, wings and sensor modular	High, spare parts abundant and modular	Unknown, Sensor changeable, otherwise closed system
Usual survey area	5,000–10,000 m ²	~5000 m ²	> 2 km ²	> 2 km ²	> 10,000 m ²
Field suitability ³	good	medium	excellent	good	excellent

² Payload-dependent

³ suitability for the field geologist/mineral exploration during extended field work including remote area

2.1.3 Acquired and integrated data types — optical and magnetics

The basis for data acquisition in all disciplines of remote sensing is a sensor deployed on a platform that collects information about a target from a distance. Payload and platform limitations define the used sensors (Manolakis et al., 2016). Sensor weight correlates with its spectral characteristics, available image channels and resolution.

Less sensor channels potentially reduces camera weight and dimension. Therefore, most large-area RGB and multispectral data acquisitions were done using the fixed-wing UAS (Table 2.2). Hyperspectral data was captured using the Senop Rikola (Senop, Kangasala, Finland). Magnetic data acquisition used either a multicopter solution, the Sensys Magdrone R1 (SENSYS Sensorik & Systemtechnologie GmbH, Bad Sarrow, Germany), or the integrated Radaï Oy fixed-wing UAS for geophysical surveys.

Each data acquisition method requires a defined procedure that is introduced in this work. Correspondingly, each data set requires different processing methods, is dependent on conditions during any survey day and inherits specific inaccuracies during data acquisition and processing. Analysis of the data is conducted using a suite of commercial and open-source software platforms. Highly important in this work is the MEPHySTo software package for drone-borne image processing (Jakob et al., 2017).

A second key processing software is Agisoft Photoscan, now Metashape (Agisoft, St. Petersburg, Russia), for structure-from-motion photogrammetric image processing. Structure-from-motion serves as auxiliary data to enable and support hyperspectral and magnetic data integration, georeferencing and interpretation in form of high-resolution orthophotos and 3D models. Workflows and applications are published in numerous studies and reports (Westoby et al., 2012; James and Robson, 2014; Bemis et al., 2014; Gonçalves and Henriques, 2015; Blistan et al., 2016; Thiele et al., 2017; Dering et al., 2019; James et al., 2019, 2020).

Regarding geospatial mapping, Quantum GIS (QGIS Development Team, 2020) for data structuring, mapping and interpretation was used. Further essential software suits are Geosoft Oasis Montaj (Seequent, Toronto, Ontario, Canada) and ModelVision (Tensor Research Pty Ltd, Greenwich NSW, Australia) for geophysical processing and modelling, TecGems (Andreani and Gloaguen, 2016) was used for geomorphologic investigations. For additional data processing, statistical analysis and plotting, Python (van Rossum, Guido and Drake Jr, 1995) and R (RStudio Team, 2020) was used.

2.1.4 Case study approach

This thesis focuses on 3 case studies from high-latitude environments with different geological, topographic and climatic conditions. Important considerations are research design, data acquisition, data analysis, validation, and reliability. Another aspect of case study research is to assess the repeatability and applicability of a method under field conditions, and to describe findings related to the relevant features of a study. Case studies are rooted in real-life scenarios, and hence require a proper justification of all aspects and methods used within (Meyer, 2001; Crowe et al., 2011; Pan and Tan, 2011).

The case study method applied in this thesis aims to conduct the UAS-based field experiments with tailored flight plans and specific sampling, according to the expected geologic targets. Hence, the encountered topographic and surface conditions require a flexible UAS flight planning to ensure safe flight operation at optimal survey coverage. The sensors for data acquisition and the principal processing workflow are similar for the three sites. For example, the Rikola hyperspectral camera and the Magdrone fluxgate magnetometer are not bound to one multicopter type. However, significant differences lie in the integration, analysis, and interpretation of the geologic results, and furthermore in the challenges during each survey.

Lastly, it is essential to present the single case studies in a way to derive transversal recommendations which are relevant for a general use of UASs in mineral exploration. Similarities and differences in the three case studies are combined in an overview (Table 2.3) to illustrate the aspects that can be taken and transferred to other exploration scenarios. As such, the case studies provided in this thesis encompass a geologic variety with directly and indirectly detectable targets, topographic and climatic defiance and technical as well as logistical challenges. That variety induces the proposed sensor combination which in turn prompts general data processing and specific preparation steps. The succeeding integration and interpretation is largely target-controlled and involves spectral and structural data aspects as well as modelling at different complexity levels.

Chapter 2 – General methods

Table 2.3 General and specific aspects of the data acquisition, processing and integration workflow.

Acquisition				
Case study		A (Otanmäki)	B (Siilinjärvi)	C (Qullissat)
Exploration type		Brownfield	Brownfield	Greenfield–Brownfield
Surveyed area		0.05 km²	0.7 km²	35 km²
Terrain		flat	flat–moderate	strong topography, undulating
Climate/Weather		Subarctic, fair	Subarctic, fair-clouds, fog	Arctic, clear
Outcrop condition		partly covered with vegetation and sediment, enclosed by high forest stand		mainly concealed, lichen, debris, dense vegetation, mass movements
Remoteness		low	low	high
Commodity/ Rock type		Fe-Ti-V/Gabbro-Anorthosite	Apatite/ Carbonatite-Glimmerite	Ni-Cu PGE/Flood basalt
Target	direct	Magnetite-Ilmenite	REE	Fe-alteration (e.g., goethite, hematite)
	indirect	-	Magnetite	Magnetite, pyrrhotite, native iron
Sensor and UAS	Optics	HSI, MSI, RGB	HSI, MSI, RGB	MSI, (HSI, RGB)
	Magnetics	Fluxgate, Proton-based (ground surveying), Fluxgate base station		
	Multicopter	Tholeg, Aibot	Tholeg, Aibot	Tholeg, DJI Mavic
	Fixed-wing	eBee Plus, Albatros		
Validation data	Ground	XRF, handheld spectroscopy, magnetic susceptibility and field, GCP	handheld spectroscopy, structural measurements, magnetic field, GCP	handheld spectroscopy, magnetic susceptibility
	Laboratory	-	XRD, magnetic susceptibility, optical microscopy	optical and BSE microscopy, magnetic susceptibility, satellite
	Legacy	magnetic susceptibility, aeromagnetics	Aeromagnetics	XRF, magnetic susceptibility, Aeromagnetics, ground magnetics, drillhole logs
Processing				
General	Hyperspectral	Dark current subtraction, Co-registration, radiometric and topographic correction, geolocation, matching to RGB orthophoto, empirical line calibration from radiance to reflectance		
	Multispectral	calibration from radiance to reflectance, image matching, point cloud creation, orthophoto, elevation model		
	Magnetic	Data cleaning, flight line preparation, diurnal correction, heading correction, tie-line levelling, filtering		
	Photogrammetry	Integrate ground control, image matching, create sparse and dense point cloud, orthomosaics, elevations, contours		
Specific	Image and DSM	Dimensionality reduction (MNF)	Dimensionality reduction and feature extraction (OTVCA)	Topographic filtering (slope, TPI)
	Magnetics	Minimum curvature grid resolution, filtering and transformation (such as directional derivatives, analytic signal, upward continuation)		
Integration				
Classification		Unsupervised and supervised (k means, SAM)	Supervised (SVM)	Spectral band ratios
Modelling		Basic resource modelling	Forward modelling, digital outcrop modelling	Magnetic vector inversion
Interpretation		Iron occurrence estimation, lineament map	Digital structural measurements, surface-subsurface geologic map and profiles	Complex geologic 3D model in depth, surface description, anomaly detection

2.2 *Optical remote sensing*

Remote sensing imaging is the contactless acquisition of information from a distant target and the implementation of data processing and interpretation, by using sensors that measure the interaction between electromagnetic radiation and surface (Manolakis et al., 2016). The sun as energy source provides the solar irradiance ($\text{W}\cdot\text{m}^{-2}$) which passes through the column of atmosphere to an area. Passive optical sensors (photon detectors) used by cameras capture the electromagnetic radiation (radiance at sensor) reflected from an area, called reflectance. The photon energy is defined as

$$E = h\nu = \frac{hc}{\lambda} \quad 2.1$$

where h = Planck's constant⁴, ν = frequency, c = speed of light and λ = light wavelength. It is seen that E is in inverse relation to λ . Consequently, the response of a sensor to a wavelength range is defined by the detector material and its material-specific sensitivity towards certain electromagnetic wavelengths. Semiconductor-based detectors consist of different alloys. The common Si-based CMOS detectors are light-weight, have high signal-noise-ratio (SNR) and are conductive at room temperature. Their photon sensitivity wavelength range is usually between 400–1,100 nm, as such they form the basis of RGB, multispectral and hyperspectral cameras in that spectrum. An extended wavelength range is detectable with actively cooled PbS or InGaAs based detectors that are responsive between 1000–2,600 nm (Landgrebe, 2005). Accordingly, many such camera systems require high UAS payload (> 5 kg) and energy consumption, and their optical pathways can be complex, resulting in a large sensor size that exceeds the capabilities of most commercially available UAS platforms.

Multiple processes along the path of light (path radiance) from target to sensor occur and are added to the measured signal, for example scattering, diffuse sky irradiance, atmospheric disturbance, diffuse reflections and more, resulting in undesirable radiometric noise (Jensen, 2014). That is an inherent issue for satellite and airborne optical remote sensing, and for UAS imaging to a certain degree as well, and increases with distance to target. Reflectance becomes increasingly affected by atmospheric attenuation during its path. A wider field of view from a scene leads to amplified diffuse reflectance, e.g., from water bodies.

⁴ $h = 6.626070 \cdot 10^{-34}$ Js

The received power flux ϕ (in watt) of an instrument in a spectral interval $\lambda \dots \lambda + \Delta\lambda$ is given as:

$$\phi = \tau_a L_\lambda A_p \beta^2 \Delta\lambda \quad 2.2$$

with τ_a = atmospheric transmittance, L_λ = pixel spectral radiance ($\text{W} \cdot \text{m}^{-2} \cdot \text{sr}^{-1} \cdot \mu\text{m}^{-1}$), A_p = sensor aperture, β = instantaneous field of view (rad), $\Delta\lambda$ = spectral interval (Landgrebe, 2005).

To describe surface characteristics in spectral geology, we assume in this thesis that all targets behave as Lambertian or diffuse reflectors, i.e., rough surfaces that reflect radiation uniformly in all directions. Diffuse reflectance as dominant reflectance type is therefore the target of interest and is quantified by a reflectance spectrum. A reflectance spectrum is defined as reflected incident radiation, as a function of radiation wavelength (Manolakis et al., 2016).

UAS-based sensors can measure a surface adequately close to mitigate adjacency and atmospheric effects (Landgrebe, 2005) and thus capture reflectance spectra with more local properties. It is assumed that the UAS-captured reflectance is not significantly altered due to the short target–sensor distance, usually < 100 m. Calibration from radiance (radiated intensity towards certain direction in $\text{W} \cdot \text{m}^{-2} \cdot \text{sr}^{-1}$) to reflectance (relative quantity, e.g. in % or between 0–1) in this work is always applied by using a known ground reference spectrum and a regression technique known as the empirical line method (Karpouzli and Malthus, 2003). Computationally intensive atmospheric models doing sensor radiance estimations, such as MODTRAN (Berk et al., 1998) are not necessary for these case studies. A further assumption is that spectral image frames acquired by UAS-based cameras are in nadir to the ground, for multicopter and fixed wing UAS alike. These approach omits the necessity to precisely measure the absolute and relative camera orientation (roll, pitch, yaw) during image acquisition. It would be possible to measure absolute and relative camera orientations by using an inertial measurement unit (IMU) on the camera, but could introduce further errors than it reduces. The eBee camera on UAS records positional data with its internal IMU and tests during this thesis in Agisoft’s photogrammetric workflow have shown that reconstructed model geometries can be severely distorted when using additional camera positions. Secondly, the multicopter-based hyperspectral camera is always attached to a gimbal that corrects camera position and a nadir view from the platform (Figure 2.2c).

2.2.1 Multispectral- and hyperspectral imaging

The type of optical data acquired here is the image frame in the form of an n-dimensional image matrix of $x \times y$ pixels and λ , that is spectral dimension and is stored per pixel (number of

channels; Figure 2.3). An image sensor defines the spatial pixel dimension per frame (Jensen, 2014). The pixel size of an image is also defined as ground sampling distance (GSD) where each pixel covers a specific surface area, influenced by sensor distance to ground. Reducing the altitude of the UAS during image acquisition results in a decreased GSD, where a pixel covers less surface materials, resulting in less-mixed image spectra (see Dering et al., 2019).

Camera calibration and image quality is dependent on a multitude of factors. High spatial and spectral precision is imperative for complex targets, for example in agriculture where minute differences of cropland monocultures reveal important information on plant vigour or soil fertility. In geology, where small structures, minute spectral absorptions or surfaces changes are important targets, we require good radiometric or geometric calibration techniques and high spectral quality per pixel (Kelcey and Lucieer, 2012; de Oliveira et al., 2016; Jakob et al., 2017; Hakala et al., 2018; Tu et al., 2018). However, most of the geologic targets of this thesis, with the exception for the work on rare earth detection using UAS (Booyesen et al., 2020b), have a relatively large spatial footprint of decimetres to meters. Using the spectral mean or median of a larger group of pixels is adequate in many cases to detect or outline a target. Also important are clearly visible geologic boundaries, for example of contacts or dykes which necessitates sub-meter pixel resolutions.

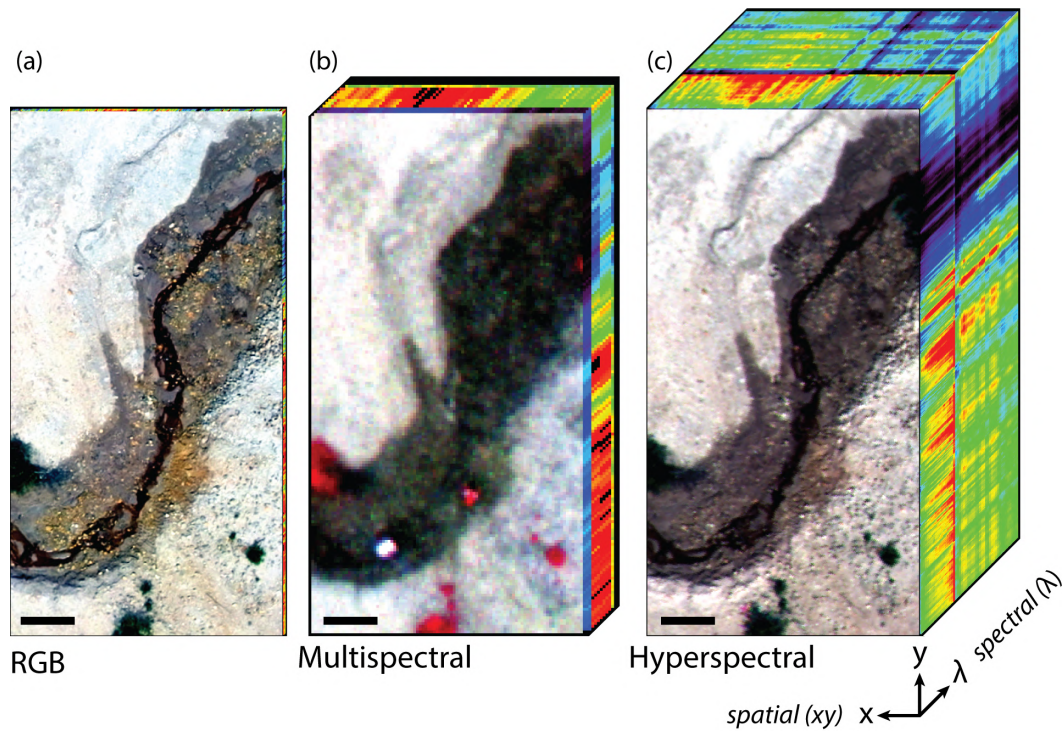


Figure 2.3 Comparison of three image types from the same scene, acquired from a mine waste dump in Litov (CZ). Spatial data is presented in 2D (x - y axes) and spectral information per pixel is indicated as 3D dimension along the λ (z) axis. The black scale bar measures 2 m length with a scene area of 195 m². (a) RGB orthophoto from Parrot S.O.D.A. camera with 3 bands in high spatial resolution (GSD 2.5 cm). (b) Multispectral false-colour image from Parrot Sequoia camera featuring 4 discrete spectral bands (band 3, 2, 1; GSD 10.5 cm) (c) Hyperspectral false-colour image from Senop Rikola camera featuring 50 discrete spectral bands (bands 17,7, 1, GSD 3.7 cm).

The spectral bands along λ are either fixed and defined by the optical bandpass filters of the camera, or can be modulated by using an interferometer. Optical filters allow only a certain range of radiation to reach the camera detector. The Fabry-Perrot interferometer of the Rikola camera (Honkavaara et al., 2013) provides a flexible setup to choose from tens to hundreds of narrow spectral bands. Tunable Fabry-Perrot technology utilizes an electric current-steered piezo-actuated interferometer which acts as thin mirror element to provide narrow wavelengths. These are chosen by changing the mirror distance (Marinelli et al., 1999).

Spectral channels are the quantized spectral dimension of the electromagnetic spectrum. The information content per pixel spectrum can be processed and analysed in various ways, e.g., visual interpretation, mapping wavelength-specific absorption regions, supervised and unsupervised classifications, dimensionality reductions and machine learning techniques. In particular, a hyperspectral image with hundreds of channels is a challenging data type has required research on advanced classifiers to cope with the amount of information (Benediktsson and Ghamisi, 2015; Ghamisi et al., 2017). Hyperspectral sensors on UAS is a relatively recent advance, but the development of further processing routines and applications is ongoing (Adão et al., 2017).

2.2.2 Image spectroscopy for geologic application

For image and reflectance spectroscopy, the target is to acquire a spectral signature of surface material for analysis and interpretation in tens to hundreds of bands (Goetz et al., 1985). Spectral ranges are usually defined (Jensen, 2014) in ultraviolet (UV; 100–400 nm), visible (VIS; 400–700 nm), near infrared (NIR; 700–1300 nm), shortwave infrared (SWIR; 1000–2500 nm). Visible to near-infrared (VNIR; 400–1000) is the used range for UAS-based images in this work, for handheld spectra we use the VNIR-SWIR.

Multispectral band ranges are often set strategically by camera producers for agricultural market application, where the camera characteristics are optimised for the spectral properties of vegetation, specifically for plant health monitoring. For example, the Parrot Sequoia multispectral camera has fixed spectral bands (550 nm, 660 nm, 735 nm, 790 nm) for vegetation index mapping (Assmann et al., 2019). Applying imaging spectroscopy to geology as one main goal of this work is bound to the spectral range of each included sensor (Figure 2.4). A multispectral instrument acquired in MULSEDRO (introduced in chapter 6 of this thesis) named the ‘msCam’ provides 16 discrete, uniformly distributed channels in the VNIR to ensure sufficient spectral coverage.

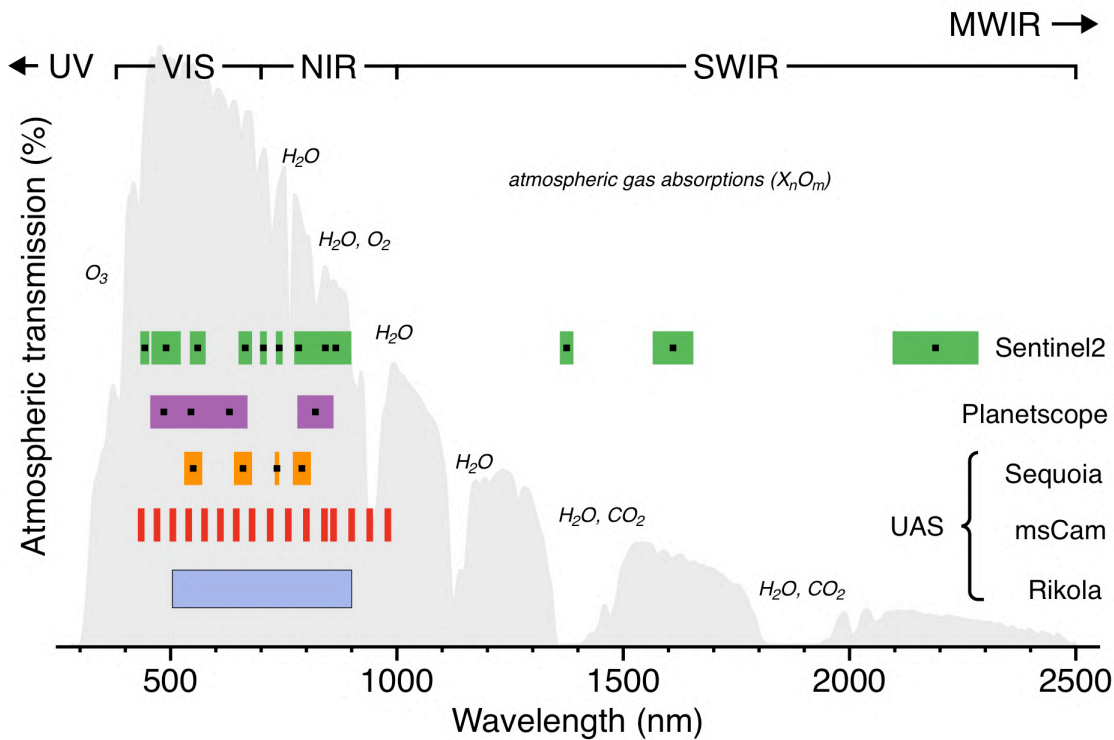


Figure 2.4 The spectral transmission for the solar radiation that passes through the atmosphere. Various gases absorb parts of the electromagnetic radiation, resulting in the depicted atmospheric windows. Spectral channels of the five main image sources from this thesis are shown for comparison. Coloured bars indicate spectral bandwidth. Rikola, msCam and Sequoia are UAS-based, Planetscope and Sentinel2 instruments are satellite-based.

Geologic materials are rarely pure and each image pixel contains a mixture of different materials, called end-members. Mixtures of spectra are intimate (non-linear) or macroscopic (linear), depending on the amount of photon reactions in the material, before their reflected light reaches the sensor (Manolakis et al., 2016). When photons enter a surface, measurable interactions occur that provide information about structure, material-mineral abundance and are material-specific or diagnostic (Clark and Roush, 1984).

Diagnostic characteristics of a spectrum are for example emissions, reflections, absorptions or the general curve shape. Those characteristics are often called features and can be interpreted to distinguish and identify materials, such as minerals, rock types and vegetation. Spectral variation are for example caused by grain and crystal size, crystal structures, and chemical compositions atom substitution. Absorption is based on the atomic microstructure where photons interact with the electron-populated shells of atoms and ions, according to Beer-Lambert's law of light attenuation. Sources of absorptions are electronic and vibrational processes (Clark, 1999).

Electronic processes, such as charge-transfer absorptions and crystal field effects are found in VNIR-SWIR ranges and cause absorption bands useful for mineral identification. Iron, the 4th most abundant element in the earth's crust (Frey and Reed, 2012) is a prominent example in the application of geological remote sensing applications, for mine waste monitoring and mineral identification (Swayze et al., 2000; Mielke et al., 2014; van der Werff and van der Meer, 2015). Iron-bearing minerals have specific absorption features in the VNIR-SWIR (Crowley et al., 2003).

The valence state of an atom, lattice symmetries and the coordination number change the energy levels for electrons to take place. Iron occurs in numerous minerals and has multiple oxidation states (e.g., Fe^{2+} , Fe^{3+} ; electron configuration Fe: $[\text{Ar}]4s^23d^6$) and VNIR spectroscopy is effective at identifying electron-transition related absorptions. For example, charge transfer bands between 750–950 nm, 550–650 nm and narrowly at 450 nm are common features of ferric iron. Ferrous iron shows a broader feature between 900–1100 nm, and narrow bands at 450 nm, 510 nm and 550 nm (Sherman, 1985; Sherman and Waite, 1985; Crowley et al., 2003). Hence, iron-bearing minerals are well-suited proxies for spectroscopy in the VNIR range and show distinguishable features (Figure 2.5). Absorption properties such as edges, shoulders, local maxima and minima are indicators for atoms, molecules or mineral (Clark, 1999). Their wavelength positions and depth are diagnostic features for targeting and identification. For example, the reflectance maximum between 750–760 nm helps to distinguish between hematite and goethite, provided that the instrument has the necessary spectral resolution (Figure

2.5a). A sensors available band position and spectral range are crucial for identification, when using ratios and diagnostic positions. Also, minerals that show only weakly developed diagnostic features in the VNIR–SWIR (spectrally flat, e.g. magnetite, pyrite, pyrrhotite Figure 2.5b) are subject to alterations (Morris et al., 1985) and can be identified subsequently via proxies. Spikes across the spectrum are caused by the overall low reflectance which increases noise and requires a different calibration material, such as a darker calibration panel.

Molecular vibrational processes in the VNIR-SWIR are caused by resonance among radiation and chemical bonds, for example O-H, H₂O, C-O, CO₃, Al-OH, Fe-O, Mg-O to name a few (Hunt, 1977; Hunt and Ashley, 1979). Distinguished spectral features that were identified during field spectroscopy are presented in the subsequent chapters 3, 4 and 5 (e.g., Chapter 4.4.1, Figure 4.5).

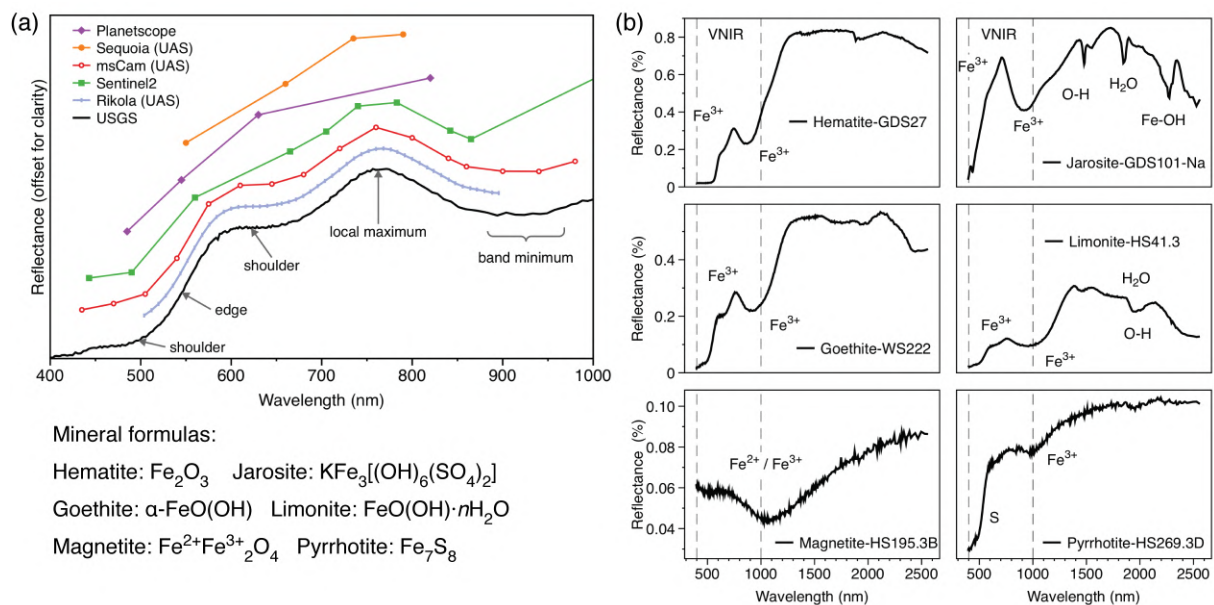


Figure 2.5 A reflectance spectrum for Goethite WS222 (from USGS spectral library; Kokaly et al., 2017) is resampled to (a) the wavelength ranges of sensors used in this work. The resampled spectra represent an idealized case with minimum noise which is not always the case. (b) Examples of iron-bearing spectra from the USGS spectral library are shown between 400–2500 nm. Absorption edges, shoulders, maxima and minima are useful identifiers. The last row illustrates two spectra regarded as non-diagnostic in VNIR–SWIR, but small surface impurities or exchanged atoms in the crystal lattice alter the curve shape visibly.

Image spectroscopy has become a useful tool for geologists, geochemists and mineral explorers, who need to identify subtle rock alterations, distinguish rock types or target orebodies (Kruse, 1998). Applications for multispectral and hyperspectral spectroscopy are growing well beyond the use of satellite (van der Meer et al., 2012) and high-flying aircraft (Rodger et al., 2012).

Spectral analysis for mineral identification in VNIR and SWIR can be applied rapidly and is non-invasive. An advantage are results during field work and from hard-to-access areas by using UAS-based sensors (Kirsch et al., 2018). Mineral abundance and composition maps can

be generated based on spectral endmembers recorded in spectral libraries from study sites (Booyesen et al., 2020a) or from publicly accessible reference libraries (Crowley et al., 2003; Kokaly et al., 2017; Fasnacht et al., 2019; Koerting et al., 2019).

2.2.3 Development of a fixed-wing-based multispectral camera

A prototype multispectral camera system was designed, constructed and tested in the course of this study. The camera is optimised for geologic outcrop mapping using a fixed-wing UAS, e.g., in active mines, exploration sites, and tailing areas. Unfortunately, extended tests of the camera with the Tholeg PX8-12 multicopter in Freiberg were postponed indefinitely, due to the pandemic situation.

In the project, Radai Oy conducted the implementation of the hardware with the integration of the camera into their fixed-wing UAS and flew the first test missions.

This study focused on the imaging performance, image quality and tests of optimal settings for image processing and preliminary spectral evaluation. The camera named *msCam* (Figure 2.6) was designed to satisfy the UAS's given boundary conditions: namely restricted payload and high velocity. The imaging system consists of two 8 band cameras resulting in a combined wavelength range of 435–980 nm of the electromagnetic spectrum. Therefore, the camera provides 16 spectral bands at a slightly extended wavelength range as compared to the Rikola camera. A concluding assessment is pending but has the opportunity to demonstrate multispectral capacities at reduced costs. Appendix G includes preliminary results of successful data acquisition and processing. Several surveys were flown at the Ahmosuon airfield and at Siilinjärvi mine, both targets were flown in Northern Finland.

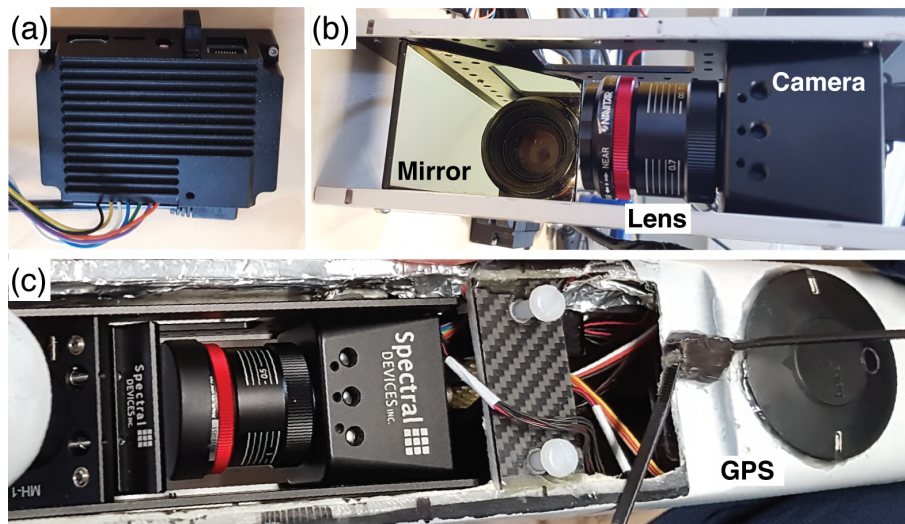


Figure 2.6 The integrated *msCam* components. (a) Data logger unit SBC-1 stores images during flight. (b) The *msCam* in mirror sledge, with the tilted mirror that guides upwelling light onto the camera lens. (c) The *msCam* is mounted inside the UAS fuselage, view from top side.

2.3 Magnetic sensing

2.3.1 Basics regarding the magnetic field

Magnetism is a physical phenomenon related to magnetic fields or forces. It is related to electromagnetism which is produced by electric current, and is associated with both magnetic fields and electric fields, resulting in attractive and repulsive forces between objects. Magnetism is part of electromagnetism and one of the four known fundamental forces. A magnetic field describes a force that acts between bodies or is created by magnetic objects, such as the attraction force between two magnets. On that notion, the most basic visualisation of a magnetic system is the bar magnet. The second term from Maxwell's equations, Gauss's law of magnetic fields in its differential form states that

$$\nabla \cdot \mathbf{B} = 0 \quad (2.3)$$

where \mathbf{B} is the *magnetic induction* (Φ) or *flux density* and ∇ denotes divergence. Therefore, the field is solenoidal which implies that no magnetic monopoles exist, \mathbf{B} is irrotational and a potential field (Blakely, 1995). Magnetic anomalies are modelled as dipole (Figure 2.7a), thus an equal amount of field lines begin and terminate at opposing poles.

The magnitude of field B is measured in tesla ($1\text{T} = 1 \frac{\text{Vs}}{\text{m}^2} = 1 \frac{\text{kg}}{\text{As}^2}$), The unit nanotesla (nT) is common. Around 50,000 nT is the scalar field strength of the Earth's geomagnetic field (Telford et al., 1990) but it can vary from 25,000 nT around the equator, and up to 70,000 nT at the earth's poles (Figure 2.7b).

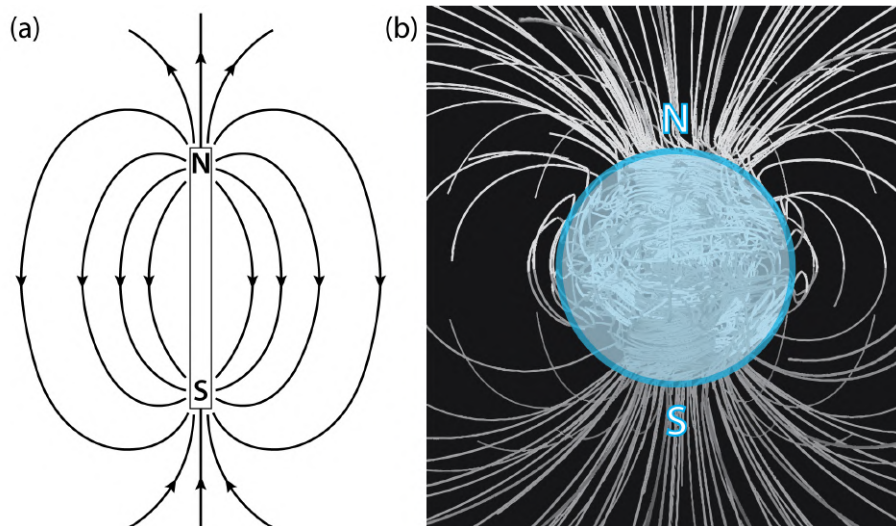


Figure 2.7 General magnetic dipole models. (a) Dipole bar magnet as classic representation for magnetism and magnetic field line direction (modified after Keary and Brooks, 1991). (b) Earth's magnetic field lines based on computer simulations, where the liquid iron core acts as a geodynamo that produces an internal electric field, that in turn creates a geomagnetic field (modified after Glatzmaiers and Roberts, 1995).

Typical magnetic anomalies resulting from the different properties of geological materials are between tens to thousands of nT. Magnetism is a vector quantity which provides both magnitude and direction, where the magnitude decreases significantly with increasing distance from the source and has anisotropic behaviour (Dentith and Mudge, 2014). The geomagnetic field vector **B** at a given point consists of its vertical and horizontal components **B_Z** and **B_H** and its angular directions, that are declination **D** and inclination **I**. **B** can be denoted by its directional components **B_X**, **B_Y**, **B_Z** (Figure 2.8a). All magnetic anomalies we measure are in superposition with the geomagnetic field (Kearey and Brooks, 1991).

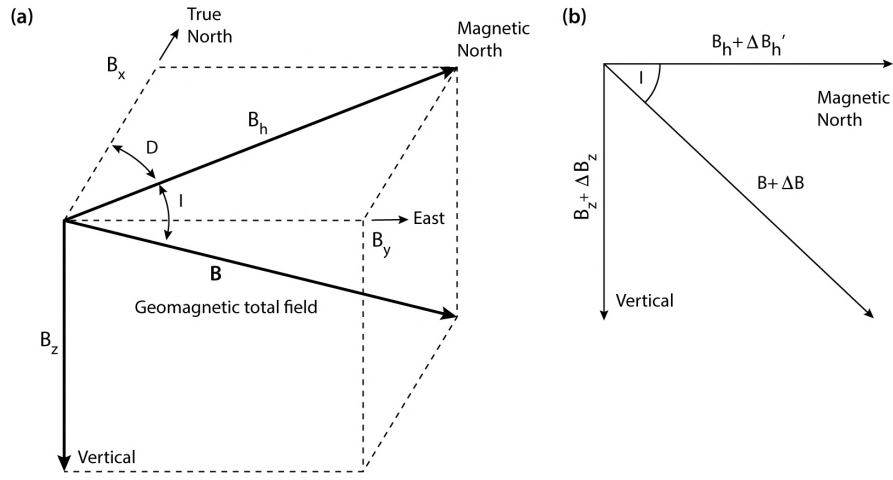


Figure 2.8 Geomagnetic field components. (a) The vector components defining the geomagnetic north field (**B_h**), true north (**B_x**), east (**B_y** or **Y**) and the downwards facing component (**B_z** or **Z**), the angles for inclination (**I**) and declination (**D**), together with the total field (**B**). (b) The magnetic field as components plus a superimposed anomaly ΔH , ΔZ and ΔF (modified after Kearey and Brooks, 1991).

The geometric elements of the geomagnetic field are related as

$$B^2 = B_h^2 + B_z^2 = B_x^2 + B_y^2 + B_z^2 \quad (2.4)$$

and we get **B** by the square root, it is useful to note that because the 3-axial fluxgate magnetometers we use measure the X, Y and Z components (Clauser, 2014).

When adding an anomalous source **B_h'** (Figure 2.8b), such as a lithology with magnetic response, the total field anomaly ΔB is given by

$$\Delta B = \Delta B_z \frac{B_z}{B} + \Delta B_h' \frac{B_h}{B} \quad (2.5)$$

and we can calculate a magnetic anomaly of an isolated magnetic pole (Kearey and Brooks, 1991). Values for local geomagnetic fields, inclination, declination and further can be obtained from the International Geomagnetic Reference Field (IGRF) or the World Magnetic Model (WMM; see also www.ngdc.noaa.gov/geomag; last accessed 19.03.2021) which model location-depending field values.

The relationship of \mathbf{B} with distance to source is defined as

$$B = \frac{\mu_0}{4\pi} \frac{M}{r^3} \sqrt{1 + 3\cos^2 \theta} \quad (2.6)$$

where μ_0 denotes magnetic permeability of vacuum⁵, \mathbf{M} a magnetic dipole, θ the elevation angle between the equator and magnetic pole and \mathbf{r} the dipole distance (Clauser, 2014). The implication in equation 2.8 is crucial for magnetic measurements, it infers that measured field intensity between magnetic object and observer/sensor decreases by in an inverse cube relationship at growing distance. UASs with their capability to fly much closer to a target than aircraft and helicopter thus can achieve higher resolution of the target. The material property of the geologic entities we measure is the magnetisation \mathbf{J} and a magnetic anomaly is created from a magnetisation contrast. \mathbf{J} is denoted as

$$\mathbf{J} = \mathbf{J}_i + \mathbf{J}_r \quad (2.7)$$

where \mathbf{J}_i is the induced and \mathbf{J}_r the remanent part of the magnetisation. The induced magnetisation is coming from an external magnetic field, such as the geomagnetic field or an activation field with the *magnetic field strength* \mathbf{H} . The remanent magnetisation in rocks can be induced by chemical and physical processes or by imprinting the geomagnetic field at a reversed polarity during rock formation and cooling below the Curie temperature (Dentith and Mudge, 2014). We could observe this phenomenon in our magnetic measurements in data from Greenland (Chapter V). The relation between \mathbf{B} and \mathbf{H} is defined as

$$\mathbf{B} = \mu_0 \mathbf{H}. \quad (2.8)$$

Frequently, the direction of \mathbf{J} points along the direction of \mathbf{H} . To compare the strength of \mathbf{J} for minerals and rocks, the unitless magnetic susceptibility κ is introduced in relation to \mathbf{J} as

$$\mathbf{J} = \kappa \mathbf{H} \quad (2.9)$$

where κ gives an approximation of the kind of material, rock or mineral at hand. Magnetic properties of rocks with induced and remanent magnetization, magnetic anisotropy and further phenomena define the measured magnetic response of lithologies. Remanent material expresses magnetization in a magnetic zero field (i.e. laboratory measurements) and records its paleomagnetic history during formation (Clark, 2014). Lithologies encountered in this work expressed different magnetic behaviour and various κ ranges. For quartz and dolomite, κ varies between 1×10^{-5} – 1×10^{-4} SI-units while for iron-rich basalt, higher values between 0.01–0.2 SI-units are possible (Clauser, 2014). Magnetite (Fe_3O_4) is known as a mineral with one of the

⁵ $4\pi * 10^{-7} \text{ Vs/Am}$

highest magnetic susceptibilities with κ in ranges between 1–5.7 SI-units (Harrison et al., 2005). The highest magnetic susceptibility we measured in this study (0.4 SI-units), was acquired from a rock specimen from the Illukunnguaq Ni-Cu dyke on Disko Island, West Greenland. Further accounts of susceptibilities are found in various textbooks (Blakely, 1995; Dentith and Mudge, 2014) and publications (Hunt et al., 1995). To validate UAS-based magnetics, we measured magnetic susceptibilities of rocks from Finland and Greenland as part of my data acquisition strategy and subsequently in the laboratory.

2.3.2 Magnetic sensors used on UAS

The main instrument used in this study is the fluxgate magnetometer. It found application during World War II to detect submarines from airborne platforms (Kearey and Brooks, 1991). A fluxgate magnetometer is generally built from two corresponding high-permeability ferrite cores with primary and secondary windings around each core. The primary windings are in series connection and face the opposing direction. An alternating current is flowing through them until core saturation, meanwhile secondary coils are magnetized by the field created from the primary coils. Without any external magnetic field, all internally created fields would sum to zero. When an ambient field enters instrument space, the saturation changes for ferrite cores and the fields becomes asymmetrical. These differences create induced voltage changes, and their magnitude is proportional to the ambient magnetic field (Kearey and Brooks, 1991). Fluxgates are most often designed in a set of three orthogonal sensor units aligned in X, Y, Z direction which allow the detection of all three components of the ambient field (Nabighian et al., 2005) and the calculation of the total field (Equation 2.5). Fluxgates measurements have inaccuracies that can be caused by sensor misalignment and heading among other things, and thus a frequent calibration is advised to obtain reproducible measurements (Gavazzi et al., 2016).

The total magnetic intensity or ambient field as a scalar is measured by scalar magnetometers such as the proton-precession or the optically pumped magnetometer. Proton-precession magnetometers measure the precession frequency of protons in a proton-rich fluid, such as purified decan or hydrogen. Around the fluid container, a copper coil with a direct current creates a magnetic field (Ampère-Maxwell law) according to which the protons align (high spin). When current is switched off, the atoms realign in the direction of the ambient field (low spin). The spin transition creates a measurable electromagnetic field which is proportional to the ambient field (Nabighian et al., 2005). Ground-based magnetic surveys in this thesis were

conducted with the GEM Systems GSM-19 magnetometer (GEM Systems, Markham, Ontario, Canada) which uses the Overhauser effect for higher precision and sampling frequency.

Optically pumped magnetometers work with optical-transmission/radio-frequency spectroscopy principles, using a glass cell containing an evaporated alkali metal (e.g., Cs, Rb, K). The vaporized metal atoms have single-valence electrons that are distributed randomly between two energy levels with a separation energy equivalent to a frequency of visible light. Under an external magnetic field, the stable energy level is split proportional to the strength of the field. When light of a particular frequency is beamed on the vapour, the valence electrons are forced into a higher energy level of this split state (optical pumping). When all valence bands are saturated, the absorption is complete and the glass cell becomes transparent, since electrons can no longer absorb photons. An additional radio signal at a defined frequency (Larmor frequency) forces the electrons to redistribute back on a lower valence state, which renders the gas-cell opaque again. The Larmor frequency as a function is proportional to the ambient magnetic field which is determined by that relationship (Nabighian et al., 2005).

Important for UAS-based application are some technical differences between fluxgates and proton, respectively optical pumped magnetometers. For example, the sampling frequency is lower with optical pumped magnetometers, but the measurement sensitivity is higher. Thus, these technical differences determine the suitability of each magnetometer type in a UAS application. Based in the previous literature review, 57 studies could be identified that includes descriptions of the UAS type and the magnetic sensor (Figure 2.9). Scalar magnetometers were the majority at the current stage.

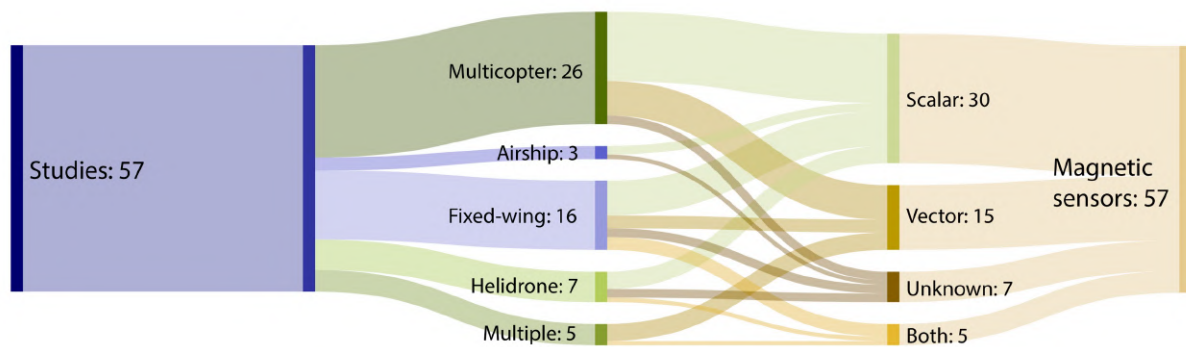


Figure 2.9 Sankey flow diagram showing UAS (left) and magnetic sensor (right) combinations, based on available case studies (Chapter 1.2.2).

2.3.3 Fluxgate magnetometer used in this study

The multi-copter magnetic system used in this study (Jackisch et al., 2019b) provided data from numerous test sites in Germany (Madriz, 2019), Finland and Greenland. We used the

commercial fluxgate magnetometer Magdrone R1 that is rigidly attached below the multicopter. The system uses a FGM3D/75 fluxgate sensor to measure the magnetic flux density within a range of $\pm 75,000$ nT at a permanent sampling frequency of 200 Hz. This system operates autonomously and has a battery charge for ~ 2 h, sufficient for several survey flights. An internal GPS records its geolocation relative to the sensor axis orientation at 20 Hz. Ease-of-use with an on-off switch to start data recording is an advantage, as well as the low weight, power consumption and high ruggedness. Both the magnetic signal and GPS location data are saved on an internal solid-state memory module and downloaded with manufacturer software, preferably after a single survey or each survey day.

A further advantage of a rigidly attached magnetometer as opposed to the usually cable-towed total field magnetometer is the known position relative to the UAS, which can be used for corrections. With a spatial distance of 50 cm between fluxgate magnetometer to the multicopter, electromagnetic noise caused by motors and UAS electronics are inherent (Tuck et al., 2018). Cable-towed magnetometers usually receive less noise because of larger sensor distance (> 2 m). Though, side and frontal winds could cause quick movements during the flight and impose an unpredictable sway on a towed magnetometer, which induces low-frequency noise during the measurements. Additionally, optically pumped and precession magnetometers feature construction related measurement dead-spots (Walter et al., 2018).

Noise from electric motors has critical impact if it cannot be distinguished from low-frequency signals associated with geological bodies. Visualization and distinction is possible in the frequency domain (Walter et al., 2019). For the Tholeg multicopter, the generated noise is of higher frequencies than those of geological bodies, and can be visualized using fast Fourier transformations (FFT) and designed low-pass filters (Oppenheim et al., 1999). Induced electromagnetic noise can contribute several hundred nanotesla (Figure 2.10a–c). To demonstrate that geologic signals and USA noise could be separated sufficiently, a spectrogram of TMI raw data for the 15 m Magdrone flight during the Otanmäki survey is shown (see Figure 3.11; Jackisch et al., 2019b, 2019a). The fluxgate magnetometer recorded the motor noise during the high-power outputs of the Tholeg UAS starting phase, which lasts ~ 4 seconds in the provided example.

A spectrogram illustrates the time-frequency distribution by using a window-based FFT transformation. Input signals are divided up into small segments of equal distances, to determine the frequency-time distribution for a specific time frame at the beginning of the survey (Figure 2.10d). High noise is visible as several irregular high-frequency signals between 70–100 Hz, in the upper quadrant of the plotted spectrogram (Figure 2.10d). The peaks

represent electric motor influence where 100 Hz would be equivalent to a motor rotation of ~6000 rpm which corresponds to a UAS in flight mode.

Further, noise sources, such as vibrations of the UAS fuselage, servo motions and eddy currents (Jirigalatu et al., 2021), are distributed in a medium frequency range. In the bottom section of the spectrogram (0–10 Hz), low-frequency signals caused from geological entities containing magnetite are measured. Geologic anomalies tend to reach hundreds of nanotesla and more, depending for example on mineral composition, depth, volume, shape, alteration stage, remanence and further (Dentith and Mudge, 2014).

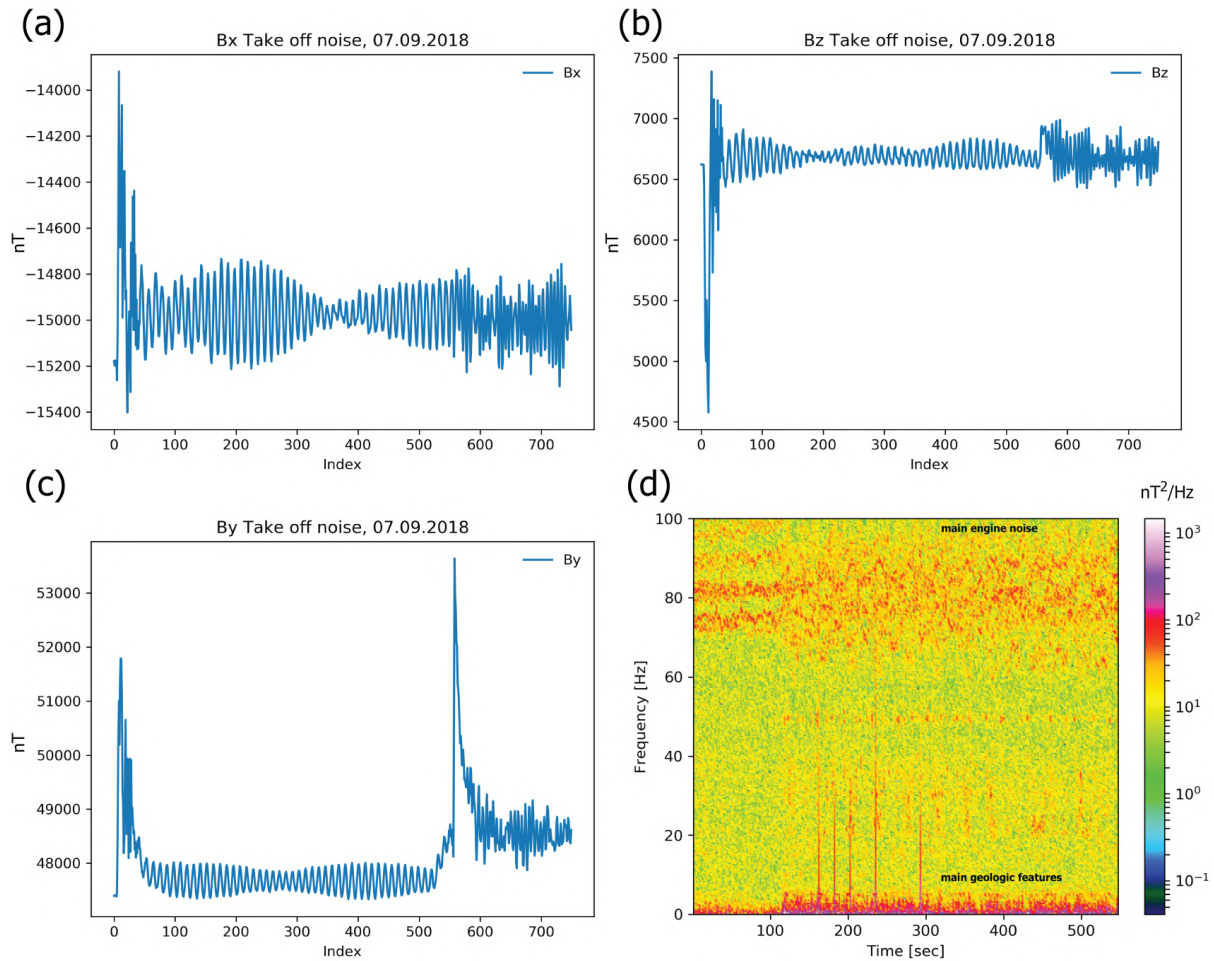


Figure 2.10 Examples of magnetic interference measured during Tholeg UAS take-off phase (Data from Jackisch et al., 2019). (a–c) B-field recordings of the X, Y and Z fluxgate axes during first field test in Otanmäki, Finland. (d) Spectrogram from parts of a single flight 15 m above ground. Electric motor noise and vibrational noise are present at high frequencies (20–100 Hz), geologic signatures are recorded at low frequencies (0–5 Hz). The Power spectral density is given in $\text{nT}^2 \cdot \text{Hz}^{-1}$, colour-coded with logarithmic scale in SciPy module (Jones et al., 2001).

2.3.4 Magnetic survey approach

The principal survey workflow for UAS magnetics is according to standard airborne survey protocols (Teskey et al., 1991; Reeves, 2006). The required equipment is a fluxgate magnetometer for the UAS and a base station magnetometer to record diurnal fluctuations of

the magnetic field, which are subtracted from the survey data. A base station should be located at a distance of > 10 m from the operators, automobiles, buildings, and in about 2 m above the ground, as soil magnetisation is possible and would affect the induced field. In case the base station has a malfunction, an alternative diurnal correction could be applied by using station-based magnetic field data, which are available from a global network of magnetic observatories (e.g., www.intermagnet.org, last accessed 12.02.2021). The observatory should be in the local vicinity (several tens of kilometres).

UAS-induced noise and induced, dynamic electromagnetic noise can be assessed by rotating the UAS, with the fluxgate magnetometer attached, around each main axis for at least 360° while adding half-circle rolling movements. Such procedures are advised to retain the highest accuracy for fluxgate measurements (Munsch et al., 2007; Gavazzi et al., 2019; Le Maire et al., 2020). In this work, an analogue method was applied for all fixed-wing magnetic surveys (Merayo et al., 2000; Pirttijärvi, 2003, 2015). For dynamic in-flight noise assessment and heading correction, the UAS can be programmed to fly a figure of merit (FOM) which resembles a clover leaf/shamrock figure for directional calibration and is based on experience of airborne survey (Reeves, 2006). For our fixed-wing magnetic surveys, conducting a FOM is not necessary and the heading correction is conducted by equivalent layer modelling (Pirttijärvi, 2003) and included in the obtained magnetic susceptibility models.

Flight path design is a crucial aspect and defines survey costs, area, size and number of detectable anomalies. Flight line distance for commercial surveys is defined by the contractor requirement or approximate target size, usually with a rule of thumb of 1.5–2 times the nominal survey altitude. The survey line spacing will vary depending on the expected magnetic response, the maximum depth to basement and the dimensions of the survey area. Flight lines should be perpendicular to the main strike direction of the geologic features for high magnetic contrast. Point sampling density along survey lines is defined by the magnetometer sampling rate, the GPS tagging frequency and the velocity.

Due to increasing sampling intervals of digital magnetometers, gaps along lines can result from GPS sampling limitations and could be mitigated by using for example polynomial spline point interpolation (Reeves, 2006; Isles and Rankin, 2013). A 2D grid of interpolated magnetic survey line data using kriging, weighted average or minimum curvature splines is commonly the final product of processing, before magnetic filters and transformations are applied (Smith and Wessel, 1990).

It is significant to recognise the effect of UAS survey altitude (terrain clearance) and its relation to anomaly detection. Measuring close to the surface results in higher resolution, however some

regions contain magnetized surface layers that create high-frequency noise, such as volcanic debris, ferricrete and glacial till (Parker Gay, 2004). In the following, some aspects of magnetic survey and interpretation are described and visualized. In theory, with increasing depth of a body or with rising survey altitude, the geophysical signal amplitude diminishes rapidly (Blakely, 1995). Traditionally, this behaviour is not always observed and strongly depending on a bodies structure, shape, mineral content and magnetic-remanent behaviour (Dentith and Mudge, 2014).

A computed response of synthetic geologic bodies, as used in forward modelling and inversion, can demonstrate the behaviour of the measured magnetic response (Jessell, 2001), i.e., amplitude, wavelength, and magnetic vector components in 3D (Figure 2.11; with figures from the atlas of structural geophysics, Jessell, 1997).

With increasing depth, the wavelength magnitude of deeper (regional) and near-surface (residual) anomaly sources changes. Resolution decreases, the signal of smaller objects diminishes, and deeper structures and regional fields dominate the magnetic response. Increasing depth results in larger wavelength, meaning coarse or barely resolved body edges and higher ambiguity. In the illustrated example, the superposition of the component fields and the oblique external field creates asymmetric responses in B_x , B_y , B_z at 200 m depth. The anomalous field decays with depth, at 1000 m the remaining signal amplitude is significantly reduced, and smaller bodies are barely detectable, leading to a loss of structural information for the shown synthetic bodies.

Since geologic forward modelling for interpretation is used in this work, its value depends on the signal's magnitude, data quality and sensor characteristics. In the scope of this work, triaxial-fluxgate sensors were used on UAS, scalar and vector base station magnetometers were used, but only the total magnetic field data were used for interpretation and modelling. Further details covering multicopter and fixed-wing UAS magnetics are detailed in chapter 3.3.5.

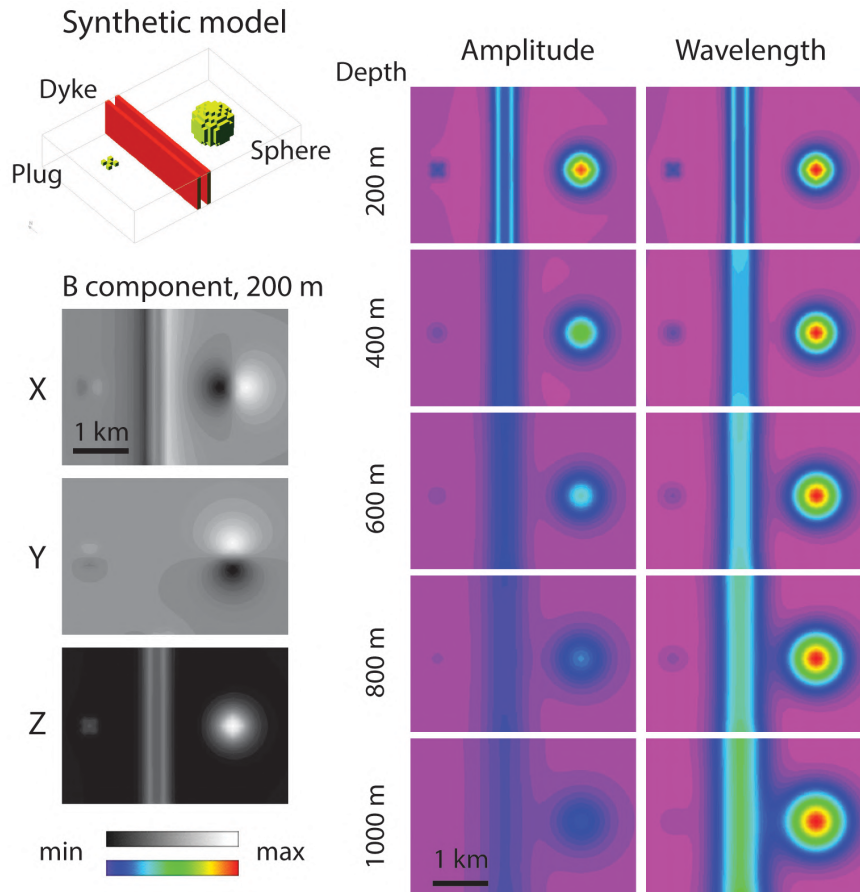


Figure 2.11 Synthetic, buried 3D geologic bodies (Images modified after Jessell, 1997) have their computed magnetic response measured on the surface. Dimensions of five plugs are 200 m, two dykes are 200 m in width, the sphere has 1 km radius. Body depths are increased progressively between 200–1000 m. $\kappa = 0.01$ SI, background = 0 SI, North is up, Inclination = 50° , Intensity $B = 50,000$ nT.

2.3.5 Applications of filters to magnetic data

With the ambiguity of magnetic signal sources, data processing should enhance interpretation potential, for example to distinguish shallow from deep sources, improve structural trends and body edges, reduce noise and enable modelling techniques. Transformations and filters (Chapter 4.4.3 and 5.3.1) applied in spatial and frequency domains on magnetic data are common tools to reduce ambiguity, aid to create geological interpretation and investigate susceptibility distributions. Gradient filters (high and low pass) are useful instruments to increase the clarity of geological structures at surface or greater depths.

Magnetic fields are potential fields that satisfy Laplace's equation, which includes without limitation, that those fields are comprised of multiple sine waves. Therefore, a field measured at a reference surface can predict field strength at different elevations using for example the Fourier transformation (Kearey and Brooks, 1991). Those field continuations have the direction terms upward and downward, with the former being prone to uncertainty because all shorter signal wavelengths are amplified, which increases noise. The upward continuation enhances

deeper structures, regional trends and attenuates shorter wavelengths. Further applications are e.g., comparison of ground survey with UAS data, merging survey data to reference surfaces and altitude simulations (Henderson and Zietz, 1949; Blakely, 1995).

Another common tool is the first vertical derivative (1VD, Paine, 1986), which calculates the vertical gradient of magnetic data and is a numerical substitute to two-sensor gradient data. The 1VD improves geometric details of magnetized bodies and aides definition of spatial dimensions and geological structure (Isles and Rankin, 2013).

Figure 2.12 illustrates the impact of 1VD filtering and upward continuation, using survey data acquired during this study. The plot shows three image rows each containing the magnetic survey product and filtered data products: 1VD and upward continuations at three levels. Visibly, the derivatives sharpen anomaly edges, but also enhances noise. Upward continuations smooth out smaller anomalies and enhance the regional field with increasing altitude. The strength of the anomaly decrease is evidence to the depth of a body or magnetic mineral contents. Some additional filters are introduced in chapters 4 and 5.

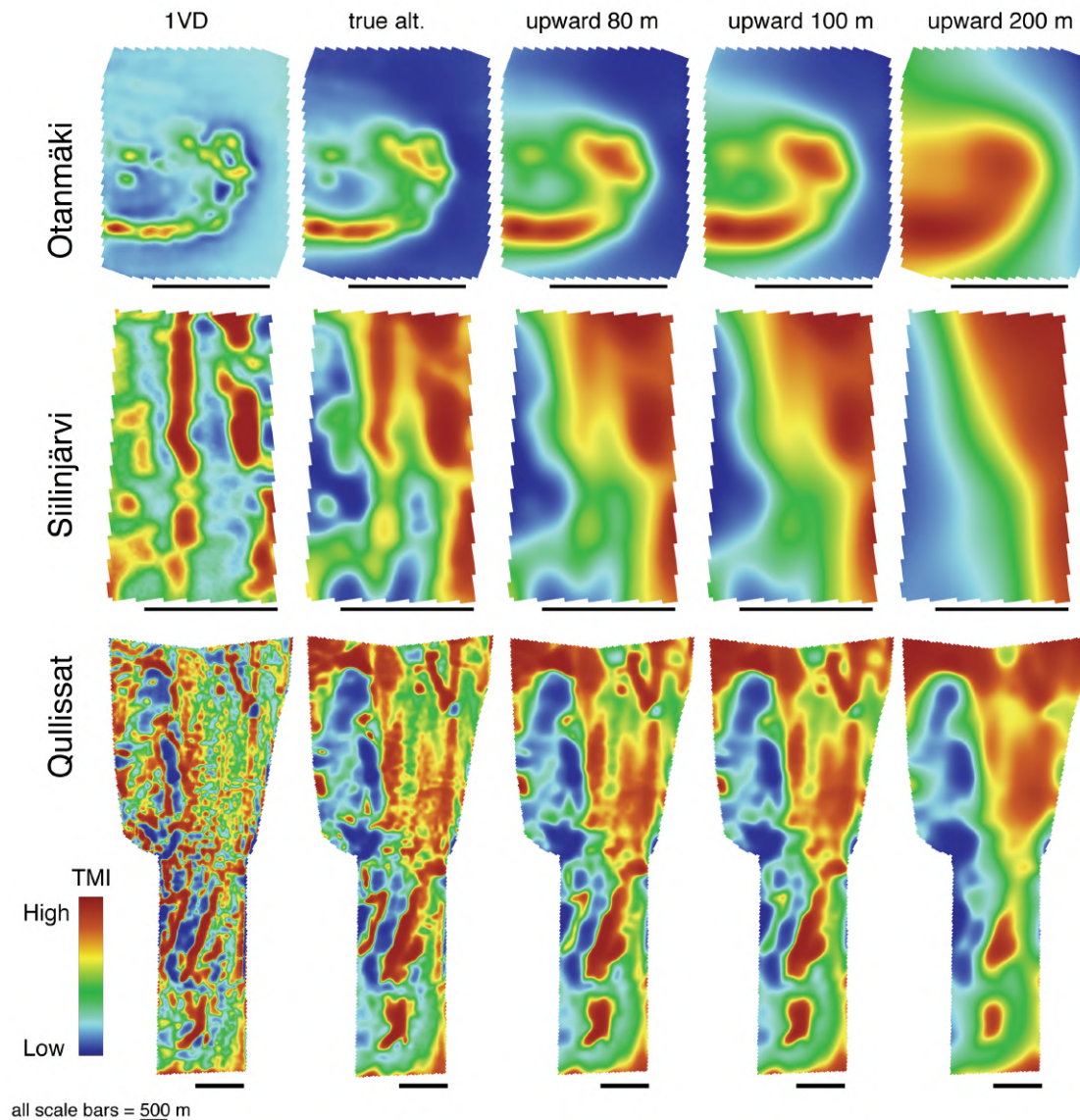


Figure 2.12 Upward continuation and derivative of magnetic survey data conducted in this work. The rows include the fixed-wing UAS total magnetic intensity data from each survey area (Otanmäki and Siilinjärvi, Finland; Qullissat in Greenland). The columns from left to right are: first vertical derivative (1VD), true altitude data, upward continuation to 80 m, 100 m and 200 m. Data from Jackisch et al., 2019, 2020 and Chapter V.

References

- Aasen, H., Honkavaara, E., Lucieer, A., and Zarco-Tejada, P.J., 2018, Quantitative remote sensing at ultra-high resolution with UAV spectroscopy: A review of sensor technology, measurement procedures, and data correction workflows: *Remote Sensing*, v. 10, p. 1–42, doi:10.3390/rs10071091.
- Adão, T., Hruška, J., Pádua, L., Bessa, J., Peres, E., Morais, R., and Sousa, J.J., 2017, Hyperspectral imaging: A review on UAV-based sensors, data processing and applications for agriculture and forestry: *Remote Sensing*, v. 9, doi:10.3390/rs9111110.
- Andreani, L., and Gloaguen, R., 2016, Geomorphic analysis of transient landscapes in the Sierra Madre de Chiapas and Maya Mountains (northern Central America): Implications for the North American-Caribbean-Cocos plate boundary: *Earth Surface Dynamics*, v. 4, p. 71–102, doi:10.5194/esurf-4-71-2016.

- Assmann, J.J., Kerby, J.T., Cunliffe, A.M., and Myers-Smith, I.H., 2019, Vegetation monitoring using multispectral sensors — best practices and lessons learned from high latitudes: *Journal of Unmanned Vehicle Systems*, v. 7, p. 54–75, doi:10.1139/juvs-2018-0018.
- Bemis, S.P., Micklethwaite, S., Turner, D., James, M.R., Akciz, S., Thiele, S.T., and Bangash, H.A., 2014, Ground-based and UAV-Based photogrammetry: A multi-scale, high-resolution mapping tool for structural geology and paleoseismology: *Journal of Structural Geology*, v. 69, p. 163–178, doi:10.1016/J.JSG.2014.10.007.
- Benediktsson, J.A., and Ghamisi, P., 2015, Spectral-spatial classification of hyperspectral remote sensing images: Boston, Artech House, v. 1, 284 p.
- Berk, A., Bernstein, L.S., Anderson, G.P., Acharya, P.K., Robertson, D.C., Chetwynd, J.H., and Adler-Golden, S.M., 1998, MODTRAN cloud and multiple scattering upgrades with application to AVIRIS: *Remote sensing of Environment*, v. 65, p. 367–375.
- Blakely, R.J., 1995, *Potential Theory in Gravity and Magnetic Applications*: Cambridge, Cambridge University Press, doi:10.1017/CBO9780511549816.
- Blistan, P., Kovanič, Ľ., Zelizňaková, V., and Palková, J., 2016, Using UAV photogrammetry to document rock outcrops: *Acta Montanistica Slovaca*, v. 21, p. 154–161.
- Booyesen, R., Gloaguen, R., Lorenz, S., Zimmermann, R., and Nex, P.A.M., 2020a, Geological Remote Sensing: Elsevier Inc., 1–14 p., doi:10.1016/b978-0-12-409548-9.12127-x.
- Booyesen, R., Jackisch, R., Lorenz, S., Zimmermann, R., Kirsch, M., Nex, P.A.M., and Gloaguen, R., 2020b, Detection of REEs with lightweight UAV-based hyperspectral imaging: *Scientific Reports*, v. 10, doi:10.1038/s41598-020-74422-0.
- Clark, D.A., 2014, Methods for determining remanent and total magnetisations of magnetic sources—a review: *Exploration Geophysics*, v. 45, p. 271–304.
- Clark, R.N., 1999, Spectroscopy of rocks and minerals and principles of spectroscopy, in Andrew N. Rencz ed., *Manual of remote sensing, Volume 3, Remote sensing for the earth sciences*, Hoboken, NJ, Wiley, *Manual of remote sensing 1*, v. 3, p. 3–58.
- Clark, R.N., and Roush, T.L., 1984, Reflectance spectroscopy: Quantitative analysis techniques for remote sensing applications: *Journal of Geophysical Research: Solid Earth*, v. 89, p. 6329–6340, doi:10.1029/JB089iB07p06329.
- Clauser, C., 2014, *Einführung in die Geophysik*: Berlin-Heidelberg, Springer-Verlag, 414 p., doi:10.1007/978-3-642-04496-0.
- Colomina, I., and Molina, P., 2014, Unmanned aerial systems for photogrammetry and remote sensing: A review: *ISPRS Journal of Photogrammetry and Remote Sensing*, v. 92, p. 79–97, doi:10.1016/j.isprsjprs.2014.02.013.
- Crowe, S., Cresswell, K., Robertson, A., Huby, G., Avery, A., and Sheikh, A., 2011, The case study approach: *BMC Medical Research Methodology*, v. 11, p. 100, doi:10.1186/1471-2288-11-100.
- Crowley, J.K., Williams, D.E., Hammarstrom, J.M., Piatak, N., Chou, I.-M., and Mars, J.C., 2003, Spectral reflectance properties (0.4–2.5 μm) of secondary Fe-oxide, Fe-hydroxide, and Fe-sulphate-hydrate minerals associated with sulphide-bearing mine wastes: *Geochemistry: Exploration, Environment, Analysis*, v. 3, p. 219–228, doi:10.1144/1467-7873/03-001.

- Dentith, M., and Mudge, S.T., 2014, *Geophysics for the Mineral Exploration Geoscientist*: Cambridge, Cambridge University Press, v. 1, 455 p., doi:10.1007/s00126-014-0557-9.
- Dering, G.M., Micklethwaite, S., Thiele, S.T., Vollgger, S.A., and Cruden, A.R., 2019, Review of drones, photogrammetry and emerging sensor technology for the study of dykes: Best practises and future potential: *Journal of Volcanology and Geothermal Research*, v. 373, p. 148–166, doi:10.1016/j.jvolgeores.2019.01.018.
- Fasnacht, L., Vogt, M.-L., Renard, P., and Brunner, P., 2019, A 2D hyperspectral library of mineral reflectance, from 900 to 2500 nm: *Scientific Data*, v. 6, p. 268, doi:10.1038/s41597-019-0261-9.
- Frey, P.A., and Reed, G.H., 2012, The Ubiquity of Iron: *ACS Chemical Biology*, v. 7, p. 1477–1481, doi:10.1021/cb300323q.
- Gaffey, C., and Bhardwaj, A., 2020, *Applications of Unmanned Aerial Vehicles in Cryosphere : Latest Advances and Prospects*:
- Gavazzi, B., Le Maire, P., Mercier de Lépinay, J., Calou, P., and Munschy, M., 2019, Fluxgate three-component magnetometers for cost-effective ground, UAV and airborne magnetic surveys for industrial and academic geoscience applications and comparison with current industrial standards through case studies: *Geomechanics for Energy and the Environment*, v. 20, p. 100117, doi:10.1016/j.gete.2019.03.002.
- Gavazzi, B., Le Maire, P., Munschy, M., and Dechamp, A., 2016, Fluxgate vector magnetometers: A multisensor device for ground, UAV, and airborne magnetic surveys: *Leading Edge*, v. 35, p. 795–797, doi:10.1190/tle35090795.1.
- Ghamisi, P., Plaza, J., Chen, Y., Li, J., and Plaza, A.J., 2017, Advanced Spectral Classifiers for Hyperspectral Images: A review: *IEEE Geoscience and Remote Sensing Magazine*, v. 5, p. 8–32, doi:10.1109/MGRS.2016.2616418.
- Goetz, A.F.H., Vane, G., Solomon, J.E., and Rock, B.N., 1985, Imaging spectrometry for earth remote sensing: *Science*, v. 228, p. 1147–1153, doi:10.1126/science.228.4704.1147.
- Gonçalves, J.A., and Henriques, R., 2015, UAV photogrammetry for topographic monitoring of coastal areas: *ISPRS Journal of Photogrammetry and Remote Sensing*, v. 104, p. 101–111, doi:10.1016/j.isprsjprs.2015.02.009.
- Hakala, T. et al., 2018, Direct Reflectance Measurements from Drones: Sensor Absolute Radiometric Calibration and System Tests for Forest Reflectance Characterization: *Sensors*, v. 18, doi:10.3390/s18051417.
- Harrison, R.J., Dunin-Borkowski, R.E., Kasama, T., Simpson, E.T., and Feinberg, J.M., 2005, *Magnetic Properties of Rocks and Minerals: Treatise on Geophysics: Second Edition*, v. 2, p. 609–660, doi:10.1016/B978-0-444-53802-4.00048-8.
- Hassanalain, M., and Abdelkefi, A., 2017, Classifications, applications, and design challenges of drones: A review: *Progress in Aerospace Sciences*, v. 91, p. 99–131, doi:10.1016/j.paerosci.2017.04.003.
- Henderson, R.G., and Zietz, I., 1949, The upward continuation of anomalies in total magnetic intensity fields: *Geophysics*, v. 14, p. 517–534.
- Honkavaara, E., Saari, H., Kaivosoja, J., Pölönen, I., Hakala, T., Litkey, P., Mäkynen, J., and Pesonen, L., 2013, Processing and Assessment of Spectrometric, Stereoscopic Imagery Collected Using a Lightweight UAV Spectral Camera for Precision Agriculture: *Remote Sensing*, v. 5, doi:10.3390/rs5105006.

- Hunt, G.R., 1977, Spectral signatures of particulate minerals in the visible and near infrared: *Geophysics*, v. 42, p. 501–513.
- Hunt, G.R., and Ashley, R.P., 1979, Spectra of altered rocks in the visible and near infrared: *Economic Geology*, v. 74, p. 1613–1629, doi:10.2113/gsecongeo.74.7.1613.
- Hunt, C.P., Moskowitz, B.M., and Banerjee, S.K., 1995, Magnetic properties of rocks and minerals: Rock physics and phase relations: A handbook of physical constants, v. 3, p. 189–204.
- Isles, D.J., and Rankin, L.R., 2013, Geological interpretation of aeromagnetic data: Perth, Society of Exploration Geophysicists and Australian Society of Exploration, v. 1, 365 p.
- Jackisch, R. et al., 2020, Integrated Geological and Geophysical Mapping of a Carbonatite-hosting Outcrop in Siilinjärvi, Finland, Using Unmanned Aerial Systems: *Remote Sensing*, v. 12, doi:10.3390/RS12182998.
- Jackisch, R., Madriz, Y., Zimmermann, R., Pirttijärvi, M., Saartenoja, A., Heincke, B.H., Salmirinne, H., Kujasalo, J.-P., Andreani, L., and Gloaguen, R., 2019a, Drone-borne hyperspectral and magnetic data integration: Otanmäki Fe-Ti-V deposit in Finland: *Remote Sensing*, v. 11, doi:10.3390/rs11182084.
- Jackisch, R., Pirttijärvi, M., Salmirinne, H., Kärenlampi, K., Heincke, B., Jylänki, J., Zimmermann, R., Sørensen, E.-V., Middleton, M., and Madriz, Y., 2019b, Acquisition and Processing Report of the MULSEDRO EIT RM Project from the Otanmäki Fe-Ti-V Deposit, Finland: GTK Open File Research Report, p. 124.
- Jakob, S., Zimmermann, R., and Gloaguen, R., 2017, The Need for Accurate Geometric and Radiometric Corrections of Drone-Borne Hyperspectral Data for Mineral Exploration: *MEPHySTo-A Toolbox for Pre-Processing Drone-Borne Hyperspectral Data: Remote Sensing*, v. 9, p. 88, doi:10.3390/rs9010088.
- James, M. et al., 2020, Volcanological applications of unoccupied aircraft systems (UAS): Developments, strategies, and future challenges: *Volcanica*, p. 67–114, doi:10.30909/vol.03.01.67114.
- James, M.R., Chandler, J.H., Eltner, A., Fraser, C., Miller, P.E., Mills, J.P., Noble, T., Robson, S., and Lane, S.N., 2019, Guidelines on the use of structure-from-motion photogrammetry in geomorphic research: *Earth Surface Processes and Landforms*, v. 2084, p. 2081–2084, doi:10.1002/esp.4637.
- James, M.R., and Robson, S., 2014, Mitigating systematic error in topographic models derived from UAV and ground-based image networks: *Earth Surface Processes and Landforms*, v. 39, p. 1413–1420.
- Jensen, J.R., 2014, Remote sensing of the environment : an Earth Resource Perspective: Essex, Pearson Education Limited, 619 p.
- Jessell, M.W., 1997, Atlas of structural geophysics: Melbourne, Australia, Australian Crustal Research Centre, Australian Crustal Research Centre Technical Publication, 154 p.
- Jessell, M., 2001, Three-dimensional geological modelling of potential-field data: *Computers & Geosciences*, v. 27, p. 455–465, doi:https://doi.org/10.1016/S0098-3004(00)00142-4.
- Jirigalatu, J., Krishna, V., da Silva, E., and Døssing, A., 2021, Experiments on magnetic interference for a portable airborne magnetometry system using a hybrid unmanned aerial vehicle (UAV): *Geoscientific Instrumentation, Methods and Data Systems*, v. 10, p. 25–34, doi:10.5194/gi-10-25-2021.

- Jones, E., Oliphant, T., and Peterson, P., 2001, SciPy: Open Source Scientific Tools for Python, Scipy for Python: www.scipy.org (accessed 08.05.2021).
- Karpouzli, E., and Malthus, T., 2003, The empirical line method for the atmospheric correction of IKONOS imagery: *International Journal of Remote Sensing*, doi:10.1080/0143116021000026779.
- Kearey, P., and Brooks, M., 1991, *An introduction to geophysical exploration*. 2nd edition: Blackwell Scientific Publications, 263 p.
- Kelcey, J., and Lucieer, A., 2012, Sensor correction of a 6-band multispectral imaging sensor for UAV remote sensing: *Remote Sensing*, v. 4, p. 1462–1493, doi:10.3390/rs4051462.
- Kim, B., 2020, Aeromagnetic Exploration using Unmanned Aerial Vehicles: Current and Future Trends: *Geophysics and Geophysical Exploration*, v. 23, p. 178–191, doi:<https://doi.org/10.7582/GGE.2020.23.3.00178>.
- Kirsch, M., Lorenz, S., Zimmermann, R., Tusa, L., Möckel, R., Hödl, P., Booysen, R., Khodadadzadeh, M., and Gloaguen, R., 2018, Integration of terrestrial and drone-borne hyperspectral and photogrammetric sensing methods for exploration mapping and mining monitoring: *Remote Sensing*, v. 10, doi:10.3390/rs10091366.
- Koerting, F., Koellner, N., Kuras, A., Boesche, N.K., Rogass, C., Mielke, C., Elger, K., and Altenberger, U., 2019, A solar optical hyperspectral library of rare earth-bearing minerals, rare earth oxides, copper-bearing minerals and Apliki mine surface samples: *Earth System Science Data Discussions*, v. 2019, p. 1–23, doi:10.5194/essd-2019-228.
- Kokaly, R.F., Clark, R.N., Swayze, G.A., Livo, K.E., Hoefen, T.M., Pearson, N.C., Wise, R.A., Benzal, W.M., Lowers, H.A., and Driscoll, R.L., 2017, USGS spectral library version 7: US Geological Survey U.S. Geological Survey Data Series 1035, 61 p.
- Kroll, A., 2013, Evaluation of an Unmanned Aircraft for Geophysical Survey: ASEG Extended Abstracts, v. 2013, p. 1–4, doi:10.1071/aseg2013ab328.
- Kruse, F. a, 1998, *Advances in Hyperspectral Remote Sensing for Geologic Mapping and Exploration: Geophysics*, p. 2005–2007.
- Landgrebe, D.A., 2005, *Signal theory methods in multispectral remote sensing*: John Wiley & Sons, Hoboken, NJ, v. 29, p. 529.
- Lee, S., and Choi, Y., 2016, Reviews of unmanned aerial vehicle (drone) technology trends and its applications in the mining industry: *Geosystem Engineering*, v. 19, p. 197–204, doi:10.1080/12269328.2016.1162115.
- Madriz, Y., 2019, Drone-borne geophysics: magnetic survey for mineral exploration [unpublished MSc thesis]: Freiberg, TU Bergakademie Freiberg, 88 p.
- Le Maire, P., Bertrand, L., Munsch, M., Diraison, M., and Géraud, Y., 2020, Aerial magnetic mapping with an unmanned aerial vehicle and a fluxgate magnetometer: a new method for rapid mapping and upscaling from the field to regional scale: *Geophysical Prospecting*, p. 1–13, doi:10.1111/1365-2478.12991.
- Manolakis, D., Lockwood, R., and Cooley, T., 2016, *Hyperspectral Imaging Remote Sensing: Physics, Sensors and Algorithms*: v. 1, 701 p.
- Marinelli, W.J., Gittins, C.M., Gelb, A.H., and Green, B.D., 1999, Tunable Fabry-Perot etalon-based long-wavelength infrared imaging spectroradiometer: *Applied Optics*, v. 38, p. 2630–2639, doi:10.1364/ao.38.002594.

- van der Meer, F.D., van der Werff, H.M.A., van Ruitenbeek, F.J.A., Hecker, C.A., Bakker, W.H., Noomen, M.F., van der Meijde, M., Carranza, E.J.M., de Smeth, J.B., and Woldai, T., 2012, Multi- and hyperspectral geologic remote sensing: A review: *International Journal of Applied Earth Observation and Geoinformation*, v. 14, p. 112–128, doi:10.1016/j.jag.2011.08.002.
- Merayo, J.M.G., Brauer, P., Primdahl, F., Petersen, J.R., and Nielsen, O. V, 2000, Scalar calibration of vector magnetometers: *Measurement science and technology*, v. 11, p. 120.
- Meyer, C.B., 2001, A case in case study methodology: *Field methods*, v. 13, p. 329–352.
- Mielke, C., Boesche, N.K., Rogass, C., Kaufmann, H., Gauert, C., and de Wit, M., 2014, Spaceborne mine waste mineralogy monitoring in South Africa, applications for modern push-broom missions: *Hyperion/OLI and EnMAP/Sentinel-2: Remote Sensing*, v. 6, p. 6790–6816, doi:10.3390/rs6086790.
- Morris, R. V, Lauer, H.V.J., Lawson, C.A., Gibson, E.K.J., Nace, G.A., and Stewart, C., 1985, Spectral and other physicochemical properties of submicron powders of hematite (α -Fe₂O₃), maghemite (γ -Fe₂O₃), magnetite (Fe₃O₄), goethite (α -FeOOH), and lepidocrocite (γ -FeOOH): *Journal of geophysical research*, v. 90, p. 3126–3144, doi:10.1029/jb090ib04p03126.
- Munsch, M., Boulanger, D., Ulrich, P., and Bouiflane, M., 2007, Magnetic mapping for the detection and characterization of UXO: Use of multi-sensor fluxgate 3-axis magnetometers and methods of interpretation: *Journal of Applied Geophysics*, v. 61, p. 168–183, doi:10.1016/j.jappgeo.2006.06.004.
- Nabighian, M.N., Grauch, V.J.S., Hansen, R.O., LaFehr, T.R., Li, Y., Peirce, J.W., Phillips, J.D., and Ruder, M.E., 2005, The historical development of the magnetic method in exploration: *Geophysics*, v. 70, doi:10.1190/1.2133784.
- de Oliveira, R.A., Tommaselli, A.M.G., and Honkavaara, E., 2016, Geometric Calibration of a Hyperspectral Frame Camera: *Photogrammetric Record*, v. 31, p. 325–347, doi:10.1111/phor.12153.
- Oppenheim, A. V, Schafer, R.W., Buck, J.R., and Lee, L., 1999, *Discrete-time Signal Processing* (University of Michigan, Ed.): Michigan, Prentice Hall, Prentice Hall international editions, 870 p.
- Paine, J.W., 1986, A comparison of methods for approximating the vertical gradient of one-dimensional magnetic field data: *Geophysics*, v. 51, p. 1725–1735.
- Pan, S.L., and Tan, B., 2011, Demystifying case research: A structured–pragmatic–situational (SPS) approach to conducting case studies: *Information and Organization*, v. 21, p. 161–176, doi:10.1016/j.infoandorg.2011.07.001.
- Park, S., and Choi, Y., 2020, Applications of unmanned aerial vehicles in mining from exploration to reclamation: A review: *Minerals*, v. 10, p. 1–32, doi:10.3390/min10080663.
- Parker Gay, S., 2004, Glacial till: A troublesome source of near-surface magnetic anomalies: *The Leading Edge*, v. 23, p. 542–547.
- Pirttijärvi, M., 2003, Numerical modeling and inversion of geophysical electromagnetic measurements using a thin plate model [PhD thesis]: University of Oulu, Oulu, Finland, 44 p.
- Pirttijärvi, M., 2015, Ryssänlampi magnetic survey using Radai UAV system and its comparison to airborne and ground magnetic data of GTK: Radai Ltd., 26 p., https://tupa.gtk.fi/raportti/arkisto/73_2015.pdf (accessed June 2020).

- QGIS Development Team, 2020, QGIS Geographic Information System.: software, www.qgis.osgeo.org (accessed May 2021).
- Reeves, C., 2006, Aeromagnetic Surveys. Principles, Practice & Interpretation: Earthworks, p. 155, doi:10.1007/BF01465543.
- Ren, H., Zhao, Y., Xiao, W., and Hu, Z., 2019, A review of UAV monitoring in mining areas: current status and future perspectives: *International Journal of Coal Science & Technology*, v. 6, p. 320–333, doi:10.1007/s40789-019-00264-5.
- Rodger, A., Laukamp, C., Haest, M., and Cudahy, T., 2012, A simple quadratic method of absorption feature wavelength estimation in continuum removed spectra: *Remote Sensing of Environment*, v. 118, p. 273–283, doi:10.1016/j.rse.2011.11.025.
- van Rossum, Guido and Drake Jr, F.L., 1995, Python reference manual: Amsterdam, Centrum voor Wiskunde en Informatica Amsterdam: www.python.org, (accessed May 2021).
- RStudio Team, 2020, RStudio: Integrated Development Environment for R: software, www.rstudio.com (accessed May 2021).
- Said, K.O., Onifade, M., Githiria, J.M., Abdulsalam, J., Bodunrin, M.O., Genc, B., Johnson, O., and Akande, J.M., 2020, On the application of drones: a progress report in mining operations: *International Journal of Mining, Reclamation and Environment*, v. 00, p. 1–33, doi:10.1080/17480930.2020.1804653.
- Sherman, D.M., 1985, The electronic structures of Fe³⁺ coordination sites in iron oxides: Applications to spectra, bonding, and magnetism: *Physics and Chemistry of Minerals*, v. 12, p. 161–175, doi:10.1007/BF00308210.
- Sherman, D.M., and Waite, T.D., 1985, Electronic spectra of Fe³⁺ oxides and oxide hydroxides in the near IR to near UV.: *American Mineralogist*, v. 70, p. 1262–1269.
- Smith, W.H.F., and Wessel, P., 1990, Gridding with continuous curvature splines in tension: *Geophysics*, v. 55, p. 293–305.
- Stöcker, C., Bennett, R., Nex, F., Gerke, M., and Zevenbergen, J., 2017, Review of the Current State of UAV Regulations: *Remote Sensing*, v. 9, doi:10.3390/rs9050459.
- Swayze, G.A. et al., 2000, Using imaging spectroscopy to map acidic mine waste: *Environmental Science and Technology*, v. 34, p. 47–54, doi:10.1021/es990046w.
- Telford, W.M., Geldart, L.P., and Sheriff, R.E., 1990, *Applied Geophysics*: Cambridge, Cambridge University Press, v. 2, 770 p.
- Teskey, D., Barlow, R., Hood, P.J., Lefebvre, D., Paterson, N., Reford, M., and Watson, D., 1991, Guide to aeromagnetic specifications and contracts: Geological Survey of Canada, open file, v. 2349, p. 73.
- Thiele, S.T., Grose, L., Samsu, A., Micklethwaite, S., Vollgger, S.A., and Cruden, A.R., 2017, Rapid, semi-automatic fracture and contact mapping for point clouds, images and geophysical data: *Solid Earth*, v. 8, p. 1241–1253, doi:10.5194/se-8-1241-2017.
- Tu, Y.-H., Phinn, S., Johansen, K., and Robson, A., 2018, Assessing Radiometric Correction Approaches for Multi-Spectral UAS Imagery for Horticultural Applications: *Remote Sensing*, v. 10, doi:10.3390/rs10111684.
- Tuck, L., Samson, C., Laliberte, J., Wells, M., and Bélanger, F., 2018, Magnetic interference testing method for an electric fixed-wing unmanned aircraft system (UAS): *Journal of Unmanned Vehicle Systems*, v. 6, doi:10.1139/juvs-2018-0006.

- Walter, C., Braun, A., and Fotopoulos, G., 2018, Impact of 3-D attitude variations of a UAV magnetometry system on magnetic data quality: *Geophysical Prospecting*, p. 1–15, doi:10.1111/1365-2478.12727.
- Walter, C., Braun, A., and Fotopoulos, G., 2019, Spectral Analysis of Magnetometer Swing in High-Resolution UAV-borne Aeromagnetic Surveys: 2019 IEEE Systems and Technologies for Remote Sensing Applications Through Unmanned Aerial Systems, STRATUS 2019, p. 1–4, doi:10.1109/STRATUS.2019.8713313.
- van der Werff, H., and van der Meer, F., 2015, Sentinel-2 for mapping iron absorption feature parameters: *Remote Sensing*, v. 7, p. 12635–12653, doi:10.3390/rs71012635.
- Westoby, M.J., Brasington, J., Glasser, N.F., Hambrey, M.J., and Reynolds, J.M., 2012, “Structure-from-Motion” photogrammetry: A low-cost, effective tool for geoscience applications: *Geomorphology*, v. 179, p. 300–314, doi:10.1016/j.geomorph.2012.08.021.
- Yao, H., Qin, R., and Chen, X., 2019, Unmanned Aerial Vehicle for Remote Sensing Applications—A Review: *Remote Sensing*, v. 11, doi:10.3390/rs11121443.
- Zhong, Y., Wang, X., Xu, Y., Wang, S., Jia, T., Hu, X., Zhao, J., Wei, L., and Zhang, L., 2018, Mini-UAV-Borne Hyperspectral Remote Sensing: From Observation and Processing to Applications: *IEEE Geoscience and Remote Sensing Magazine*, v. 6, p. 46–62, doi:10.1109/MGRS.2018.2867592.

III

Chapter 3 — A first test of UAS in Finland

Mine sites that host iron and related ores are favourable for magnetic and hyperspectral surveying. Size and topography can challenge ground-based and airborne data acquisition. Thus, an integrated acquisition of magnetic and hyperspectral data using drones is beneficial for direct mapping in high resolution with rapid and frequent intervals.

To evaluate acquisition and processing routines, a brownfield mine site in Otanmäki served as test area for experimental drone studies. For the first time, a novel fluxgate magnetometer was integrated on a multicopter and created magnetic data reaches near the quality of standard ground survey. It was shown that the spectrally non-diagnostic magnetite is traceable via hyperspectral proxies. The considerable amount of acquired research data and analysis were conveyed in a technical report⁶, and the work was published in **Remote Sensing**⁷, from which the following chapter originates. This chapter presents the data processing chain and demonstrates that magnetic and hyperspectral drone-based investigations are highly useful to create first-order ore occurrence maps.

⁶ Jackisch, R., Pirttijärvi, M., Salmirinne, H., Kärenlampi, K., Heincke, B., Jylänki, J., Zimmermann, R., Sørensen, E.-V., Middleton, M., and Madriz, Y., 2019, Acquisition and Processing Report of the MULSEDRO EIT RM Project from the Otanmäki Fe-Ti-V Deposit, Finland: GTK Open File Research Report, p. 124.

⁷ **Jackisch, R.**, Madriz, Y., Zimmermann, R., Pirttijärvi, M., Saartenoja, A., Heincke, B.H., Salmirinne, H., Kujasalo, J.-P., Andreani, L., and Gloaguen, R., 2019, Drone-borne hyperspectral and magnetic data integration: Otanmäki Fe-Ti-V deposit in Finland: *Remote Sensing*, v. 11, doi:10.3390/rs11182084.

Drone-Borne Hyperspectral and Magnetic Data Integration: Otanmäki Fe-Ti-V Deposit in Finland.

Robert Jackisch^{1,*}, Yuleika Madriz¹, Robert Zimmermann¹, Markku Pirttijärvi², Ari Saartenoja², Björn H. Heincke³, Heikki Salmirinne⁴, Jukka-Pekka Kujasalo⁴, Louis Andreani¹ and Richard Gloaguen¹

¹Helmholtz-Zentrum Dresden-Rossendorf, Helmholtz Institute Freiberg for Resource Technology, Division “Exploration Technology”, Chemnitz Str. 40, 09599 Freiberg, Germany

²Radaï Oy, Teknologiantie 18, 90470 Oulu, Finland

³Geological Survey of Denmark and Greenland, Øster Voldgade 10, 1350 København, Denmark

⁴Geological Survey of Finland, Lähteentie 2, 96400 Rovaniemi, Finland

Abstract

The technical evolution of unoccupied aerial systems (UAS) for mineral exploration advances rapidly. Recent sensor developments and improved UAS performance open new fields for research and applications in geological and geophysical exploration among others. In this study, we introduce an integrated acquisition and processing strategy for drone borne multi sensor surveys combining optical remote sensing and magnetic data. We deploy both fixed wing and multicopter UAS to characterize an outcrop of the Otanmäki Fe-Ti-V deposit in central Finland. The lithology consists mainly of gabbro intrusions hosting ore bodies of magnetite ilmenite. Large areas of the outcrop are covered by lichen and low vegetation. We use two drone borne multi and hyperspectral cameras operating in the visible to near infrared parts of the electromagnetic spectrum to identify dominant geological features and the extents of ore bodies via iron indicating proxy minerals. We apply band ratios and unsupervised and supervised image classifications on the spectral data, from which we can map surficial iron bearing zones. We use two setups with three axis fluxgate magnetometers deployed both by a fixed wing and a multi copter UAS to measure the magnetic field at various flight altitudes (15 m, 40 m, 65 m). The total magnetic intensity (TMI) computed from the individual components is used for further interpretation of ore distribution. We compare to traditional magnetic ground based survey data to evaluate the UAS based results. The measured anomalies and spectral data are validated and assigned to the outcropping geology and ore mineralization by performing surface spectroscopy, portable X ray fluorescence (pXRF), magnetic susceptibility, and traditional geologic mapping. Locations of mineral zones and magnetic anomalies correlate with the established geologic map. The integrated survey strategy allowed a straightforward mapping of ore occurrences. We highlight the efficiency, spatial resolution, and reliability of UAS surveys. Acquisition time of magnetic UAS surveying surpassed ground surveying by a factor of 20 with a comparable resolution. The proposed workflow possibly facilitates surveying, particularly in

areas with complicated terrain and of limited accessibility, but highlights the remaining challenges in UAS mapping.

Keywords: UAS; hyperspectral; multispectral; magnetic; mineral exploration; drone; iron minerals; Otanmäki

3.1 Introduction

The demand for raw materials is steadily growing in our technology driven societies. In Europe, industry and businesses depend heavily on direct and indirect raw material imports (metal ores, fossil energy carriers) (Schoer et al., 2012). The difficulty of providing selected critical raw materials by European producers is increasing—e.g., for rare earth elements (Massari and Ruberti, 2013)—and therefore innovative technologies in exploration and recycling are needed to decrease dependencies on non-domestic imports of raw materials. In this context, we see a high demand for the exploration of new deposits and/or small or less profitable prospects to sustain the need for metallic and raw materials (Ali et al., 2017; European Commission, 2017; Gloaguen et al., 2018) and therefore inaccessible or formerly non-lucrative mineral deposits are needed (Henckens et al., 2016). However, mineral exploration in Europe has to fit to our present societal and economic standards, meaning that sustainable, non-invasive, and efficient exploration strategies are required. Following these requirements, exploration in little explored regions can be started with regional survey approaches, e.g., large-scale satellite and regional airborne mapping. For areas and targets identified as potentially prospective, more detailed investigations are usually performed including—e.g., helicopter airborne surveying and extensive field campaigns. Local airborne surveys cover up to hundreds of square kilometers, but require infrastructures such as airports, fuel, and trained personnel. Additionally, the resolution is restricted by wider line spacing and higher flight altitude that limit the detection or characterization of smaller ore bodies and mineralization. Finally, ground based surveying that includes geophysics, drilling, and extensive sampling are applied to obtain detailed knowledge from identified deposits.

In this context, lightweight unmanned aerial systems (UAS) equipped with optical remote sensing and geophysical sensors are particularly attractive to investigate potential deposits in difficult or environmentally sensitive areas. UAS are able to operate autonomously over a given target, are easily deployable, and have short turn-around times for collecting high resolution data-sets with uniform coverage. Their costs are low and their flexibility is high for planning, timing, and logistics compared to a traditional airborne survey. Relevant information is obtained rapidly and the operation requires less personnel with adequate training and flight

permissions. UAS user-friendliness increases with the availability of light-weight and durable batteries, open-source autopilots, flight controllers, and means of customization.

However, UAS-based surveying is restricted by national regulations (Stöcker et al., 2017) and practical considerations such as safety aspects. In most countries, it is usually possible to operate in visual-line-of-sight (VLOS) and there are weight limits for flight operations. For mineral exploration, UAS systems are therefore mainly attractive for small-to-medium-sized survey areas, limited to some tens of square kilometers, which means that they compete with local-sized airplane and helicopter surveys and may become a complement to ground based surveys (Parshin et al., 2018).

Accordingly, a multitude of UAS applications (Colomina and Molina, 2014) have emerged over the past five years including mine surveillance (Rauhala et al., 2017), slope stability assessment in mining (Salvini et al., 2017), agriculture (Zarco-Tejada et al., 2013), infrastructure and construction work (Ham et al., 2016), archaeology (Koucká et al., 2018), forestry (Näsi et al., 2015), disaster monitoring (Restas, 2015), coastal environmental studies (Mancini et al., 2013) and ground water research (Rahman et al., 2017). Digital elevation models obtained from UAS can deliver resolutions in (sub-)centimeter range, and are superior to conventional mapping techniques in terms of survey area, time, and target accessibility (James and Robson, 2014; Bemis et al., 2014).

Hyper- and multispectral cameras are sensors that are frequently used on UAS, although their application has mostly been limited to agriculture. UAS use for mineral mapping is still underrepresented in scientific literature, but recent studies show great potential (Malehmir et al., 2017). Example studies apply UAS, or a combination of UAS and terrestrial scans to identify lithological structures and map lithologic domains (Kirsch et al., 2018; Dering et al., 2019). For geophysical applications, UAS-based magnetics is attractive since recent sensors are rugged and lightweight (Gavazzi et al., 2016). Acquisition and processing strategies from conventional airborne measurements can be adapted for UAS surveys.

Recent studies highlight the potential of UAS to locate man-made ferrous bodies superficially buried in soil having sizes and weights that reflect the properties of unexploded ordnance (UXO; Tezkan et al., 2011) and to map shallow volcano-related structures and magma bodies (Koyama et al., 2013), using combustion-engine UAS helicopters with optically-pumped magnetometers.

Promising mapping results show the potential of multicopter UAS to perform on par with traditional aeromagnetism (Cunningham et al., 2018, Parvar et al., 2018). The used optical pumped magnetometers were suspended on cables below the UAS. The influence of orientation

changes for such magnetometer mountings was investigated (Callum et al., 2018) and resulted in attitude recommendations. In contrast to UAS heli- and multicopter, autonomous fixed-wings provide the design suitable for long-range magnetic surveys of even larger areas (Samson et al., 2010).

Although applications of single sensors become more common and the techniques more well-developed, we observe a lack of combining separate survey techniques and, hence, to gain the full geoscientific information simultaneously. The main objective of our study is thus to evaluate the potential of integrated UAS-based remote sensing and geophysical techniques for mineral exploration. We compare those fast and effective survey strategies to traditional ground survey methods in the Otanmäki Fe-Ti-V deposit in Central Finland. We combine UAS-based data including multi- and hyperspectral remote sensing, magnetics, and structure-from-motion multi-vision stereo (SfM-MVS) photogrammetry, to create value for UAS methods in geology. More specifically for the iron ore deposit in Otanmäki, the motivation of this work is to map iron ore distributions and evaluate ore prospectivity. We chose those UAS-borne sensor types because 1) magnetic field variations are predominantly caused by changing (induced and permanent) magnetization of the iron ore, thus, magnetics is well-suited to determine the distribution of ore lenses and grade estimation; 2) multi- and hyperspectral imaging allows to map surficial alteration of iron minerals in the visible (VIS) and near-infrared (NIR) range of the electromagnetic spectrum. However, magnetite and ilmenite as the main ore minerals in Otanmäki are spectrally featureless in VIS-NIR. Therefore, the objective of this study is to investigate how far it is possible to locate those using proxy minerals, e.g., hematite. The combination of both methods is relevant, because the magnetic anomalies are predominantly caused by magnetite and accordingly, complementary information is collected from magnetic data not obtainable from hyperspectral data. Besides, magnetic measurements from UAS have limited spatial resolution and therefore hyperspectral data can help to more precisely assign anomalies to specific ore lenses or geologic units.

We use both fixed-wing and multicopter UAS for surveying because 1) multicopter allow for controlled low altitude flights with high-resolution sensors; and 2) fixed-wing UAS can quickly map larger areas with light-weight equipment. For ground validation of the UAS results, we conducted a ground magnetic survey, in-situ measurements including spectroscopy, determination of magnetic susceptibility, and laboratory investigations. With ground truthing, we verify the remote sensing results and are able to give accuracy assessments of different techniques. Finally, we point out difficulties for surveying that arise from external conditions, e.g., weather conditions and surface obstructions.

3.2 Location and Geology

3.2.1 Regional Setting and Description of the Study Area

The study area is located on the premise of the former Otanmäki Fe Ti V mine in central Finland, about 200 km southeast of the city Oulu (Figure 3.1).

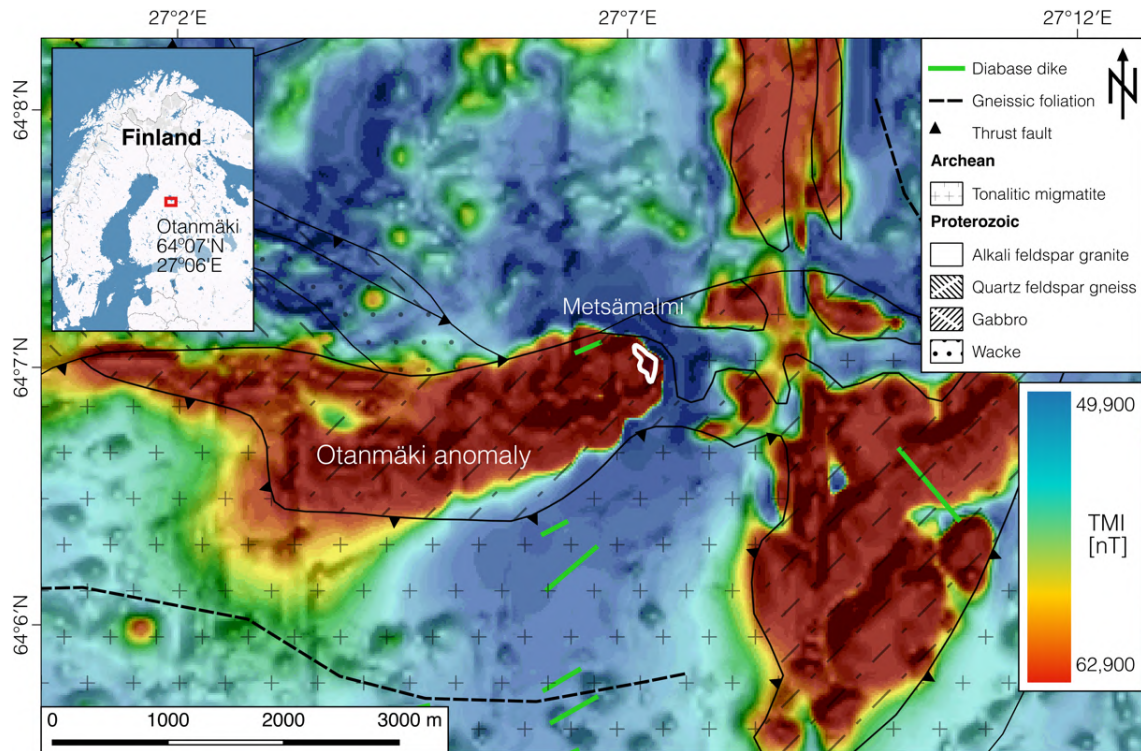


Figure 3.1 Hill-shaded total magnetic intensity (TMI) map of the Otanmäki area, central Finland, that is based on regional airborne surveys from GTK (Airo, 2005). Main regional geologic structures and units are plotted on top. Our study area, the Metsämalmi outcrop, is marked as a white polygon.

The main target is the exposed Metsämalmi (‘wood ore’ in Finnish) outcrop that is situated on the eastern edge of a large magnetic anomaly (Figure 3.1). The anomaly is associated with the Otanmäki gabbroic intrusion hosting the magnetite-ilmenite ore deposit (Pääkkönen, 1956). The outcrop has a size of about 28,000 m² and is located in a birch tree forest (Figure 3.2a). Much of its barren rock surface consists of high-grade ore lenses (see photographs from high-grade ore bodies and detailed geological map in Figure 3.2b & c, respectively) and it was cleared in the early 1980s for possible open pit mining. However, the decision to close the Otanmäki mine was made shortly afterwards and the Metsämalmi area was left unmined. Large spots (hand-size) of lichen cover its rock surfaces, and an area in the central part of about 30 × 10 m was cleaned up with a high-pressure cleaner some days before the surveys to improve the conditions for hyperspectral surveying.

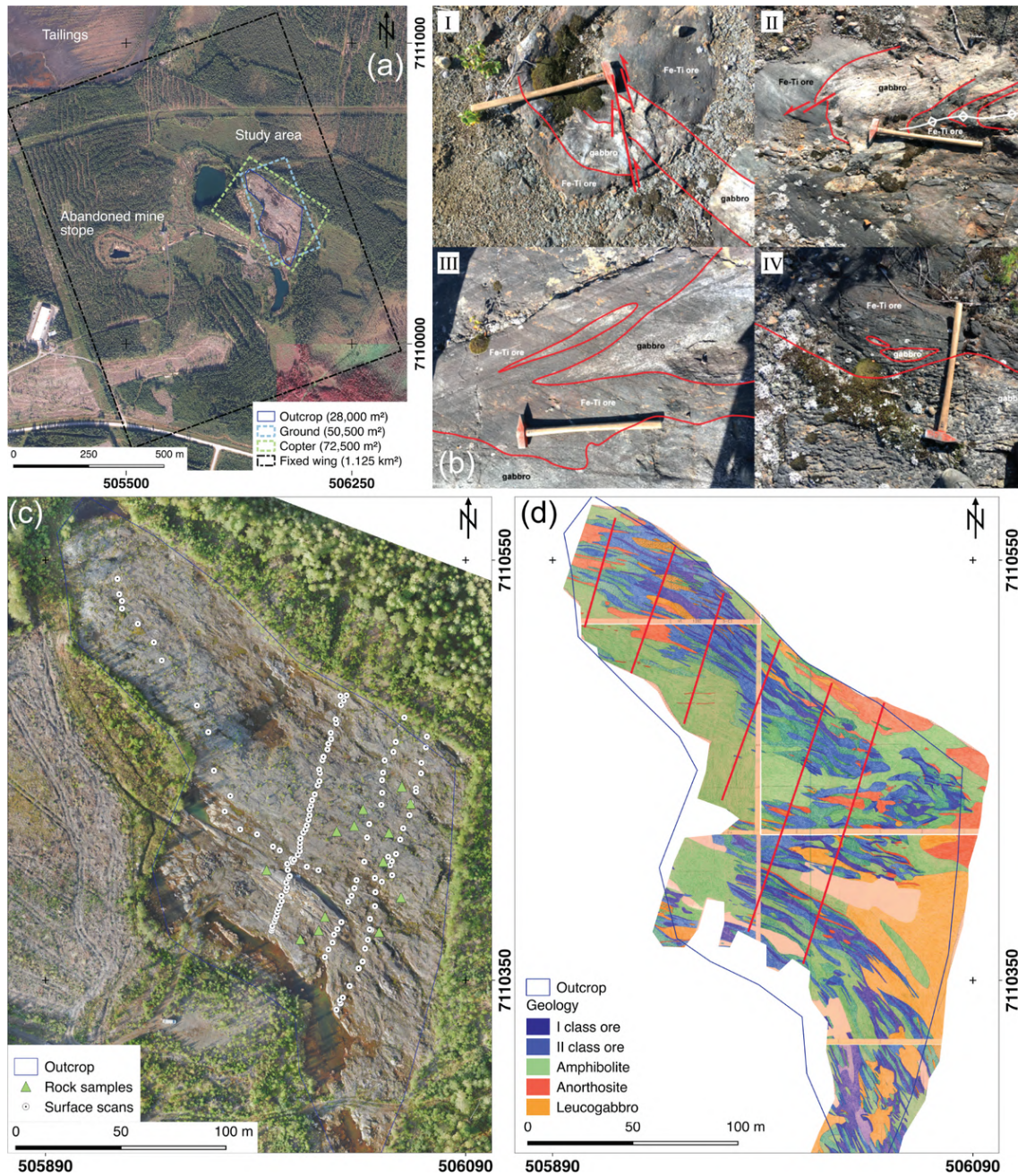


Figure 3.2 (a) Location of the study area at Otanmäki, central Finland. Rectangles outline the areas of the different magnetic surveys. (b) Photos (I–IV) from the surface of the Metsämalmi outcrop show magnetite-ilmenite ore lenses and host rock (gabbro). Hammer handle length for scale is ~1 m. (c) UAS-borne orthophoto shows sampling locations at the Metsämalmi outcrop. (d) Geologic map from Metsämalmi that is provided by company Otanmäki Mine Oy (modified). Larger parts of the outcropping area are mapped as high grade (Class I) ore that contains 60–70 % of magnetite and ilmenite. Red lines indicate surface measurements (i.e., magnetic susceptibilities along scan lines) performed by Otanmäki Mine Oy.

Apart from the Metsämalmi outcrop, the bedrock in the Otanmäki area is poorly exposed and rocks are largely covered by glacial overburden with a thickness of 1–3 meters. Therefore, geophysical surveys play an important role in regional studies to understand the hard rock geology (e.g., originally, the Fe-Ti-V ores were discovered by magnetic measurements). One example is the low altitude airborne regional magnetic survey from 1979 that was collected

within the national airborne geophysical program (see Airo, 2005). This survey uniformly covers the complete Otanmäki area (Figure 3.1) and was flown on an average flight altitude of 37 m and with a (in-)line spacing of 200 meters, with lines oriented in N–S direction.

3.2.2 Geologic Setting

The vanadiferous magnetite ilmenite ore deposits in the Otanmäki area are located within 2.06 Ga old gabbroic intrusions, which hosts ore within areas (Figure 2b) composed of metamorphosed gabbro, leucogabbro anorthosite, and lensoidal bodies of massive/semi massive oxide ore (Lindholm and Anttonen, 1980; Huhma, H., Hanski, E., Kontinen, A., Vuollo, J., Mänttari I., Lahyey, 2018). The intrusions were emplaced into Archaean migmatitic tonalite trondhjemite granodiorite gneisses, but they also have sharp, fault defined contacts against gneissic 2.05 Ga old, A type granites, and intermediate rocks (Otanmäki suite), hosting some Nb Zr REE mineralizations. The southern border of the anomaly is a thrust fault line.

The magnetite ilmenite ore bodies in the Otanmäki gabbro intrusion are scattered within a 50–200 m wide and approximately 5 km long ore bearing zone having numerous unequally sized and irregularly shaped ore lenses. The ore lenses within this zone are typically sub vertical, 2–200 m long and 3–50 m thick, generally EW trending and dipping N at 70–90° (Lindholm and Anttonen, 1980). In addition, the rocks in the ore zone are typically pervasively recrystallized and deformed, and the ore zone is folded into a syncline structure at its eastern end. The synform plunges to SW at about 40–60° and the ore zone descends along the fold axis. Based on drilling, the ore zone is known to extend down to a depth of 800 m and gravity based modeling suggests continuation of the intrusion down to a depth of 2 km (Lindholm and Anttonen, 1980, Lahti, I., Salmirinne, H., Kärenlampi, K. and Jylänki, 2018).

The average modal mineralogy of the Otanmäki high grade ore is composed of magnetite (35–40%), ilmenite (25–30%), and sulphides (1–2%) (Hokka, J. and Lepistö, 2018). Ore types are divided into three classes depending on their Fe oxide mineral content. Class I ore has a magnetite and ilmenite content of more than 50 wt %. Main gangue are silicate minerals such as chlorite, hornblende and plagioclase. Sulphide minerals (pyrite, chalcopyrite, and pyrrhotite) can make up to 20% of host rocks and ore. The distribution of mapped class I and II ore lenses in the Metsämalmi outcrop area is shown in Figure 2d. Due to the correlation between ore grade (iron content) and the amount of magnetite, the mining company considered magnetic susceptibility measurements as cost saving technique to estimate the ore.

3.3 Methods and Survey Strategies

We describe the different UAS based technologies that were used in the field campaign, as well as the acquisition strategies and the workflows to acquire and process the different datasets. For the different UAS, we introduce the platforms and employed sensors and define technical details. The sensors on the multicopters, i.e., magnetometer and frame based hyperspectral camera are exchangeable within a few minutes. The reasons for this are twofold: on one hand, the different sensors require different acquisition strategies (e.g., stop and go for hyperspectral imaging vs. continuous for magnetics). On the other hand, take-off weight is reduced, resulting in longer flight duration.

3.3.1 Survey Outline

Figure 3.3 shows photographs from different UAS types that were used in this field campaign, and their technical parameters and specifications are given in Table 3-1. Data acquisitions with all sensors and UAS types follow along pre-programmed survey patterns based on GPS points, but starts and landings are done manually. We performed ground (Figure 3.2c) and UAS surveys over the course of three days in September 2018. Weather conditions were favourable with mild temperatures, little cloud coverage, weak wind ($\sim 3\text{--}7$ km/h) and scarce gusts. The flight altitudes are given above ground level (AGL), and range between 15–65 m AGL.

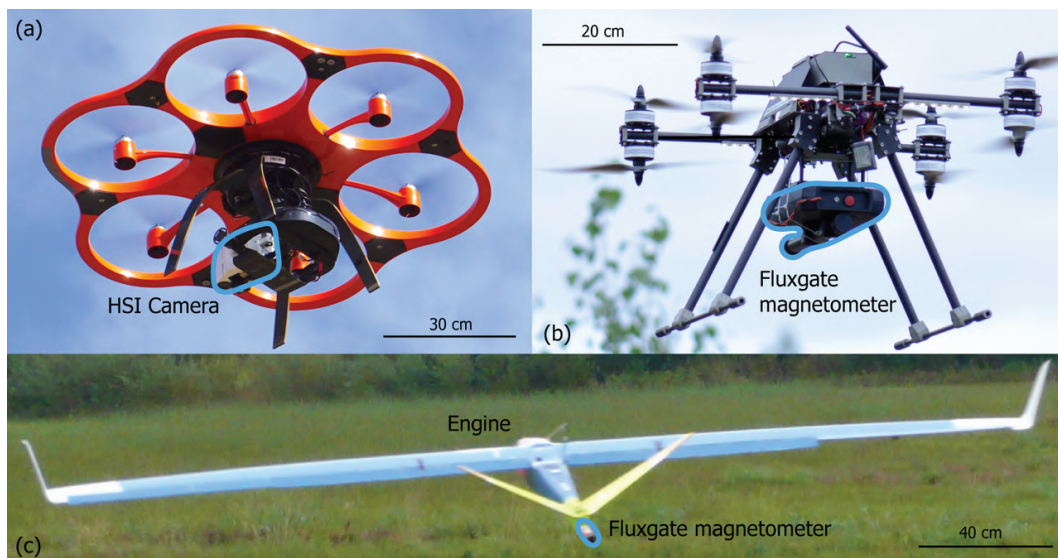


Figure 3.3 (a) Aibot UAS equipped with the HSI camera Rikola. (b) Tholeg UAS with a standalone MagDrone fluxgate magnetometer. (c) Radai's Albatros fixed-wing UAS with a fluxgate sensor in the tail.

Table 3-1 Technical details of the used UAS. The eBee plus instrument is not shown in Figure 3.3.

Model	Tholeg Tho-R-PX8-12	Aibotix Aibot X6v.2	SenseFly Ebee Plus	Radai Albatros VT
Type	Multicopter	Multicopter	Fixed-wing	Fixed-wing
Rotors	8	6	1	1
MTOW*	10 kg	7 kg	1.1 kg	5 kg
Size	70 × 70 × 35 cm	105 × 105 × 45 cm	110 cm wingspan	2.8 m wingspan
Flight time	20–25 min	12–15 min	59 min	180 min
Velocity	0–40 km/h	0–30 km/h	40–110 km/h	50–110 km/h
Payload	4.5 kg	2 kg	~0.2 kg	2 kg
Sensor	Fluxgate magnetometer	Rikola HSI camera	RGB camera, 4 band multispectral camera	Fluxgate magnetometer

*Maximum take-off weight.

3.3.2 Multispectral UAS Imaging

We conducted multispectral imaging (MSI) with a Sensefly eBee Plus fixed wing UAS. The ebee Plus is equipped with the lightweight Parrot Sequoia (1.2 Mpixel) four channel multispectral global shutter camera. Its multispectral bands are centred at 550 ± 40 nm (green), 660 ± 40 nm (red), 735 ± 10 nm (red edge), and 790 ± 40 nm (NIR). Automatic radiometric calibration was performed prior to the flight using a synthetic reference panel provided by the manufacturer. The UAS captured 98 multispectral scenes at 84 m AGL along the programmed flight path, in order to ensure sufficient image overlap. The orthomosaic was processed in Agisoft Photoscan, using optimized multispectral processing option and protocols (James et al., 2016), with the green band as master band. Processing parameters for the image alignment were set to ‘high quality’, while the key point and tie point limit was set to 40,000 and 4,000, respectively, and used with reference preselection. Outlier tie points were removed manually using the gradual selection tool prior to dense image matching (maximum reprojection root mean square error (RMSE) achieved: 0.2 or 3.16 pixel; mean RMSE: 0.1 or 0.39 pixel) followed by optimization of the bundle adjustment. Based on the resulting dense point cloud, an orthomosaic was generated with a ground resolution of 7.4 cm/pixel. Due to low sun elevation in the northern hemisphere (sun altitude 25° ; azimuth 228° at 16:00 local time) and late time of the day during data acquisition, we applied a topographic correction using the c-factor correction using the Python-based MEPHysTo image processing toolbox (Jakob et al., 2017).

3.3.3 Hyperspectral UAS Imaging

Hyperspectral UAS borne data are captured with the Senops Rikola Hyperspectral Imager. This snapshot sensor has the advantage of acquiring full frame data for up to 50 spectral bands, thus having high frame coherence towards each other with the UAS flying along a stop and go data

acquisition plan at 30 m altitude AGL. Table 2 lists the camera parameters used for the survey (Makelainen et al., 2013).

Table 3-2 Technical data and settings of the Rikola camera during flight operation.

Parameter	Value
Image Resolution	1010 × 648 Pixel
Bands	50
Spectral range	504–900 nm
Spatial / Spectral resolution	3 cm / 8 nm
FWHM	~14 nm
Band integration time	10–50 ms (depending on illumination)
Focal length	9 mm
F-number	2.8
Weight	720 g

Pre-processing of the HSI data was again performed with the Mephysto toolbox (Jakob et al., 2017). Images are co-registered, corrected for geometric effects (lens- and topographic correction) and georeferenced to the RGB orthophoto acquired by SfM-MVS (see Section 3.3.4). We used the empirical line method for radiometric conversion from radiance to reflectance (Karpouzli and Malthus, 2003). For the calibration, we used three PVC reference panels (shades of black, grey, and white) with known spectral signatures. As the HSI scenes generally showed low reflectance, calibration with the grey panel gave satisfying image contrast. As for the multispectral survey, main factor to be corrected is the low sun azimuth. We removed in-scene vegetation using a NDVI-mask (normalized difference vegetation index), (Tucker, 1979) for both the multi- and hyperspectral mosaics with a threshold of > 0.3 . Smaller water bodies were removed manually. On the masked data, we applied a minimum noise fraction (MNF, Green et al., 1988) transformation for dimensionality reduction and noise filtering. Subsequently, we applied a k-means (Tou and Gonzalez, 1974) unsupervised clustering, with the first 20 MNF bands as input (Kruse et al., 1993). The number of k-means target classes was determined based on prior field observations. We concluded, that six classes are suitable to account for the different surface features (gabbro, iron-bearing minerals, water, remaining vegetation, soil-debris, noise) and are used for the final output.

Band ratios were used to determine the positions and potential absorption depths for the broad iron absorption feature in hyper- and multispectral imagery and handheld scans. We used the band position for the iron feature at ~900 nm and band reflectance peaks between 750–760 nm, as those positions are as relevant in our application as, e.g., the curve shape (van Ruitenbeek et al., 2006). The broad spectral iron feature is caused by a charge-transfer absorption that is diagnostic for iron-bearing minerals (Hunt and Ashley, 1979).

Finally, supervised spectral classification is applied on the processed HSI by using the spectral angle mapper (Kruse et al., 1993). SAM measures the similarity between a reference and an image spectrum by computing the angle between spectra in an n -dimensional (n = bands) space. Small angles between spectra do indicate high material similarity. Previous studies showed that the SAM technique is well-suited for hyperspectral images featuring of iron-bearing mineralogy (Kirsch et al., 2018).

Our experiences with iron-related spectra show that spectral smoothing on the input HSI with a Savitzky-Golay filter (Savitzky and Golay, 1964) of second order and a filter width of 3–5 points (depends on input spectral resolution) increases the accuracy of SAM classifications by removing spectral noise (Jackisch et al., 2018). We used the following samples taken from the USGS library (Kokaly et al., 2017) for classification:

- Hematite GDS27 ($\alpha\text{-Fe}_2\text{O}_3$ – pure hematite) → proxy for iron-oxides (Puranen, 1989)
- Goethite WS222 (FeOOH – polymorphous with akaganeite, feroxyhyte, and lepidocrocite) → proxy for iron oxide-hydroxide
- Jarosite GDS 99 Ky200C Syn ($\text{KFe}^{+3}_3(\text{SO}_4)_2(\text{OH})_6$ – synthetic) → proxy for iron-sulphates

These spectral signatures are chosen as proxies for the expected minerals that categorize the major iron bearing groups (Lindholm and Anttonen, 1980). Spectral angles from 0.10–0.15 rad using 0.01 rad step-size were applied to achieve the resulting supervised classification. The resulting classes are sieved with a four-pixel neighbourhood kernel to reduce secluded pixels, assuming the maps spatial accuracy is high.

3.3.4 Structure-from-Motion Multi-Vision Stereo Photogrammetry

Orthophotos and digital surface models (DSM) of the Metsämalmi outcrops were created by drone borne SfM-MVS photogrammetry. The DSM can be used to correct for altitude variations of magnetic data and illumination effects in the hyperspectral data while the orthophoto is used to geo reference the HSI. Moreover, the orthomosaic is valuable to understand geologic structures and serves as a reference image for ground sampling points.

We used the Sensefly eBee Plus UAS featuring a 20 MPix S.O.D.A. RGB camera for acquisition of nadir images (technical details in Table 3). Image overlap was set to 80% forward and 70% sideways. In total, 12 ground control points were distributed on the outcrop, to precisely geo reference the final photogrammetric model.

Again, we performed the SfM MVS workflow using Agisoft PhotoScan following protocols recommended (James et al., 2016; Smith et al., 2016). Processing parameters for the image

alignment were set to ‘high quality’ and we choose the reference preselection option. Outlier tie points were subsequently removed using the gradual selection tool prior to the dense image matching. We removed tie points detected in less than three images and set a maximum threshold for image re-projection errors to 0.5 (41.69 pixels), to only use tie points below that value for dense cloud matching. The dense image matching or point cloud construction was run at ‘high quality’ with the depth filtering set to ‘aggressive’. The accuracy of the SfM-MVS point cloud was validated based on the measured GCP (ground control points) versus estimated GCP positions in Agisoft PhotoScan. The DSM is computed with an average grid spacing of 4.3 cm/pixel. Finally, an orthophoto with a resolution of 2.2 cm/pixel is computed by seamlessly merging overlapping images. The TecGEMS toolbox (Andreani and Gloaguen, 2016) is used to automatically extract structural information such as lineaments, ridges, and discontinuities from the DSM. The lineaments were validated with field observations (see Figure 3.2b).

Table 3-3 Acquisition parameters of the created orthophoto and DSM from two cameras.

	SODA	Sequoia
Images / Altitude	241 / 103 m AGL	98 / 84 m AGL
Orthophoto / DSM – Ground pixel resolutions	2.2 cm / 4.3 cm	7.4 cm / -
GCPs number / Mean GCP RMSE	12 / 8.1 cm	11 / 43.8 cm

3.3.5 Copter-Borne Magnetic Measurements

For magnetic measurements with the multicopter we applied a calibrated triaxial fluxgate magnetometer (MagDrone R1; SenSys; Sensys Sensorik & Systemtechnologie GmbH, 2018). It measures the magnetic flux density within a range of $\pm 75,000$ nT and features a sampling frequency of 200 Hz. Further parameters of the magnetometer are given in Table 3-4. The autonomous system can measure up to 2 hours and records GPS data (latitude, longitude, altitude, GPS time) at 20 Hz intervals. Magnetic measurements are interpolated onto coordinate points using GPS time stamps. Recorded data are saved on an internal solid state memory module.

Table 3-4 Parameters of SenSys MagDrone R1 UAS-borne fluxgate magnetometer system (Sensys Sensorik & Systemtechnologie GmbH, 2018)

Parameter	Value
Resolution	> 0.15 nT
Baseline error (200 Hz sampling)	< 4 nT
Fluxgate axes declination	$\leq \pm 0.5^\circ$
Weight	800 g

The MagDrone is rigidly attached below the UAS centre (Figure 3a). The axes of the magnetometer are aligned parallel and perpendicular to the main axis of the UAS fuselage, in a distance of 50 cm to the engines. During automated flight operation with an average velocity of 5 m/s sampling point inline distance is ~ 0.5 m. The drone followed a pre-defined flight plan. We performed surveys at different flight altitudes to investigate following applications:

- 15 m: Collect a UAS magnetic dataset close to surface, but within acceptable flight safety margins, for dense spatial coverage approaching the resolution of ground magnetics.
- 40 m: Compare multicopter and fixed wing data at similar operation height.
- 65 m: Perform high altitude UAS survey to examine the regional behaviour of the anomaly and to have a dataset that can serve as a reference for upward continuations of the other datasets.

Acquisition parameters and results for the surveys at three flight heights are summarized in Table 3-5. We conducted a calibration flight, using cardinal and inter cardinal directions, at the beginning of each survey, within altitudes of 30–40 m AGL, to obtain proper heading corrections for each flight line (Madriz, 2019). Further processing steps are given in Figure 3.4.

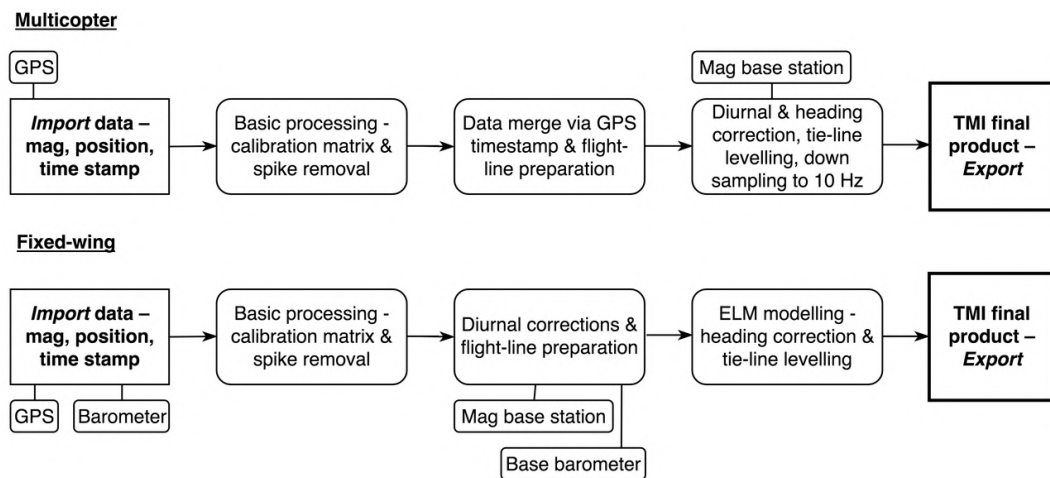


Figure 3.4 Principal magnetic processing workflows for UAS surveys. The workflows differ slightly, and the ELM technique is not applied on the multicopter data for this study.

During the 15 m survey (Figure 3.5b), the z component of the MagDrone magnetometer was saturated for about 1% of the collected magnetic data points. Also, the strong magnetic anomaly disturbed the orientation of the compass used for UAS navigation such that the multicopter flight lines (Figure 3.5) show some deviations from the original flight plan.

Table 3-5 Parameters of the magnetic surveys. Survey time includes take-off and landing.

Method	Area	Survey Length	Height AGL	Survey Time	Speed	Inline/Tie-line Spacing
Ground Survey	50,500 m ²	9.5 km	1.7 m	3 days	~0.1 m/s	10/ - m
Multicopter*	19,000 m ²	4.1 km	15 m	32 min	5 m/s	7/20 m
Multicopter	37,000 m ²	3.2 km	40 m	19 min	5 m/s	20/80 m
Multicopter	72,500 m ²	3.7 km	65 m	25 min	5 m/s	35/60 m
Fixed-wing	1.14 km ²	69.6 km	40 m	57 min	20 m/s	40/40 m

* two flights.

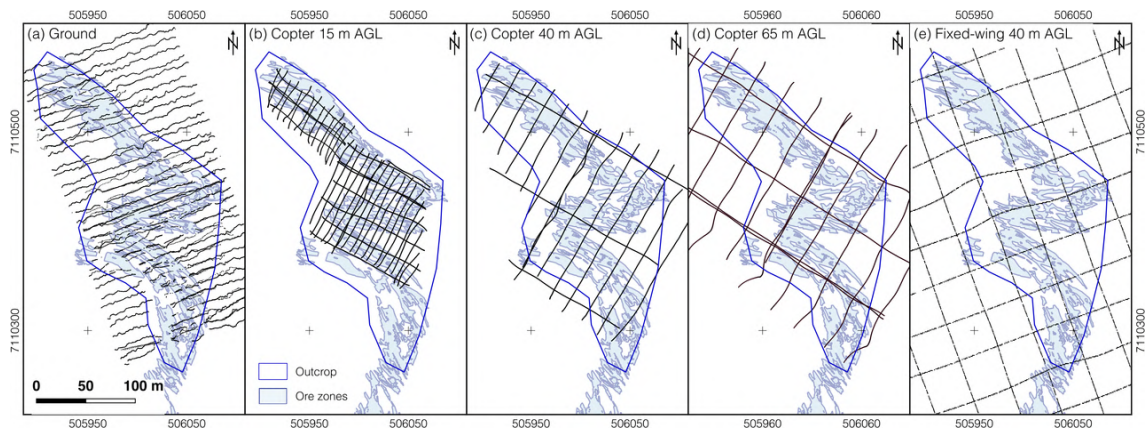


Figure 3.5 Acquisition patterns of the different magnetic surveys across the mapped ore zones (light blue polygons) in the Metsämalmi outcrop (flight lines are shown as dark blue lines): (a) ground survey; (b) 15 m multicopter; (c) 40 m multicopter; (d) 65 m multicopter; (e) 40 m fixed-wing magnetics.

To account for the diurnal variations, a magnetic base station (SenSys MagBase) was set up. It was located with a distance of several hundred meters outside of the high magnetic anomaly to avoid that the changes of the induced magnetic field related to the outer field variations have a measurable impact on the recordings. The total field B_t is computed and its variation is used to correct the drone-borne magnetic total field data. The calculated IGRF (International Geomagnetic Reference Field), considered as the background in the area at the time given, was about 53,056 nT (Declination: 11.3°; Inclination: 75.8°). During processing, we applied a fluxgate offset calibration matrix (provided by the manufacturer) for MagDrone and MagBase data to account for non-orthogonality between the individual field components. In general, the data processing workflow follows standard protocols for airborne magnetic measurements (e.g., Leliak, 1961).

3.3.6 Fixed Wing Magnetic Measurements

Fixed wing UAS magnetic measurements were conducted with the Albatros VT UAS, shown in Figure 3.3c. Survey objective was to capture data on a kilometer scale with dense line spacing and therefore high resolution. The magnetic field is measured by a digital triaxial fluxgate

magnetometer that is located in the tail boom of the UAS. The components of the magnetic field, the GPS position and time, and barometric pressure are recorded by the datalogger.

After manual take off, the UAS flight is controlled by an autopilot software and follows predefined waypoints over the eastern part of the Otanmäki deposit, including the Metsämalmi outcrop. The UAS follows the terrain topography based on a 10×10 m DSM grid provided by the National Land Survey of Finland. The flight performance is controlled online both via a telemetry link and/or a 3G/4G mobile link.

The surface area of the Otanmäki survey site is about 1.2 km² and the planned survey comprises a uniform pattern of orthogonal in lines (azimuth 30° from north) and cross lines (azimuth 120 degrees from north) with 40 m line spacing (see Table 3-1). The nominal flight altitude was 40 m AGL. Similar to the multicopter survey, a nearby stationary base station records the diurnal changes of the magnetic field (triaxial fluxgate magnetometer) and barometric pressure.

The data processing was made using the RadaiPros software, that allows interactive data correction and quality control. The processing steps are summarized in Figure 4. The equivalent layer modelling (ELM) is used in RadaiPros to compute the total field data on an even grid at a constant elevation level by applying a deterministic inversion to the measured magnetic data. The inversion is based on linearized least squares method with adaptive damping (Pirttijärvi, 2003) and lateral 2D constraining as in Occam's method (Constable et al., 1987).

We used the minimum curvature interpolation to create the final TMI maps from all datasets. All steps of data integration were conducted in Quantum GIS. Survey paths for ground based magnetics (see Section 3.8) as well as flight lines of the multicopter and the fixed wing magnetics are shown in Figure 5, with their corresponding flight altitudes plotted. The terrain elevation ranges from 140.5–143.9 m, meaning that no height adjustments were required in the survey profiles. The line angles between multicopter surveys compared to ground and fixed wing survey differ. The intention of the multicopter line direction was to survey perpendicular to the main strike of the mapped surface geology, while the latter focused also on the regional shape of the outcrop. Table 3-5 presents further magnetic survey details.

The multicopter surveys with flight heights of 15 m and 40 m were collected on the 6 September 2018, between 12:50–2:10 p.m. local time. The survey in 65 m altitude was conducted during the 7 September 2018 between 10:18–10:48 a.m. local time, the fixed wing survey was completed on the 4 September 2018, between 9:00–10:00 a.m. local time. The duration of these flights covers the take-off of the MagDrone, flight operations and landings. Average point distances in inline direction were ~0.025 m. The observed daily TMI variations did not exceed 15 nT during any flight event.

3.3.7 Ground Truth—Magnetic Survey

A systematic ground magnetic survey was done by GTK to have a reference dataset for the UAS based surveys. The survey area has a size of 160×310 m (Figure 3.5a) and covers the complete outcrop area. Due to the relatively flat terrain and good accessibility the survey path lines are parallel with small gaps in inaccessible parts (e.g., ponds and piles of sharp rocks). However, an inaccessible water body caused a data gap in the SW area. The line spacing was 10 m and line direction 70 degree clockwise. A GEM GSM 19 Overhauser magnetometer was used in walking mode. An average station spacing of 0.5 m along the lines was achieved. Diurnal variations of the magnetic field were removed using base station recordings, which were measured in a magnetically quiet area outside the anomalous Otanmäki gabbro intrusion. Because of extreme TMI values and strong gradients over Metsämäalmi area, obtaining reliable values was challenging, even though the gradient tolerance of the Overhauser magnetometer is above 10,000 nT/m. The largest measured field value (136,662 nT) exceeds the upper limit of the specified operating range (20,000–120,000 nT). Therefore, we performed the measurements with constant speed and re logging.

3.3.8 Ground Truth—pXRF, Spectroscopy, Susceptibility, Sampling

We performed in situ geochemical analysis at 46 locations (see Figure 3.2c) using a Bruker S1 Titan 800 handheld XRF with predefined settings (using the ‘Geochem’ calibration mode). In Geochem mode, all elements heavier than Fe are measured with 45 kV and an Al-Ti filter in the first measurement phase, followed by a second phase for the light elements with 15 kV and no filter. The soil check sample report is used as reference standard. A calibration sample with known constituents was provided by the manufacturer (Bruker, 2014) to ensure proper measurements.

Handheld spectral measurements of rock surfaces ($n = 51$) were taken using a Spectral Evolution PSR 3500 portable spectroradiometer. The spectra were recorded in the VNIR/SWIR part of the electromagnetic spectrum (400–2500 nm) with a spectral resolution of 3.5 nm (1.5 nm sampling interval) in VNIR and 7 nm (2.5 nm sampling interval) in the SWIR, using a contact probe (8 mm spot size) with internal light source. Radiance values were converted to reflectance using a pre calibrated PTFE panel (Zenith polymer) with >99% reflectance in the VNIR and >95% in the SWIR range. Each spectral record consists of 10 individual measurements, which were taken consecutively and averaged. We analysed the spectral data and extracted characteristic features, e.g., absorption depths, primarily between 700–900 nm for this study. Magnetic susceptibility scans ($n = 91$) were taken with an uncalibrated SatisGeo

KT 6 Kappameter. Representative rock samples ($n = 13$) of the main lithological units were taken for follow up laboratory analysis. Further, we investigated the textural relationship between gabbro, anorthosite, and the magnetite ilmenite ore (referred as Fe Ti ore in the images; see Figure 3.2bI-IV). Ore, gabbro, and anorthosite layers are mostly preserved in their magmatic textural relationship (Figure 3.2b.I). In some parts, the succession is folded and sheared (Figure 3.2b.II).

3.4 Results

3.4.1 UAS Multispectral Imagery

The resulting multispectral image mosaic is depicted in Figure 3.6. While having limited spectral information, the increased spatial coverage is the main advantage of this fixed wing survey and supplements the multicopter HSI data in areas not captured by HSI.

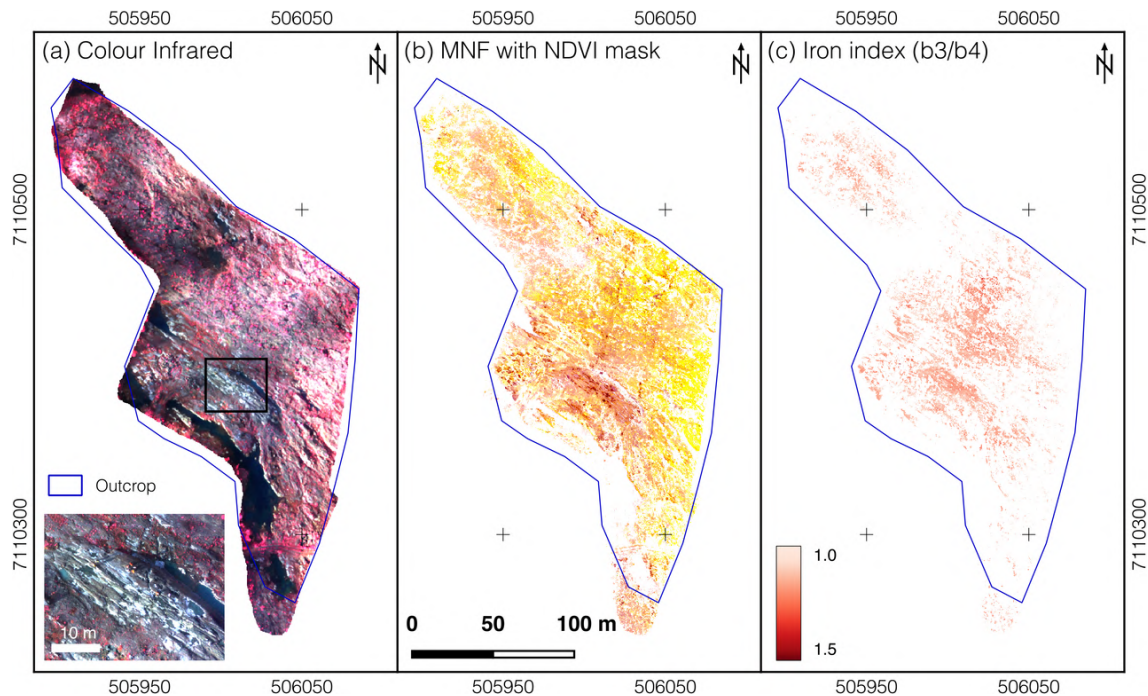


Figure 3.6 Results of multispectral fixed-wing survey. (a) CIR (colour infrared) plot of camera bands 3, 2, and 1. Enhanced map pronounces outcrop ridge area, where the surface was cleaned before the survey. (b) RGB bands after NDVI cut and MNF transformation with using 4, 3, and 1. (c) Band ratio of bands 3/4 with 735/790 nm.

The Sequoia CIR image (Figure 3.6) encompasses the entire outcrop. We identify only little vegetation coverage in the eastern and south-eastern parts of the outcrop. The NDVI mask removes a significant part of pixel in the western region (Figure 3.6b). The main features in the image are associated with gabbroic rocks and ilmenite magnetite rock zones in the southern part of the outcrop. Brighter orange yellow spots (Figure 3.6b) are related to gabbroic zones and secondary iron minerals. The MNF composite highlights geological characteristics and we

can trace structures more easily, for example the shape of outcropping ore bodies. Two parallel trenches, created by surface sampling with a rock saw, are identified in the image centre after MNF transformation.

We calculated an iron band ratio (735/790 nm) for the Sequoia dataset (Figure 3.6c). The ratio indicates iron related absorption (iron oxides and hydroxides) using the right shoulder of the $\text{Fe}^{2+}/\text{Fe}^{3+}$ charge transfer absorption (Hunt and Ashley, 1979), associated with decreasing reflectance. Similar studies (Jackisch et al., 2018) showed that this simple method is suited to evaluate UAS HSI images. We identify zones of apparent iron absorption, that are layered on top of the rock surfaces.

3.4.2 UAS Hyperspectral Imagery

In total, we covered 17,180 m² of the Metsämalmi outcrop with UAS HSI data. Parallel ground reconnaissance and the results of multispectral imaging suggested that the eastern part of the outcrop as promising location for remote sensing studies. The other part is densely covered by vegetation (lichen, shrubs, twigs, and young trees). We chose to omit the western area for further interpretation of HSI data. The eastern area is captured by three rows of overlapping HSI scenes (8,370 m²) mosaiced into one image (Figure 3.7). Some hyperspectral scenes have only little or no overlap, as opposed to the used flight plan. We explain this by heading deviations, induced by some distortions of the UAS's magnetic compass that were caused by the high magnetic anomalies in the area. Roughly 30 % of pixels from this mosaic are associated with vegetation and removed with a NDVI mask. The bright patches on the southern ridge are associated with gabbroitic rocks surrounding Fe-Ti-V ore bodies (Figure 3.7a) which were identified during the ground based field survey. The sorted MNF false color image (Figure 3.7b) shows increased contrast of surface features associated with the different geologic features (Luo et al., 2016). We observed increasing vegetation with small patches in the south, growing to a dense cover in the northern area.

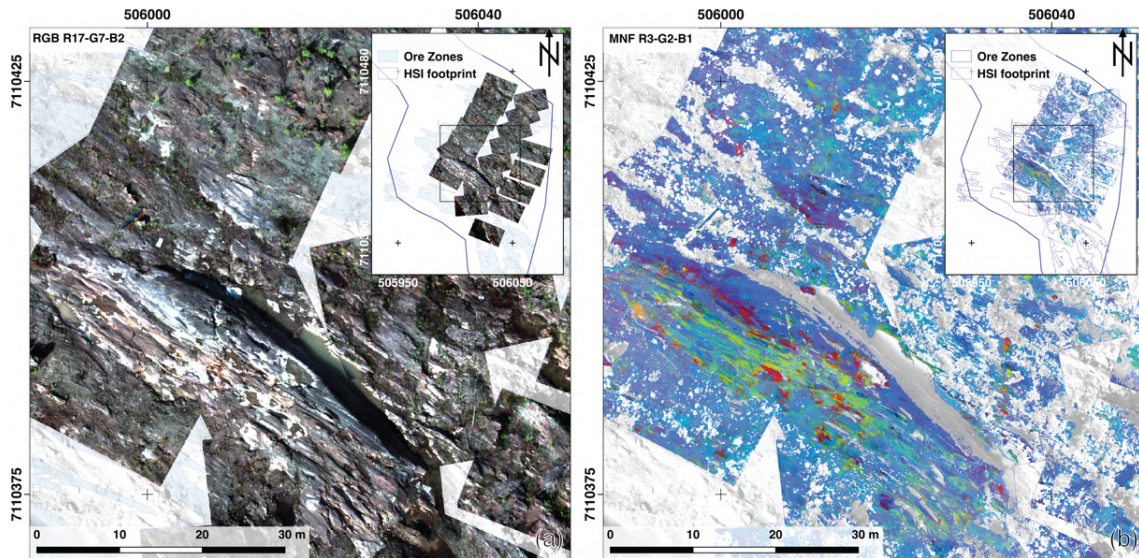


Figure 3.7 Results from hyperspectral data collected from the multicopter. (a) RGB plot (bands 17, 7, 2) of the HSI mosaic from the eastern part of the outcrop (the inset map shows the whole mosaic). The map enhances surface details and includes an area with pronounced occurrences of gabbroic host rock and iron ore lenses. (b) RGB plot of eigenimages 3, 2, 1 from the same area after a MNF transformation was applied to the hyperspectral mosaic. The eigenimages of the MNF outline surfacing shapes and textures. Red and green colors highlight outcropping iron stains and blue colors are associated with area of the host rock surface and remaining soil-vegetation mixture.

The SAM classification in Figure 3.8a shows the distribution of mapped iron oxides and iron sulphates. We could classify a significant amount of iron oxide and only little iron sulphate, which corresponds to handheld spectroscopy observations. Just two handheld spectra corresponded to iron sulphate. The used iron mineral proxy spectra hematite and goethite are labelled as ‘iron oxide’, and jarosite as ‘iron sulphate’. Two classes from the unsupervised k-means classification (5 % change threshold for the cluster centres, 100 iterations) are associated with the in situ observed features of iron staining and gabbro. The discarded classes were related to noise, soil vegetation mixed pixel that remained after NDVI filtering, and potentially redundant features caused by illumination changes. The results for k-means and SAM with respect to the iron minerals are qualitatively comparable, but the SAM classification yields 36.2 % less categorized pixels.

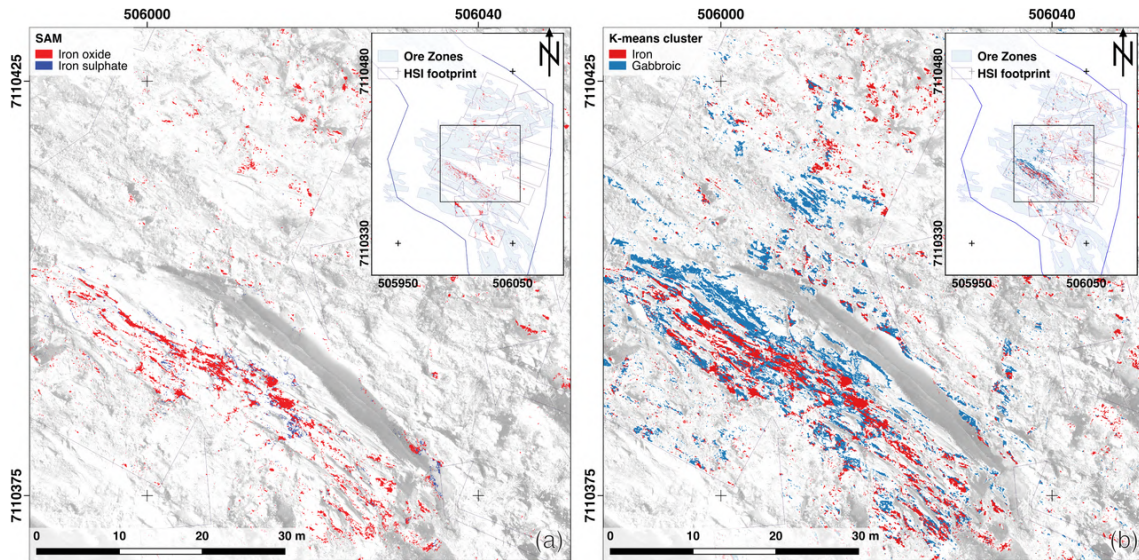


Figure 3.8 (a) Result of SAM mapping using input spectra from the USGS spectral library (Kokaly et al., 2017). (b) Result of unsupervised k means clustering, where two classes represent iron proxies and gabbroic rock surfaces. Different iron minerals are combined in the iron class.

We show exemplary spectra acquired from HSI data in Figure 3.9. They were created by selecting spectra from representative spots in the data (Figure 3.7a) and combine them in major surface categories (iron oxide, iron sulphate, host rock plus soil, lichen). The selection is based on both observations during the field campaign and inspections of HSI data. We removed five bands in the spectral range of 624–671 nm, where a sensor artefact is noticeable as a flat section. The exemplary spectra related to iron oxide and rock–soil mixture (Figure 3.9a and c) show small reflectance spread, while the ones associated with iron sulphate and lichen remnants (Figure 3.9b and d) show larger standard deviations. The average spectral reflectance is low ($< 30\%$), which is expected from the study site’s dark surface.

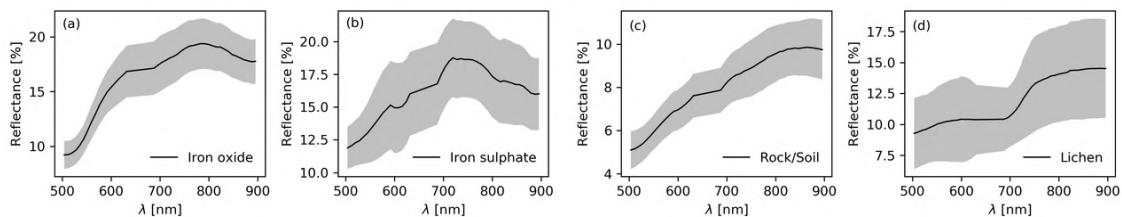


Figure 3.9 Plots from exemplary spectra that are extracted from the UAS borne hyperspectral datasets at pixels, where individual spectra are clearly associated with specific surface materials. 20 spectra are grouped per exemplary spectrum with its standard deviation plotted in a grey shaded envelope: (a) Iron oxide ($\sigma = 2.1$); (b) Iron sulphate ($\sigma = 2.9$); (c) Host rock in mixture with top soil ($\sigma = 1.1$); (d) Lichen remnants ($\sigma = 3.4$).

3.4.3 Handheld Spectroscopy

Figure 3.10 illustrates the spectral categories that are derived from field spectra acquired along the most western N–S running traverse shown in Figure 3.2c. The diagnostic absorption features we observe are representative for the mapped geology of Metsämalmi. Distinctive hydroxyl

absorption bands around 1400 nm and 1900 nm are visible. The charge transfer with broad absorption between 800–950 nm (Hunt and Ashley, 1979) is dominant for iron bearing categories (Figure 3.10a, b, and d). In particular, the absorption features for hematite, jarosite, and goethite can be observed in the iron alteration category (Figure 3.10d), which were attributed to iron sulphate/oxide classes in UAS borne hyperspectral data. The standard deviation of the iron alteration is small, as seen in Figure 3.9a and Figure 3.10d. Amphiboles can be recognized by a specific absorption related to the Mg OH vibrational overtone at 2310 nm and 2380 nm. The 2200 nm absorption feature was prominent in most spectra and is related to the Al OH overtone and typical for sheet silicates and was prominent in most spectra.

The Al OH feature at 2200 nm, with an accumulation between 2200–2206 nm was mainly found on soil surfaces. The Mg-OH overtone bending (Hunt, 1977) around 2300–2350 nm is related to amphibole rich rocks (i.e., abundant in amphibolite), and occurs in magnetite bearing rocks, as well as gabbroic surfaces.

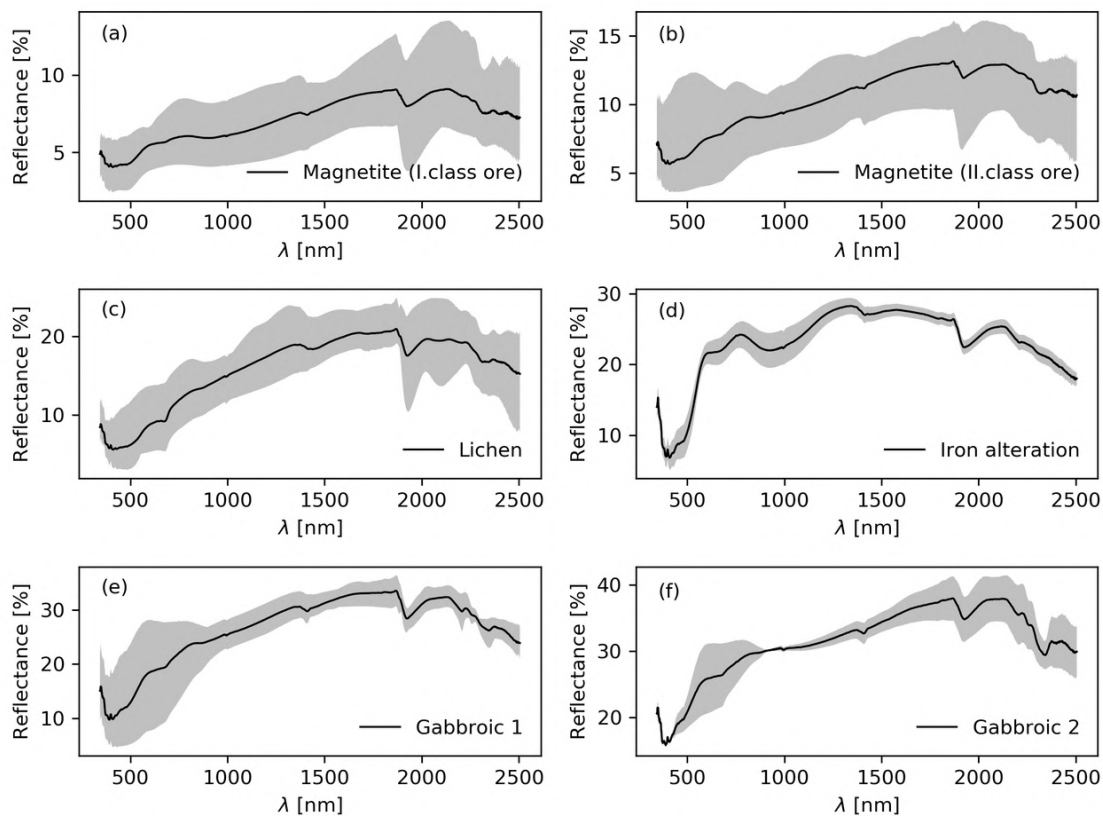


Figure 3.10 Results of the acquired handheld spectra after sorting them by unsupervised clustering. The clusters were attributed to magnetite, iron alteration, gabbroic rock, and lichen using k-means with six input classes, and refined together with field observations at the scanned spots. Calculated mean spectra are indicated as black lines and the minimum and maximum spectral values are described by the grey envelopes.

3.4.4 UAS-HSI Accuracy Assessment

We conducted an accuracy assessment to validate the HSI classifications from SAM and k means and compared them with the handheld spectra. The 51 handheld scans were scrutinized and labelled according to their major properties: (i) iron oxide hydroxide (contains magnetite in that category), (ii) iron sulphate, (iii) gabbro; and (iv) lichen. This categorization ensures distinguishable spectra in the spectral range of the Rikola camera. We created a look up table and attributed the major spectral features between 500–900 nm. Other observed spectral absorption features are related to amphiboles (e.g., hornblende), biotite and clay minerals (e.g., illite, smectite; according to USGS reference spectra). A strong absorption at ~670 nm is diagnostic for chlorophyll and here caused by abundant lichen. From the examined spectra, 21 showed clear iron features with some mixture between hematite, goethite, and jarosite. We labelled the hematite goethite mixture as iron oxide and jarosite as iron sulphate, respectively. A map layer with the labeled handheld scans was spatially joint with the SAM result map and classified pixels were counted. We created an eight pixel buffer around each handheld scan point position to address the measurement deviation. We achieve an overall accuracy of 68.1% for SAM. To validate the k-means approach, 43 spectral points with iron features or gabbroic characteristics (e.g., amphiboles) were considered within the UAS HSI mosaic. K-means could not distinguish between two iron features, therefore we grouped iron oxide and iron sulphates with one label, and use gabbroic as second surface label. The k means iron class also contains all of the SAM iron oxide pixels. We obtain an overall accuracy of 84.9 % for k-means.

3.4.5 Magnetism—Ground and UAS Borne

The magnetic measurements with the different UAS platforms, as well as the ground measurements, are presented as TMI in Figure 3.11. We observe that the TMI anomalies from the magnetic ground survey correlate well with the location of known magnetite ilmenite ore lenses (Figure 3.2d). TMI values measured on the ground above known ore zone are high (broadly in a range of 60,000–120,000 nT) indicating the magnetite signature, which is expected, considering that the highest graded ores in Otanmäki contain 35–40% magnetite (Ill, J. et al., 1985).

The alignment of anomalies from the four UAS surveys with three different heights at 15 m, 40 m, and 65 m are generally in agreement with the overall observed distribution of ore lenses at the surface (compare Figure 3.11b-e with Figure 3.2d). The 15 m flight (Figure 3.11b) captures similar locations of the anomalies lows and highs as seen in the ground data (Figure 3.11a). However, the actual shape of anomalies from the surveys at 15 m AGL differ already quite a

bit from mapped ore lenses at the surface, due to the reduced resolution and the larger impact of deeper ore bodies with larger distance to the surface. With further increasing altitudes of the surveys at 40 and 65 m AGL (Figure 3.11c, d & e), the more regional field with broader wavelengths and impact from deeper sources become gradually more dominant. In addition, the coarser line spacing of surveys made at 40 m and 60 m altitude, particularly in the fixed wing survey, which has the widest line spacing, further lowers the resolution and prohibit resolving the details observed in the ground based and 15 m altitude survey even after filtering is applied.

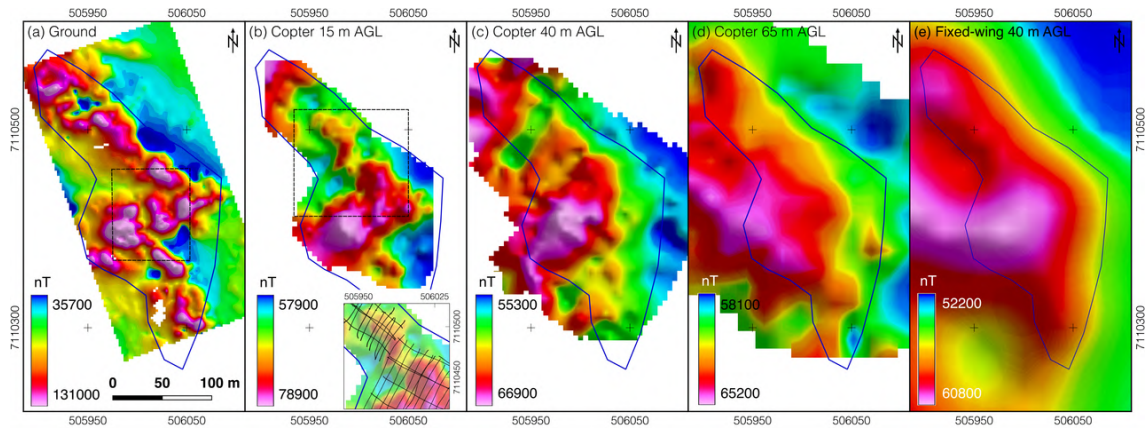


Figure 3.11 TMI plots from all magnetic surveys with flight heights given in agl, blue line defines the outcrop border. (a) Ground survey—dashed square outlines the reference area for Table 3-6. (b) Multicopter survey at 15 m flight height, consisting of two stitched flights, seen in inset map. (c) Multicopter survey at 40 m AGL. (d) Multicopter survey at 65 m AGL. (e) Fixed-wing survey at 40 m AGL.

Statistical details for the magnetic field from the different surveys at the Metsämalmi outcrop area are given for a defined reference area in Table 3-6 (see this area outlined with a rectangle in Figure 3.11a).

Table 3-6 Comparison of TMI grid values from the same area, shown in Figure 3.11a.

Parameter (B _t)	Ground Survey	Multicopter 15 m AGL	Multicopter 40 m AGL	Multicopter 65 m AGL	Fixed-Wing 40 m AGL
Min.	37,480 nT	60,130 nT	61,100 nT	60,610 nT	56,400 nT
Max.	131,490 nT	78,980 nT	67,370 nT	64,790 nT	61,240 nT
Mean	68,140 nT	69,960 nT	64,250 nT	63,170 nT	59,320 nT

Note that in Figure 3.11e, only a small part of the resulting 40 m fixed wing survey is presented and that the complete survey of $\sim 1 \times 1$ km covers large parts of the Otanmäki ore deposit and the adjacent rock units (results from areas apart from the outcrop are not presented here). For all surveys, we observe a high magnetic anomaly in the central part of Metsämalmi (Figure 3.11). Particularly for the fixed wing survey, it is observed that magnetic values follow a general lateral trend, having a negative gradient towards the north-eastern

border of the marked outcrop area. We also noticed that the highest magnetic anomalies were located at the same positions for all five surveys.

Figure 3.12 compares two profiles of TMI values from the 15 m UAS and ground magnetic survey, whose data are upward continued to 15 m. The magnetic profiles have a good overall resemblance in shape and intensity and suggest a high correlation of both datasets.

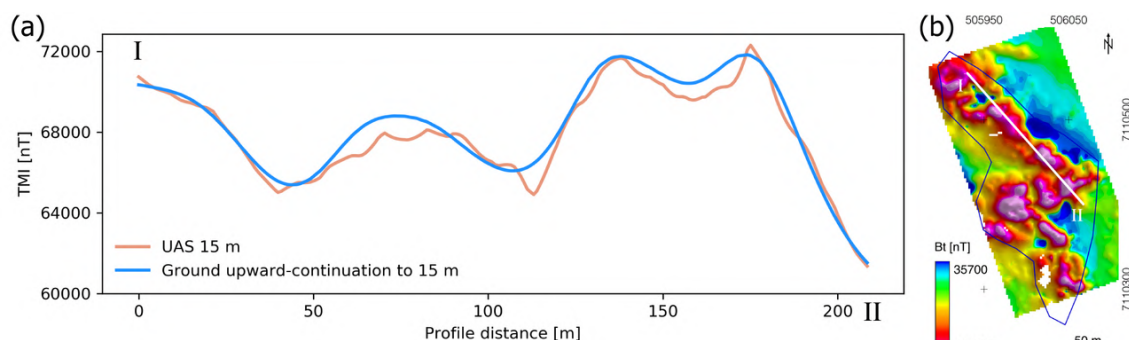


Figure 3.12 The total magnetic intensity extracted from the ground magnetic survey and multi-copter survey made at a flight height of 15 m AGL along a profile (see I and II in b) across the outcrop area. To better compare the datasets, the ground data has been upward-continued to 15 m. (b) The location of the extraction profile shown as a white line on the TMI map of the ground survey.

3.4.6 Geochemistry

The four main elemental constituents (Figure 3.13a) of Metsämalmi are measured by pXRF ($n = 72$, values in average (avg.) wt % (weight %) in their oxide forms (see Figure 13a). Bulk constituents are silica (21.9 wt % avg. SiO_2), followed by iron (17.9 wt % avg. Fe_2O_3), aluminium (6.9 wt % avg. Al_2O_3) and titan (3.2 wt % avg. TiO_2). The silica content shows the widest range, while iron concentrations have the most outliers. Sulphur and vanadium oxide content amount to ~ 1.0 wt % and 0.1 wt %, respectively. Therefore, those two lie outside of the pXRF calibration and are not plotted here.

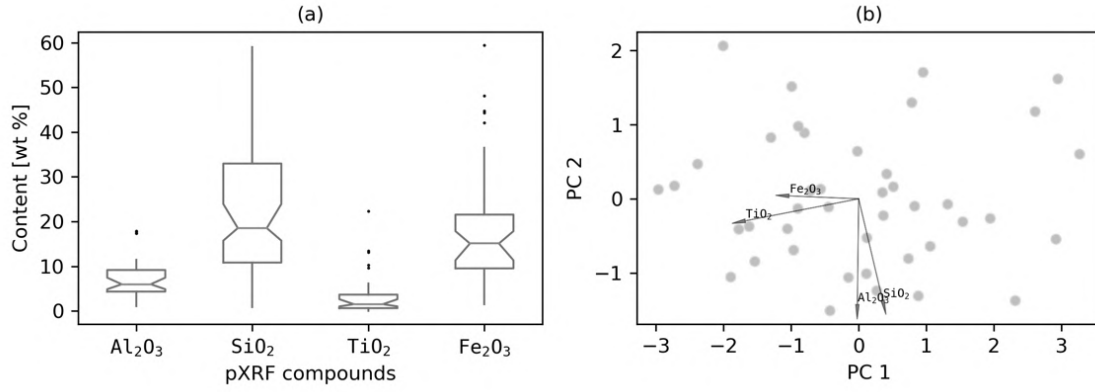


Figure 3.13 Boxplot distribution of pXRF measurements of the major compounds, with black dots represent outliers. (b) Biplot of the first two principal components, with PCA scores as grey dots, after transformation of the four selected compounds (rays represent measured pXRF compounds), that describe the outcrop's major elemental compositions.

We applied principal component analysis of the elemental compositions to visualize the relationship between the element variables (Jolliffe and Cadima, 2016). The values for V and S were excluded from the PCA, due to strong outliers. The pXRF data was converted into log ratios by the log ratio transformation (Aitchison, 1982; Otero et al., 2005) for scale invariance and to avoid spurious correlations (Pawlowsky-Glahn and Buccianti, 2011), and the PCA was applied on the transformed values (first two PC's explain 92% of the variance). The log ratios Si/Al and Fe/Ti are approximately constant, since the variable rays are close (Figure 3.13b). The log-ratios between Fe and Ti versus Si and Al do not correlate, which is seen as the orthogonal vector pairs. Hence, Ti occurrence correlates with iron abundance, and therefore in the present case we can use iron occurrence as proxy for ilmenite presence.

3.4.7 Integration of Ground Truth and Multicopter Data

The pXRF iron readings and computed iron ratios from handheld spectroscopy are mapped in Figure 3.14a. The depicted values spatially correlate with the mapped ore zones. Figure 3.14b displays five selected surface profiles of susceptibility measurements ($n = 4,524$) ranging between 0–1 SI units. With point distances between 2–3 cm per scan, those spots enable the tracing of main ore zones. We regard those measurements as quantitative evidence of high susceptibility of the top surface material and discard remnant magnetization.

The multicopter TMI data from the 15 m AGL flight is plotted in Figure 14c, together with the HSI footprint and the result of the SAM iron classification. Generally, we observe increased surface iron occurrence aloft high TMI values. Iron absorption is also observed, right above the water table of small water bodies due to weathering, and along the HSI mosaic's NS axis. The prominent lateral ridge in the south of the HSI features most iron-indicating pixels, while also

showing the highest TMI values in all magnetic plots (Figure 3.11a). The corresponding measurements of ground validation are presented in Section 3.4.8.

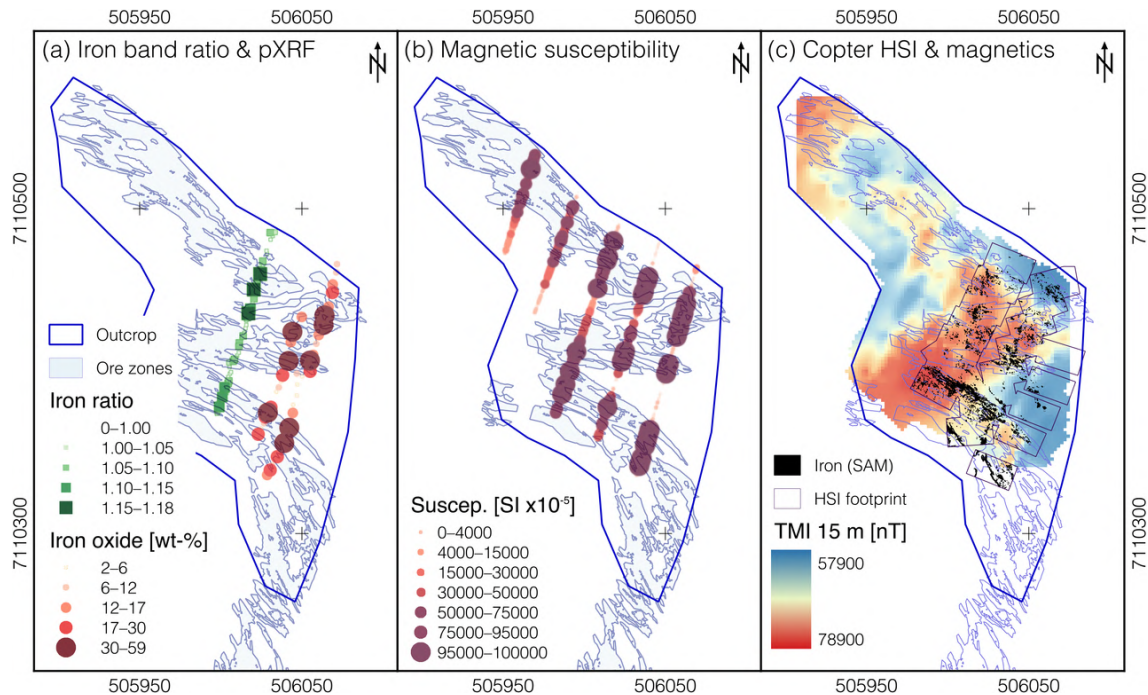


Figure 3.14 Comparison of ground-based measurements and multi copter magnetic data. (a) Point plot of iron band ratio (760/888 nm) from handheld spectroscopy and pXRF values taken along one respectively two sampling lines during the field campaign. (b) Point plots of magnetic susceptibility collected by the Otanmäki Mine Oy were measured along five profiles with an inline sampling distance of ~3 cm and line spacing of ~25 m. (c) Comparison of iron indications from SAM-HSI classification (increased pixel size for better visibility) and TMI map from the multicopter (15 m AGL and 2 m grid spacing). The blue polygons in all three figures sketch the mapped ore zones.

3.4.8 Data Integration

Surface observations with different techniques allow a characterization of the general area and reflect the originally mapped local geology and mineralogy (i.e., magnetite, ilmenite, amphiboles, gabbro). We compare the different GNSS measured ground validation and UAS borne datasets (Figure 3.15). The extracted measurements were taken on the same spot as the corresponding pixel of UAS data. The correlation coefficients (Pearson's correlation r) show an overall agreement. The high correlation ($r = 0.83$) for pXRF vs. susceptibility (Figure 3.15a) compares ore bodies with best ore grades, that should contain high iron content. The highest observed pXRF iron oxide content (41.5 wt % Fe) was described optically as 'pure magnetite' in the field. The UAS-HSI band ratio is probed with the known validation points, and compared with the iron ratios ($r = 0.80$) of the handheld spectrometer (Figure 3.15b). Likewise, values from both UAS camera sample spots are plotted (Figure 3.15c), to compare the Sequoia with the Rikola performance ($r = 0.63$).

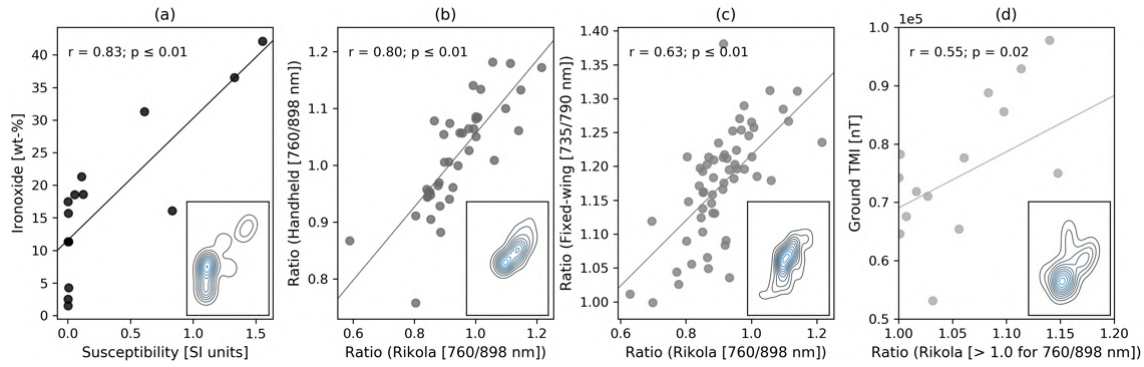


Figure 3.15 Scatter plots showing the relationships of different scanning methods from the outcrop, point pairs on the same location, or from the same pixel. The Pearson correlation r and significance p are given for each pair. (a) Correlation plot for handheld magnetic susceptibility vs. pXRF iron oxide. (b) Correlation for UAS Rikola iron band ratio (760/898 nm) vs. handheld iron band ratio (760/898 nm). (c) Correlation for UAS Rikola iron band ratio (760/898 nm) vs. fixed wing eBee iron band ratio (735/790 nm). (d) Correlation of Rikola iron band ratio (760/898 nm) vs. ground TMI. The inset plot in each bottom right corner distributes the kernel density per variable pair.

An illustration of extracted ground magnetic measurements compared with iron absorption depths depicts an association ($r = 0.55$) with the trend visible in Figure 3.15d. The correlations demonstrate, that the datasets from multiple sources can be jointly interpreted.

3.4.9 Geologic Interpretation and Ore Class Estimation

With a joint interpretation of all acquired UAS borne datasets, we can give a semi-automatic structural interpretation and ore occurrence estimation (Carranza, 2009). Structural features (lineaments and discontinuities) show us the directional trend in the outcrop. The extraction (Figure 3.16a) was done automatically and help to map the structural NW–SE trend. However, as vegetation and debris cover could not completely be removed from the DEM, the extracted lineaments were manually refined afterwards.

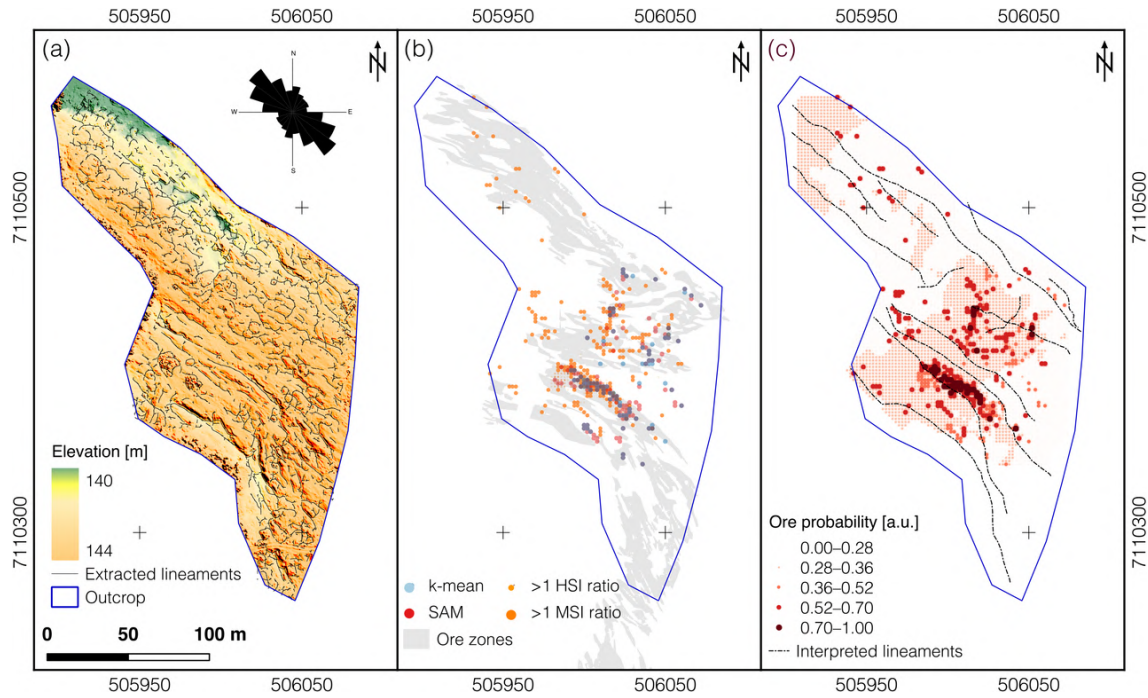


Figure 3.16 (a) Sfm-MVS DSM clipped to the outcrop surface. Plotted on top are automatically extracted lineament features. Rose plot as line direction histogram shows NW–SE trending of extracted lineaments ($n = 12,311$). (b) Combined UAS-borne MSI and HSI classification (semi-transparent colors) and iron ratio results, resampled to the 2 m grid size of the 15 m multicopter TMI grid. (c) Integrated results of spectral and magnetic UAS-survey, giving a probability for ore occurrences, where higher values indicate alignment of detected features (a.u. = arbitrary unit). Further directional context is given by the interpreted surface lineaments, based on the automatically extracted lineaments.

For the purpose of data integration, we first resampled different grid resolutions to one. We choose the 15 m UAS TMI as a representative footprint. In order to rescale and match data to the UAS TMI grid, the HSI and MSI data were resampled to 2 m grid size, using the mean cell values (Figure 3.16b). We estimated an ore prospectivity in the following:

- MSI and HSI UAS surface classifications were binarized (unclassified and classified pixels are either 0 or 1) and the 15 m TMI data was normalized between 0–1. By doing so, mostly the highest TMI areas contribute to the surface feature map.
- Normalized weighted arithmetic mean of the HSI, MSI and TMI datasets was computed.
- High values in the resulting map (Figure 3.16c) represent high ore probability.
- Interpreted lineaments are spatially joined with the proceptivity map to give structural context.

Finally, Figure 3.16c allows an estimation of ore occurrence along the surface. We observe a relationship between iron-indication surface pixel and sub surface magnetic features, that follow the directional trend of the local morphology. The directional trend of the iron ore from NW to SE is illustrated.

3.5 Discussion

3.5.1 Consequences of UAS Imaging

The results of multispectral survey require careful examination. With the Sequoia camera, the bandwidths of band 3 (10 nm) vs. band 4 (40 nm) differ, therefore band 4 covers important spectral characteristics of iron bearing minerals (e.g., hematite, goethite, jarosite, and copiapite). Still, the comparison of HSI vs. MSI indicates a correlation (Figure 3.16c). The MSI data seems to overestimate iron abundance and reasons are likely differing sampling distances, randomly distributed lichen coverage, and mainly the challenge to spectrally detect magnetite. The two excavated sampling ridges along the outcrop feature iron stains, which indicates displaced weathered surface or even fresh rock. The spectral artefact of the HSI camera between ~636–650 nm, is caused by its two sensor design (Tommaselli et al., 2018) and was removed. We recommend an HSI camera setting of 50 bands with 8 nm spectral resolution as most effective to maintain a balance between spectral density and SNR.

Noise reduction by PCA techniques (i.e., MNF) increases the reliability of our unsupervised classifications. We observe that in MNF transformed hypercubes, features (e.g., surface patterns related to geology and morphology) remain even in high order, low variance MNF dimensions. Unsupervised separation of surface classes (i.e., k-means) is based on spectrally contrasting mineral groups. In the presented case, the surface distinctions account predominantly for iron rich and iron poor rock surfaces. Further examination and correlation of classification results with field observations and orthophotography imply that the achieved separations are associated with iron bearing and gabbroic areas. We found that iron sulphates are not resolved by k-means and are partially mixed in the resulting iron class.

The SAM classification achieved a separation of iron oxides hydroxides and iron sulphates with reduced classified pixels. This reduction can be caused by illumination changes or strongly mixed surface materials. The Metsämalmi outcrop has been exposed for several decades, that leads to significant cover of surface portions by lichen, shrubs and small trees, that we observed in situ. Thus, important features were hidden to the UAS cameras, which affects for example the correlation of ground TMI and UAS-HSI (Figure 3.15d). The mentioned surface cleaning is possibly uneconomic, but we had no direct influence on the procedure. Advantage of the frame based HSI camera is the capability to create spatially undistorted images, even under wrong flight headings of the UAS, caused by magnetic interference.

3.5.2 Consequences of UAS Magnetic Measurements

We compare the UAS survey with ground data for a benchmark. The ground survey took two full days in the field to cover 50,500 m². A similar area was covered using two UAS flights in ~45 minutes. Data processing time is not considered, since we developed the processing routines during this study and those can be applied quickly. The sensors z component saturation in 1 % of the magnetic raw data was caused by the combination of an extremely strong anomaly, shallow flight height and the magnetometer's measurement range. This can be avoided by using a similarly constructed fluxgate magnetometer with a larger dynamic range or a slight increase of the survey altitude. Also, the strong regional magnetic field influences every measurement and makes a comparison (for example Figure 3.15d) challenging. The navigation and recovery of the UAS's absolute position is also influenced by the anomaly and caused a slight shift between two fused survey flights (Figure 3.11b). Structural field measurements with a geologic compass were strongly affected by the local magnetic field, which made field observations challenging.

Flight line geometry is a fundamental aspect of magnetic survey; hence, we observe differences between the 40 m copter and 40 m fixed-wing data. The applied cell size in the minimum curvature interpolation also contributes to mapping differences. (Figure 3.11c and (Figure 3.11e show varying TMI ranges, and the values of Table 3-6 indicate contrasting centres. One major reason for the differences in the data of both altitudes are orientation and density of the flight pattern. The 40 m multicopter flight had denser lines, was flown perpendicular to the strike of ore bodies, and captured higher anomaly amplitudes at different locations. Furthermore, the workflows of multicopter and fixed wing data surveys are slightly different. The fixed-wing acquisition uses a combination of ancillary sensor input and inversion modelling, while the multicopter uses calibration flights and benefits from its capability of getting closer to the surface. The used ELM for the fixed wing survey reduces effects of varying flight altitude and uneven data point sampling. It also removes high frequency noise and artefacts (e.g., from electric power lines and UAS engine noise) provided that their wavelength is short compared to the size of the elements used in the computed layer model. Yet, the results of both UAS survey methods allow the visualization of the anomaly patterns. We note that the relative altitude measurements per UAS flight slightly deviate per line. We observed an upward drift (~1 m/10 min) in the barometer records for the 65 m, which could be caused by an atmospheric pressure change. It is assumed that all our multicopter measurements endure an altitude deviation of at least ± 1 m from the unknown true values, based of GPS and barometer data evaluation. Non-linear sensor noise and the creation of aliasing effects takes place which

induces a binning effect on the sampling process. Studies suggested methods to address UAS noise, for example an increase of the sensor distance to noise sources and an adapted compensation in real time or in post processing (Tuck et al., 2018, 2019).

3.5.3 Can Drone Borne Analysis Compete with Airborne Survey and Outperform Ground Based Acquisition?

For optical remote sensing, the Sequoia camera data shows the possibilities (large area) and limitations (insufficient bands) of a multispectral UAS camera for mineral exploration. We note the correlation ($r = 0.63$) between a working concept (i.e., UAS HSI) and this experiment (UAS MSI). The lichen debris cover reduced the total amount of visible rock containing pixels by roughly 30 %. Image classifications of remaining areas reveal iron bearing alteration minerals, that we used as proxies for the target mineral magnetite. Ground spectroscopy validated the hyperspectral results ($r = 0.80$), however the chosen study area had harsh conditions for this hypothesis. The overall accuracy of SAM for two iron minerals is reported with 68 %, while the unsupervised k means classification for iron oxide and host rock is 84 %. We used various instruments to validate the UAS borne datasets in situ. The results of pXRF scans during our fieldwork correspond with results reported by the mining company.

We observe a correlation ($r = 0.55$) between UAS HSI iron ratio vs. ground truth TMI. Again, the strong regional anomaly skews those observations. To avoid spurious correlation, we examined outliers and none are removed from the data set. In that regard, we stress out the fundamental difference, as the TMI signal is the superposition from any subsurface anomaly of differing depth, while the UAS HSI data arises from the surface alone.

In terms of image resolution, the UAS imagery performs satisfying and creates pixel sizes of 2.2 cm (orthophoto), 3.0 cm (HSI), and 7.4 cm (MSI), while the mean point distance between handheld spectral measurements is 2 m. Those data are orthorectified by accurate GCPs. Similarly, the 15 m UAS magnetics feature a line spacing of 7 m, while the ground survey achieved 10 m. Evidently, using UAS reduces time and effort to achieve quality results for a reasonable aerial coverage. We observe that the time needed, as seen in Table 5, outperforms ground-based survey. With our current setup and an estimation based on the survey times and line spacing, we achieved 7.6–8.9 line km per hour (UAS in air time). Still, ground sampling is required, and survey time constraints could be mitigated in countries with abundant low cost workforce. The data processing, while under constant development, can be done in hours, results in meaningful maps during a field campaign, and creates streamlined and efficient workflows. The tested sensors require some calibration effort, and the UAS provides flexibility

by a quick release connector used to rapidly switch from magnetic to hyperspectral instruments. A further UAS advantage is the possibility to carry out the surveys by one trained person, that can fly different UAS types over any kind of terrain. We note that the characteristics of the survey area need to be specified, e.g., to avoid such deviations from the flight patterns caused by the high TMI.

We see several outcomes of integrating various UAS datasets:

1. Consistency of models is maintained (e.g., high spatial precision).
2. Improved reliability and reduced errors in mapping and predictions.
3. Classification of domains (e.g., minerals, surface and subsurface structures) that consist of several non-linear features.
4. The applicability of multi spectral UAS data for derivation of traces, structures, and shapes of geological features.

3.6 Conclusions

Within two-and-a-half days of fieldwork, a detailed mapping of the Metsämalmi outcrop in the Otanmäki mining district was achieved. The dataset includes surficial morphology, mineral distributions and the shape of the local magnetic anomaly at five scales. We used hyperspectral image mosaics with band ratios and classification algorithms to delineate iron bearing mineral phases on the surface. We covered three magnetic flight altitudes (15 m, 40 m, and 65 m AGL) on an outcrop scale with a multicopter, and performed a regional scale survey (40 m AGL with 69 km of survey lines) using a fixed wing UAS. The magnetic data acquisitions were performed fast, and flight planning for the magnetic surveys was optimized to cover as much of the outcrop as possible, while staying under the maximum battery endurance of the UAS.

Data integration of dense magnetic susceptibility profiling correlates well with magnetic field mapping and ore occurrences. The high resolution surface imagery and subsurface information of the magnetic field are fused and jointly interpreted. Their combined plot leads to a semi automatically created geologic map that distributes iron occurrences which directly relate to the ore. Based on the multiple datasets for the Metsämalmi area, we draw the following conclusions:

- Iron bearing phases can be successfully mapped by both UAS borne multi and hyperspectral sensors in the VNIR.
- UAS borne fluxgate magnetometers are able to map magnetic anomalies under survey conditions.

- Low altitude (i.e., 15 m AGL) multicopter magnetic data correlates to ground survey magnetic data, while higher flight altitude data describes the regional magnetic field.
- Magnetic anomalies can be associated to spectral anomalies at the surface by using ground truth.
- UAS HSI and magnetic survey complement each other.

The combination of light weight UAS technology with RGB, multi and hyperspectral cameras and fluxgate magnetometers is advantageous and created a basis for integrated data analysis. We demonstrate that the UAS approach for non-invasive mineral exploration based on integration of remote sensing and geophysical techniques is successful, based on comparable UAS and ground survey results. The joint UAS datasets for the prospectivity map display how extracted lineaments, spectra, and magnetics form a base map for visual interpretation. Our findings highlight the advantages of UAS as a practical, fast, and comfortably deployable geoscientific tool, that creates high resolution data within short turnaround times.

In summary, we conclude that UAS borne surveys can compete with ground surveying, while having a reduced cost overhead. We assume that integrated UAS surveys in mineral exploration and mining will reduce the amount needed of exploration drillings in future. Time for ground personnel to be exposed in dangerous areas will be limited and the repeated acquisitions can be used for further examination of targets and environments, during the entire mine life cycle. The presented survey approach should be further tested on more and different types of geologic targets in the future.

Author contributions: Conceptualization, R.J., R.Z., B.H., and R.G.; Analysis HSI & MSI, R.J.; Analysis Mag, Y.M., M.P., R.J., H.S., J.K., and R.G.; Investigation, R.J., Y.M., R.Z., and M.P.; Resources, R.G., A.S., H.S., J.K., and B.H.; Software, Y.M., M.P., R.J., L.A. and H.S.; Validation, R.J.; Visualization, R.J. and Y.M.; Writing—original draft, R.J.; Writing—review & editing, R.Z., B.H., M.P., R.G., Y.M., and H.S.; Supervision, B.H. and R.G.

Funding: This project was funded by the European Union within EIT RawMaterials in the project Mulsedro (MultiSensorDrones).

Acknowledgements: EIT Raw Materials and the European Union, Jouko Jylänki (Otanmäki Mine Oy), Kimmo Kärenlampi (University of Oulu), Maarit Middleton (GTK), Erik Vest Sørensen (GEUS), Sara Salehi (GEUS), Peter Sorjonen Ward (GTK). We thank the anonymous reviewers.

Conflicts of Interest: The authors declare no conflict of interest.

References

Schoer, K.; Weinzettel, J.; Kovanda, J.; Giegrich, J.; Lauwigi, C. Raw Material Consumption of the European Union—Concept, Calculation Method, and Results. *Environ. Sci. Technol.* 2012, 46, 8903–8909.

- Massari, S.; Ruberti, M. Rare earth elements as critical raw materials: Focus on international markets and future strategies. *Resour. Policy* 2013, 38, 36–43.
- Ali, S.H.; Giurco, D.; Arndt, N.; Nickless, E.; Brown, G.; Demetriades, A.; Durrheim, R.; Enriquez, M.A.; Kinnaird, J.; Littleboy, A.; et al. Mineral supply for sustainable development requires resource governance. *Nature* 2017, 543, 367–372.
- The European Commission. Communication from the Commission to the European Parliament, the Council, The European Economic and Social Committee and the Committee of the Regions on the 2017 list of Critical Raw Materials for the EU, Brussels, Belgium, 13.09.2017.
- Gloaguen, R.; Ghamisi, P.; Lorenz, S.; Kirsch, M.; Zimmermann, R.; Booysen, R.; Andreani, L.; Jackisch, R.; Hermann, E.; Tusa, L.; et al. The Need for Multi-Source, Multi-Scale Hyperspectral Imaging to Boost Non-Invasive Mineral Exploration. In *Proceedings of the IGARSS 2018-2018 IEEE International Geoscience and Remote Sensing Symposium*, Valencia, Spain, 22–27 July 2018; pp. 7430–7433.
- Henckens, M.L.C.M.; van Ierland, E.C.; Driessen, P.P.J.; Worrell, E. Mineral resources: Geological scarcity, market price trends, and future generations. *Resour. Policy* 2016, 49, 102–111.
- Stöcker, C.; Bennett, R.; Nex, F.; Gerke, M.; Zevenbergen, J. Review of the current state of UAV regulations. *Remote Sens.* 2017, 9, 459.
- Parshin, A.V.; Morozov, V.A.; Blinov, A.V.; Kosterev, A.N.; Budyak, A.E. Low-altitude geophysical magnetic prospecting based on multirotor UAV as a promising replacement for traditional ground survey. *Geo-Spat. Inf. Sci.* 2018, 1–8, doi:10.1080/10095020.2017.1420508.
- Colomina, I.; Molina, P. Unmanned aerial systems for photogrammetry and remote sensing: A review. *ISPRS J. Photogramm. Remote Sens.* 2014, 92, 79–97.
- Rauhala, A.; Tuomela, A.; Davids, C.; Rossi, P.M. UAV remote sensing surveillance of a mine tailings impoundment in Sub-Arctic conditions. *Remote Sens.* 2017, 9, 1–14.
- Salvini, R.; Mastroiocco, G.; Seddaiu, M.; Rossi, D.; Vanneschi, C. The use of an unmanned aerial vehicle for fracture mapping within a marble quarry (Carrara, Italy): Photogrammetry and discrete fracture network modeling. *Geomat. Nat. Hazards Risk* 2017, 8, 34–52.
- Zarco-Tejada, P.J.; Guillén-Climent, M.L.; Hernández-Clemente, R.; Catalina, A.; González, M.R.; Martín, P. Estimating leaf carotenoid content in vineyards using high resolution hyperspectral imagery acquired from an unmanned aerial vehicle (UAV). *Agric. For. Meteorol.* 2013, 171–172, 281–294.
- Ham, Y.; Han, K.K.; Lin, J.J.; Golparvar-Fard, M. Visual monitoring of civil infrastructure systems via camera-equipped Unmanned Aerial Vehicles (UAVs): A review of related works. *Vis. Eng.* 2016, 4, 1.
- Koucká, L.; Kopačková, V.; Fárová, K.; Gojda, M. UAV Mapping of an Archaeological Site Using RGB and NIR High-Resolution Data. *Proceedings* 2018, 2, 351.
- Näsi, R.; Honkavaara, E.; Lyytikäinen-Saarenmaa, P.; Blomqvist, M.; Litkey, P.; Hakala, T.; Viljanen, N.; Kantola, T.; Tanhuanpää, T.; Holopainen, M. Using UAV-Based Photogrammetry and Hyperspectral Imaging for Mapping Bark Beetle Damage at Tree-Level. *Remote Sens.* 2015, 7, 15467–15493.

- Restas, A. Drone applications for supporting disaster management. *World J. Eng. Technol.* 2015, 3, 316.
- Mancini, F.; Dubbini, M.; Gattelli, M.; Stecchi, F.; Fabbri, S.; Gabbianelli, G. Using Unmanned Aerial Vehicles (UAV) for High-Resolution Reconstruction of Topography: The Structure from Motion Approach on Coastal Environments. *Remote Sens.* 2013, 5, 6880–6898.
- Rahman, M.M.; McDermid, G.J.; Strack, M.; Lovitt, J. A New Method to Map Groundwater Table in Peatlands Using Unmanned Aerial Vehicles. *Remote Sens.* 2017, 9, 1057.
- Bemis, S.P.; Micklethwaite, S.; Turner, D.; James, M.R.; Akciz, S.; Thiele, S.T.; Bangash, H.A. Ground-based and UAV-Based photogrammetry: A multi-scale, high-resolution mapping tool for structural geology and paleoseismology. *J. Struct. Geol.* 2014, 69, 163–178.
- James, M.R.; Robson, S. Mitigating systematic error in topographic models derived from UAV and ground-based image networks. *Earth Surf. Process. Landf.* 2014, 39, 1413–1420.
- Malehmir, A.; Dynesius, L.; Paulusson, K.; Paulusson, A.; Johansson, H.; Bastani, M.; Wedmark, M.; Marsden, P. The potential of rotary-wing UAV-based magnetic surveys for mineral exploration: A case study from central Sweden. *Lead. Edge* 2017, 36, 552–557.
- Kirsch, M.; Lorenz, S.; Zimmermann, R.; Tusa, L.; Möckel, R.; Hödl, P.; Booyesen, R.; Khodadadzadeh, M.; Gloaguen, R. Integration of Terrestrial and Drone-Borne Hyperspectral and Photogrammetric Sensing Methods for Exploration Mapping and Mining Monitoring. *Remote Sens.* 2018, 10, 1366.
- Dering, G.M.; Micklethwaite, S.; Thiele, S.T.; Vollgger, S.A.; Cruden, A.R. Review of drones, photogrammetry and emerging sensor technology for the study of dykes: Best practises and future potential. *J. Volcanol. Geotherm. Res.* 2019, doi:10.1016/j.jvolgeores.2019.01.018.
- Gavazzi, B.; Le Maire, P.; Munsch, M.; Dechamp, A. Fluxgate vector magnetometers: A multisensor device for ground, UAV, and airborne magnetic surveys. *Lead. Edge* 2016, 35, 795–797.
- Tezkan, B.; Stoll, J.B.; Bergers, R.; Großbach, H. Unmanned aircraft system proves itself as a geophysical measuring platform for aeromagnetic surveys. *First Break* 2011, 29, 103–105.
- Koyama, T.; Kaneko, T.; Ohminato, T.; Yanagisawa, T.; Watanabe, A.; Takeo, M. An aeromagnetic survey of Shinmoe-dake volcano, Kirishima, Japan, after the 2011 eruption using an unmanned autonomous helicopter. *Earth Planets Sp.* 2013, 65, 657–666.
- Cunningham, M.; Samson, C.; Wood, A.; Cook, I. Aeromagnetic Surveying with a Rotary-Wing Unmanned Aircraft System: A Case Study from a Zinc Deposit in Nash Creek, New Brunswick, Canada. *Pure Appl. Geophys.* 2018, 175, 3145–3158.
- Parvar, K.; Braun, A.; Layton-Matthews, D.; Burns, M. UAV magnetometry for chromite exploration in the Samail ophiolite sequence, Oman. *J. Unmanned Veh. Syst.* 2018, 6, 57–69.
- Callum, W.; Braun, A.; Fotopoulos, G. Impact of 3-D attitude variations of a UAV magnetometry system on magnetic data quality. *Geophys. Prospect.* 2018, 1–15, doi:10.1111/1365-2478.12727.
- Samson, C.; Straznicky, P.; Laliberté, J.; Caron, R.; Ferguson, S.; Archer, R. Designing and Building an Unmanned Aircraft System for Aeromagnetic Surveying. In *SEG Tech. Progr. Expand. Abstr.* 2010; pp. 1167–1171, doi:10.1190/1.3513051.
- Airo, M.-L. Aerogeophysics in Finland 1972–2004: Methods, System Characteristics and Applications. In *Spec. Pap.-Geol. Surv. Finl*; 2005; Volume 39, 197p.

- Pääkkönen, V. Otanmäki—The Ilmenite Magnetite Ore Field in Finland. In Bull. la Commision Geol. Finlande; 1956, Geological Survey of Finland: Espoo, Finland, pp. 87.
- Lindholm, O.; Anttonen, R. Geology of the Otanmäki mine. In Proc. 26th Int. Geol. Congr. Guid. to Excursions 078 A+C, Part 2 (Finland); Häkli, T.A., Ed.; 1980; pp. 25–33.
- Huhma, H., Hanski, E., Kontinen, A., Vuollo, J., Mänttari, I., Lahyey, J. Sm–Nd and U–Pb isotope geochemistry of the Palaeoproterozoic mafic magmatism in eastern and northern Finland. *Bulletin* 2018, 405, 150.
- Lahti, I., Salmirinne, H., Kärenlampi, K.; Jylänki, J. Geophysical surveys and modeling of Nb–Zr–REE deposits and Fe–Ti–V ore-bearing gabbros in the Otanmäki area, central Finland. *GTK Open File Work Report* 2018, 75, 1–31.
- Hokka, J.; Lepistö, S. JORC Report-Mineral Resource Estimate for Otanmäki V-Ti-Fe Project; Geological Survey of Finland: Espoo, Finland, 2018.
- James, M.R.; Robson, S.; d’Oleire-Oltmanns, S.; Niethammer, U. Optimising UAV topographic surveys processed with structure-from-motion: Ground control quality, quantity and bundle adjustment. *Geomorphology* 2017, 280, 51–66.
- Jakob, S.; Zimmermann, R.; Gloaguen, R. The Need for Accurate Geometric and Radiometric Corrections of Drone-Borne Hyperspectral Data for Mineral Exploration: MEPHySTo-A Toolbox for Pre-Processing Drone-Borne Hyperspectral Data. *Remote Sens.* 2017, 9, 88.
- Makelainen, A.; Saari, H.; Hippi, I.; Sarkeala, J.; Soukkamaki, J. 2D Hyperspectral Frame Imager Camera Data in Photogrammetric Mosaicking. *Int. Arch. Photogramm. Remote Sens. Spat. Inf. Sci.* 2013, 1, 263–267.
- Karpouzli, E.; Malthus, T. The empirical line method for the atmospheric correction of IKONOS imagery. *Int. J. Remote Sens.* 2003, 24, 1143–1150.
- Tucker, C.J. Red and photographic infrared linear combinations for monitoring vegetation. *Remote Sens. Environ.* 1979, 8, 127–150.
- Green, A.A.; Berman, M.; Switzer, P.; Craig, M.D. A Transformation for Ordering Multispectral Data in Terms of Image Quality with Implications for Noise Removal. *IEEE Trans. Geosci. Remote Sens.* 1988, 26, 65–74.
- Tou, J.T.; Gonzalez, R.C. Pattern recognition principles. Addison-Wesley Pub. Co.: Boston, MA, USA 1974.
- Kruse, F.A.; Lefkoff, A.B.; Boardman, J.W.; Heidebrecht, K.B.; Shapiro, A.T.; Barloon, P.J.; Goetz, A.F.H. The spectral image processing system (SIPS)—interactive visualization and analysis of imaging spectrometer data. *Remote Sens. Environ.* 1993, 44, 145–163.
- van Ruitenbeek, F.J.A.; Debba, P.; van der Meer, F.D.; Cudahy, T.; van der Meijde, M.; Hale, M. Mapping white micas and their absorption wavelengths using hyperspectral band ratios. *Remote Sens. Environ.* 2006, 102, 211–222.
- Hunt, G.R.; Ashley, R.P. Spectra of altered rocks in the visible and near infrared. *Econ. Geol.* 1979, 74, 1613–1629.
- Savitzky, A.; Golay, M.J.E. Smoothing and Differentiation of Data by Simplified Least Squares Procedures. *Anal. Chem.* 1964, 36, 1627–1639.
- Jackisch, R.; Lorenz, S.; Zimmermann, R.; Möckel, R.; Gloaguen, R. Drone-Borne Hyperspectral Monitoring of Acid Mine Drainage: An Example from the Sokolov Lignite District. *Remote Sens.* 2018, 10, 385.

- Kokaly, R.F.; Clark, R.N.; Swayze, G.A.; Livo, K.E.; Hoefen, T.M.; Pearson, N.C.; Wise, R.A.; Benz, W.M.; Lowers, H.A.; Driscoll, R.L.; et al. USGS Spectral Library Version 7; U.S. Geological Survey: Reston, VA, USA, 2017, 61 p.
- Puranen, R. Susceptibilities, Iron and Magnetite Content of Precambrian Rocks in Finland. Geological Survey of Finland, Report of Investigation 90, 1989.
- Smith, M.W.; Carrivick, J.L.; Quincey, D.J. Structure from motion photogrammetry in physical geography. *Prog. Phys. Geogr.* 2016, 40, 247–275.
- Andreani, L.; Gloaguen, R. Geomorphic analysis of transient landscapes in the Sierra Madre de Chiapas and Maya Mountains (northern Central America): Implications for the North American-Caribbean-Cocos plate boundary. *Earth Surf. Dyn.* 2016, 4, 71–102.
- Sensys Sensorik & Systemtechnologie GmbH. SENSYS FGM3D Matrix of Technical Parameters. SenSys: Rabenfelde, Germany, 2018, 3.
- Madriz, Y. Drone-Borne Geophysics: Magnetic Survey for Mineral Exploration. M.Sc. Thesis, TU Freiberg, Freiberg, Germany, 2019.
- Leliak, P. Identification and Evaluation of Magnetic-Field Sources of Magnetic Airborne Detector Equipped Aircraft. 1961, 3, 95–105.
- Pirttijärvi, M. Numerical Modeling and Inversion of Geophysical Electromagnetic Measurements Using a Thin Plate Model. Ph.D. Thesis, University of Oulu, Oulu, Finland, 2003.
- Constable, S.C.; Parker, R.L.; Constable, C.G. Occam's inversion: A practical algorithm for generating smooth models from electromagnetic sounding data. *Geophysics* 1987, 52, 289–300.
- Bruker, Bruker S1 Titan Model 600/800 GeoChem 2014 Data Sheet. Bruker: Kennewick, USA, 2014.
- Luo, G.; Chen, G.; Tian, L.; Qin, K.; Qian, S.E. Minimum Noise Fraction versus Principal Component Analysis as a Preprocessing Step for Hyperspectral Imagery Denoising. *Can. J. Remote Sens.* 2016, 42, 106–116.
- Hunt, G.R. Spectral signatures of particulate minerals in the visible and near infrared. *Geophysics* 1977, 42, 501–513.
- Illi, J.; Lindholm, O.; Levanto, U.-M.; Nikula, J.; Pöyliö, E.; Vuoristo, E. Otanmäen kaivos. In *Vuoriteollisuus/Bergshanteringen no 2*. In Finnish with English summary; Vuorimiesyhdistys: Vaanta, Finland, 1985; pp. 98–107.
- Jolliffe, I.T.; Cadima, J. Principal component analysis: A review and recent developments. *Philos. Trans. R. Soc. A Math. Phys. Eng. Sci.* 2016, 374, 20150202.
- Aitchison, J. The Statistical Analysis of Compositional Data. *J. R. Stat. Soc. Ser. B* 1982, 44, 139–160.
- Otero, N.; Tolosana-Delgado, R.; Soler, A.; Pawlowsky-Glahn, V.; Canals, A. Relative vs. absolute statistical analysis of compositions: A comparative study of surface waters of a Mediterranean river. *Water Res.* 2005, 39, 1404–1414.
- Pawlowsky-Glahn, V.; Buccianti, A. *Compositional Data Analysis: Theory and Applications*; Wiley: Weinheim, Germany, 2011; ISBN 9780470711354.
- Carranza, E.J.M. *Geochemical Anomaly and Mineral Prospectivity Mapping in GIS*; 2009; Volume 11, ISBN 978-0-444-51325-0.

- Tommaselli, A.M.G.; Santos, L.D.; Berveglieri, A.; Oliveira, R.; Honkavaara, E. A study on the variations of inner orientation parameters of a hyperspectral frame camera. *ISPRS-Int. Arch. Photogramm. Remote Sens. Spat. Inf. Sci.* 2018, 42–1, 429–436.
- Tuck, L.; Samson, C.; Laliberte, J.; Wells, M.; Bélanger, F. Magnetic interference testing method for an electric fixed-wing unmanned aircraft system (UAS). *J. Unmanned Veh. Syst.* 2018, 6, 177–194.
- Tuck, L.; Samson, C.; Polowick, C.; Laliberté, J. Real-time compensation of magnetic data acquired by a single-rotor unmanned aircraft system. *Geophys. Prospect.* 2019, 67, 1637–1651.

VI

Chapter 4 – Innovative methods in an extended workflow.

The workflow presented in the previous chapter respected a direct target with limited spectral variability and clear geophysical responses in a confined test areal. Consequently, an extended drone-test scenario including 3D modelling was imperative. The Siilinjärvi phosphate mine (Case study B) with its apatite-bearing carbonatite intrusion presents a set-up with complex geology and challenging light conditions and was visited two times during MULSEDRO's run-time. The first survey in 2017 was brief and demonstrated⁸ the framework and potential for the subsequent research.

To use the encountered ambiguous spectral signals, the low magnetic responses and outcrop surface partly veiled by clay dusts, a complex workflow was developed. A fusion of high-resolution RGB, spectral and structural data with magnetic forward modelling resulted in a digital outcrop model at a scale of 0.5 km². The developed workflow on sensor integration and surface-subsurface mapping that provides confidence and guidelines in drone-use for the technologically driven mining industry. The results of chapter VI were presented in a mineral exploration special issue of Remote Sensing⁹. The quality of the multicopter hyperspectral survey during favourable conditions became part of a novel aspect of drone-based surveying, the direct and non-invasive detection of the rare-earth-element absorptions in the electromagnetic near-infrared range¹⁰.

⁸ Heincke, B., **Jackisch, R.** et al., 2019, Developing multi-sensor drones for geological mapping and mineral exploration: setup and first results from the MULSEDRO project: Geological Survey of Denmark and Greenland Bulletin, v. 43, p. 2–6.

⁹ **Jackisch, R.**, Lorenz, S.; Kirsch, M.; Zimmermann, R.; Tusa, L.; Pirttijärvi, M.; Saartenoja, A.; Ugalde, H.; Madriz, Y.; Savolainen, M.; Gloaguen, R. Integrated Geological and Geophysical Mapping of a Carbonatite-Hosting Outcrop in Siilinjärvi, Finland, Using Unmanned Aerial Systems. Remote Sens. 2020, 12, 2998.

¹⁰ Booyesen, R., **Jackisch, R.**, Lorenz, S., Zimmermann, R., Kirsch, M., Nex, P.A.M., and Gloaguen, R., 2020, Detection of REEs with lightweight UAV-based hyperspectral imaging: Scientific Reports, v. 10.

Integrated Geological and Geophysical Mapping of a Carbonatite-Hosting Outcrop in Siilinjärvi, Finland, Using Unmanned Aerial Systems

Robert Jackisch¹, Sandra Lorenz¹, Moritz Kirsch¹, Robert Zimmermann¹, Laura Tusa¹, Markku Pirttijärvi², Ari Saartoenoja², Hernan Ugalde³, Yuleika Madriz¹, Mikko Savolainen⁴ and Richard Gloaguen¹

¹ Helmholtz-Zentrum Dresden-Rossendorf, Helmholtz Institute Freiberg for Resource Technology, Division “Exploration Technology”, Chemnitz Str. 40, Freiberg 09599, Germany; r.jackisch@hzdr.de (R.J.); s.lorenz@hzdr.de (S.L.); m.kirsch@hzdr.de (M.K.); r.zimmermann@hzdr.de (R.Z.); l.tusa@hzdr.de (L.T.); y.madriz-diaz@hzdr.de (Y.M.); r.gloaguen@hzdr.de (R.G.)

² Radai Oy, Teknologiantie 18, Oulu 90590, Finland; markku.pirttijarvi@radai.fi (M.P.); ari.saartoenoja@radai.fi (A.S.)

³ DIP Geosciences, 100 Burris Street, Hamilton ON L8M 2J5 Canada; hernan.ugalde@dipgeosciences.com

⁴ Yara Suomi Oy, Nilsiantie 50, Siilinjärvi 71801, Finland; mikko.savolainen@yara.com

Abstract

Mapping geological outcrops is a crucial part of mineral exploration, mine planning and ore extraction. With the advent of unmanned aerial systems (UASs) for rapid spatial and spectral mapping, opportunities arise in fields where traditional ground-based approaches are established and trusted, but fail to cover sufficient area or compromise personal safety. Multi-sensor UAS are a technology that change geoscientific research, but they are still not routinely used for geological mapping in exploration and mining due to lack of trust in their added value and missing expertise and guidance in the selection and combination of drones and sensors. To address these limitations and highlight the potential of using UAS in exploration settings, we present an UAS multi-sensor mapping approach based on the integration of drone-borne photography, multi- and hyperspectral imaging and magnetics. Data are processed with conventional methods as well as innovative machine learning algorithms and validated by geological field mapping, yielding a comprehensive and geologically interpretable product. As a case study, we chose the northern extension of the Siilinjärvi apatite mine in Finland, in a brownfield exploration setting with plenty of ground truth data available and a survey area that is partly covered by vegetation. We conducted rapid UAS surveys from which we created a multi-layered data set to investigate properties of the ore-bearing carbonatite-glimmerite body. Our resulting geologic map discriminates between the principal lithologic units and distinguishes ore-bearing from waste rocks. Structural orientations and lithological units are deduced based on high-resolution, hyperspectral image-enhanced point clouds. UAS-based magnetic data allow an insight into their subsurface geometry through modelling based on magnetic interpretation. We validate our results via ground survey including rock specimen sampling, geochemical and mineralogical analysis and spectroscopic point measurements. We

are convinced that the presented non-invasive, data-driven mapping approach can complement traditional workflows in mineral exploration as a flexible tool. Mapping products based on UAS data increase efficiency and maximize safety of the resource extraction process, and reduce expenses and incidental wastes.

Keywords: unmanned aerial systems; hyperspectral; multispectral; magnetic; geologic mapping; drones; UAV

4.1 Introduction

Investigating the earth's surface using unmanned aerial systems (UAS) is becoming popular in the earth sciences, as they provide a tool for fast, flexible and high-resolution data acquisition. The integration of spectral and geophysical UAS-based information offers a refined scale between airborne and ground surveys. Numerous studies and reviews have investigated the potential of UAS for various applications, e.g., in the fields of agriculture and forestry, structural geology, and sedimentology (Bemis et al., 2014; Adão et al., 2017; Fairley et al., 2018; Jackisch et al., 2018; Kim et al., 2019; Padró et al., 2019; Dering et al., 2019).

UAS offer multiple potential applications in the exploration and mining industry. In mining environments, UAS are nowadays routinely used for topographical surveys, material volume calculation and post-mining environmental monitoring (Lee and Choi, 2016; Ren et al., 2019). In the context of mineral exploration, UASs provide a non-invasive way to determine vectors towards ore occurrence at deposit scale. Successful applications of UAS-based surveys in mineral exploration were used to explore rare earths using spectral imaging (Booyesen et al., 2019) and target uranium deposits using radiometric gamma survey (Parshin et al., 2018). UAS geophysical magnetic mapping was employed in exploration for iron, zinc, chromite, or gold deposits (Malehmir et al., 2017a; Cunningham et al., 2018; Parvar et al., 2018; Walter et al., 2020). UAS-based photogrammetric surface models were used to explore structurally controlled gold deposits (Sayab et al., 2018).

Within the development of an exploration project, drilling is the decisive step for validation and modeling. It represents one primary decision-making tool (Halдар, 2018) and at the same time is the most cost-intensive part of mine planning (Marjoribanks, 2010). Hence, UAS-based non-invasive and socially acceptable data acquisition (e.g., geophysical and hyperspectral) combined with robust data-processing methods can help decision-makers minimize investment risks and optimize the drilling program (Abedi and Norouzi, 2012).

Most of the above-mentioned studies only employ single sensors to derive geoscientific data. A combination of information from different sensors allows for a more robust geological

interpretation. The combination of spectral and magnetic data has long been recognized as a potent tool in airborne mineral exploration (Slavinski et al., 2010), because of their capability to provide both surface and subsurface information. Bridging the observation gap between airborne and ground surveying, UASs provide the possibility of carrying different sensors to acquire high-resolution spatial, spectral and temporal data (Beyer et al., 2019; Heincke et al., 2019) which contribute to the understanding of geologic settings (van der Meer et al., 2012).

UAS-based hyperspectral imaging and magnetics were identified as a promising sensor combination for direct targeting of iron ores (Jackisch et al., 2019), using surficial proxy iron-bearing minerals and high magnetic susceptibility. While there is ample scientific literature on using UAS for geological investigations, UAS are not established in the mineral exploration and mining industry. Arguably, that is due to a lack of case studies, processing and validation schemes, and dedicated software. This study showcases the value of multi-sensor UAS data and provides a guideline to maximize UAS potential in exploration scenarios in order to provide support to exploration geologists.

Here, multi- and hyperspectral drone-based imagery is used to delineate and classify surface lithologies using data fusion. Magnetic data are used to survey the extension of lithologic features and close observation gaps. The data provided by the different sensors are fused and supervised image classification is used to separate spectrally non-distinct rock types. Thus, we can link surface and subsurface information as indicators for mineral occurrences, relating surface classifications to magnetic minerals as lithologic proxies. Our final result is a UAS-borne digital geologic outcrop model, augmented by UAS data-based magnetic forward modeling and validated by a ground-truthing strategy for indirect exploration targeting. This study, to our knowledge at the time, is the first to attempt this integrated approach used for UAS data in geologic mapping and mineral exploration.

Our area of investigation is the Siilinjärvi apatite ore mine in Finland (Puustinen, 1971). The site is an ideal testing ground due to the wealth of existing evaluation data, including geophysical (Luoma et al., 2016; Malehmir et al., 2017b; Laakso, 2019; Da Col et al., 2020) structural–geological (Pajunen et al., 2017; Kauti, Tuomas, Skyttä, Pietari, Koivisto, Emilia, Savolainen, 2019; Mattsson et al., 2019), geochronological, and mineralogical information (Tichomirowa et al., 2006; Carlsson, M., Eklund, O., Fröjdö, S., Savolainen, 2019). We used two on-site survey days to acquire high-resolution UAS data and ground validation in an area of about 1 km². We introduce our general and transferable workflow, which we adapt to the specifications of our survey site, show results and interpretation and finalize in five concluding statements.

4.2 *Materials and Methods*

In this section, we lay out the UAS survey approach. Our proposed workflow is based upon two fixed-wing UASs, one for magnetic and one for RGB and multispectral measurements, and one multicopter UAS for detailed hyperspectral data acquisition. Both fixed-wings cover the complete target area with high spatial resolution but in reduced spectral detail. The multicopter, on the other hand, provides high spectral resolution but reduced spatial coverage as it acquires data at a lower altitude and pace. This allows higher detail for selected areas of interest within the survey area. We show that the methodic combination of fixed-wings and multicopter complement each other. In the following subsection, we define the proposed workflow (Figure 4.1), introducing data processing routines and the used ground truthing methods that include spectroscopy, magnetic susceptibility, and structural measurements for a successful field campaign.

4.2.1 UAS Data Acquisition Method

We collect RGB and multispectral images (MSI) with a fixed-wing UAS. Structure-from-motion multi view stereo (SfM-MVS) photogrammetric workflows allow us to construct a digital surface model and an orthomosaic from RGB and MSI orthophotos. RGB information, that provides the highest spatial resolution, is used to identify geological structures. MSIs provide additional spectral information compared to RGB images, and a much larger footprint than hyperspectral image (HSI) data in this acquisition setup. All images are geotagged from the drone's onboard GPS. Images are rectified using a number of ground control points.

The resulting SfM-MVS digital surface model (DSM) is used for topographic correction and referencing of the HSI, and for structural analysis. By means of CloudCompare (www.danielgm.net/cc, vers. 2.11) and its Compass tool plugin (Thiele et al., 2017), we semi-automatically trace and define best-fit planes for faults, foliation, and lithologic contacts directly on the point cloud. For ambiguous areas, supporting UAS data layers (e.g., HSI, magnetics) are re-examined in the 3D environment.

We acquire UAS-based hyperspectral data frames with pre-coded flight paths in stop-and-go mode along the outcrop to maximize UAS surface coverage. We employ UAS-borne frame-based cameras because of their advantage in creating full image frames which, in our experience, are inherently less distorted than push-broom scanner data. For all HSI data, we manually crop water bodies and non-geologic structures such as roads and vegetated zones from the mosaics, or use semi-automatic masking with a spectral vegetation index.

We conduct UAS-based magnetic surveys using a fixed-wing drone to collect a high-resolution magnetic data set over the survey area, using predefined flight plans. Subsequently, we apply standard magnetic interpretation methods to inspect the shape and dimensions of the measured magnetic anomalies. The analytic signal or total gradient amplitude method (Nabighian, 1972) is utilized to estimate the location and depth of anomaly sources, as this function is independent of source magnetization direction (Hinze et al., 2013). Furthermore, we compute the first vertical derivative from total magnetic intensity (TMI) data to enhance the magnetic anomalies and reduce residual influences (Vacquier et al., 1951).

4.2.2 Data Products: Feature Extraction, Supervised Image Classification and Magnetic Forward Modelling

We perform data fusion on a “noisy” outcrop to reduce ambiguity of interpretation while increasing detection confidence and accuracy of classifications (Khaleghi et al., 2013). The feasibility of such a fusion approach was laid out for different lithologies at laboratory scale where multi-source hyperspectral and photogrammetric techniques were combined (Lorenz et al., 2019). We apply spatially constrained feature extraction on the UAS-based optical imagery for a consistent classification as part of our multi-sensor data approach to enhance image classification results. The orthogonal total variation component analysis (OTVCA) is used to reduce data dimensionality (Rasti et al., 2016). It optimizes a cost function to obtain the best representation for multi-layer image data in lower-dimensional feature space, while giving a spatial smoothness over local neighbouring pixels by minimizing the total variation of the image signal. OTVCA is robust towards non-systematic, random noise (e.g., salt-and-pepper noise) and has increased weight on neighboring pixels during the dimensionality reduction (Ghamisi et al., 2017).

For supervised image classification, we choose the support vector machine (SVM) algorithm with Gaussian radial basis function (RBF) kernel, using the library for support vector machines (LibSVM) toolbox (Chang and Lin, 2011). RBF-SVM is proven to perform well with heterogeneous classes and sparse training data, both of which are common cases in geological mapping (Ghamisi et al., 2017). Training and validation samples or pixels are defined by selecting pixel aggregates from the HSI data in a GIS environment from points with defined lithologies. The number of training/validation classes varies according to our field observations of the local lithologies.

For a 3D integration and interpretation of our UAS magnetic data, we use forward modelling. Model geometries are established by the UAS-based orthoimagery, hyperspectral mosaics and

the DSM. The photogrammetric 3D outcrop model and ground measurements provide constraints on strike/dip and azimuth of the source bodies. Magnetic susceptibility values assigned to the modeled bodies are taken from published literature (Almqvist et al., 2017; Malehmir et al., 2017b; Laakso, 2019) and from additional measurements collected with a handheld susceptibility sensor over selected rock samples.

4.2.3 The Adapted Workflow Conducted for this Survey

We summarize the main characteristics of used sensors here (Table 4-1) and for specific technical details of our UAS workflow and data acquisition, we refer to Appendix D and (Jackisch et al., 2019).

Table 4-1. Sensors with technical specifications and platforms used for experimental data during this study.

Senor Type / Carrier platform	Sensor	Resolution Spatial / Spectral	Bands / Sampling Range / Frequency	Data Product
Snapshot camera / Fixed-wing UAS	Parrot S.O.D.A.	5472 × 3648 / –	3 / RGB / 0.3 Hz	Orthomosaic-RGB, digital surface model
Snapshot camera / Fixed-wing UAS	Parrot Sequoia	1280 × 960 / 10–40 nm (FWHM)	4 / 550–790 nm / 0.3 Hz	Orthomosaic multispectral
Frame-based camera / Multicopter UAS	Senop Rikola	1010 × 648 / 8 nm	50 / 504–900 nm / manual	Orthomosaic hyperspectral
Three-component fluxgate / Fixed-wing UAS	Radaï magnetometer	– / 0.5 nT	1 / ±100,000 nT / 10 Hz	Magnetic raster grid

We used the senseFly eBee Plus fixed-wing (www.sensefly.com, senseFly, Cheseaux-sur-Lausanne, Switzerland) equipped with either a high-resolution RGB camera (www.parrot.com, Parrot S.O.D.A., Parrot SA, Paris, France), or a multispectral camera (Parrot Sequoia). Processing of RGB and multispectral drone-based data was conducted in Agisoft Photoscan (vers. 1.4, Agisoft Ltd., St. Petersburg, Russia) following recommended protocols (James et al., 2016, 2019).

Our used hyperspectral frame camera was the Senop Rikola hyperspectral imager (www.senop.fi, Senop, Oulu, Finland). The camera was stabilized by a gimbal (roll and pitch axes) and transported on board of the Aibotix Aibot X6v2 multicopter (www.leica-geosystems.com, Leica Geosystems, Heerbrugg, Switzerland). Automatic HSI georeferencing, mosaicking and application of topographic corrections (c-factor method) on each HSI scene based on the photogrammetric DSM was conducted after Jakob et al., 2017 (Jakob et al., 2017).

We applied the empirical line method (Karpouzli and Malthus, 2003) to convert the images from radiance to reflectance units, using ground calibration targets.

Magnetics were flown with a composite material fixed-wing UAS Albatros VT2 from Radai Oy (www.radai.fi, Radai Ltd., Oulu, Finland). This UAS utilizes a three-component fluxgate magnetometer, a cost-reducing drone-based sensor (Gavazzi et al., 2019), attached to the drone's tail boom. With 2.5 m of wingspan and a flight endurance of roughly 3 h, it can easily cover outcrops at square kilometer scales. The survey was flown with traverse lines at 30 m spacing, 99.4° azimuth and tie lines at 60 m spacing and 9.4° azimuth. The fixed-wing follows the topography along the flight plan based on any available high-resolution digital elevation model. In this case, we used publicly available data from the National Land Survey of Finland. Magnetic data processing involved removal of spikes and duplicate points, compensation of the fluxgate magnetometer, computation of the total magnetic intensity from the compensated component magnetic data and removal of diurnal effects. Position coordinates, time stamps, barometric pressure and the three-component magnetic data were recorded simultaneously by data logging hardware. An equivalent source algorithm (equivalent layer model (ELM) after Pirttijärvi, 2003) was utilized to prepare the final TMI grid for the survey with the minimum curvature gridding method of ELM data at 15 m cell size. The software Model Vision (vers. 16.0, Tensor Research Pty Ltd., Greenwich, Australia) was used for subsequent forward modeling. Five magnetic profiles crossing along the E–W direction on top and near the main trenches were used in the forward model. A number of simplified bodies with tabular geometries were modeled until a reasonable root mean square error (3–5%) between the measured and synthetic TMI response was achieved. Covering the known lithologies, ground sampling locations of rock specimens ($n = 23$) and ground control points ($n = 19$) were localized with a Trimble global navigation satellite system (GNSS) kit (Trimble R5 base station, Trimble R10 rover; Trimble Inc., Sunnyvale, USA). An overview of the complete workflow is shown in Figure 4.1.

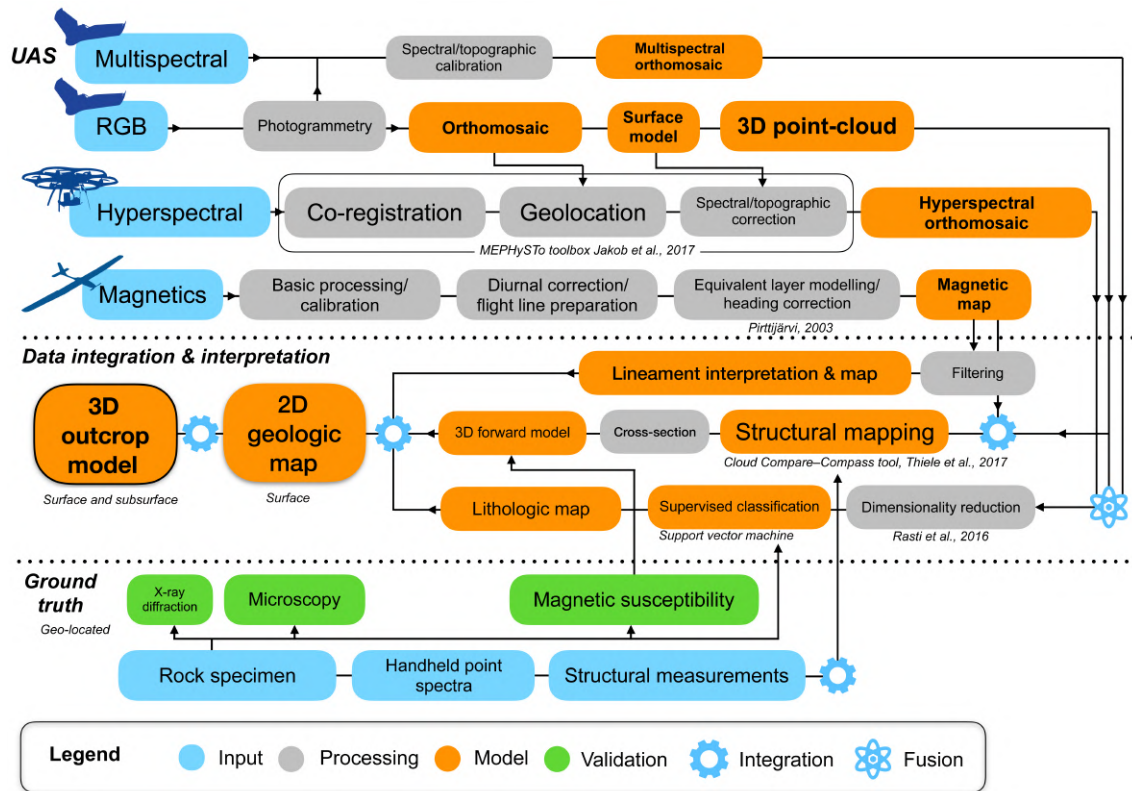


Figure 4.1. Detailed chart of proposed data-driven unmanned aerial system (UAS) based integration and modelling workflow.

4.2.4 Ground Truthing and Laboratory Validation

Data integration at multiple scales, using local ground truth, airborne magnetics, and regional geology is an established method that can provide excellent results and meaningful geologic interpretations (Austin et al., 2013). Our ground-truthing program involves rock sampling, as well as structural ($n = 38$) and spectral measurements ($n = 336$) and ground-based photogrammetry. All ground samples are geolocated using GNSS. All rock samples are cut and polished for optical investigation and some for analysis with selected geochemical and mineralogical methods.

We take several structural measurements (geological compass), which we incorporate in forward modelling of magnetic data. Main observations are made for contacts, orientation of dykes, and foliation. During the outcrop studies, we record point representative spectra using a portable spectroradiometer in the available wavelength range of 400–2500 nm. We use selected scans as reference for the supervised image classifications (see Appendix A for point distribution and spectrometer specifications).

Laboratory validation methods, which represent traditional geological, mineralogical, and petrophysical verification methods, are selected to confirm our field observations, and to extract further geologic information from the study site itself. All measurements are conducted on

collected rock specimens in the laboratory. Thin section samples are created from specimens covering all main lithologies of the outcrop and examined with optical and polarized light microscopy. Magnetic susceptibility and X-ray diffraction analysis is applied on selected samples (see Appendix D for additional information).

4.3 Case Study: The Siilinjärvi Carbonatite Complex

Here, we introduce the test area together with the geology. The Siilinjärvi carbonatite complex is situated 20 km north of the city of Kuopio in central Finland and extends for 16 km in N–S and 1.5 km in E–W directions (Figure 4.2a), with an estimated depth of 800 m (Malehmir et al., 2017b). It is one of the oldest known carbonatites with an Archean age of $2.6 \text{ Ga} \pm 10 \text{ Ma}$, according to U–Pb zircon dating (Tichomirowa et al., 2013). The Siilinjärvi mine extracts carbonatite–glimmerite-hosted apatite ore for fertilizer production as one of the biggest producers in Europe.

4.3.1 Local Geology and Study Area

The carbonatite intrusion was emplaced into basement gneiss and deformed by the Svecofennian orogeny at 1.8 Ga (Poutiainen, 1995). Local rock types are fenite, gneiss, carbonatite–glimmerite, diabase, and other dykes (e.g., local diorites). The central carbonatite–glimmerite ore body has a tabular form, is up to 900 m in width, and is surrounded by a fenite margin created by carbonatite-derived alkali metasomatism of the granite–gneiss country rock and syenite (O’Brien et al., 2015).

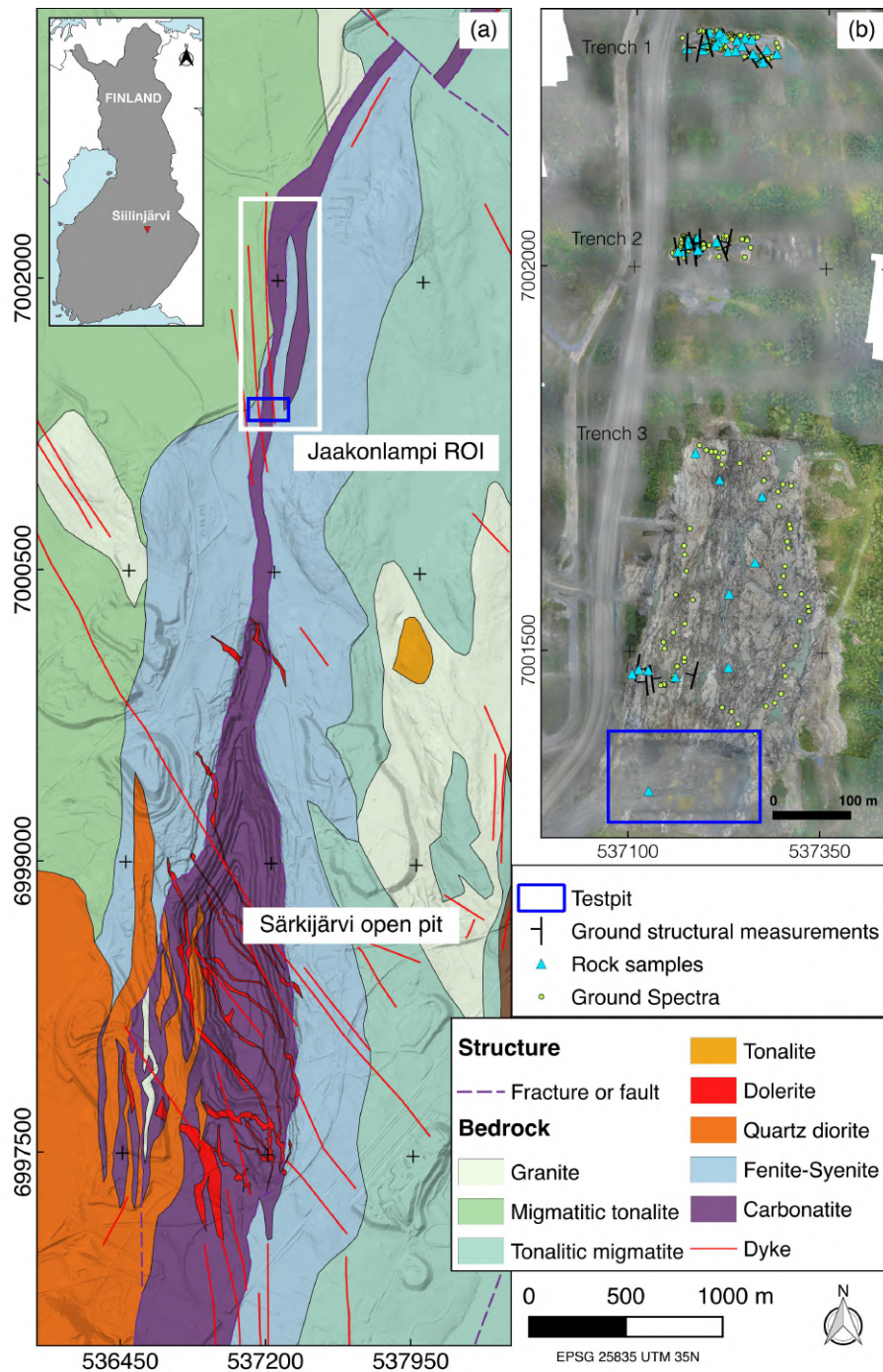


Figure 4.2. (a) Official geologic map; bedrock of Finland; scale-free map © Geological Survey of Finland 2019, <http://hakku.gtk.fi>, that combines data of different map scales. The Jaakonlampi region of interest (ROI) includes our test area for UAS survey. (b) UAS-based orthophoto of the Jaakonlampi ROI, showing structural measurements, rock sample positions and ground spectroscopy.

Brittle and ductile deformation caused structural segmentation of the carbonatite complex and surrounding rock, expressed as sharp boundaries within some areas of intermixed diabase, fenite, tonalite and carbonatite–glimmerite. Fenites as metasomatic products of diorite and gneiss are found in the magmatic contact zones between country rock and carbonatite–

glimmerite (Puustinen, 1971). This halo of fenitized rocks contains microcline, orthoclase, amphibole, and pyroxene, as well as carbonate, zircon, and quartz.

Several generations of mafic dykes (dolerite) cut the Siilinjärvi intrusion in NW–SE and NNW–SSE directions, with widths ranging from centimeters to meters (O’Brien et al., 2015). Most of the dykes are steeply dipping and, depending on their generation, were subjected to deformation (Mattsson et al., 2019). Sheared feldspar-rich pegmatite dykes with widths varying from 1–50 m were recently discovered by a large-scale drilling program in the Jaakonlampi area (Salo, 2016) and are exposed on the surface. Structural emplacement of the dykes is still not fully understood, but given their size and increased magnetic susceptibilities, they could be an important component of forward modelling.

4.3.2 The Jaakonlampi Test Area

Situated 1.2 km north of the Särkijärvi main pit, the Jaakonlampi area (Figure 4.2b) provided the test zone for our UAS survey. Jaakonlampi extends ~1 km in the northern direction and is characterized by three distinct exploration trenches, which from north to south, henceforth we refer to as trench 1, trench 2, and trench 3. The mine company expanded the exploration program for trench 3 in 2018 and removed significant soil overburden, uncovering a large exploration trench (Figure 4.3c). However, the recent uncovering resulted in some remains of sand and clay on top of trench 3’s surface, challenging subsequent image classifications.



Figure 4.3. Photographic illustrations of the applied field methods, data acquisition by UASs and ground truthing, and overviews for the visited outcrops in the Jaakonlampi area. (a) Hyperspectral survey using multicopter UAS. (b) Magnetic fixed-wing UAS. (c) Ground spectroscopy and geo-locating on trench 3. (d) Trench 1 during hyperspectral survey. (e) Ground sampling on trench 2 including structural measurements and spectral surface scans. (f) Contact between dolerite dyke and feldspar-rich pegmatite intrusions. (g) Photograph of the test pit wall that marks the southern survey end zone.

Within the glimmerite, the carbonatite is featured as thin, sub-vertical veins. The composition of carbonatite is mainly calcite, apatite (1.4–2.3 vol.%) and magnetite (1 vol.%). On average, the ore contains 65% phlogopite, 19% carbonates, 10% apatite, 5% richterite, and 1% accessories that are mainly magnetite and zircon (O'Brien et al., 2015). The composition of the three trenches (Figure 4.3c–f) is similar to the general configuration of the Siilinjärvi deposit.

The southern-located trench 3 connects seamlessly to a so-called test pit (Figure 4.3g), an outcrop wall which presents a vertical geologic cross section of the lithological units further used in this study:

- Carbonatite–glimmerite (CGL) and carbonatite (CRB)
- Dolerite (DL)
- Feldspar-rich pegmatite veins (FSP-PEG)

- Fenite (resp. syenitic fenite or fenite-syenite) (FEN-SYN)
- Glimmerite (GL)
- Granite–gneiss (GRGN)

4.4 Results

We present the mapping results sorted by method. Survey conditions, camera settings, and technical UAS-related data are found in Appendix D (Table D1). All trenches and the forested areas in between were surveyed by high-resolution RGB and multispectral UAS images and UAS magnetics. Additional hyperspectral imaging covers trench 1 completely, the western half of trench 2 (the other half was submerged by water), and the northern half of trench 3. Visual observation of the test pit wall showed dipping bodies between 70–90°, broadly striking along N–S.

4.4.1 Ground Spectroscopy and Principal Lithologic Representation

We measured the three trenches in situ with a representative dense spectral point sampling campaign (Figure 4.2b) at trench 1 and 2 (275 locations). For trench 3, we conducted a broader sampling sweep (61 locations, 37 of those covered by UAS-based HSIs and MSIs). While understanding the spectral differences of the lithologies, we selected training samples for the supervised classification (Figure 4.1, last row) guided by the ground spectra (representative spectra in Figure 4.4), the RGB mosaic, and the OTVCA layers.

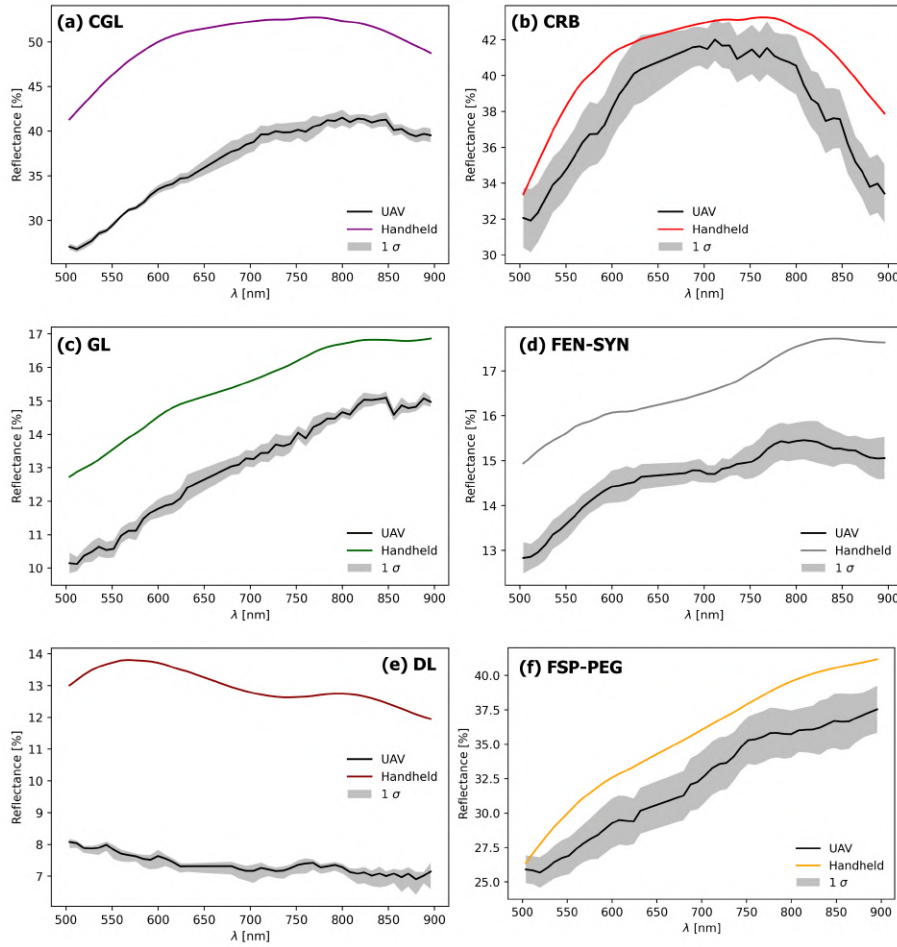


Figure 4.4. (a–f) Representative hyperspectral image (HSI) drone-based spectra compared to handheld point scans from the same lithologies and in direct spatial neighbourhood, plotted between 504–900 nm. Spectra were manually extracted from representative spots of the main lithologies. GCL = Carbonatite–glimmerite; CRB = Carbonatite; GL = Glimmerite; FEN-SYN = Fenite–syenite; DL = Dolerite; FSP-PEG = Feldspar–pegmatite.

A relatively broad absorption between 900–1200 nm is attributed to the Fe^{2+} content in calcite and dolomite-rich carbonatite (Gaffey, 1985). We detected rare earth element (REE) related absorptions at 580 ± 10 nm, 740 ± 10 nm, and 800 ± 10 nm (Figure 4.5b, Neave et al., 2016). A spectral shift from calcite-rich to dolomite-rich carbonatite is visible in our point scans, at the spectral minima transition from 2320 nm to 2340 nm (Figure 4.5c), related to vibrational processes of CO_3 combinations and overtones (Hunt, 1977; Clark, 1999). For glimmerite spectra, rich in phlogopite and biotite, we observe characteristic OH^- features at 1380 ± 10 nm and Mg-OH vibrational bands at 2320 ± 10 nm and 2380 ± 5 nm (Hunt, 1977). Carbonates are likely to influence the position of the absorption minima here. Hydroxyl group absorption features are seen for fenitized syenite spectra at 2315 nm and 2385 nm. Dolerite spectra show the lowest overall reflectance, weak $\text{Fe}^{2+}/\text{Fe}^{3+}$ charge-transfer absorptions at 800 nm (Hunt and Ashley, 1979) due to iron alteration but a prominent absorption at 1920 nm (OH^- related). Feldspar-rich pegmatites, expressing a larger spectral variety and incorporating Fe^{2+} and

pronounced OH- features are found at 1410 nm, 2200 nm (Al-OH), and 2350 nm (Mg-OH). We observed apatite in carbonatite–glimmerite rock samples as a possible proxy for REE occurrence.

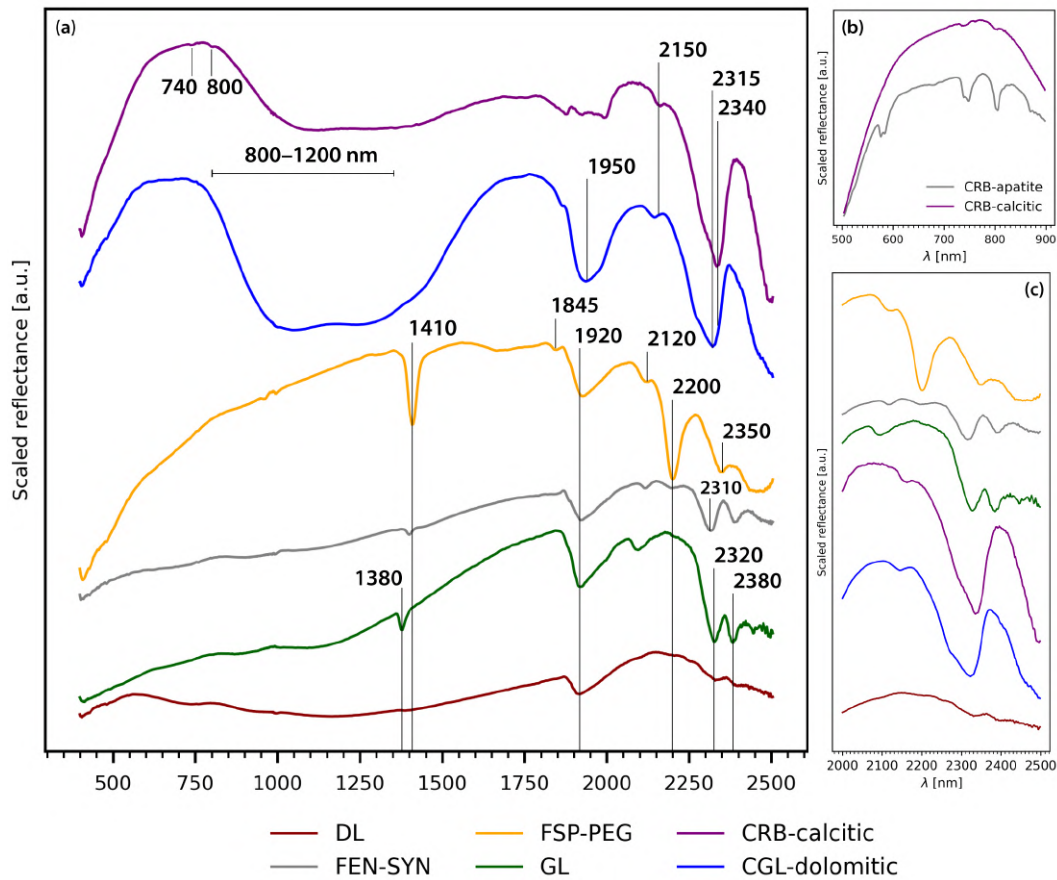


Figure 4.5. (a) Six selected handheld scans, representative for the mapped lithologies, plotted between 450–2500 nm and with indicated positions of spectral absorptions. (b) Zoom within the available UAS-based HSI wavelength window (504–900 nm) showing two carbonatites, where both apatite-rich carbonatites express some rare earth element-related absorption. (c) Enhanced view of the shortwave-infrared region between 2000–2500 nm, same color legend. DL = Dolerite; FSP-PEG = Feldspar–pegmatite; CRB = Carbonatite; CGL = Carbonatite–glimmerite; FEN-SYN = Fenite–syenite; GL = Glimmerite.

4.4.2 UAS-Based Optical Remote Sensing Observations

The RGB orthophoto (Figure 4.6a), the MSI mosaic (Figure 4.6b) and the HSI mosaics (Figure 4.6c) provide first-order information for subsequent interpretation. Low ceiling clouds were present during the RGB acquisition flight, producing horizontal grey stripes in the data. Occasional leftover dirt patches reduce the spectral quality in some HSI scans of trench 3. Topographic expressions are seen in the UAS-based DSM (ground sampling distance 10.6 cm; Figure 4.6d). The eBee RGB and MSI orthomosaics envelope the complete rock outcrop extension, which is covered by vegetation stripes between trenches 1 and 2 and between trenches 2 and 3. HSI mosaics were acquired completely for trenches 1 and 2. Trench 2 was partly covered with water on large surface portions. Low illumination conditions during the

HSI acquisition of trench 3 reduced the spectral quality for all scans there. We augment the data set of trench 3 by using two additional data layers (DSM, MSIs) from the area. Those additional layers were resampled to the common lowest resolution (from the DSM) and fused with the HSI data set before applying the dimensionality reduction by OTVCA to improve supervised image classification.

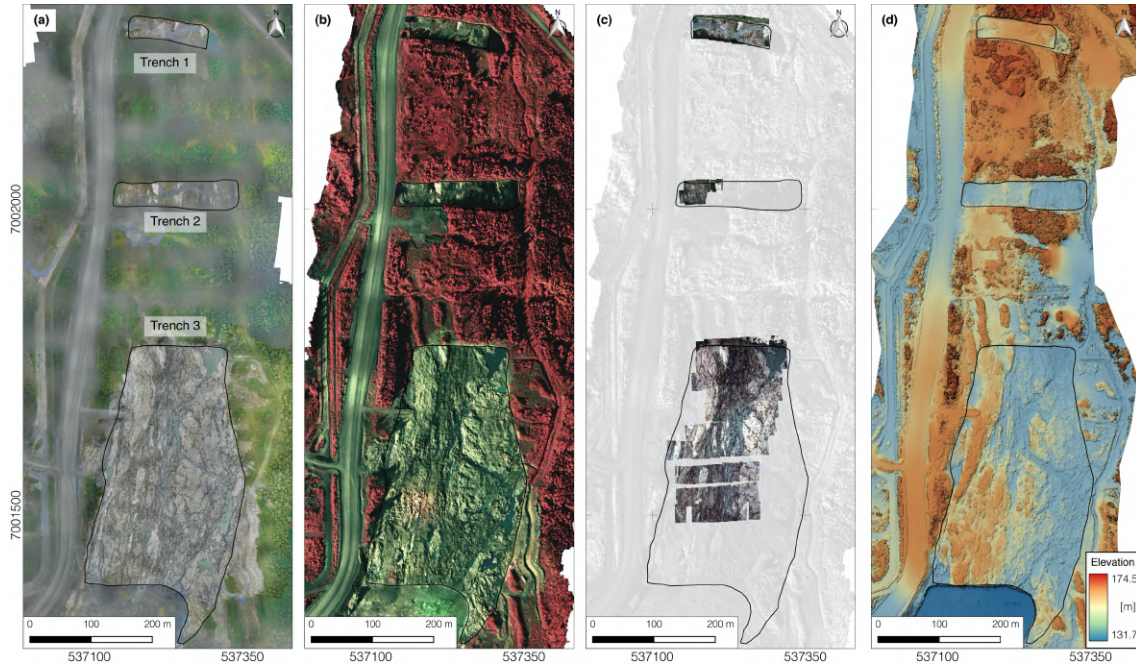


Figure 4.6. Overview of image-based data products showing the three trenches, with the test pit at the southern end of trench 3. (a) RGB orthomosaic from the eBee Plus UAS and S.O.D.A. camera. (b) Multispectral false-colour infrared mosaic from the eBee Plus UAS and Sequoia camera (bands 735 nm, 660 nm, 550 nm). (c) Hyperspectral false-color RGB mosaic from Rikola camera images (bands 650 nm, 551 nm, 504 nm) flown on multicopter UAS. (d) Hillshaded digital surface model derived from SfM-MVS photogrammetry, based on eBee Plus orthophotos, elevation in meters above sea level.

The OTVCA-based false-colour band combinations we selected for high variations are shown in Figure 4.7a and Figure 4.7b. Only the merged multi-sensor OTVCA bands for trench 3 (Figure 4.7c) contain MS, RGB, and DSM data. Fusing those additional data layers for the classification of trench 3 helped to close some data coverage gaps of the hyperspectral survey (Figure 4.7c). The final classification produced by the SVM classifier and visual inspection was used to create the surface geology map. The resulting overall accuracy (OA) for all three trenches ($> 90\%$ OA each) is acceptable. Overall supervised classification accuracies with used ground truth are as follows in mean accuracy (MA), OA, and kappa coefficient (κ): trench 1 – MA 96.5, OA: 95.3, κ : 0.94; trench 2 – MA 91.0, OA: 90.0, κ : 0.88; trench 3 – MA 95.3, OA: 95.3, κ : 0.95. We refer to Appendix A for visualized training and validation samples, as well as confusion matrices per trench classification. Although we achieved high classification accuracies, three falsely classified zones are identified (Figure 4.7f), i.e., a large block of

carbonatite (25 m length) in the fenitized syenite and a stripe of dolerite extending into the feldspar–pegmatites and the mine road.

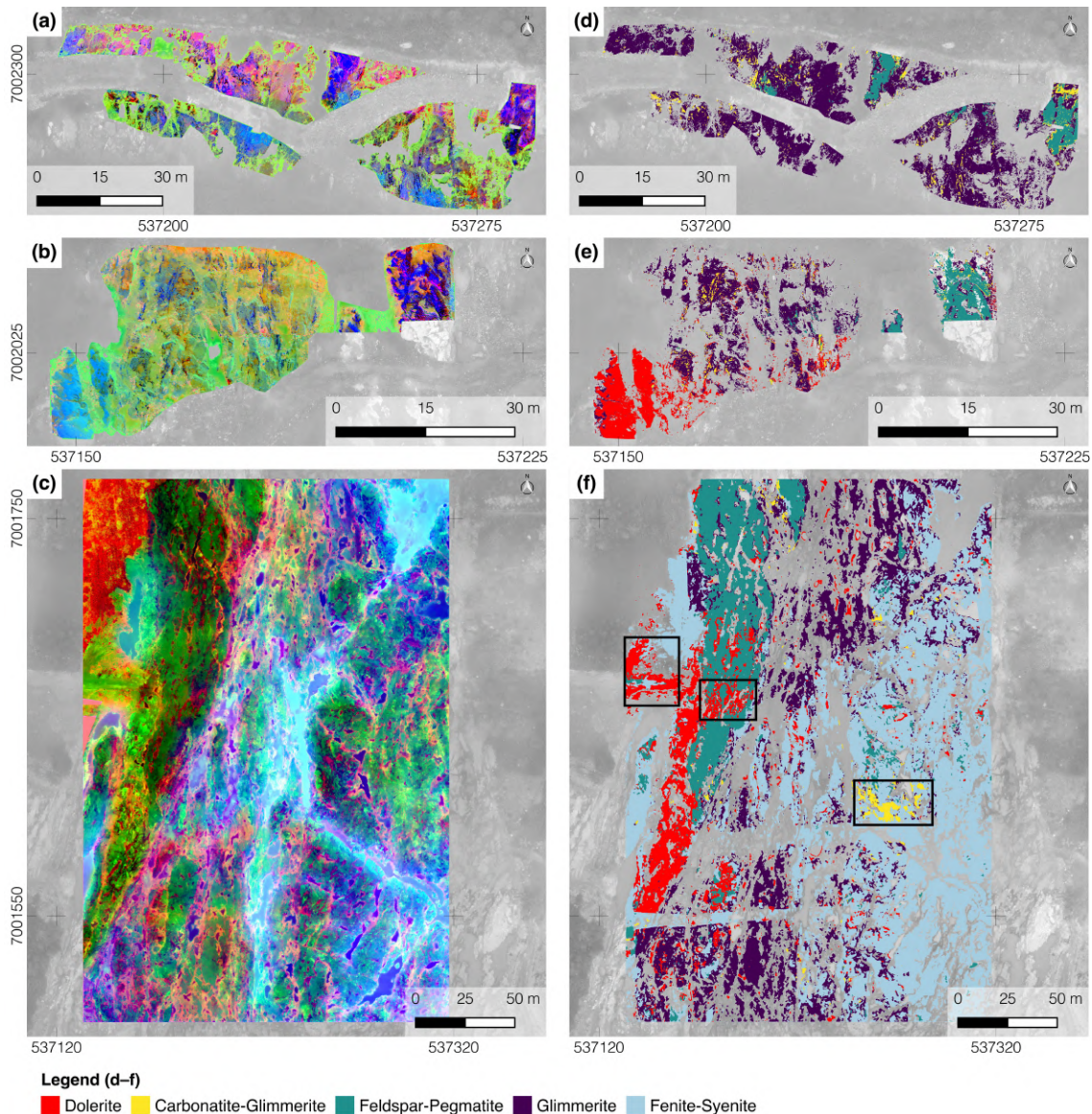


Figure 4.7. Display of feature extractions (a–c) and supervised classification maps where only the geologically meaningful classes are shown for comparison (d–f), plotted on a grayscale UAS-RGB background orthophoto. (a) Trench 1 – Orthogonal total variation component analysis (OTVCA) colour combination bands 2, 1, 4. (b) Trench 2 – OTVCA colour combination bands 2, 1, 3. (c) Trench 3 – OTVCA colour combination bands 3, 5, 2. (d) Trench 1 – Support vector machine (SVM) supervised image classification. (e) Trench 2 – SVM supervised image classification. (f) Trench 3 – SVM supervised image classification. Black frames highlight misclassified zones.

4.4.3 UAS-based Magnetic Observations

Magnetic data interpretation is based on the processed TMI (Figure 4.8a) and filtered data products. The total survey length was ~39 km, with a mean flight height of 48 m above sea level (a.s.l.), a sampling line point distance of 2.1 m, and a mean velocity of 17.7 m/s. We show regional airborne magnetics (Airo, 2005) modified after Geologic Survey of Finland © 2016) for comparison (Figure 4.8b). The regional field shows a decreasing tendency towards the west.

A pronounced magnetic anomaly, with values reaching 400 nT, is heading in the north to south direction. At the centre of trench 3, the TMI trend is decreasing. A TMI field strength reduction is visible at the southern end of trench 3 above the vertical wall of the test pit.

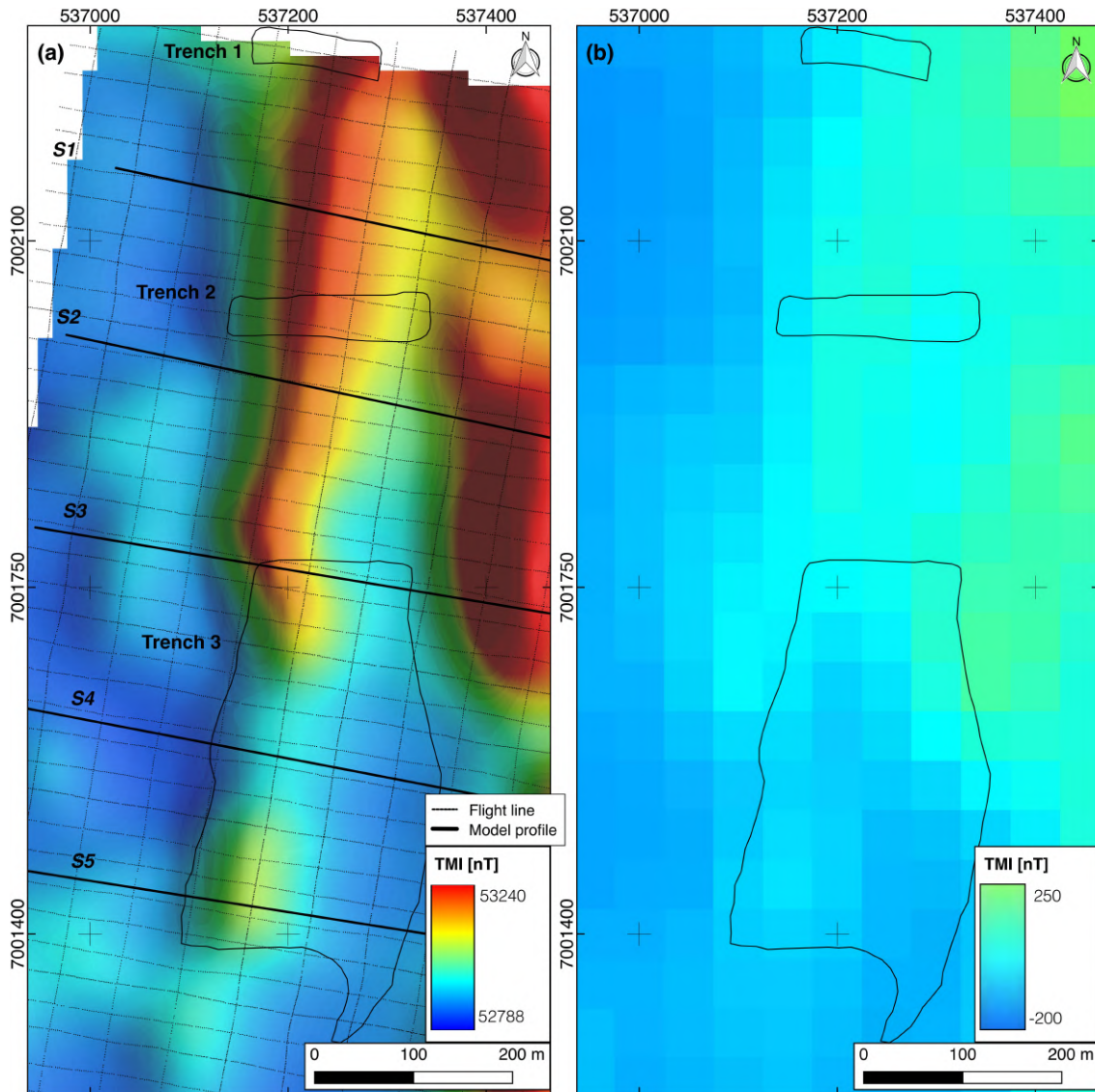


Figure 4.8. (a) Total magnetic intensity data plotted with shaded relief and UAS flight paths as stippled lines from fixed-wing magnetics. Recovered in-line sampling distance after processing varies between 1.5–2.2 m. Bold black profile lines are used in magnetic forward modelling. (b) Regional aeromagnetic data from the Geological Survey of Finland (40 m nominal flight altitude, 200 m line spacing; colours are hard-coded; definitive magnetic reference field version 1965 removed from the data).

The first vertical derivative (1VD, Figure 4.9a) sharpens the edge of the N–S trending anomaly and the 1VD outlines the distinct transition from low to high TMI values, which we interpreted as possible lithologic contact between country rock and fenite. By using the analytic signal (AS), which serves to minimize the impact of any magnetic remanence on the observed magnetic anomaly pattern, we enhance magnetic contacts, interpreted here as carbonatite–glimmerite and country rock (Figure 4.9b). Based on the aforementioned image classification

(Figure 4.7f), the western border of the dolerite unit could be traced, which is running from N–S through the whole study area. A decrease in the vertical gradient magnitude is seen again in the centre of trench 3, where the shear zone is located (Figures. Figure 4.2 and Figure 4.9) (Salo, 2016). The spatial width and field strength of the central anomaly could be related to the volume of material replaced by the non-magnetic feldspar-rich pegmatite dykes. The magnetic low at the centre of trench 3, starting 50 m north from the test pit, is measured atop the observed fold and shear tectonics, where magnetic minerals are altered, displaced, or destroyed (Burkin et al., 2019). The two spatially large, oval-shaped anomalies cross above the eastern map border of Figure 4.8a.

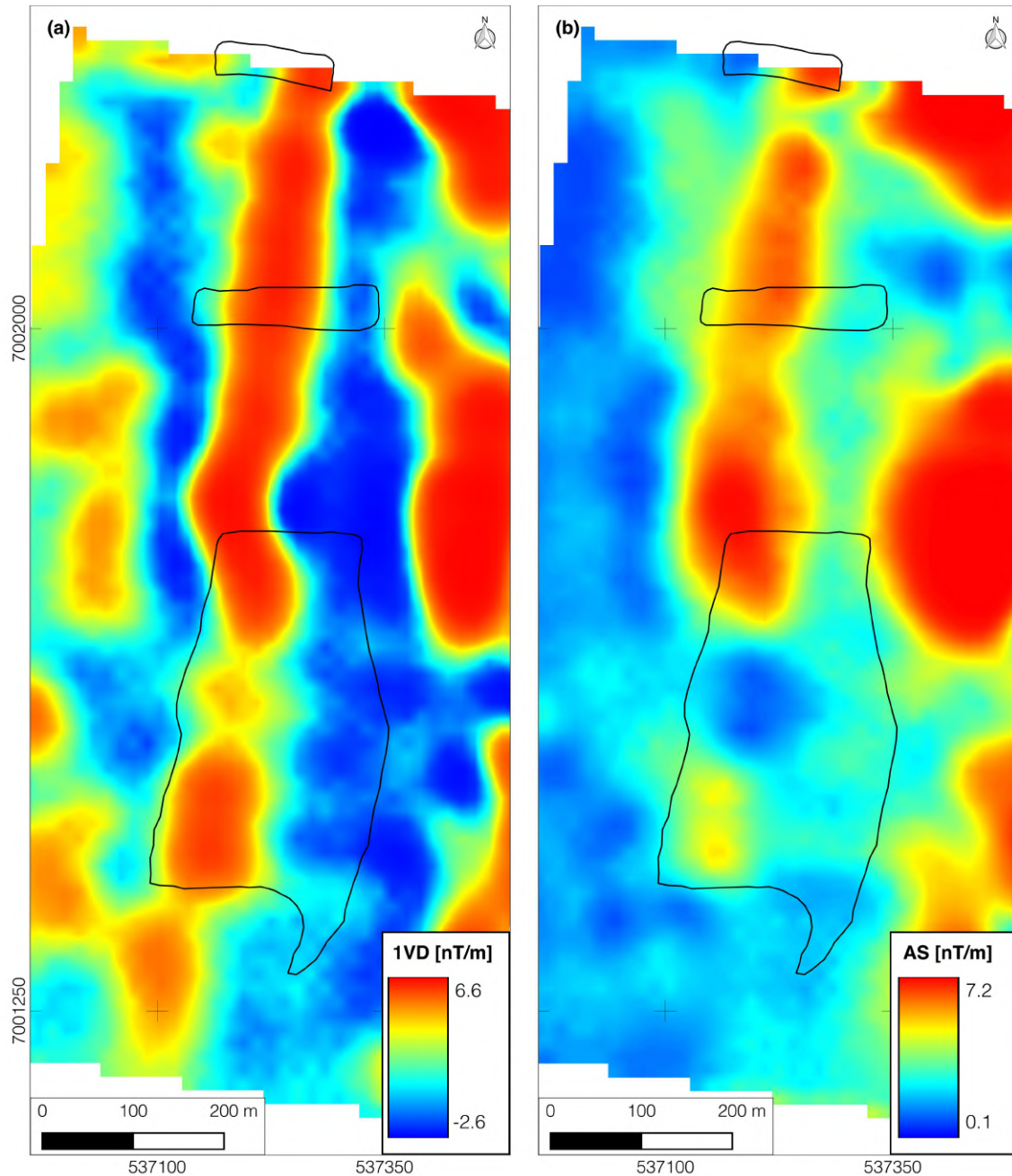


Figure 4.9. Comparison of magnetic data at different scales with black outlines representing the trenches. (a) Analytical signal from UAS total magnetic intensity (TMI) data. (b) First vertical derivative from UAS TMI data.

4.4.4 Geologic Modelling and Ground Magnetic Susceptibility

Magnetic susceptibility measurements are imperative for a supporting forward model as a secondary data derivative, based on UAS magnetics. The susceptibility ranges of our sampled lithologies are aligned with values presented in the literature and our own sampling. Table 4-2 lists susceptibility ranges for the relevant lithologies.

Table 4-2. Augmented value range for magnetic susceptibilities based on reference literature and own measurements, values given in SI units.

Lithology	Almqvist et al., 2017	V. Laakso, 2019	Measured	Used
Dolerite	1.26×10^{-4} – 1.29×10^{-3}	1.0×10^{-2} – 1.6×10^{-1}	7.0×10^{-4} – 1.35×10^{-2}	1.0×10^{-5} – 1.7×10^{-2}
Carbonatite– Glimmerite	4.27×10^{-4} – 2.09×10^{-1}	1.3×10^{-1} – 2.1×10^{-1}	1.0×10^{-4} – 1.1×10^{-2}	3.2×10^{-3} – 2.5×10^{-2}
Feldspar– Pegmatite	–	0 – 5.0×10^{-4}	7×10^{-5} – 1.4×10^{-4}	1.0×10^{-5} – 5.0×10^{-4}
Fenite	–	1.3×10^{-1} – 1.5×10^{-1}	1×10^{-6} – 1×10^{-5}	–

We constructed a model, starting with simple cuboidal geometries, and advanced to polygonal tabular sheets, with their surface geometry constrained by our UAS-based surface geologic map (Figure 4.10). UAS-based DSM data were used to constrain the top surface of each polygon. An approximate maximum depth of 250 m meters was imposed, based here on available literature information for the study area. Body geometry (strikes and dip, width, azimuth) were taken from photogrammetric interpretation and compared with our own ground measurements. Initial susceptibility values were assigned to geological units on the basis of the literature and measured susceptibilities (Table 4-2). Optimization of the model was achieved using the inversion tool provided with the ModelVision software. After continuous reiterations, a root mean squared error between synthetic and modelled TMI response of 3–5% was reached per profile. In our model (cross section in Appendix B) one implication could be that the dolerites we measured can reach magnetic susceptibilities close to carbonatite–glimmerite. Yet, this could be an observation at only some depth or related to shearing. The dolerites are known to be low or non-magnetic in the mine area (personal communication, Yara chief mine geologist). The modelling results are integrated in Section 5.1 with the surface data for the final mapping. Extracted body boundaries are used to refine the surface map in a 2D cross section depth map over trench 3 (Figure 4.10c).

4.5 Data Integration and Validation

In this section, we present the integrated results of our UAS mapping approach, bringing together data acquired with UAS platforms and ground survey. All analyses and maps were conducted and created in Quantum GIS (vers. 3.4, QGIS development team). The inferred lithologies between the outcrop trenches are mapped using the UAS magnetic observations. The following link to the integrated 3D model is available online at <https://skfb.ly/6U6Xo> (last accessed).

4.5.1 Geologic Mapping and Interpretation

Structural features (e.g., foliations, discontinuities, lineaments) and contours are interpreted visually in magnetic and DSM data, and with finer detail aided by the RGB orthophotos (Figure 4.8a). We produced magnetic contours from TMI, AS, and 1VD data. To do so, we calculated the contour lines from TMI and for filtered magnetics, to obtain magnetic isolines per data set in quartered data range steps and subsequently kept only each isoline representing the 50 % data threshold. Thus, one isoline shows the arithmetic data threshold representing a mean. We observe that the TMI and 1VD isoline are superimposed along the western border of the main anomaly in the centre of trench 3. This might reflect a well-expressed, deep contact of carbonatite–glimmerite and country rock. The ‘mag gradient’ outlines the observed field decrease (centre of trench 3; Figure 4.9). The geologic surface interpretation (Figure 4.10b) brings together all data sources: RGB orthophoto, supervised classification of HSIs, and fused data. We extracted 66 discontinuities manually for the three trenches (sum of length: 4.46 km), with a mean length of 50 m per structure. We mapped a high density of features along trench 3, as a result of high contrast in both RGB and HSI mosaics. The visual overlap of RGB, HSIs, DSM and magnetics aided the extraction when contacts or boundaries were blurred or ambiguous. The shear zone in the south-east of trench 3 (Figure 4.10c) expresses visible lineament offsets and a dense fracture pattern in RGB data. We do not infer fenite as there are too few surface observations for reference, but the magnetics indicate a contact between carbonatite–glimmerites and fenites.

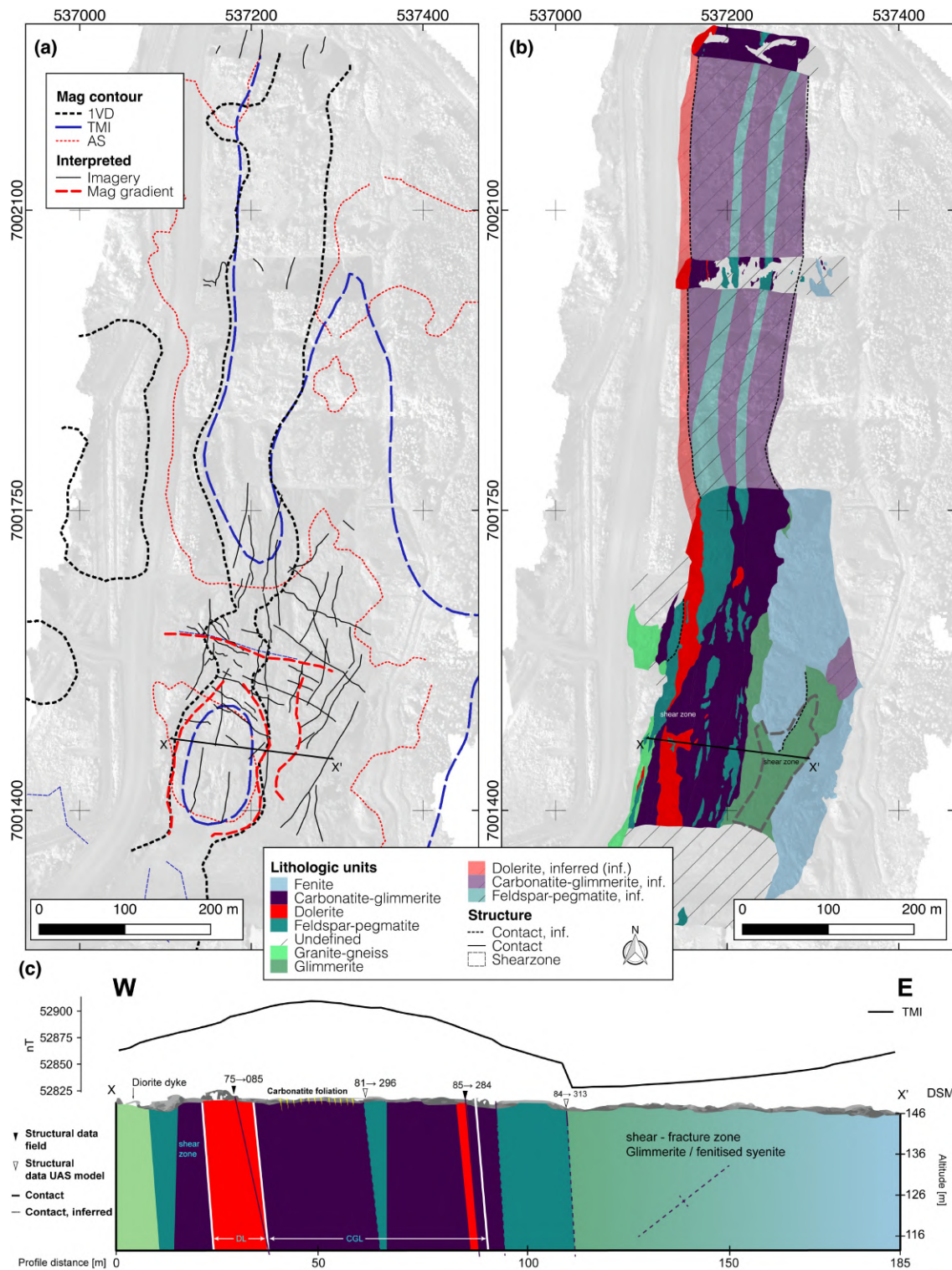


Figure 4.10. Structural and geological information is synthesized. A semi-transparent MSI mosaic is set as a background for referencing on both maps. (a) Extracted isolines from magnetics (Mag contour) are shown together with structural interpretations as observed discontinuities and lithologic contacts, based on UAS-based point clouds, digital surface model (DSM), and orthophotos. (b) Interpreted geologic map of surface lithologies. Colour legend valid for (b) and (c), which shows an interpreted profile plot crossing trench 3. Main lithologies are drawn from surface mapping and extended in depth, based on forward modelling and structural measurements from photogrammetry; TMI response plotted above DSM. Orientation of planar features is indicated in dip→dip direction. In the shear zone, the magnetic anomaly is diminished, possibly caused by subsequent alteration and relocation of magnetite. A small diorite intrusion was observed during field mapping.

We infer that the lithologies carbonatite–glimmerite, dolerite, and feldspar–pegmatite continue their N–S trend and intersect with the surficial identified structures. A good example is the case for dolerite and feldspar–pegmatite, which we can observe for trenches 1 and 2 (Figure 4.10a and Figure 4.10b compare observed vs. inferred lithologies). Additionally, we map the smaller carbonatite features based on HSI classifications and show them as overlaying foliation (Figure 4.11). A 3D representation of the pit wall is seen in Figure 4.12.

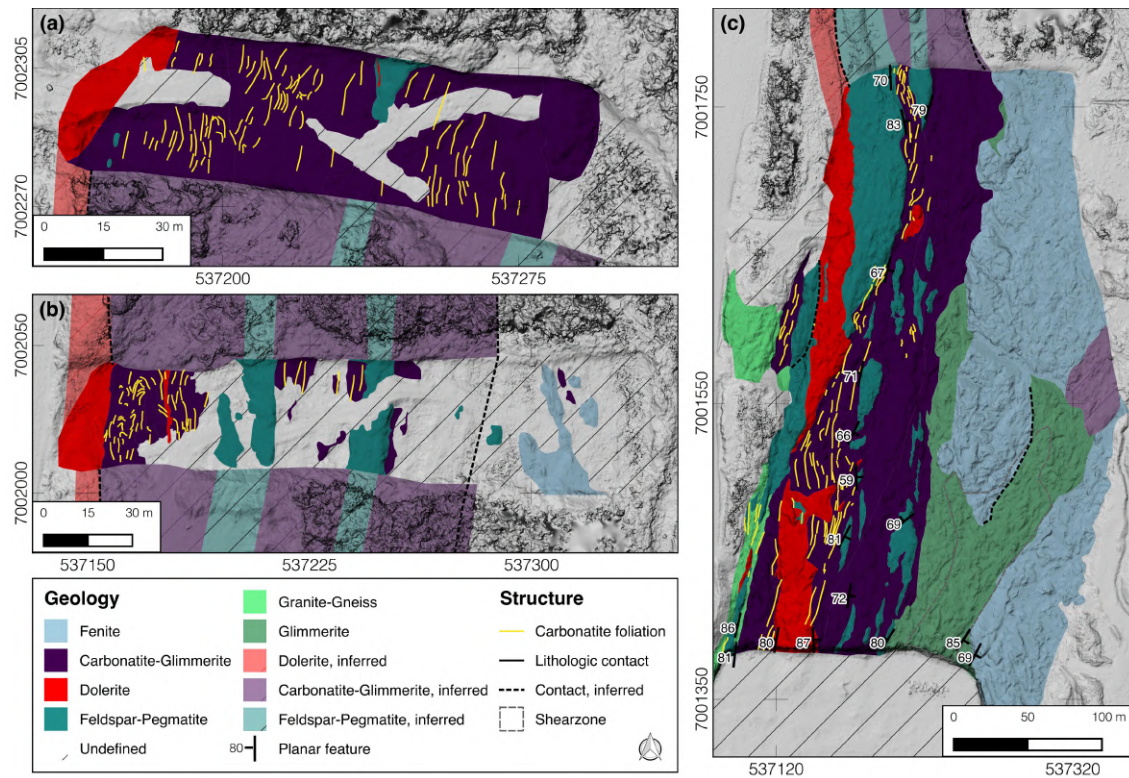


Figure 4.11. Enlarged maps of the interpreted geology from the three surveyed trenches. Gray background shows a hillshaded representation of UAS-based DSM to add topographic contrast. (a) Trench 1. (b) Trench 2. (c) Trench 3.

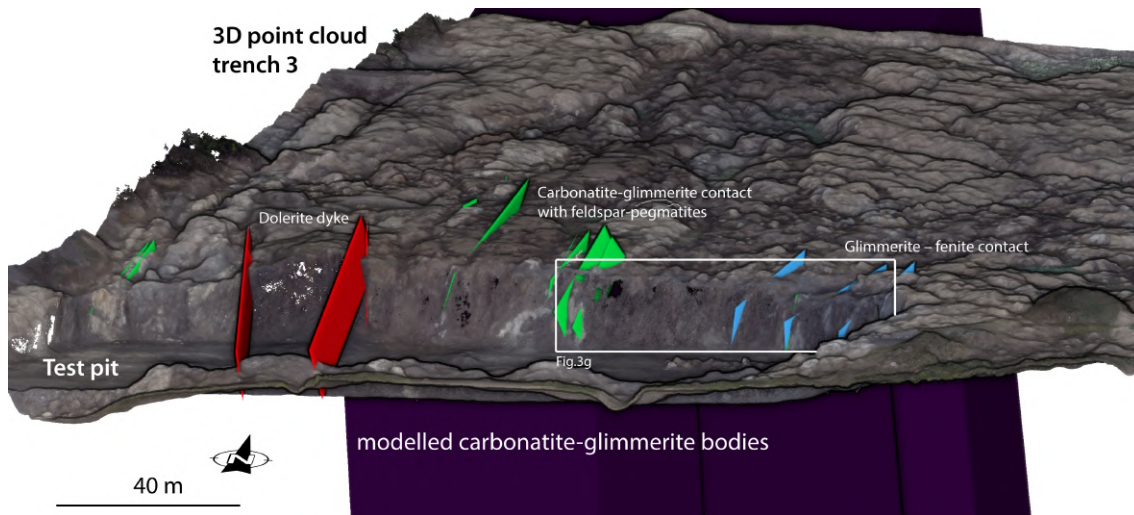


Figure 4.12. Enlarged view on an orthographically projected point cloud of trench 3 (see also Figure 4.1a and Figure 4.2g), showing the test pit wall with 3D best-fit planes for digital structural measurements. The white box highlights the field photograph of Figure. 3g. A 3D version is found online at <https://skfb.ly/6U6Xo>.

By applying the Cloud Compare compass tool (Thiele et al., 2017) we could extract 21 contact planes between feldspar–pegmatite and glimmerite, 10 dolerite contacts, and 6 glimmerite–fenite contact planes, all of which were located in trench 3 (Figure 4.12). The largest dolerite dyke had a diameter of ~30 m. Trenches 1 and 2 expressed few topographic differences to extract meaningful contact planes.

4.5.2 Mineralogic Validation and Additional Observation

We deployed optical microscopy (Appendix D) and X-ray diffraction (XRD) methods for mineralogical analysis. The microscopy of carbonatite–glimmerite shows calcite, a homogeneous distribution of magnetite grains ranging in size from microns to millimeters, and larger pyrite crystals. We observed idiomorph magnetite in rock thin sections of carbonatite–glimmerite, glimmerite, and dolerite. Magnetite seems to be in co-occurrence with pyrite. Combining microscopy and XRD, we detect some presence of magnetite in several mapped carbonatite–glimmerite and glimmerite units of this study. XRD of a bulk handheld specimen collected from carbonatite–glimmerite shows 1.8 wt.% of magnetite. Further evidence of magnetic minerals was only observed in one dolerite sample (2.4 wt.%). We did not identify magnetic minerals in the remaining lithologies from microscopy (fenitized syenite, feldspar–pegmatite). Moreover, XRD patterns detect calcite, apatite, biotite, pyrite, quartz, albite, ankerite, and actinolite (Appendix D).

4.5.3 Validation of Structural Observations

The results of the digitally extracted structural measurements are summarized (Figure 4.13) and compared with the ground measurements. High image contrast and geometric expression were found at the test pit of trench 3, and therefore used for extraction. Thirty-two contact points, 6 foliations, and 2 dykes (carbonatite, dolerite) were measured in situ during the field campaign. Digital point cloud measurements of apparent large units were extracted mainly on the test pit wall for dolerite, carbonatite–glimmerite and fenite features. Twenty contacts between carbonatite–glimmerite and feldspar–pegmatite, 10 dolerite dykes, and 6 glimmerite–syenite–fenite contacts were extracted digitally. Our structural observations of the Jaakonlampi area show an N–S trend, which is consistent with the formerly described N–S striking foliation trend of the host rock (Puustinen, 1971), and shearing along the contacts of intrusions with host rocks (O’Brien et al., 2015). Structural orientations of contacts, dykes and foliations are comparable in their main trends (Figure 4.13a, b, and d). Smaller feldspar–pegmatite units (Figure 4.13e and f) were measurable along the carbonatite–glimmerite in trench 3. The rather flat surfaces, low topography and reduced RGB image contrast of trenches 1 and 2 could not provide sufficient contrast for usable structural measurements. NW–SE-oriented shearing affects structural expressions in our study area (Figure 4.13c). Several shearing events were identified in the Jaakonlampi area (four deformation stages with D1 || D3 identified in Salo, 2016). At the shear zone of trench 3, we observed contacts of carbonatite–glimmerite with granite–gneiss and an occasional absence of the fenite–syenite halo.

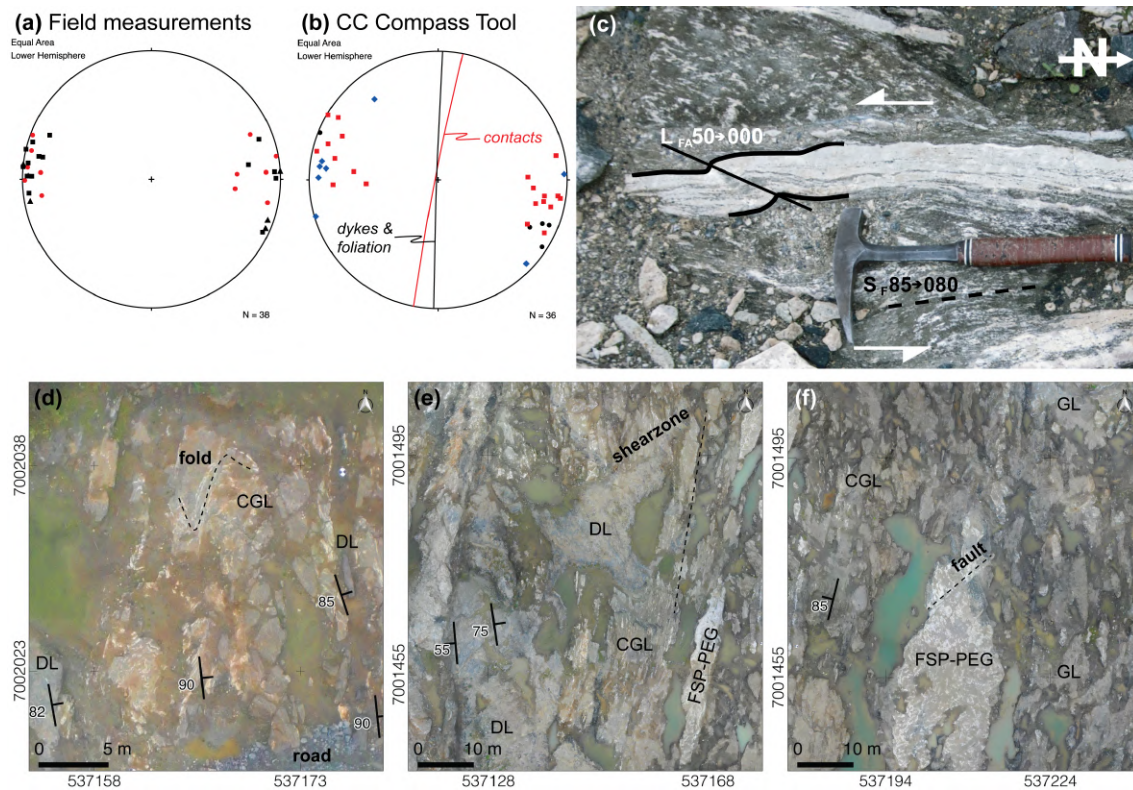


Figure 4.13. First row (a–c) shows a compilation of structural data from field work and point cloud analysis. Second row (d–f) presents UAS-based RGB orthophoto zooms with exemplary structural features. (a) Structural orientations obtained from field measurements. Triangle: foliation, circle: contacts, box: dykes. (b) Structural orientations resulting from point cloud analysis using the Cloud Compare Compass tool. Circle: contact FSP-GL, box: contact FSP-CGL; diamond: dolerite dykes. Large circles in (b) are the mean planes derived from weighted contouring (Kamb contours (Cardozo and Allmendinger, 2013)) for the respective sub-groups. (c) Field photograph showing detail of the structures and relationship of carbonatite and glimmerite from trench 2. Hammer for scale (length 33 cm). Notation is “Plunge→Trend” for linear (L) and “Dip→Dip Direction” for planar (S) features. (d) Close-up of RGB UAS orthophoto of trench 2, with a folded carbonatite–glimmerite section. (e–f) UAS-RGB close-ups of trench 3’s southern shear zone, showing a larger block of dolerite, relocated. Feldspar–pegmatite (pinch and swell and/or boudinage) dyke indicates horizontal displacement. Planar features measured with compass in the field.

4.6 Discussion

4.6.1 Assessing the General UAS Survey Workflow with Focus on Image Data

We tested a survey approach that is only limited by the external conditions for UAS operations, such as weather and legislation. Our multi-sensor UAS toolkit aids geologic ground mapping, i.e., at around 1 km² (Jackisch, 2020). Our combination of different UAS-based sensors fills spatial gaps during the survey, and provides a wealth of interpretable data. Extracted spectroscopic and magnetic observations complement each other to capture surface and subsurface information, which allows an integrated geologic interpretation. Furthermore, we expand the coverage of the survey area by complementing missing areas with data from other sensors.

As expected from our lithologies at hand, a full class distinction based solely on HSI and RGB data was not feasible at first. Here, sensor integration substantially improved the UAS-based supervised image classifications. Some lithological boundaries seen in spectral data are expressed in the DSM topography. For example, classification accuracy for the feldspar–pegmatite intrusion and dolerite contacts was improved by including the DSM layer in the OTVCA feature extraction of trench 3, because those lithologies are more extruded. Particularly for trench 3, the occasional clay–soil patches smear larger surfaces and the cloudy weather during this data acquisition made it worthwhile to include additional information. OTVCA takes spatial relationships of multi-dimensional data (i.e., dozens of image channels) into consideration. By optical inspection, the selection of 13–20 bands of each extracted OTVCA data set of the three trenches (equalling 20–30% of the provided number of input bands) for the SVM classifier was feasible. Optical inspection means here that OTVCA bands with obvious noise content (stripes, artefacts, contrast gradients) are discarded. With a careful selection of training samples, we obtained a classification in good agreement with geologic ground mapping.

The multicopter-based hyperspectral data could identify spatially small (~5 cm), spectrally pronounced anomalies, i.e., fine carbonatite lenses and is effective at the given outcrop dimension. The same lenses are visible in RGB, but cannot be distinguished spectrally, e.g., from feldspar–pegmatite rubble. Some lithologies (feldspar–pegmatite, fenite–syenite, granite–gneiss) are hardly discernible due to their lack of characteristic spectral features in the VNIR range. For example, average reflectance of fenite–syenite was similar or higher than for feldspar–pegmatite and granite–gneiss.

However, we could still discriminate those rocks by using the machine learning-based spatially constrained feature extraction. OTVCA allowed us to pass not only spectral information, but also slight spatial, textural, or overall reflectance changes to the classifier. With a set of representative, well-defined training points, the classifier is able to assign meaningful labels even to classes lacking any indicative spectral features. While delivering a good classification performance, this approach is highly dependent on good-quality training data. UAS short-wave infrared (SWIR) sensors would add more confidence to the classification and allow a direct, spectroscopic analysis of a much wider range of mineralogical features, however, their pricing and weight is still an obstacle. Light-weight VNIR sensors in combination with advanced, open-source machine learning techniques, have been shown to offer a cheaper, but still reliable, alternative for the discrimination of known lithological domains.

Furthermore, we see a high feasibility when UAS spectroscopy is used for, e.g., iron oxides and rare earth element identification. Neodymium and dysprosium are promising targets for remote sensing studies (Neave et al., 2016). We observed specific rare earth element-related absorptions in VNIR regions of handheld spectra in local apatite (Figure 4.5b). For mapping, we are particularly interested in spectral absorption of Fe^{2+} bands in the range of 800–1200 nm as a target for the HSI camera. Further CO_3 related absorption around 2330 nm, indicative for carbonate mineralogy (i.e., carbonatite), is only detectable in the SWIR range of handheld spectroscopy (Rowan et al., 1986; Rowan and Mars, 2003).

To assist with UAS magnetic mapping, first-order results from UAS-based RGB orthophotos are available directly after each flight (Figure 4.6a). Orthomosaics could be further used to optimize and refine magnetic flight plans in the field, if important anomalies are identified. While atmospheric conditions influenced the data quality acquired from optical sensors, the magnetics could be flown with a low cloudy ceiling or over wet surfaces without any disturbance. Line spacing, altitude, and sampling frequency of UAS magnetics define the features we can resolve physically, and therefore the size of targets we can model and interpret. We consider that the fixed-wing UAS probably created more valuable data for mapping with high surface coverage. Fixed-wing flight endurance was not exhausted with the current target area. In this case study, the following surface coverages were achieved per sensor:

- Magnetics: 0.695 km² (interpolated grid surface from 39-line km)
- MSI: 0.649 km²
- RGB: 0.623 km²
- HSI: 0.047 km² (sum of HSI flights)

The used UAS-fitted workflows are matured to a high user friendliness and could be flexibly adapted to all mining and exploration scenarios, where high resolution and spatial coverage is required. Safety concerns for detailed mapping along pit walls are mitigated by UAS mapping, when used for vertical outcrop scanning along unstable wall sections (Kirsch et al., 2019).

Our UAS mapping could improve the planning of material extraction processes in the mine. The volume of less profitable rock material can be reduced, which limits resource use and costs for additional drilling and curtails waste rock. Production schedules and mine layout planning could be improved. As example from UAS magnetics, we infer that the ore body cuts or continues below a mine road in the west on the outcrops, which could require a geotechnical repositioning of said infrastructure (Figure 4.2b and Figure 4.9a, west of trench 1). Once regular UAS surveys become best practice for open-pit drilling, drill locations could be predefined in detailed orthophotos and subsurface drill orientations could be optimized by model-based

interpretation of 3D data. In active mines, optical imagery is already implemented for explosive energy distribution optimization (Valencia et al., 2019).

4.6.2 Further Implications of UAS Magnetic Surveys and Added Understanding of the Local Geology

UAS-based magnetics revealed the subsurface extension and trend of the glimmerite–carbonatite body between the trenches, and was validated on the trench surface. A high potential for ground- or UAS-based magnetic surveys to study lateral extension of those ore bodies was noted before (Malehmir et al., 2017b), together with the recognition of the high magnetic susceptibility of Siilinjärvi carbonatite.

The shape and direction of magnetic anomalies directly correlate with the extension of the lithologies at hand. For example, we interpret the pronounced trend (Figure 4.9a, eastern trench border) in the TMI-1VD as contact of the magnetic carbonatite with an intruded dolerite dyke. Furthermore, we interpret the TMI-AS as the estimated maximum width of glimmerite–carbonatite for this survey site. The two large anomalies crossing the eastern survey border (Figure 4.8) are likely part of much deeper granite–gneiss country rocks, however, neither hyperspectral data nor rock samples of those zones were acquired.

We conclude that the abundant magnetite in the targeted lithologies is mostly responsible for the detected magnetic anomalies in UAS data, while fenite can be disregarded (Matias Carlsson, personal communication). The average magnetite content in the deposit is 1 wt.% (Puustinen, 1971), and is a highly abundant accessory mineral of both glimmerite and carbonatite (Heilimo et al., 2013). Minor contents of pyrite, pyrrhotite, and some chalcopyrite occurrence form sulphide minerals in locally high abundance (O'Brien et al., 2015). Sövitte, a carbonatite variety, can carry 1–2% of magnetite, often together with apatite, biotite, and pyrochlore (Le Bas, 1987). Although another source for high susceptibilities could be the mafic dykes, those are smaller in dimension as compared to the carbonatite–glimmerite and local fenite.

In a rock thin section of a dolerite sample, pyrite and magnetite were observed and confirmed by XRD measurements. For the glimmerite rocks, para- and ferrimagnetic effects can increase magnetic susceptibility in phlogopite due to magnetite domains in significant fractions (Borradaile and Werner, 1994). Two-dimensional structural interpretation of the shear zones suggests an increasing mixture of ore and waste rocks in trench 3 (Figure 4.12 and Figure 4.13 e, f). Possibly, feldspar–pegmatites ascended near trench 3 and extruded laterally along the carbonatite–glimmerite contacts, following a path of least resistance. To magnetically detect and model smaller dolerite dykes, a denser flight line pattern is recommended for higher spatial

resolution. It was noted before (Puustinen, 1971) that aeromagnetic surveying cannot resolve the carbonatite–glimmerite, however, this is now possible with UAS-based magnetic surveying.

4.7 Conclusion

This study introduced a cohesive multi-sensor survey approach using optical and geophysical UAS sensors. We integrated UAS-based surface and sub-surface data to create a digital outcrop model for precise geology mapping. Detailed surface information from high-resolution orthophotos and structural trends from point clouds provided information to map geologic features at the centimeter scale. We measured structural constraints of carbonatite–glimmerite, mafic dykes, and feldspar-rich pegmatite on digital outcrop twins. Furthermore, we used a sensor fusion approach and machine learning methods for a supervised classification of outcropping rocks, partially covered by soil and captured during unfavorable atmospheric conditions.

With hyperspectral data, we were able to identify and distinguish apatite-bearing lithologies from waste rock, i.e., feldspar-rich pegmatite intrusions and country rock. Based on UAS-borne magnetics, we created a surface-constrained forward model aided by measured and adapted magnetic susceptibilities to extract subsurface information, which revealed the extent of ore-bearing carbonatite–glimmerite. We observed this carbonatite structure at outcropping trenches, visible along the test pit wall, plunging into the subsurface and traced further based on magnetic data.

The presumed high magnetic anomaly of carbonatite–glimmerite was measured in detail by a UAS. The scale and resolution of the magnetics covered all trenches in one UAS flight. Our survey lasted for two field work days, and included a spectral surface sampling campaign. All UAS flights were conducted in parallel to the sampling with a combined flight time of <6 hours in total. The principal conclusions and highlights of this study are:

1. Rapid, flexible and automatized UAS-based surveying of lithologic surface and subsurface features, using light-weight multi-sensor technology, resulted in a 3D outcrop interpretation and provided material and structural information as a valuable alternative to time-consuming ground surveying.
2. Forward modelling of UAS-based magnetic data provided insight on orientation and depth of lithologies concealed from surface observation, here, UASs provided a link between 2D and 3D mapping.

3. Challenges arose in the integration of high-resolution HSI data at smaller scales and missing overlap between outcrops, together with spectrally inert rock types at the given spectral range.
4. Integration and fusion of topographic and spectral data using supervised surface classification of spectrally non-distinct targets with a support vector machine on dimensionality-reduced feature extraction data was successful in overcoming the challenges.
5. We recommend the use and combination of fixed-wing UASs for target-based surveying in the RGB, multispectral, and magnetic domains for advanced geologic mapping and interpretation, while using multicopter-borne HSI data for potential non-distinct lithology discrimination, sub-decimetre feature mapping and to identify features of narrow spectral range.

From this study, we observe that photo-based geology is transformed by UAS imaging techniques into automatic procedures, where magnetic and hyperspectral methods could become state of the art. MSIs and HSIs would stand next to the already implemented photogrammetric methods, to add potential for less invasive, data-driven mineral exploration and mining. UAS-based SWIR cameras will extend the range of identification for target lithologies, and future geophysical UAS sensors such as gravity, radiometric, and electromagnetic methods will extend the depth and resolution of observations.

Author Contributions: Conceptualization, R.J., M.K., S.L., R.Z., and R.G.; analysis: HSI, MSI, 3D: R.J.; analysis Mag: R.J. with support from H.U.; investigation: R.J., R.Z.; ground work: R.J., R.Z., M.K., Y.M., and L.T.; resources: R.G., A.S., and M.S.; software: S.L., M.P., R.J., and H.U.; validation: R.J., R.Z., and M.K.; visualization: R.J.; Writing—original draft: R.J.; writing—review and editing: M.K., R.Z., S.L., L.T., Y.M., R.G., and H.U.; supervision: R.G. All authors have read and agreed to the published version of the manuscript.

Funding: The research work was funded through the European Union and the EIT Raw Materials project “MULSEDRO” (grant id: 16193).

Acknowledgments: We thank Yara Oy and Aleksi Salo for allowing our research on the mine site and providing geological insights, and Martin Sonntag for magnetic susceptibility measurements at the petrophysical laboratory of TU Bergakademie Freiberg. We thank Björn H. Heincke (GEUS) and Heikki Salmirinne (GTK) for support and expertise during the work. Furthermore, we thank Robert Möckel and Doreen Ebert for conducting XRD measurements and Prof. Emer. William Morris for support in drafting the manuscript, and Lucas Pereira and Florian Rau for text improvements. We thank Louis Andreani, Gabriel Unger and Benjamin Melzer for supportive mapping during field work and Ziad Altoum for aiding in laboratory preparation (HZDR-HIF). The work was funded through the European Union and the EIT Raw Materials project “MULSEDRO”.

Conflicts of Interest: The authors declare no conflict of interest.

References

- Kim, J.; Kim, S.; Ju, C.; Son, H. II Unmanned Aerial Vehicles in Agriculture: A Review of Perspective of Platform, Control, and Applications. *IEEE Access* 2019, 7, 105100–105115.

- Adão, T.; Hruška, J.; Pádua, L.; Bessa, J.; Peres, E.; Morais, R.; Sousa, J.J. Hyperspectral imaging: A review on UAV-based sensors, data processing and applications for agriculture and forestry. *Remote Sens.* 2017, 9, 1110.
- Bemis, S.P.; Micklethwaite, S.; Turner, D.; James, M.R.; Akciz, S.; Thiele, S.T.; Bangash, H.A. Ground-based and UAV-Based photogrammetry: A multi-scale, high-resolution mapping tool for structural geology and paleoseismology. *J. Struct. Geol.* 2014, 69, 163–178.
- Dering, G.M.; Micklethwaite, S.; Thiele, S.T.; Vollgger, S.A.; Cruden, A.R. Review of drones, photogrammetry and emerging sensor technology for the study of dykes: Best practises and future potential. *J. Volcanol. Geotherm. Res.* 2019, 373, 148-166.
- Fairley, I.; Mendzil, A.; Togneri, M.; Reeve, D.E. The use of unmanned aerial systems to map intertidal sediment. *Remote Sens.* 2018, 10, 1918.
- Jackisch, R.; Lorenz, S.; Zimmermann, R.; Möckel, R.; Gloaguen, R. Drone-Borne Hyperspectral Monitoring of Acid Mine Drainage: An Example from the Sokolov Lignite District. *Remote Sens.* 2018, 10, 385.
- Padró, J.; Carabassa, V.; Balagué, J.; Brotons, L.; Alcañiz, J.M.; Pons, X. Science of the Total Environment Monitoring opencast mine restorations using Unmanned Aerial System (UAS) imagery. *Sci. Total Environ.* 2019, 657, 1602–1614.
- Lee, S.; Choi, Y. Reviews of unmanned aerial vehicle (drone) technology trends and its applications in the mining industry. *Geosystem Eng.* 2016, 19, 197–204.
- Ren, H.; Zhao, Y.; Xiao, W.; Hu, Z. A review of UAV monitoring in mining areas: current status and future perspectives. *Int. J. Coal Sci. Technol.* 2019, 6, 320–333.
- Booyesen, R.; Zimmermann, R.; Lorenz, S.; Gloaguen, R.; Nex, P.A.M.; Andreani, L.; Möckel, R. Towards multiscale and multisource remote sensing mineral exploration using RPAS: A case study in the Lofdal Carbonatite-Hosted REE Deposit, Namibia. *Remote Sens.* 2019, 11, 2500.
- Parshin, A.; Grebenkin, N.; Morozov, V.; Shikalenko, F. Research Note: First results of a low-altitude unmanned aircraft system gamma survey by comparison with the terrestrial and aerial gamma survey data. *Geophys. Prospect.* 2018, 66, 1433–1438.
- Malehmir, A.; Dynesius, L.; Paulusson, K.; Paulusson, A.; Johansson, H.; Bastani, M.; Wedmark, M. The potential of rotary-wing UAV-based magnetic surveys for mineral exploration : A case study from central Sweden. *The Leading Edge.* 2017, 7, 552–557.
- Cunningham, M.; Samson, C.; Wood, A.; Cook, I. Aeromagnetic Surveying with a Rotary-Wing Unmanned Aircraft System: A Case Study from a Zinc Deposit in Nash Creek, New Brunswick, Canada. *Pure Appl. Geophys.* 2018, 175, 3145-3158.
- Parvar, K.; Braun, A.; Layton-Matthews, D.; Burns, M. UAV magnetometry for chromite exploration in the Samail ophiolite sequence, Oman. *J. Unmanned Veh. Syst.* 2018, 6, 57–69.
- Walter, C.; Braun, A.; Fotopoulos, G. High-resolution unmanned aerial vehicle aeromagnetic surveys for mineral exploration targets. *Geophys. Prospect.* 2020, 68, 334–349.
- Sayab, M.; Aerden, D.; Paananen, M.; Saarela, P. Virtual structural analysis of Jokisivu open pit using “structure-from-motion” Unmanned Aerial Vehicles (UAV) photogrammetry: Implications for structurally-controlled gold deposits in Southwest Finland. *Remote Sens.* 2018, 10, 1296.

- Haldar, S. *Mineral Exploration Principles and Applications*; 2nd ed.; Elsevier: Amsterdam, the Netherlands, 2018; ISBN 978-0-12-814022-2.
- Marjoribanks, R. *Geological methods in mineral exploration and mining*; Springer Science & Business Media, Berlin, Germany, 2010; ISBN 9783540743705.
- Abedi, M.; Norouzi, G.H. Integration of various geophysical data with geological and geochemical data to determine additional drilling for copper exploration. *J. Appl. Geophys.* 2012, 83, 35–45.
- Slavinski, H.; Morris, B.; Ugalde, H.; Spicer, B.; Skulski, T.; Rogers, N. Integration of lithological, geophysical, and remote sensing information: A basis for remote predictive geological mapping of the Baie Verte Peninsula, Newfoundland. *Can. J. Remote Sens.* 2010, 2, 99–118.
- Beyer, F.; Jurasinski, G.; Couwenberg, J.; Grenzdörffer, G. Multisensor data to derive peatland vegetation communities using a fixed-wing unmanned aerial vehicle. *Int. J. Remote Sens.* 2019, 40, 9103–9125.
- Heincke, B.; Jackisch, R.; Saartenoja, A.; Salmirinne, H.; Rapp, S.; Zimmermann, R.; Pirttijärvi, M.; Vest Sörensen, E.; Gloaguen, R.; Ek, L.; et al. Developing multi-sensor drones for geological mapping and mineral exploration: setup and first results from the MULSEDRO project. *Geol. Surv. Denmark Greenl. Bull.* 2019, 43, 2–6.
- Van der Meer, F.D.; van der Werff, H.M.A.; van Ruitenbeek, F.J.A.; et al. Multi- and hyperspectral geologic remote sensing: A review. *Int. J. Appl. Earth Obs. Geoinf.* 2012, 14, 112–128.
- Jackisch, R.; Madriz, Y.; Zimmermann, R.; Pirttijärvi, M.; Saartenoja, A.; Heincke, B.H.; Salmirinne, H.; Kujasalo, J.-P.; Andreani, L.; Gloaguen, R. Drone-borne hyperspectral and magnetic data integration: Otanmäki Fe-Ti-V deposit in Finland. *Remote Sens.* 2019, 11, 2084.
- Puustinen, K. *Geology of the Siilinjärvi Carbonatite Complex, Eastern Finland*. Bull. la Commision Geol. Finlande 249, 1971, 1–43.
- Luoma, S.; Majaniemi, J.; Kaipainen, T.; Pasanen, A. GPR survey and field work summary in Siilinjärvi mine during July 2014. *Geol. Surv. Finland. Arch. Rep.* 2016, 1–39.
- Malehmir, A.; Heinonen, S.; Dehghannejad, M.; Heino, P.; Maries, G.; Karell, F.; Suikkanen, M.; Salo, A. Landstreamer seismics and physical property measurements in the siilinjärvi open-pit apatite (phosphate) mine, central Finland. *Geophysics* 2017, 82, B29–B48.
- Laakso, V. Testing of reflection seismic, GPR and magnetic methods for mineral exploration and mine planning at the Siilinjärvi phosphate mine site in Finland. Master's thesis, University of Helsinki, Helsinki, Finland, 2019.
- Da Col, F.; Papadopoulou, M.; Koivisto, E.; Sito, L.; Savolainen, M.; Socco, L.V. Application of surface-wave tomography to mineral exploration: a case study from Siilinjärvi, Finland. *Geophys. Prospect.* 2020, 68, 254–269.
- Pajunen, M.; Salo, A.; Suikkanen, M.; Ullgren, A.-K.; Oy, Y.S. Brittle structures in the south-western corner of the Särkijärvi open pit, Siilinjärvi carbonatite occurrence. *Geol. Surv. Finland. Arch. Rep.* 2017, 38, 1–38.
- Mattsson, H.B.; Högdahl, K.; Carlsson, M.; Malehmir, A. The role of mafic dykes in the petrogenesis of the Archean Siilinjärvi carbonatite complex, east-central Finland. *Lithos* 2019, 342–343, 468–479.

- Kauti, Tuomas, Skyttä, Pietari, Koivisto, Emilia, Savolainen, M. 3D modelling of the dolerite dyke network within the Siilinjärvi phosphate deposit. In Proceedings of the Visual3D conference – Visualization of 3D/4D models in geosciences, exploration and mining; Luleå, Sweden, 1–2 October 2019; pp. 33.
- Tichomirowa, M.; Grosche, G.; Götze, J.; Belyatsky, B. V.; Savva, E. V.; Keller, J.; Todt, W. The mineral isotope composition of two Precambrian carbonatite complexes from the Kola Alkaline Province - Alteration versus primary magmatic signatures. *Lithos* 2006, 91, 229–249.
- Carlsson, M., Eklund, O., Fröjdö, S., Savolainen, M. Petrographic and geochemical characterization of fenites in the northern part of the Siilinjärvi carbonatite-glimmerite complex, Central Finland. In Proceedings of the Geological Society of Finland, Abstracts of the 5th Finnish National Colloquium of Geosciences; Helsinki, Finland, 2019, pp. 29.
- Thiele, S.T.; Grose, L.; Samsu, A.; Mickelthwaite, S.; Vollgger, S.A.; Cruden, A.R. Rapid, semi-automatic fracture and contact mapping for point clouds, images and geophysical data. *Solid Earth* 2017, 8, 1241–1253.
- Nabighian, M.N. The Analytic Signal Of Two-Dimensional Magnetic Bodies With Polygonal Cross-Section: Its Properties And Use For Automated Anomaly Interpretation. *GEOPHYSICS* 1972, 37, 507–517.
- Hinze, W.J.; von Frese, R.R.B.; Saad, A.H. Gravity and Magnetic Exploration; Cambridge University Press: Cambridge, England, 2013; ISBN 9780511843129.
- Vacquier, V.; Steenland, N.C.; Henderson, R.G.; Zietz, I. Interpretation of Aeromagnetic Maps; Geological Society of America, United States, 1951; ISBN 9780813710471.
- Khaleghi, B.; Khamis, A.; Karray, F.O.; Razavi, S.N. Multisensor data fusion: A review of the state-of-the-art. *Inf. Fusion* 2013, 14, 28–44.
- Lorenz, S.; Seidel, P.; Ghamisi, P.; Zimmermann, R.; Tusa, L.; Khodadadzadeh, M.; Contreras, I.C.; Gloaguen, R. Multi-sensor spectral imaging of geological samples: A data fusion approach using spatio-spectral feature extraction. *Sensors* 2019, 19, 2787.
- Rasti, B.; Ulfarsson, M.O.; Sveinsson, J.R. Hyperspectral Feature Extraction Using Total Variation Component Analysis. *IEEE Trans. Geosci. Remote Sens.* 2016, 54, 6976–6985.
- Ghamisi, P.; Yokoya, N.; Li, J.; Liao, W.; Liu, S.; Plaza, J.; Rasti, B.; Plaza, A. Advances in Hyperspectral Image and Signal Processing: A Comprehensive Overview of the State of the Art. *IEEE Geosci. Remote Sens. Mag.* 2017, 5, 37–78.
- Chang, C.C.; Lin, C.J. LIBSVM: A Library for support vector machines. *ACM Trans. Intell. Syst. Technol.* 2011, 2, 27.
- Almqvist, B.; Högdah, K.; Karell, F.; Malehmir, A. Anisotropy of magnetic susceptibility (AMS) in the Siilinjärvi carbonatite complex, eastern Finland. In Proceedings of the Geophysical Research Abstracts; EGU General Assembly: Vienna, Austria, 23–28 April 2017, pp. 9887.
- James, M.R.; Robson, S.; D’Oleire-Oltmanns, S.; Niethammer, U. Optimising UAV topographic surveys processed with structure-from-motion: Ground control quality, quantity and bundle adjustment. *Geomorphology* 2016, 280, 51–66.
- James, M.R.; Chandler, J.H.; Eltner, A.; Fraser, C.; Miller, P.E.; Mills, J.P.; Noble, T.; Robson, S.; Lane, S.N. Guidelines on the use of structure-from-motion photogrammetry in geomorphic research. *Earth Surf. Process. Landforms* 2019, 2084, 2081–2084.

- Jakob, S.; Zimmermann, R.; Gloaguen, R. The Need for Accurate Geometric and Radiometric Corrections of Drone-Borne Hyperspectral Data for Mineral Exploration: MEPHySTo-A Toolbox for Pre-Processing Drone-Borne Hyperspectral Data. *Remote Sens.* 2017, 9, 88.
- Karpouzli, E.; Malthus, T. The empirical line method for the atmospheric correction of IKONOS imagery. *Int. J. Remote Sens.* 2003, 5, 1143–1150.
- Gavazzi, B.; Le Maire, P.; Mercier de Lépinay, J.; Calou, P.; Munsch, M. Fluxgate three-component magnetometers for cost-effective ground, UAV and airborne magnetic surveys for industrial and academic geoscience applications and comparison with current industrial standards through case studies. *Geomech. Energy Environ.* 2019, 20, 100117.
- Pirttijärvi, M. Numerical modeling and inversion of geophysical electromagnetic measurements using a thin plate model. Ph.D. dissertation, University of Oulu, Oulu, Finland, 2003.
- Austin, J.R.; Schmidt, P.W.; Foss, C.A. Magnetic modeling of iron oxide copper-gold mineralization constrained by 3D multiscale integration of petrophysical and geochemical data: Cloncurry District, Australia. *Interpretation* 2013, 1, T63–T84.
- Tichomirowa, M.; Whitehouse, M.J.; Gerdes, A.; Götze, J.; Schulz, B.; Belyatsky, B. V. Different zircon recrystallization types in carbonatites caused by magma mixing: Evidence from U-Pb dating, trace element and isotope composition (Hf and O) of zircons from two Precambrian carbonatites from Fennoscandia. *Chem. Geol.* 2013, 353, 173–198.
- Poutiainen, M. Fluids in the Siilinjärvi carbonatite complex, eastern Finland: fluid inclusion evidence for the formation conditions of zircon and apatite. *Bull. Geol. Soc. Finl.* 1995, 67, 3-18.
- O'Brien, H.; Heilimo, E.; Heino, P. The Archean Siilinjärvi Carbonatite Complex. *Miner. Depos. Finl.* 2015, 1, 327–343.
- Salo, A. Geology of the Jaakonlampi area in the Siilinjärvi carbonatite complex. Bachelor's Thesis, University of Oulu, Oulu, Finland, 2016.
- Gaffey, S.J. Reflectance spectroscopy in the visible and near-infrared (0.35- 2.55 micrometers): applications in carbonate petrology. *Geology* 1985, 4, 270-273.
- Neave, D.A.; Black, M.; Riley, T.R.; Gibson, S.A.; Ferrier, G.; Wall, F.; Broom-Fendley, S. On the feasibility of imaging carbonatite-hosted rare earth element deposits using remote sensing. *Econ. Geol.* 2016, 111, 641–665.
- Hunt, G.R. Spectral signatures of particulate minerals in the visible and near infrared. *Geophysics* 1977, 42, 501–513.
- Clark, R.N. Spectroscopy of rocks and minerals, and principles of spectroscopy. *Man. Remote Sens.* 1999, 3, 2–2.
- Hunt, G.R.; Ashley, R.P. Spectra of altered rocks in the visible and near infrared. *Econ. Geol.* 1979, 74, 1613–1629.
- Airo, M.-L. Aerogeophysics in Finland 1972–2004: Methods, System Characteristics and Applications. *Spec. Pap. Geol. Surv. Finl.* 2005, 39, 197.
- Burkin, J.N.; Lindsay, M.D.; Occhipinti, S.A.; Holden, E.J. Incorporating conceptual and interpretation uncertainty to mineral prospectivity modelling. *Geosci. Front.* 2019, 10, 1383–1396.
- Cardozo, N.; Allmendinger, R.W. Spherical projections with OSXStereonet. *Comput. Geosci.* 2013, 51, 193-205

- Jackisch, R. Drone-based surveys of mineral deposits. *Nat. Rev. Earth Environ.* 2020, 1, 187.
- Rowan, L.C.; Kingston, M.J.; Crowley, J.K. Spectral reflectance of carbonatites and related alkalic igneous rocks: selected samples from four North American localities. *Econ. Geol.* 1986, 81, 857–871.
- Rowan, L.C.; Mars, J.C. Lithologic mapping in the Mountain Pass, California area using Advanced Spaceborne Thermal Emission and Reflection Radiometer (ASTER) data. *Remote Sens. Environ.* 2003, 84, 350–366.
- Kirsch, M.; Lorenz, S.; Zimmermann, R.; Andreani, L.; Tusa, L.; Pospiech, S.; Jackisch, R.; Khodadadzadeh, M.; Ghamisi, P.; Unger, G.; et al. Hyperspectral outcrop models for palaeoseismic studies. *Photogramm. Rec.* 2019, 34, 385–407.
- Valencia, J.; Battulwar, R.; Naghadehi, M.Z.; Sattarvand, J. Enhancement of explosive energy distribution using uavs and machine learning. In *Proceedings of the Mining Goes Digital - Proceedings of the 39th international symposium on Application of Computers and Operations Research in the Mineral Industry*, Leiden, The Netherlands, 2019.
- Heilimo, E.; Brien, H.O.; Heino, P. Constraints on the formation of the Archean Siilinjärvi carbonatite-glimmerite complex, Fennoscandian shield. 2015. Available online: <https://bit.ly/339EGyI> (accessed on 2 June 2020)
- Le Bas, M.J. Nephelinites and carbonatites. *Geol. Soc. Spec. Publ.* 1987, 30, 53–83.
- Borradaile, G.J.; Werner, T. Magnetic anisotropy of some phyllosilicates. *Tectonophysics* 1994, 235, 223–248.



Chapter 5 – The final field test on Disko Island

The following chapter presents the submitted version¹¹ that is now published as a primary research article in the peer-reviewed journal *Solid Earth*¹². Results of the concluding field campaign on Disko Island in West Greenland are presented (Case study C). The operation was prepared thoroughly by GEUS and supported by Bluejay mining plc with infrastructure and data. Field work was done autonomously and relied on field generators to recharge UAS batteries and technical equipment for a fortnight of surveying. The drones proved their merit under these remote and precarious conditions and proved that the technology is fully capable to obtain valuable geoscientific data.

¹¹ **Jackisch, R., Heincke, B. H., Zimmermann, R., Sørensen, E. V., Pirttijärvi, M., Kirsch, M., Salmirinne, H., Lode, S., Kuronen, U., & Gloaguen, R. (2021).** Drone-based magnetic and multispectral surveys to develop a 3D model for mineral exploration at Qullissat, Disko Island, Greenland. *Solid Earth Discussions*, 2021, 1–51. <https://doi.org/10.5194/se-2021-133>.

¹² **Jackisch, R., Heincke, B. H., Zimmermann, R., Sørensen, E. V., Pirttijärvi, M., Kirsch, M., Salmirinne, H., Lode, S., Kuronen, U., & Gloaguen, R. (2022).** Drone-based magnetic and multispectral surveys to develop a 3D model for mineral exploration at Qullissat, Disko Island, Greenland. *Solid Earth*, 13(4), 793–825. <https://doi.org/10.5194/se-13-793-2022>.

UAS-based surveying and 3D modelling for exploration of the Qullissat area on Disko Island, West Greenland.

R. Jackisch¹, B. Heincke², R. Zimmermann¹, H. Salmirinne³, M. Pirttijärvi⁴, M. Kirsch¹, E. V. Sørensen², S. Lode⁵, U. Kuronen⁶, R. Gloaguen¹

¹Helmholtz-Zentrum Dresden-Rossendorf, Helmholtz Institute Freiberg for Resource Technology, Division “Exploration Technology”, Chemnitz Str. 40, 09599 Freiberg, Germany

²Geological Survey of Denmark and Greenland, Øster Voldgade 10, 1350 København, Denmark

³Geological Survey of Finland, Lähteentie 2, 96400 Rovaniemi, Finland

⁴Radai Oy, Teknologiantie 18, 90470 Oulu, Finland

⁵Norwegian University of Science and Technology, Trondheim, 7031, Norway

⁶Bluejay Mining PLC, London, W1F0DU, England

Keywords: UAS; magnetics; multispectral; mineral exploration; iron minerals; sulphides, Greenland, native iron

Abstract

Mineral exploration in the West Greenland flood basalt province is attractive because of its resemblance to the magmatic sulphide-rich deposit in the Russian Norilsk region, but it is challenged by rugged topography and partly poor exposure for relevant geologic formations. On northern Disko Island, previous exploration efforts have identified rare native iron occurrences and a high potential for Ni-Cu-Co-PGE-Au mineralization. However, Quaternary landslide activity has obliterated rock exposure at many places at lower elevations. To augment prospecting field work under these challenging conditions, we acquire high-resolution magnetic and optical remote sensing data using drones in the Qullissat area. From the data, we generate a detailed 3D model of a mineralized basalt unit, belonging to the Asuk Member (Mb) of the Palaeocene Vaigat formation.

A wide range of legacy data and newly acquired geo- and petrophysical, as well as geochemical-mineralogical measurements form the basis of an integrated geological interpretation of the unoccupied aerial system (UAS) surveys. In this context, magnetic data aims to define the location and the shape of the buried magmatic body, and to estimate if its magnetic properties are indicative for mineralization. High-resolution UAS-based multispectral orthomosaics are used to identify surficial iron staining, which serve as a proxy for outcropping sulphide mineralization. In addition, high-resolution UAS-based digital surface models are created for geomorphological characterisation of the landscape to accurately reveal landslide features.

UAS-based magnetic data suggests that the targeted magmatic unit is characterized by a pattern of distinct positive and negative magnetic anomalies. We apply a 3D magnetization vector inversion model (MVI) on the UAS-based magnetic data to estimate the magnetic properties and shape of the magmatic body. By means of using constraints in the inversion, (1) optical

UAS-based data and legacy drill cores are used to assign significant magnetic properties to areas that are associated with the mineralized Asuk Mb, and (2) the Earth's magnetic and the paleomagnetic field directions are used to evaluate the general magnetization direction in the magmatic units.

Our results indicate that the geometry of the mineralized target can be estimated as a horizontal sheet of constant thickness, and that the magnetization of the unit has a strong remanent component formed during a period of Earth's magnetic field reversal. The magnetization values obtained in the MVI are in a similar range as the measured ones from a drillcore intersecting the targeted unit. Both the magnetics and topography confirm that parts of the target unit were displaced by landslides. We identified several fully detached and presumably rotated blocks in the obtained model. The model highlights magnetic anomalies that correspond to zones of mineralization and is used to identify outcrops for sampling. Our study demonstrates the potential and efficiency of using multi-sensor high-resolution UAS data to constrain the geometry of partially exposed geological units and assist exploration targeting in difficult, poorly exposed terrain.

5.1 Introduction

Volcanic rocks of Tertiary age in Central-West Greenland exposed on e.g., Disko-Nuussuaq form part of the North Atlantic Igneous Province (Larsen et al., 2016). It is assumed that the Disko-Nuussuaq area hosts major Ni-Cu-Co-PGE deposits and, in this respect, is regarded as analogous to the Noril'sk-Talnakh Ni-Cu district in the Siberian trap basalt (Lightfoot et al., 1997; Keays and Lightfoot, 2007). Mineral exploration in the onshore parts of the basin at Disko Island and the Nuussuaq Peninsula dates back more than half a century (Pauly, 1958; Bird and Weathers, 1977; Ulff-Møller, 1990) and has regained traction recently, with 12 active mineral exploration licences that cover an area of ~9,700 km² on Disko-Nuussuaq as of April 2021 (greenmin.gl, last accessed 02.06.2021).

Large parts of the Northern Disko region provide good outcrop conditions at higher altitude, whereas the lower slopes near the coast are covered by debris from Quaternary rock falls, landslides, periglacial deposits and vegetated solifluction lobes (Pedersen et al., 2017). This complicates ground-based mineral exploration-related mapping efforts which is furthermore complicated by rugged topography and the Arctic climate.

Thus, high-resolution, multi-parameter three-dimensional models are highly useful to resolve detailed structures and develop exploration models. This has traditionally been achieved by combining results from various exploration techniques. Systematic airborne geophysical and

remote sensing surveying has been used for decades to create the uniform physical data basis for such models.

Recent development of small-scaled UAS equipped with geophysical e.g., magnetic sensors (Gavazzi et al., 2016; Malehmir et al., 2017; Parshin et al., 2018; Walter et al., 2020) as well as optical sensors, e.g., multi- and hyperspectral sensors (Booyesen et al., 2019), now makes it possible to acquire data inexpensively and with high resolution. Magnetic data are suited to map surface and subsurface structures (Le Maire et al., 2020) and reveal magnetized rock units, which give hints for the mineral composition and can indicate sulphides or iron-oxides (Gunn and Dentith, 1997). While high-resolution RGB and multispectral images can be used to detect and distinguish small-scaled mineralization traces which can guide ground teams to promising sampling areas. Ground based measurements and rock sampling are typically carried out to establish and validate relationships between physical property distributions obtained from indirect airborne and drone-borne surveying methods and the on-site mineralogy, lithology, and structures.

Geomorphological processes, e.g., the impact of landslides are often incorporated and considered in the geological interpretation. Tracing slid mineralized boulders (boulder hunting) is regarded as an effective exploration tool (Plouffe et al., 2011), and most viable when abundant bedrock geology, soil geochemistry, geochronology and geophysical methods are integrated towards in a joint mineral vectoring. In the Disko-Nuussuaq region, landslide mapping has received increased attention lately, highlighting the Nuussuaq basin as a risk area (Dahl-Jensen et al., 2004, p.; Svennevig, 2019). Landslide descriptors including scarps are hard to identify because their appearance is determined by fracture patterns and foliation. Often they are eroded or overprinted by continuing mass movements. Large, rotated blocks occur at coastal zones or are partially buried by talus. Examples of periglacial mass movements at Disko are massive rock glaciers derived by either ice or talus, in particular outside the ice-covered central island area (Humlum, 1988).

In this study we focus on an area near Qullissat on the Northern shore of Disko Island (Figure 5.1). This area is attractive for mineral exploration, where carbonaceous sandstones, shale beds and coal seams were intruded by a tabular magmatic body that is rich in both Ni-Cu-Co platinum group elements and known for native iron. It was initially explored in the early 1990s, and we have access to a general exploration framework based on the legacy mineral exploration, whose data were used for the validation of our measurements.

Although legacy exploration included several geophysical investigations such as airborne magnetic and EM surveys and six drill holes intersecting the magmatic body (Olshefsky, 1992),

the data coverage of the geophysical surveys was too coarse to develop an appropriate 3D model for the magmatic body. To establish a proper model is further challenged by the limited outcrop situation, the undulating terrain making parts difficult accessible and mass movements affecting major parts of this area.

Accounting for these conditions, we chose a surveying strategy based on drone surveys and several sensors. Magnetic measurements were carried out rapidly with a fixed-wing UAS (Jackisch et al., 2020) at low flight altitudes and with dense line spacing to get high-resolution magnetic attribute maps. In addition, we conducted a high-resolution UAS-based multispectral and photogrammetry survey intended to create a precise elevation model and to systematically identify and map outcrops, surficial blocks and locations with increased iron content as mineralization vectors. UAS-based data were supplemented with ground data from two detailed magnetic surveys, spectroradiometry and magnetic susceptibility measurements. Petrophysical measurements from one legacy drill hole in the area are incorporated to relate observed anomalies with lithology and mineralogical observations.

We link topography, surface mineralogy and the magnetic data with each other to provide both direct (e.g., map sulphide bodies by magnetic and spectroscopic measurements) and indirect (e.g., find structures such as veins and fractures or displaced iron-bearing boulders) information about potentially sulphide-enriched targets. In particular, we use the magnetic data in a 3D magnetization vector inversion (MVI), where available other information about the shape of the body and its main magnetization directions are incorporated. We use those constraints to obtain a realistic estimate of the intrusion shape and its magnetization distribution. Finally, results from all UAS and ground-based data are combined in a joint interpretation of the Qullissat area. The interpretation aims mainly (1) to better limit and define potential exploration target areas, and in addition, (2) to determine the impact of landslide processes onto the targeted magmatic body.

5.1.1 Regional geological settings

The volcano-sedimentary Nuussuaq Basin formed as a rift basin in the Early Cretaceous during rifting of the Labrador Sea-Davis Strait area (Henderson et al., 1981; Chalmers et al., 1999; Dam et al., 2009). Because of the Neogene uplift (Japsen et al., 2005; Bonow et al., 2006) parts of the basin are exposed in the onshore areas of Disko Island and Nuussuaq Peninsula in central West Greenland now. The area is made up of Cretaceous to Paleocene siliciclastic sediments of the Nuussuaq Group (Dam et al., 2009 and references therein) and Palaeogene volcanic rocks of the West Greenland Basalt Group (Pedersen et al., 2017 and references therein; Pedersen et

al., 2018 and references therein). On a regional scale, sediments were deposited in a deltaic environment in the eastern part of the basin (sandstones interbedded with mudstones) while deep marine sediments were deposited in the western part of the basin. During Late Cretaceous to Early Paleocene rifting, sediment blocks were rotated and eroded before the onset of volcanism (Chalmers et al., 1999; Dam et al., 2009).

The volcanism started in a submarine environment within the actively subsiding Nuussuaq Basin. Early eruptive products were hyaloclastites extruded from eruption centres located to the NW of Disko and Nuussuaq. As volcanics built up on the seafloor, volcanic islands were formed and with time volcanism became dominantly subaerial.

The Paleocene volcanic succession is divided into a lower (Vaigat Fm) and an upper formation (Maligât Fm) which makes up the bulk of the volcanic rocks exposed on Disko and Nuussuaq (Figure 5.1). The early volcanism of the Vaigat Fm was dominated by picritic rocks that erupted in three volcanic cycles (Larsen and Pedersen, 2009). The picritic rocks formed from melts generated through partial melting in the asthenosphere. The melts subsequently ascended through the crust and erupted at the surface without much interaction while traversing from source to surface.

Throughout the volcanic pile intervals of crustally contaminated siliceous basalt to magnesian andesite occurs (Dam et al., 2009; Pedersen et al., 2017, 2018) indicating that primary magmas at certain times got contaminated in relatively high-level magma chambers. This is evidenced by the occurrence of partly digested shale and sandstone xenoliths brought up by the volcanic rocks (Pedersen, 1977, 1977, 1985; Ulff-Møller, 1977).

5.1.2 Mineral potential

The mineral potential of the West Greenland Basalt Province has been speculated (Rosa et al., 2013) to be equivalent with the Noril'sk-Talnakh region, with the potential for major Cu, Ni, Co and PGE deposits (Keays and Lightfoot, 2007). The province has many of the metallogenic characteristics of the Noril'sk region. Key similarities are a high proportion of high temperature picritic lavas and significant volumes of sediment-contaminated basalts. When primary magmas passed through the sediments en-route to the surface, they reacted at various locations with the lower-crustal sedimentary successions of the Nuussuaq Fm, modifying the chemical composition of the magma. The globally rare native iron is observed at several places across Disko and the Nuussuaq peninsula. It is suggested that it formed by the reaction of iron present in the magma with carbonaceous sediments (e.g., marine mudstone, deltaic shales, coal seams) resulting in the precipitation of nickel-ferrous minerals and metallic iron (Pedersen et al., 2017).

Under similar conditions, contamination from sulphur-rich sediments is also responsible for the precipitation of Ni and Cu from immiscible sulphide droplets within the silicate magma that are scavenged and deposited (Sørensen et al., 2013). In a dynamic open magmatic system, where a large volume of mafic nickel-rich melt streams through dykes and sills, huge Ni-Cu-PGE deposits (conduit type nickel deposit) can be formed.

A common intrusive geometry found in large igneous provinces (LIPs) are extensive networks of tabular or saucer-shaped sills that are linked by dykes, which interact with the sedimentary basin (Barnes et al., 2016). Our main target is a flat lying magmatic body that is located near Qullissat about 1.5 km SE of a well-described native-iron bearing Asuk location (Pedersen, 1985). It was first described as the Qullissat sill (Olshefsky and Jerome, 1993; Pedersen et al., 2017) and it is derived as a higher part of the volcanic Vaigat Fm (Asuk Member), but is more than 10 km from any similar volcanic rocks. It is assumed that rock slides along the steep-slope surface (Pedersen et al., 2017) have separated mineralized blocks from the targeted magmatic body.

The presence of sulphide, graphite and native iron in the intrusion (Olshefsky and Jerome, 1993), which are all considered to be conductive, complicates an interpretation that is largely based on electromagnetic data. Detailed magnetic data can provide more insight into which components are mainly responsible for the conductivity anomalies because graphite is non-magnetic, but sulphide related minerals often show a magnetic response (Gunn and Dentith, 1997) and native iron is considered to be highly ferromagnetic (Nagata et al., 1970).

5.1.3 Geochronology and magnetic polarity of basalt members

Previous paleomagnetic investigations of volcanic strata on Disko and Nuussuaq (Deutsch and Kristjansson, 1974; Athavale and Sharma, 1975; Riisager and Abrahamsen, 1999) showed that a geomagnetic pole reversal took place at ~60.9 Ma during magnetochron C27n–C26r (Cande and Kent, 1995). About two-thirds of the lower–middle Vaigat Fm are normally polarized, but its upper third and the overlying Maligât Fm are reversely polarized.

Of importance to this paper is the Asuk Mb which formed after the C27n–C26 magnetic pole reversal (Pedersen et al., 2017). Nearby field measurements of the remanent magnetic field from the Asuk Mb were located ~25 km NW of Qullissat at a sampling altitude of 365–1450 m. Field declinations (D) between 123–154° and an inclination (I) of about -73° were reported (Athavale and Sharma, 1975). Remanent magnetic measurements were also reported from rocks (comparable in age to the Asuk Mb) of the Naujánguit Member at Qunnilik on southern

Nuussuaq (Riisager and Abrahamsen, 1999, 2000) about 60 km northwest of Qullissat, where a reverse polarization with $I = -80.7^\circ$ and $D = 228.1^\circ$ was measured.

5.1.4 Qullissat study area

The study area is located near the abandoned coal mining town called Qullissat (70.0844 N, 53.0097 W) on the Northern coast of Disko island (Figure 5.1). The study area is ~6 km long and ~3 km wide and reaches from sea level up to the steep Inussuk cliff (~600–700 m asl; Figure 5.1b). The lower parts of the study area (up to 300 m above sea level [asl]) are generally poorly exposed, debris and vegetation covered and have a relatively high abundance of landslipped strata. The geology of the area (Figure 5.1c) is described on the geological map covering the area (Pedersen et al., 2013) and in more detail, in a photogrammetric cross-section covering the area (Pedersen et al., 2017, Fig. 161, p. 180).

The lower coastal cliffs (< 100 m asl) are made up of Cretaceous sandstones with shale beds and coal seams of the Atane Fm. Most of the outcrops up to 400 m asl, are described in Pedersen et al., (2017) as native-iron bearing and several of them are displaced by landslide movements. They are assigned to the Asuk Member of the Vaigat Fm and are assumed to be part of a mineralized tabular magmatic body that is intersected by drill holes (see Section 5.3.5) being located at slightly higher elevation levels. Originally, the body was described as a sill (Pedersen et al., 2017), but very recent investigations of drill cores suggest that it is extrusively formed and may be an invasive lava flow (pers. communication with Asger Pedersen, GEUS, 2020). Above the iron-bearing outcrops, sedimentary rocks (sandstone and mudstone) are observed at a few locations that are of uncertain age, but have been tentatively correlated with the Assoq Member of the Atanikerluk Fm (Pedersen et al., 2017).

In the area immediately below the cliff faces (< 400 m asl), the Vaigat Fm is overlain by lavas of the lower Rinks Dal Member of the Maligât Fm that can be followed on the complete study area from the NW to the SE. The lowermost Rinks Dal Fm is associated with fully subaqueous lava flows consisting of breccias and hyaloclastites (Pedersen et al., 2018).

In the upper part of the study area (> 600–700 m asl) volcanic rocks of the Maligât Fm (Skarvefjeld Unit) form Inussuk cliff that looms above the Qullissat area. Towards the uppermost parts of the Inussuk Cliff subaerial lavas transition into foreset-bedded hyaloclastite before becoming entirely subaerial (Pedersen et al., 2018). Most of the high-plateau above 1,500 m are covered by ice and snow.

The location of the feeder structure or the eruption centres for the Asuk Mb on Disko are assumed to be located between Asuk and the Kuungannguaq valley about 30–50 km NW of our

study area (Pedersen et al., 2017). The andesitic magma of the Asuk Mb is supposed to be highly viscous and presumably did not spread far from its eruption site. It was shown in geochemical analysis that close to their feeder systems, some of the Asuk lavas are composite flows, with higher content of SiO₂ and later pulses of magnesian andesite and the presence of xenoliths and xenocrysts from mudstones and sandstones are wide-spread (Pedersen et al., 2017).

In some rocks there is a scarcity in Ti-Fe-oxides and an increase of iron-sulphides. At Qullissat, in particular graphite fragments are reported in the tabular body of the Asuk Mb (Olshefsky et al., 1995). The formation of graphite is explained by contact metamorphism of carbon from the carbonaceous sediments and coal seams, by heat production of the intrusions. Most lava flows are horizontally bedded and dip gently with $< 3^{\circ}$ in south-east direction (Pedersen et al., 2017).

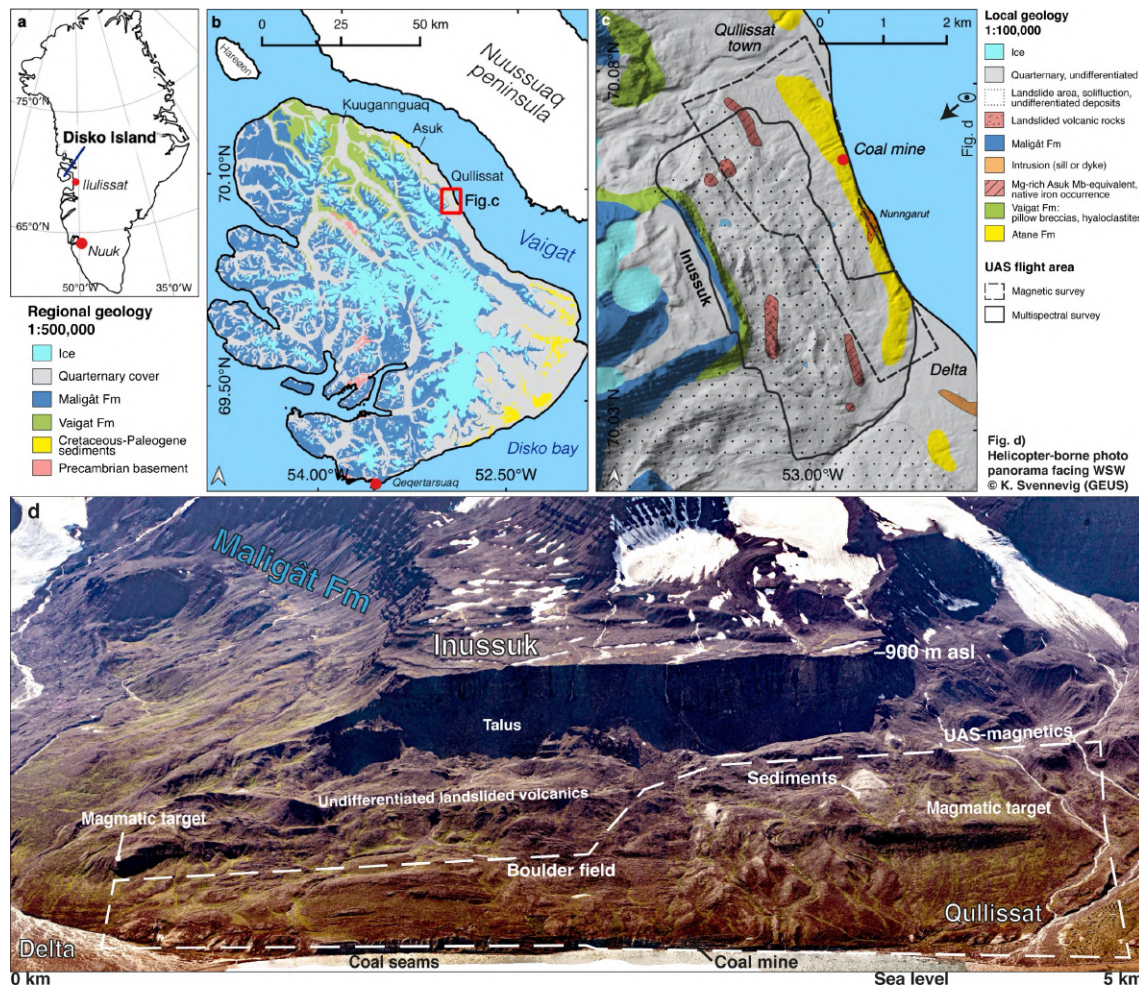


Figure 5.1 General overview of the study area on northern Disko in West Greenland. (a) The Qullissat study area is located about 125 km NW of the village Ilulissat. (b) The regional geologic map from Disko Island shows the Palaeogene basaltic Maligât and Vaigat formations, which are bedded in a Cretaceous sediment basin and are incised deeply by glacial erosion. (c) A local geologic map from our survey site around Qullissat is derived from the official geological map (Pedersen et al., 2013). Dashed and continuous lines indicate the areas of the UAS optical remote sensing and magnetic surveys, respectively. (d) Oblique overview established from stitched helicopter-based RGB photographs. The horizontal distance at coast level measures ~5 km and the Inussuk plateau is located at 900 m asl.

5.1.5 Data from former exploration

Multiple geoscientific mineral exploration related datasets have been acquired in the area around Qullissat over the last decades (Olshefsky, 1992; Olshefsky and Jerome, 1993, 1994; Olshefsky et al., 1995; Data et al., 2005). Six drill holes were drilled (Olshefsky et al., 1995) by the exploration company Falconbridge Greenland A/S in 1993 and 1994 (see locations in Figure 5.3b). Apart from one, all drill holes were located in the western part of the investigation area at altitudes of ~300–360 m asl and had depths ranging from 58–270 m. Drill holes FP93-4-1, FP94-4-2 to FP94-4-3 and FP94-4-6 only intersect the top of the mineralized magmatic body, whereas only drill hole FP94-4-5 intersect both the top and base of the magmatic body. Drill hole FP-94-4-6 (max depth: 143 m) was located at the east at low elevation level close to

coastline and did only intersect sedimentary units including coal seams and carbonaceous siltstones. Magnetic susceptibilities were measured in borehole FP94-4-5 at 0.1 m intervals along cores (Olshefsky and Jerome, 1994).

Former geophysical data at Qullissat comprised both ground-based surveys (e.g., two crossing magnetotelluric profiles (Data et al., 2005) and magnetic surveys (Olshefsky and Jerome, 1994; survey 4A in Figure 5.3c) and a local airborne survey, where both time-domain EM and magnetic (Fig. 4b) data were acquired (Olshefsky and Jerome, 1993). In addition, the Qullissat area was covered by the regional AEROMAG1997 survey (Thorning and Stemp, 1998). However, its line spacing (2 km) was too coarse to be of use in this (Figure 5.3a). Also, the local airborne survey had rather coarse line spacing of ~200–500 m and significant flight heights of ~150 m above ground level (agl) and provided only limited resolution of its magnetic data at the given outcrop scale that meant the magnetic properties of the magmatic body could not be mapped in detail (Figure 5.3b). Though, two mapped conductive anomalies from the EM measurements are potential exploration targets.

5.2 *Methods and materials*

5.2.1 Acquisition and processing of UAS-based magnetic data

The local magnetic field was measured with a digital three-component fluxgate magnetometer located in the tail boom of a fixed-wing UAS (type: Albatros VT from Radai Ltd, Oulu, Finland). During surveying, the three components of the magnetic field were stored together with GPS time, position (latitude, longitude, and altitude) and barometric pressure by a data logger (see Appendix F1). However, because the primary data logger was lost during field work, we used a backup device that did not record the UAS orientation (pitch, roll, yaw). Thus, the individual magnetic components could only be used to compute the total intensity of the magnetic field. We estimated the horizontal GPS accuracy positioning to about ± 1 m during flight. After UAS take-off, flights were controlled by an autopilot that followed predefined waypoint paths. A local magnetic base station was set up in the field during measurements to correct for the diurnal field variation in the processing.

The total surface coverage of the survey area at Qullissat was ~6.8 km², and it was realized in nine flights, which were acquired with a mean speed of 58 km/h resulting in a mean inline point sampling of 2.6 m. The separation between the SE-NW directed flight lines was 40 m (line azimuth is about 27° anticlockwise from north, Figure 5.3d). The total length of the flight lines was ~220 km and total flight times were ~3.7 h. The nominal flight height along the path was defined as 40 m above a terrain topography, which was taken from a digital elevation model

(DEM) provided by the Danish Agency for Data Supply and Efficiency (<https://dataforsyningen.dk/data/2842>, last accessed 31.05.2021). However, the real flight altitudes above ground level (agl) were larger (mean 70 m agl) because the topographic variations were significant in the survey areas and the flight path software added a safety margin for altitudes above the ground to avoid large pitch angles at steep slopes.

After basic data processing, an equivalent layer modelling (ELM, see Pirttijärvi, 2003) was applied. Here, we computed the total magnetic intensity on a regular grid (20×20 m) and at a constant altitude of 40 m above the surface. More details about the ELM method and other processing steps are provided Appendix F1. The processed magnetic anomaly map is presented in Figure 5.3d. The noise level in the final magnetic data was estimated from the low-pass filtered corrected data using a standard deviation (SD) of the 4th difference (Reeves, 2006), which ranges between ~15–85 nT in the raw magnetic data. For the low-pass filtered corrected magnetic data, the corresponding SD is ~3–6 nT.

5.2.2 Acquisition and processing of fixed-wing UAS-based multispectral and photogrammetric data

Multispectral data was acquired using a senseFly ebeePlus drone featuring a Parrot Sequoia multispectral (MSI) camera (1.2 Mpixel) with 4-channels in the VNIR spectral range. Spectral channels are centred at 550 nm (green), 660 nm (red), 735 nm (red edge) and 790 nm (NIR), respectively. The bands are sensitive to chlorophyll related absorptions but also suited for the detection of iron-related spectral features (Jackisch et al., 2019; Flores et al., 2021). For example, with a ratio of (735/790 nm) or (660/550 nm), the iron absorption associated with Fe-alteration minerals can be determined and mapped. Additional RGB images were acquired with an off-the-shelf DJI Mavic

A total number of 11 eBee MSI flights were conducted totalling 308 line km and covering an area of 12.9 km². The flight lines were set parallel to the regional slope with terrain following and with a fore- and side-overlap of 80 % and 60 % respectively. Further details are found in Appendix F2.

The images were processed employing SfM-MVS photogrammetry using Agisoft Metashape following the protocols set by various authors. The resulting merged colour-infrared (CIR) orthophoto (Figure 5.2a) and the digital surface model (DSM, Figure 5.2b) share large parts of the same surface area with the UAS magnetic survey (Figure 5.1c). For mapping and logistical reasons, we decided to cover only the topographically gentler shoreline area with magnetics including the target magmatic body.

The multispectral data were gathered to reveal surface mineral information from spectral absorptions, but also structural features as e.g., landslide features visible in the associated DSMs. Slope and topographic position index displays (TPI after Weiss, 2001) are useful tools to analyse landforms and enhance morphological forms, for example valleys, slopes, dikes, and crests. A TPI image is used to enhance the image contrast of a UAS-based slope map (Figure 5.8b) and a satellite colour-composite (Figure 5.13).

The image mosaics contain cast shadows and strongly varying illumination conditions, therefore under-illuminated parts were masked. Required topographic corrections of multispectral (MS) mosaics were performed using the MEPHySTo software (Jakob et al., 2017) and algorithms therein. The classic vegetation index (Kriegler et al., 1969) and a band ratio (band 3 by band 4, ‘iron ratio’) was computed and smoothed with a median filter (kernel size of 5×5 pixel) to reduce noise. To increase the interpretation fertility of the iron band ratio, we applied a contour algorithm (GDAL/OGR contributors, 2021) on the ratio-raster image to generate a vectorized file at 0.1 ratio interval steps. This procedure enables a qualitative interpretation aided by smoothed pixel features.

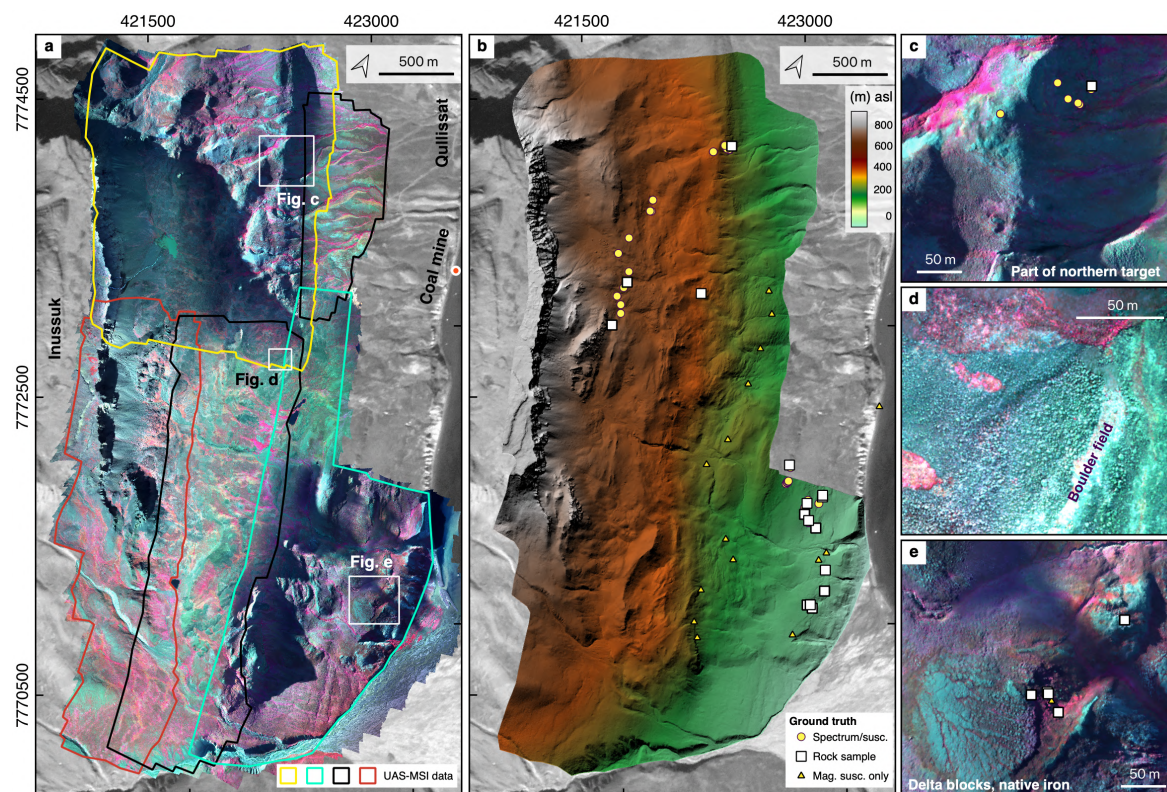


Figure 5.2 Primary data of the multispectral UAS-based surveys after basic processing. (a) Multispectral mosaic at ~20 cm GSD in false colour RGB bands 3, 2, 1. The different polygons outline the survey areas of individual flights. (b) DSM having a ~36 cm GSD. Locations of collected ground truth data are indicated with symbols. Inset maps enhance view resolution of areas that were ground-sampled during the study, such as (c) an outcrop associated to the northern part of the target magmatic (d), the central boulder field (e) and outcropping landslipped volcanic rocks in the southern part.

5.2.3 Ground-based and laboratory measurements

We carried out a number of ground-based measurements as smaller-scaled ground-based magnetic surveys, susceptibility, and spectroscopy measurements as well as lab analysis on rock samples from this area. In addition, magnetic and electric properties were measured on samples of the drill core from FP94-4-5.

5.2.4 Ground magnetic surveys

Ground based magnetic measurements were done at two different areas at Qullissat (surveys 4B and 4C in Figure 5.3c) with a GEM Systems GSM-19 Overhauser magnetometer (GEM system, Canada) having a resolution of 0.01 nT. Measures of the total magnetic field were made with a mean inline sampling of 1.12 m and 1.49 m and line spacings of 50 and 100 m, for the northern and southern survey, respectively. Time and positions were obtained by an integrated GPS receiver and were internally stored together with the magnetic data. A standard data processing for ground-based magnetic measurements was performed with Geosoft Oasis Montaj from Seequent. Diurnal variations in the total magnetic field were removed for all ground magnetic measurements using data from an observatory at Qeqertarsuaq located ~90 km away from the survey area at southern Disko Island.

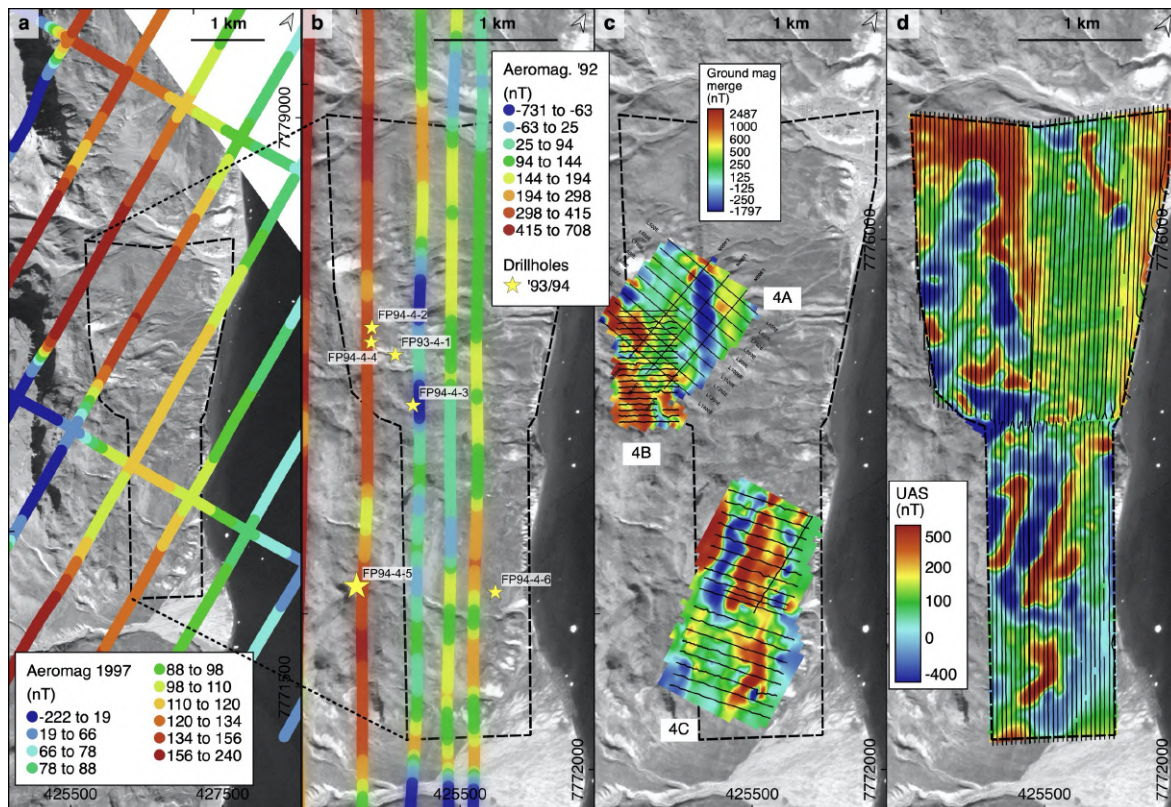


Figure 5.3 Overview of legacy airborne geophysical, ground-based magnetic and UAS-based magnetic data, with the dashed line outlining the area of our UAS-magnetic survey. The residual magnetic anomalies are shown (a) from the regional AEROMAG97 survey (Thorning and Stemp, 1998), (b) from a local exploration airborne survey (Olshefsky and Jerome, 1994) and (c) from ground-based surveys conducted by a mineral exploration company (4A; Olshefsky and Jerome, 1995) and collected during our field campaign (4B and 4C). The UAS-based magnetic anomaly is shown in (d) for comparison. Its flight lines are shown as black lines. The positions of drill holes are indicated in (b) as yellow dots.

5.2.5 Magnetic susceptibility measurements, handheld spectroscopy and grab sampling

All ground-based handheld measurements were geolocated using Garmin GPSmap64 handheld GPS device. We collected representative grab samples and made magnetic susceptibility (Figure 5.2 Figure 5.10c) as well as handheld spectroscopic measurements exclusively on basaltic rocks at Qullissat.

Magnetic susceptibilities were measured with a KT-10v2 magnetic susceptibility meter. For the majority of locations, we averaged 3–5 measurements to obtain one point value. Ground spectra were recorded with a PSR 3500 (Spectral Evolution, Haverhill, USA) in the VNIR-SWIR range (spectral range 350–2500 nm) featuring a spectral resolution of 3.5 nm (1.5 nm sampling interval) in VNIR and 7 nm (2.5 nm sampling interval) in the SWIR. Radiance values were converted to reflectance using a pre-calibrated PTFE panel (Zenith polymer) with > 99 % reflectance in the VNIR and >95 % in the SWIR range. Each spectral record consists of 10 individual measurements consecutively taken and averaged. A recalibration to reduce instrument drift was performed after 20–50 scans each. We took 3–5 measurements per

location. The areas covered with susceptibility and spectrometer measurements are the northern part of the magmatic body, a flat-lying outcrop near the shoreline sediments and at selected spots near a river delta to the total south of the investigation area (Figure 5.2c, e).

5.2.6 Petrophysical measurements on core samples from drill core FP94-4-5

The drill core from the deepest legacy drill hole FP94-4-5 is stored in the drill core archive of GEUS (Geological Survey of Denmark and Greenland) and has been accessible for this study. We selected core samples in 10 m meters intervals in a depth range from 49.5–215.7 m, which comprised samples from both the intrusion body and the sediments above and below. On these 23 samples, a variety of petrophysical properties were measured at the petrophysical lab of the GTK (Geological Survey of Finland) in Espoo. These measurements include magnetic properties, such as the induced and natural remanent magnetization (NRM) as well as the inclination and declination of the remanence, electric properties (not used in this study), e.g., the resistivity (in time and frequency domain) and the chargeability, and the dry bulk density. Samples had a diameter of ~3.5 cm and lengths between ~5–10 cm and susceptibility and NRM is measured with an AC susceptibility bridge (Puranen and Puranen, 1977) and a fluxgate magnetometer (Airo and Säätuvori, 2013), respectively. Petrophysical measurements were complemented with detailed mineralogical SEM analyses to link physical characteristics to specific components such as native iron, sulphides, graphite, and magnetite. These measurements are still ongoing; therefore the first qualitative results are presented here (during June 2021).

5.3 Results

5.3.1 Magnetic analysis

Aeromagnetic data are considered crucial to improve understanding of exploration targets in terms of size and depth and even age. Magnetic potential was illustrated on Ni-Cu PGE to discriminate magmatic suites with a complex magnetization history, such as negative magnetic anomalies, overprinting, environmental effects and metamorphosis. Natural remanent magnetization (NRM) can be inherited during crystallization of mafic rocks and cooling down to Curie temperature (Austin et al., 2013; Austin and Crawford, 2019).

From the total magnetic anomaly map of the UAS-based magnetic data (Figure 5.3d), we calculated a version that was upward-continued by 60 m to an elevation of 100 m (UP100) above ground level (agl), the first vertical derivative (VD), the analytic signal (AS) and the tilt derivative (TLD, Figure 5.4d) (Nabighian, 1972; Miller and Singh, 1994; Isles and Rankin,

2013; Dentith and Mudge, 2014). The combination of those filters helps to delineate anomaly borders, provide information on local magnetization strength and increase visual interpretation of both near-surface and deeper features (Figure 5.4).

Most of the observed magnetic anomalies are located in the western and central part of the investigation area at a topography altitude > 200 m asl and are arranged in a rather complex pattern that is trending in a NW–SE direction (strike of $\sim 320^\circ$ to 325° ; Figure 5.3d). Many of these anomalies have short wavelengths and have both distinct high and low amplitudes in the residual magnetic field (-400 to -50 nT; Figure 5.3d) and in its VD (-17 to -5 nT/m; Figure 5.4b). Since the AS shows high values for both the high and low-value anomalies (Figure 5.4c), it indicates that sharp gradients between magnetic highs and lows exist (Nabighian, 1972; Roest et al., 1992). This can be explained by an alternation of anomalies with strongly varying magnetization directions and proposes that low magnetic values are not created by lack of magnetic material, but by a significant remanent magnetization contribution that is oriented in a clearly different direction as the induced magnetization.

In the northern and southern part, some short wavelength anomalies have an elongated shape (anomalies C and D) in several of the attribute maps (Figure 5.4b, c, d). The anomaly C in the northern part is oriented about NW-SE (strike $\sim 325^\circ$), but the direction of the southern anomaly pattern D, which consists of a negative anomaly that is margined by a positive anomaly at both sides, is oriented more towards a NS direction (strike $\sim 355^\circ$). In the central part, the anomalies are distributed more chaotically and no preferred strike direction is observed (see pattern G in Figure 5.4a and on a larger scale chaotic outline in the TLD in Figure 5.4d). Several of these features (C, D, E, F and G) are also observed in the ground magnetic surveys (Figure 5.3c) confirming the reliability of anomalies identified from the UAS-based magnetic data.

Only two major short wavelength anomalies (anomalies A and B in Figure 5.4a) are located in the eastern part of the survey area. The positive anomaly A is located directly at the shore line in the central part of the survey area near the old coal mine (Figure 5.3d and Figure 5.4b, c). The positive anomaly B, which is located close to the abandoned Qullissat village, is elongated and strikes into a NW-SE direction. At its south-eastern end, a dipole-shaped anomaly is present.

These short wavelength anomalies are near-surface features that disappear in the upward continued version of the residual magnetic anomaly to 100 m agl (referred to as ‘UP100’, Figure 5.4a). Instead, negative anomalies become more pronounced in the central western part (see anomalies C, D and G in Figure 5.4a) proposing that remanent magnetization with a negative polarity is here more dominant at larger depths; while further to the north and south, the

anomalies tend to be positive at larger depths (see anomalies E and F in the south; Figure 5.4a). Characteristics of the main anomalies of A to G are summarized in Table 5.1.

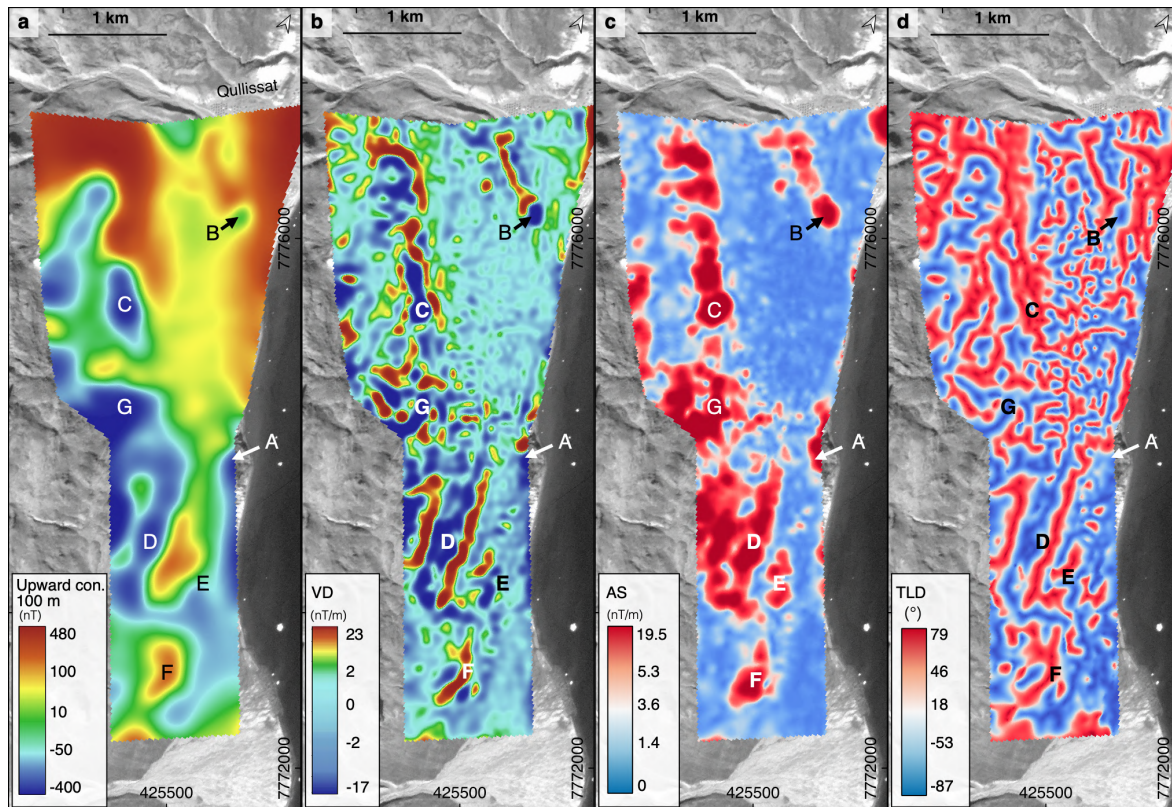


Figure 5.4 Magnetic attribute maps from the UAS-based magnetic data in the Qullissat area. (a) The magnetic anomaly upward continued (con.) to 100 m (UP100) to enhance anomalies at larger depths. (b) The first vertical derivative (VD) of the magnetic anomaly is presented to enhance narrow near-surface features (c) The analytic signal (AS) amplitude is presented to highlight areas with increased magnetization, independent of the magnetization direction. (d) The tilt derivative (TLD) is presented to highlight both surficial and deeper structures.

Table 5.1 Magnetic features identified in the residual magnetic anomaly (Figure 5.3d) and in its associated attribute maps (Figure 5.4).

No.	Description of magnetic features
A	Positive anomaly in residual anomaly, which disappears in the UP100 version; high values in the AS; isolated anomaly; associated with the ‘Nunngarut block’
B	Dipole shaped in residual anomaly map; clear magnetization in AS; presumably of anthropogenic origin
C	Pronounced negative anomaly in residual field with high negative values also in its VD and UP100; high AS values; strike towards north (328°); associated with magmatic Asuk member
D	High negative anomaly in residual field, with high negative values also in VD and UP100; high AS values, strike 348° N observed in TLD; associated with intrusion of Asuk member
E	Positive anomaly in residual magnetic anomaly that is also visible in its UP100, VD and AS at coast-near sedimentary outcrops; observed iron-alteration with sulphide mineralization in the field; called ‘coastal blocks’
F	Large positive anomaly in residual field (> 500 nT) near delta; isolated anomaly with high AS values; observed mineralization in the field; called ‘delta blocks’,

G	Chaotic pattern of magnetic anomalies is observed in the VD and TLD; in contrast, a pronounced negative magnetic anomaly is present in the UP100 of the residual magnetic anomaly; comparable to a debris flow
---	--

5.3.2 Magnetic modelling — 3-D magnetic inversion

A 3-D magnetization model of the Qullissat area was developed from our fixed-wing drone-based magnetic data using a deterministic Magnetization Vector Inversion (MVI). Employing such magnetic inversions that accounts for the full magnetization vector is a rising trend (Ellis et al., 2012; MacLeod and Ellis, 2013, 2016; Liu et al., 2017; Li et al., 2021) and has been applied, e.g., in mapping of volcanic domains with complex strata (Miller et al., 2020).

It was suggested that datasets from UAS with close flight line spacing and low ground clearance are especially suited for measuring magnetic remanence (Dering et al., 2019), and experiments confirm that they are reasonably sensitive (Cunningham et al., 2018) to indicate remanent contributions of magnetizations (Calou and Munsch, 2020).

We have chosen an MVI approach because borehole measurements show that the remanent component of the magnetization partly dominates the investigated magmatic body (see Section 5.3.5). Under such circumstances, scalar magnetic inversion only considering the induced magnetization component may generate misleading results. However, MVI suffers from a higher non-uniqueness such that additional information as from, e.g., core logs, measured petrophysical properties, surface structures and different lithologies need to be incorporated to produce geological plausible models that are consistent with other geoscience data and observations. Therefore, geologically relevant information was added stepwise as constraints during the inversion process.

The general inversion setup as described in Ellis et al. (2012), and implemented as web-based cloud solution in Oasis Montaj Geosoft VOXI is:

$$\min \phi(\mathbf{m}) = \phi_D(\mathbf{m}) + \lambda \phi_M(\mathbf{m})$$

$$\phi_D(\mathbf{m}) = \sum_{j=1}^M \left| \frac{F(\mathbf{m}_j) - d_j}{e_j} \right|^2$$

$$\phi_M(\mathbf{m}) = \phi_{M,Smooth}(\mathbf{m}) + \phi_{M,Ref}(\mathbf{m}) = \sum_{p=1}^3 \sum_{y=1}^3 |w_{y,p} \partial_y \tilde{\mathbf{m}}_p|^2 + \sum_{p=1}^3 |\mathbf{w}_{0,p} \cdot (\tilde{\mathbf{m}}_p - \tilde{\mathbf{m}}_{0,p})^T|^2$$

$$\lambda : \phi_D(\mathbf{m}) = \chi_T^2$$

with Φ being the objective function to be minimized, $\mathbf{m} = (\tilde{\mathbf{m}}_1, \tilde{\mathbf{m}}_2, \tilde{\mathbf{m}}_3) = (m_{1,1}, \dots, m_{1,N}, m_{2,1}, \dots, m_{2,N}, m_{3,1}, \dots, m_{3,N})$ being the model vector

containing the three components $p = (1, 2, 3)$ of the magnetization of all voxels $k = (1, \dots, N)$, d being the observed data vector of total magnetic field anomaly at each measuring point $j = (1, \dots, M)$ and e being their associated data errors. The resulting magnetizations are given in susceptibility equivalences and have SI units. After the targeted error weighted data misfit was reached in an inversion, the data term Φ_D and regularization term Φ_M were balanced in the objective function relative to each other, so that the solution with the highest regularization was found, i.e., the largest regularization parameter λ was selected, where the targeted chi-squared data misfit χ_T^2 as reached; for details see (Ellis et al. 2012).

In all presented inversion tests, a smoothing constraint associated with $\Phi_{M,Smooth}$ was added as regularization and an Iterative Reweighting Inversion Focus (Seequent, 2021) option for model sharpening was active. The smoothing term had in all inversion tests weights $w_{y,p}$ of 1.0 in all directions y and for all components p . In addition, the inversion was constrained towards a reference model m_0 associated with the term $\Phi_{M,Ref}$ for some inversion runs.

The 3D model base from the magnetic data of the UAS survey was discretized in $200 \times 267 \times 71$ cells in x, y and z-directions. Cell sizes in x and y directions were 20 m, whereas cell sizes in the z direction increased with depths from 10 m at 425 m asl down to 108 m at -1094 m asl. As the surface topography, we used the regional digital surface model. The ELM processed UAS total magnetic anomaly data at a constant altitude of 40 m were used as input d . An error of 5–10 nT was assumed for all data points and accounts for inaccuracies in the instrumentation and positioning, as well as for high frequency component loss during the ELM processing.

In the first run, no geological information was used in constraints (i.e., no term $\Phi_{M,Ref}$ was added). The target misfit was reached in a few iterations, as was also the case for all follow-up runs. However, the first unconstrained run resulted in a geologically unrealistic model (not presented here), where strong magnetic anomalies were partly located in areas associated with the non-magnetic sediments both below and above the magmatic body.

In a next step, the different geological units and their magnetic properties were considered in the inversion by establishing constraints of the type $\Phi_{M,Ref}$. For this, the shape of the tabular magmatic body and the location of the basalts along the Inussuk cliff faces were estimated. The upper surface of the magmatic body was constructed by interpolation of drill hole intersections of the five legacy drill holes (FP93-4-1 to FP94-4-5) and from outcrop exposures.

The top of the outcrops exposures were extracted from the drone-based DEM (Figure 5.5a). Only the deepest drill hole FP94-4-5 intersected the base of the magmatic body. To estimate the base, we considered the difference of the top (320 m asl) and base (130 m asl) of the

magmatic body in this drill hole as the general thickness (132 m) and shifted the top surface with this value downward. Afterwards, this base surface estimate was compared with the mapped geology along the surface. At locations, where the base surface intersects outcropping sediments and basalt, it was modified by shifting it upward and downward, respectively (Figure 5.5a). The foot of the basalt cliff (Maligât Fm) was partly covered by debris and therefore, the associated surface was considered as a flat and horizontal plane at 400 m asl (Figure 5.5a).

After adding the magmatic units into the model (Figure 5.5b), the remaining part of the model is assumed to be associated with non-magnetic sedimentary units, which is agreeing with field observations. To consider this information in the MVI, we set up a reference model with zero magnetization for all voxels and in three directions ($m_0 = 0$). For the voxels associated with non-magnetic sedimentary rocks, the corresponding parameter weights $W_{0,p}$ (sediments) were set to 0.5 for $p = 1, 2, 3$, but for voxels containing the magmatic units, the weights $W_{0,p}$ (basalt) were all set to 0.0 ensuring that only the sediment areas were constrained towards small magnetic values.

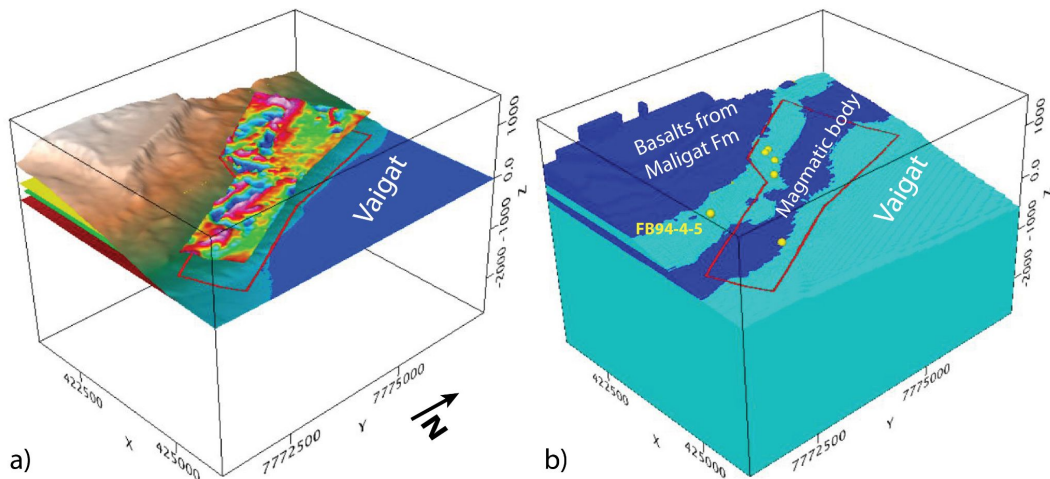


Figure 5.5 3-D voxel-based model for the magnetic inversion. (a) Topography from the regional DEM is shown together with layers associated with the base of the basalts of the cliff (yellow), and with the top (green) and base (red) of the magmatic body. In addition, the map of the total magnetic field from the fixed-wing drone survey is presented, whose data were used as input in the inversion. (b) Discretized model used in the inversion. Cells associated with the magmatic body and the basalts from the Inussuk cliff wall (both in dark blue colours) were derived from the layers presented in (a) and were differently constrained in the inversion as the remaining model (see description of the constraints in the inversion). Yellow dots indicate the locations of the drill holes, and the red polygon outlines the area covered by the fixed-wing drone survey.

Inversion results are presented in Figure 5.6Figure 5.7. Only the central part of the model is displayed that is covered by drone-based data, since the remaining areas are less well resolved. Higher magnetization values larger than 0.01 SI are almost solely placed in areas defined as the magmatic units and particularly in the mineralized body. The absolute values of the magnetization are with a few exceptions not larger than 0.1 SI (maximum value: ~ 0.15 SI).

In the eastern part, there are only two minor anomalies, which are not located within these units and marked with A and B in Figure 5.6b and no higher magnetizations are assigned to depths below the magmatic body. Within the body the resulting distribution of the magnetization direction is complex and, dependent on the anomaly, high magnetization values are observed for all three components in x- y- and z-directions. The z-component of the magnetization shows both positive and negative values for different anomalies within the magmatic body (Figure 5.6b–d). Despite the complexity, the shapes of many of the anomalies show a preferred orientation in an N–S to NNW–SSE direction (see Figure 5.7d–i).

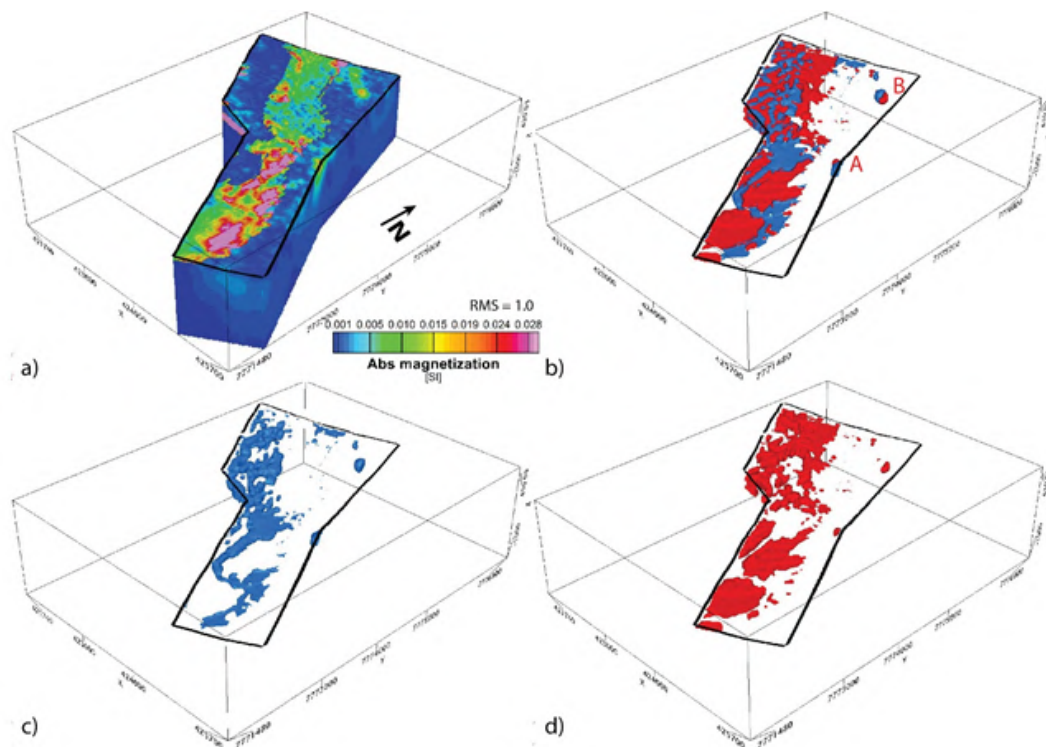


Figure 5.6 Results from the MVI test, where cells associated with sediment units were constrained towards a non-magnetic reference model, but cells associated with magmatic rocks remained unconstrained. Only the shallow central part of the model down to a depth of 1000 m is shown which was covered by data from the fixed wing survey (black polygon). (a) The final magnetization distribution is presented as absolute values of the magnetization vectors. (b) Only cells with absolute magnetization values > 0.01 SI are shown as isosurfaces. Blue and red colours are associated with locations, where the z-component of the magnetization points out of the ground (z-component is positive) and into the ground (z-component is negative), respectively. These two contributions are presented separately in (c) and (d).

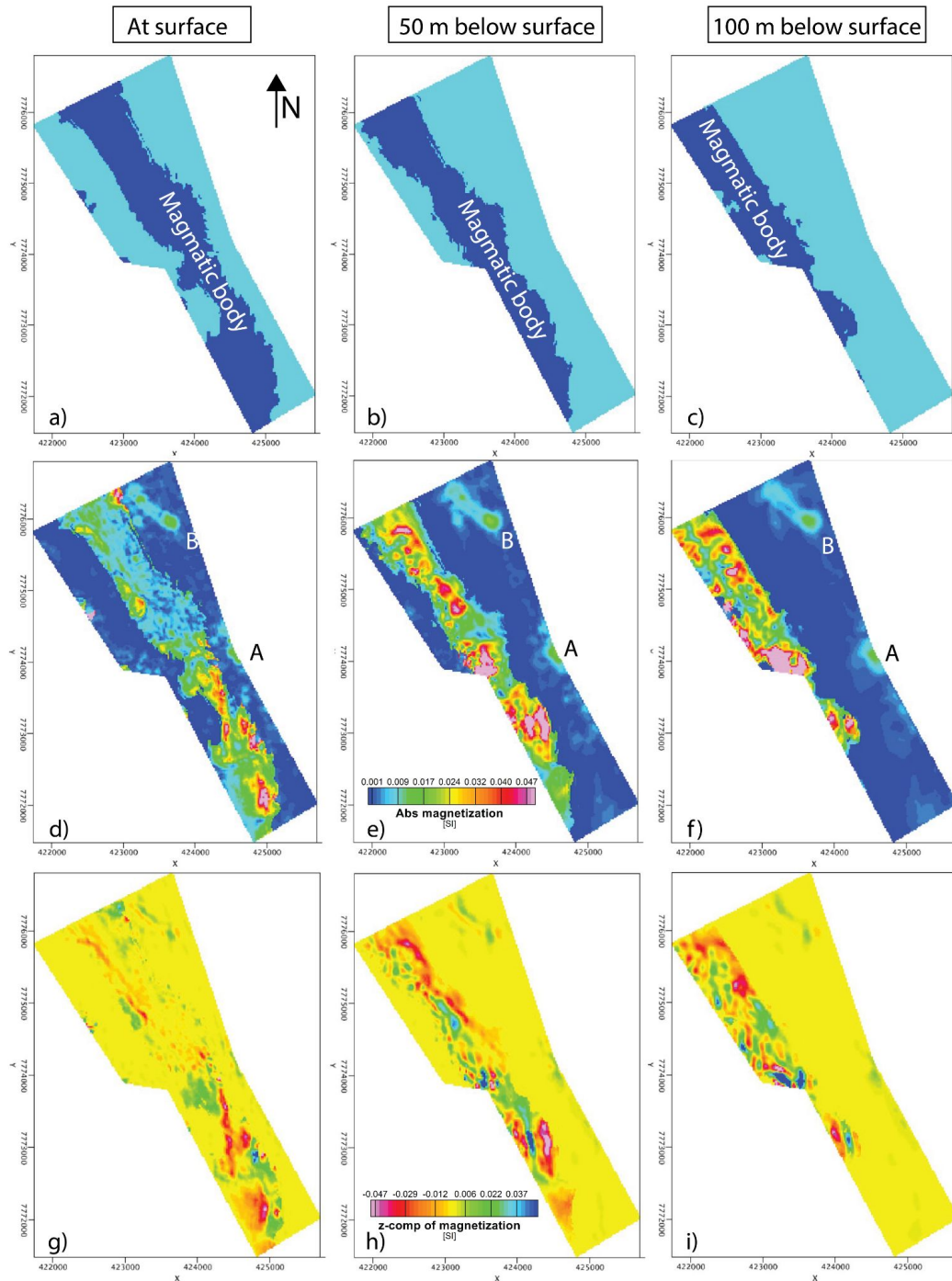


Figure 5.7 Three depth slices through the resulting inversion model, where cells associated with sediment units were constrained towards a non-magnetic reference model, but cells associated with magmatic rocks remained unconstrained. Results are considered at the surface (1st column), and 50 m (2nd column) and 100 m (3rd column) below the surface topography. In (a) to (c) the reference model is shown, where parts associated with target magmatic rocks are shown in dark blue colours. In (d) to (f) and (g) to (i), the absolute value and the z-components of the magnetization are shown.

In a last run, the impact of the magnetic field direction in the inversion was also considered. It was assumed that the earth magnetic field and the palaeomagnetic field at the formation of the Asuk Member are very much antiparallel oriented and can be described by a constraint, where the magnetization is oriented in the direction of the ongoing magnetic field (i.e., parallel if the

induced part of magnetization dominates and antiparallel if the remanent part dominates). The made assumptions, the implementation of the constraint and the resulting model of this inversion run are summarized in Appendix F3. Since the resulting model shows some artificially appearing anomaly patterns (Figure F8.10 and Figure F8.11 in Appendix F3) we doubt that a uniformly oriented magnetization is a realistic representation of the real magnetization distribution and assume that the real magnetization direction is more variable and complex.

5.3.3 Observations from UAS multispectral and photogrammetric data

Results from the optical methods allow mapping of outcrops, show a presence of iron on top of their surfaces as well as revealing landslide features as scarps and lobes. The multispectral surveys cover the whole region of interest and in addition, the cliff of Inussuk with a GSD of 36 cm (Figure 5.2b). Results from optical methods reveal landslide scarps and lobes.

The vegetation index (NDVI) mapping (Figure 5.8a) illustrates the distribution of widespread low vegetation. Its values range between 0–0.71, and pixels with NDVI >0.3 are dominated by vegetation and are masked in the following image analysis when the iron abundance is evaluated from the mosaic. Vegetation occurs mainly in the low-slopes and flat areas and in proximity to water sources near stream beds and minor water flows (up to 750 m asl). Occasionally, particularly high NDVI values are observed on top of solifluction lobes, indicating a rim of vegetation. The iron-sensitive band ratio $\frac{b3}{b4}$ shows values > 1.0 for around 8 % (1.04 km²) of the scanned surface area. These spots with elevated iron-ratios are distributed across the whole study area (Figure 5.12b). The Highest concentration of scattered blocks is found in the central landslide area and above the southern magmatic target (> 350 m asl). The Smallest blocks and outcrops that can be identified in the iron band ratio have areas down to 0.7 m².

Our high-resolution UAS-based DSM (Figure 5.2b), contour lines (Figure 5.12), the computed slope map (Figure 5.8b) and a TPI (Figure 5.12c) map were used to identify landslide related features along the presumed magmatic target area. A large backscarp (1.2 km length) is visible in Figure 5.8d at an altitude level between 320–350 m asl., and is identified in the DSM by its convex shape in the contour lines. The slope of the topography in the Qullissat area rises from the shoreline (slope 3–5°) towards the exposed basalt cliffs of Inussuk (slope : 75–89°). Streams fed by meltwater incised valleys and troughs are visible as steep slopes for example in the delta region (Figure 5.8b and d). A one kilometre-wide delta, fed by braided streams, fans out into the Vaigat Strait at the southern area (Figure 5.1d). Rockslides and landslipped blocks are

prominent in regions at elevations above 200 m and coincide with the general rockslide area shown in the local geologic map (Figure 5.1c). Some slidded blocks indicate glacial abrasion in the field.

Most of the identified outcrops have lobate forms, are strongly disintegrated and occur near the coastline (< 250 m asl). Outcrops close to the coast are often oriented parallel to the shore line. This parallel trend is repeated in the iron band ratio. A prominent feature is a ~400 m long outcrop (elevation 150–220 m asl) that marks the southern termination of the target magmatics.

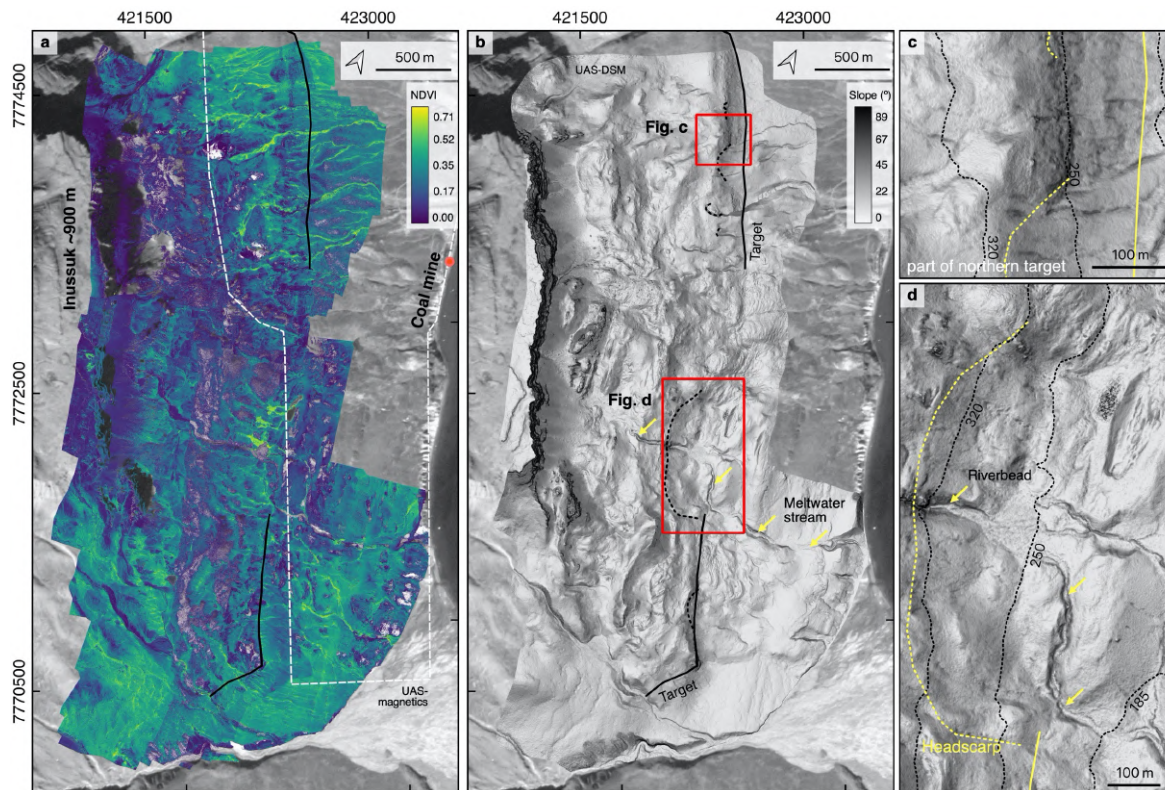


Figure 5.8 Data products derived from the UAS multispectral and photogrammetry data. The black/yellow line illustrates the basal area of the target. (a) NDVI mosaic derived from the Sequoia camera scenes depicts vegetation occurrence. (b) Slope map (in degree) illustrates the undulating topography (stippled lines are landslide scarps). Inset maps show (c) close-ups of the northern part of the magmatic target body which was sampled, (d) southern edge of said body, (e) detached blocks at the coastal area, partly covered by solifluction.

5.3.4 Ground-based spectroscopy and magnetic susceptibility

One exemplarily area was thoroughly investigated with ground based spectral scans and magnetic susceptibility measurements, which is called ‘coastal block’ in the following. Figure 5.9 shows handheld spectra from this outcrop near the coast, which was sampled carefully due to the good ground accessibility (see the close up Figure 5.12d–g). In the very same region, iron abundance is indicated by high UAS-based iron ratio as well (Figure 5.12b and e).

The characteristic iron-absorption feature between 850–930 nm (Hunt and Ashley, 1979; Crowley et al., 2003) is pronounced in most samples taken from outcrops in the Qullissat area

(Figure 5.9a). This is agreeing the observation of small staining of orange-yellow and reddish to black goethite-hematite, yellow-orange jarosite or limonite for iron-sulphide related minerals along the outcrop. A colour transition from blackish-lustrous to red on outcrop surfaces indicates a modification in surface structure. A subtle reflectance change in the VNIR absorption with an absorption band shift from 663 nm towards 671 nm indicates a subtle change from hematite to goethite (Crowley et al., 2003). Streak tests of those samples showed a reddish-brown to dark ochre colour, meaning the same minerals.

Distinct spectral features of other mineral types were not observed on the magmatic rocks, but an abundance of lichen-related absorption is visible in most spectra. Absorption patterns in the short-wave infrared region of the electromagnetic spectrum between 1730–2100 nm are caused by hydroxyl groups and can be characteristic for the presence of lichen, which occur abundant in arctic environments (Salehi et al., 2017).

We measured magnetic susceptibility exclusively on magmatic rocks. The susceptibilities are relatively high in the study area (mean value of 0.025 SI and maximum value of ~0.01 SI, Figure 5.10a). There is no major trend that the magnetic susceptibility values are varying with locations (see Figure 5.10b and c), although highest field measurement values above 0.03 SI were only observed on the basaltic outcrops in the SE and N parts, which are mapped as non-slipped rocks of the target magmatic body (Pedersen et al., 2017), and handheld scans were conducted on less weathered surfaces in shaded crevices and corners of larger blocks. Values > 0.03 SI were measured on top of smaller blocks, iron-stained weathering crusts, and on rocks from above the target magmatic body (Figure 5.10c) presumably belonging to the Maligât Fm.

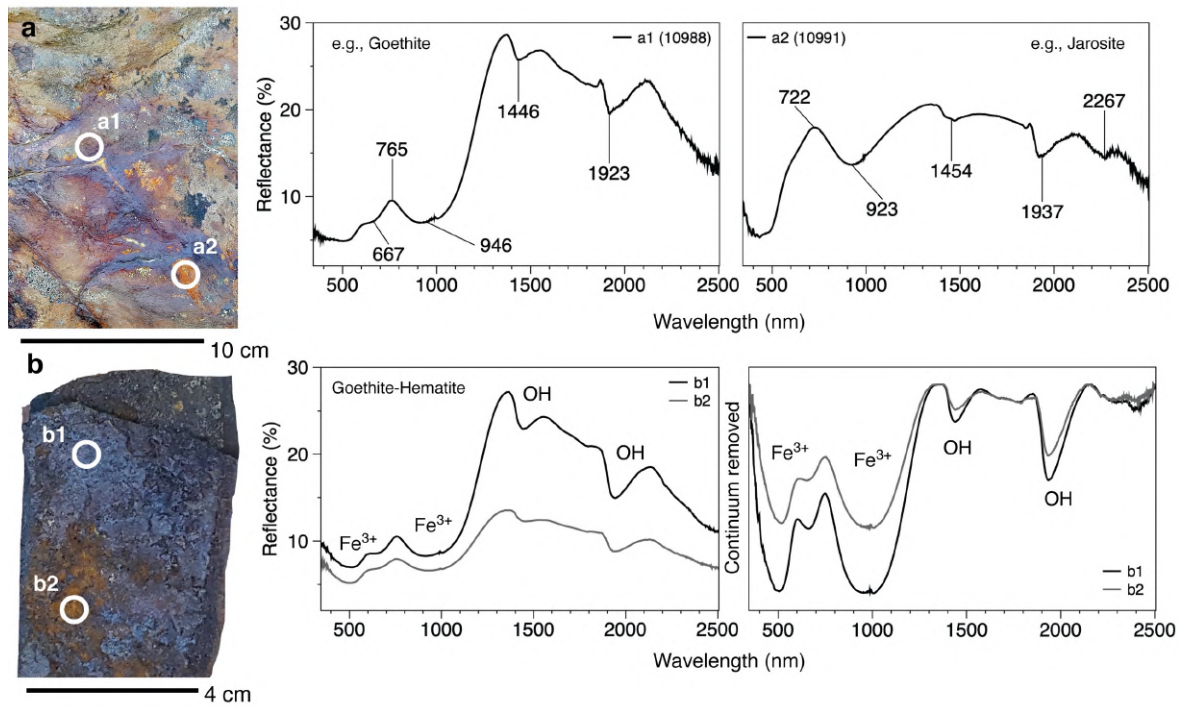


Figure 5.9 Spectral measurements taken on a typical basaltic outcrop, which correlates with the magnetic anomaly E in Figure 12 and whose optical and magnetic characteristics are shown in Figures 13 d–f. It is located at 100 m asl about 300 m east of the main slipped block (see location in Figure 5.13e). (a) The rock surface has clear iron staining and shows specific spectral absorption patterns of goethite and jarosite (absorption positions identified after Crowley et al., 2003). (b) Part of a sample (GEUS 567321) from the same outcrop was scanned under laboratory conditions. Reflectance spectra (left) and continuum removed spectra (right) highlight the iron and the OH- related absorption features, typically found in iron-hydroxides.

5.3.5 Petrophysical properties of drilling FP94-4-5

Since the drill cores were un-oriented and the actual dip of the borehole was not measured but simply assumed to be vertical (Olshefsky et al., 1995), we do not consider the measured inclination and declination for further interpretation. Therefore, we focus on the susceptibility (induced magnetization), the remanent magnetisation, the density, and the simple Königsberger ratio Q , which is the ratio between induced and remanent magnetization (Figure 5.10d, e).

Legacy drill hole FP94-4-5 was intended to probe the target magmatic for Ni, Cu, and sulphides. The drilling is the only one to intersect the whole magmatic body at Qullissat. It was drilled vertically to a depth of 270.5 m, and its location was determined based on airborne EM targets and a ground-magnetic low (Olshefsky et al., 1995). The legacy core logs describe carbonaceous sediments and sandstone (depth down hole: 0–50.2 m) above the target, an intrusive breccia (50.2–58.1 m), a mafic sill (the target; 58.1–190.5 m), and carbonaceous siltstone, sandstone and sediments (190.5–270.5 m at terminus). Several thin coal seams were reported below the magmatic target.

The magmatic target itself showed graphite xenoliths in the upper half, finely disseminated pyrite along the whole length, and native iron accumulation in millimetre-sized droplets in the lower section (177.40–190.5 m). The lower contact zone (190.5–220.8 m) showed carbonaceous siltstone with chilled margins (Olshefsky et al., 1995). The whole magmatic body expressed higher magnetic susceptibility, and a rapid increase in susceptibility at 127 m depth (Figure 5.10d, 190 m asl), down till the sediment contact. Our recent observations of the legacy core samples indicated a contact at the susceptibility jump (190 m asl, Figure 5.10e), caused by a composition change.

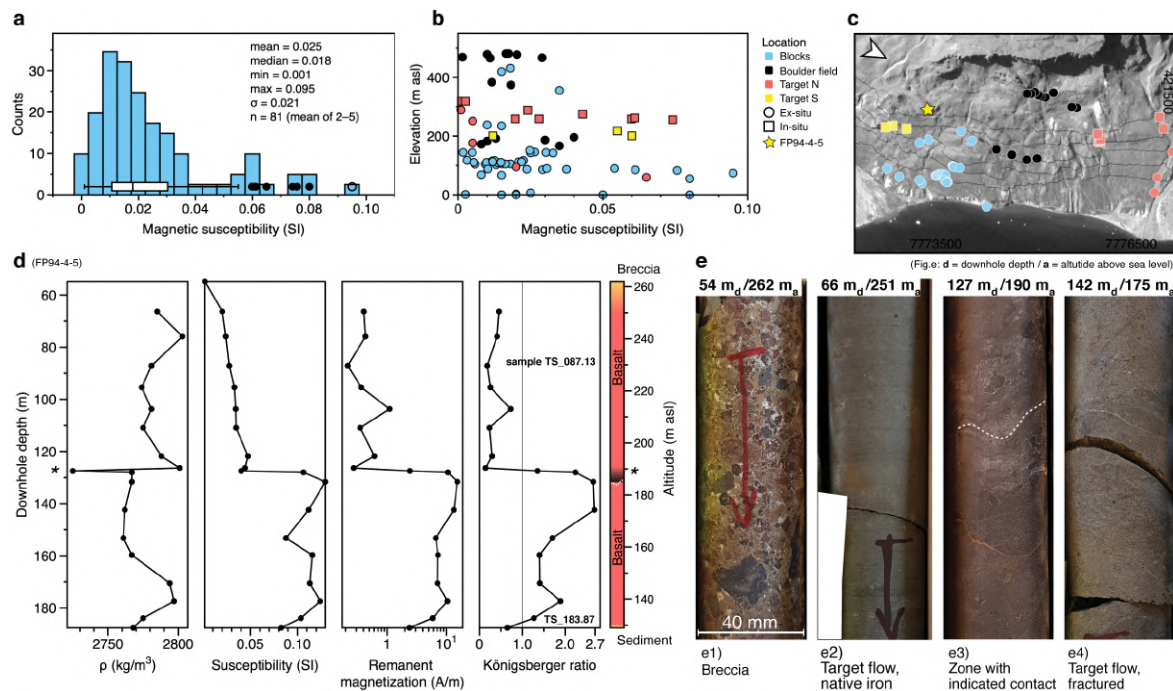


Figure 5.10 Ground-based susceptibility measurements and petrophysical logs from drill hole FP94-4-5. (a) Magnetic susceptibility distribution from handheld measurements. (b) Magnetic susceptibility is plotted against altitude (in m asl) with a location-based colour scheme. The locations are given in map (c), where ex-situ versus in-situ here means how we describe each location in the field. (d) Petrophysical measurements of density, magnetic susceptibility, remanent magnetization and computed Königsberger ratio for 19 core samples from the drill hole FP94-4-5. Geologic legend after Olshefsky and Jerome, (1994). (e) Photographs of four representative core sections with altitude above sea level.

5.3.6 Photomicrographs and SEM images

Photomicrographs and scanning electron microscopy (SEM) images (Figure 5.11) of polished thick-sections of two andesite samples (target magmatic, Figure 5.8c, e and Figure 5.13a, d, e) show a mineralogy mainly composed of olivine, pyroxene and amorphous silica, occasional graphite flakes, native iron blebs, botryoidal iron-oxide-hydroxide (presumably magnetite, Fe₃O₄) and sulphide blebs (pyrrhotite, Fe_{1-x}S). The native iron appears as finely disseminated spheres, anhedral drops and spherules, often rimmed with iron oxide and sulphides. At the sample locations near the delta, high magnetic susceptibilities were measured and a low

5.4 Discussion & Interpretation

5.4.1 Surface investigation

The iron ratios from UAS based multispectral surveys were intended to provide information about how the iron products are distributed on the surface. However, the interpretation of these data has some limitations because our spectral identification of surficial iron occurrence relies on band ratios and on a narrow spectral range. Band ratio values are affected by cast shadow in multispectral images, therefore visual inspection and comparison with additional imagery from auxiliary satellite images became useful. Band ratios above a threshold of around 3.0 for multispectral pixels are considered as unreasonably high and suggest further examination, if they occur as singular or locally isolated anomalies. However, many of these blocks could originate from talus and material flows of the adjacent Inussuk mountain wall, where the lava flows and hyaloclastites of the iron-bearing Skarvefjeld Unit (Maligât Fm) were emplaced (Figure 5.12b).

Based on field observation and previous work, the approximate elevation level for our target horizon is between 140–320 m asl. We identified moved basalt blocks as low as 80 m asl (Figure 5.14b). We estimate that the surface exposure of the target intrusive horizon is about 7.5 km² in the study area. The southern block slide and coastal boulders cover an area of around 0.56 km². Magnetic inversion modelling in joint interpretation with photogrammetric measurements suggest a total volume of 0.0231 km³ for the southern block slide. The total volume of the targeted volcanic formation in the area amounts to 0.093 km³.

The occurrence of goethite (α -FeOOH) and probably maghemite (γ -Fe₂O₃) is indicated by surface spectra (Figure 5.9). Another important contributor to the magnetic response is pyrrhotite. Magnetic anomalies caused by pyrrhotite are significant in many regions, and pyrrhotite-bearing rocks can maintain strong remanent magnetizations with higher Königsberger ratio (Clark, 1997). Preliminary relogging of drill-core FP94-4-5 suggests that pyrrhotite occurs in the upper half of the target horizon as droplet clusters or rims of native iron droplets. This is supported by the observations of Olshefsky and Jerome, 1995, and in Pedersen et al., 2017. The occurrence of iron-oxide related species of hematite and goethite may be linked to abundant magnetite occurrence in the basalt, but corrosion of native iron to alteration products is another explanation (Figure 5.9b).

Palaeomagnetic noise that does not represent the in-situ remanence in our example might include drilling-induced remanence or stress release during coring, chemical remanent magnetization induced by weathering and post-collection of weak magnetic fields (Clark,

2014). The ultrafine grain sizes we observed influence the NRM, here further in-depth analysis of magnetic micro-fabrics could help the subsequent understanding of the geochemical provenance. Thermoremanence on our investigated intrusion was possibly induced by the following Maligât volcanism, especially from the top-laying lava flows of the Rinks-Dal Mb. The magmatic body might be affected by subsequent metamorphism of post-intrusive volcanism during the Eocene events (Dam et al., 2009).

5.4.2 Joint interpretation

The integration of UAS-based magnetic, spectral and photogrammetric data fortifies our interpretation of the target magmatic. The first-order analysis of the area relies on qualitative interpretation of UAS-based spectral indices and visual inspection of the additional Planetscope satellite image. A second-order subsurface interpretation is conducted by the residual anomaly, the analytic signal and the discrete 3D model based on the magnetic vector inversion. DSLR photographs were taken from a vessel and visually extended the geologic context along the shore, closed gaps along the coal mine area with the Nunngarut block and contributed to spatial understanding (Figure 5.13d, e).

UAS-MSI based iron index assisted in identifying the main blocks and magnetic modelling extended the subsurface interpretation (Figure 5.12). Our UAS-based multispectral analysis (Figure 5.12b, c) indicates iron-related absorption in the eastern parts of the flight area and near the cliff. Two outcrops in the southeast of the study area (Figure 5.12e), which were closely investigated with ground-sampling, showed iron stains with elevated band ratio values. An iron ratio above 1.0 pinpoints outcrops and areas of interest for further ground inspection (Figure 5.12f). Following the integration of topographic indices (slope and TPI) and spectral iron index, we interpret the surface features as blocks, mineralized outcrops, and patches of amplified iron-alteration (Figure 5.12b, index values > 2.0). Iron-stained surfaces can reach sizes down to 0.7 m² (four multispectral pixels). The identified main block expresses up to 50,000 m² of measurable iron absorption (Figure 5.13a). A first indication was observed from interpretation of the detailed UAS-DSM and its derived contour lines. Its complete surface area is estimated at 0.35 km². Further, slipped features are shown in Figure 5.13b3.

Most surface blocks and outcropping buried chunks occur in proximal distance to the main block. Our starting point to search and identify those blocks was the Nunngarut block, which detached from the upper target magmatic and moved downwards until the current coastline. Geochemical sampling of said block shows an identical signature with the target magmatic. Values from sample AF0903 in Olshefsky and Jerome, 1993 show similar geochemical patterns

as GEUS sample 156690 (Pedersen et al., 2017), which is located directly on the southern extension of the target magmatic (see Figure 5.8b). Similar contents of Mg (6.5–7.6 %) and Fe (10–12 %) was reported for both rocks by Pedersen et al., 2017. Even after meticulous data cleaning, numerous pixels remain in the UAS-MSI orthomosaic that contain non-illuminated edges and shaded zones.

We mitigate this by self-checking selected absorption zones with its greyscale and CIR orthomosaic (Figure 5.2a). This ensures retention of sufficient pixels for interpretation at higher reliability. Nonetheless, careful interpretation is advised and a conservative delineation of target blocks was conducted.

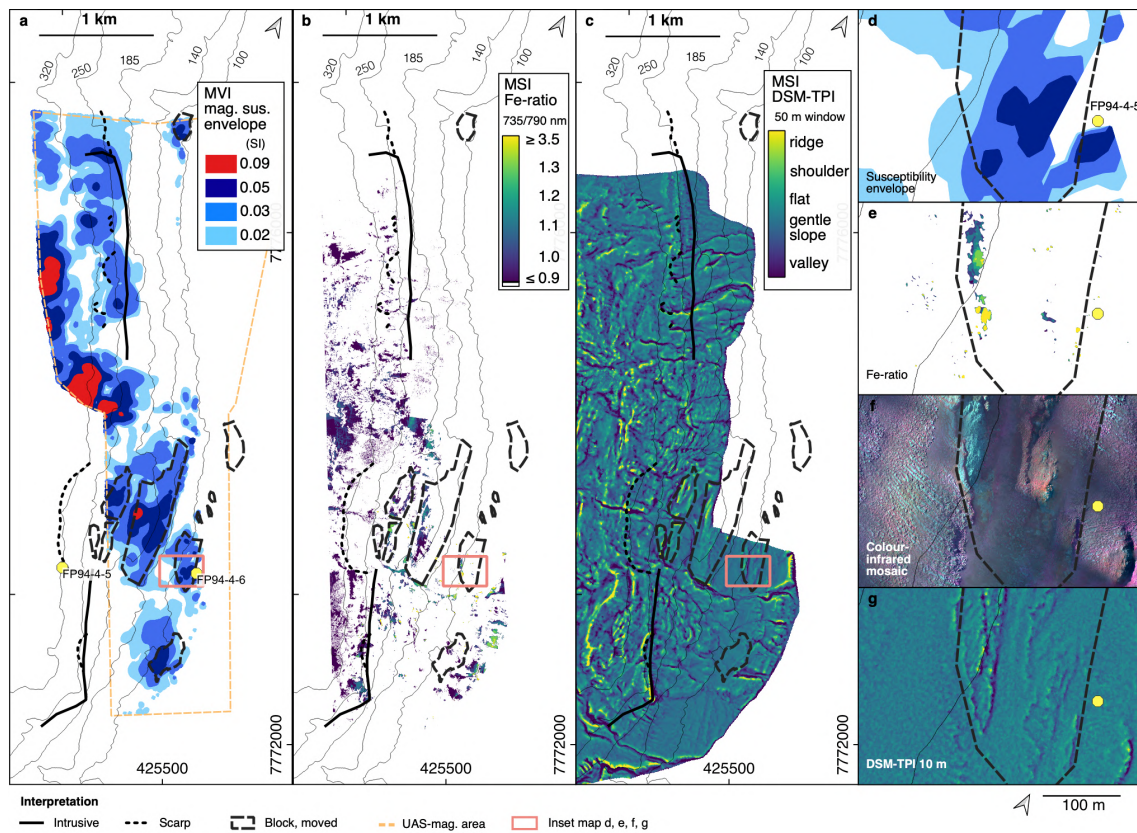


Figure 5.12 Integration of UAS-based data. (a) Isosurfaces of magnetization amplitudes obtained from the constrained MVI inversion. (b) Iron band ratio from multispectral UAS mosaics showing abundance of iron-rich alteration products on the surface (c) Photogrammetry-based TPI calculated from pixels in a 50×50 m moving window shows graduation from incised valleys, flat slopes, to ridges. (e–g) Close-ups from an area around a block close to the coastline (red rectangles in a–c), which was more detailed investigated: (d) Isosurfaces of magnetization amplitude from the MVI model, (e) iron-ratio, (f) colour-infrared composite (bands 3, 2, 1) and. (g) photogrammetric TPI calculated from pixels in a 10×10 m moving window.

We present the interpretation based on the three main data sources (Figure 5.12, Figure 5.13). Elevation measurements are extracted from photogrammetric UAS-based data, and if not applicable, from the ArcticDEM (Porter et al., 2018) (profile plots in Figure 5.13c).

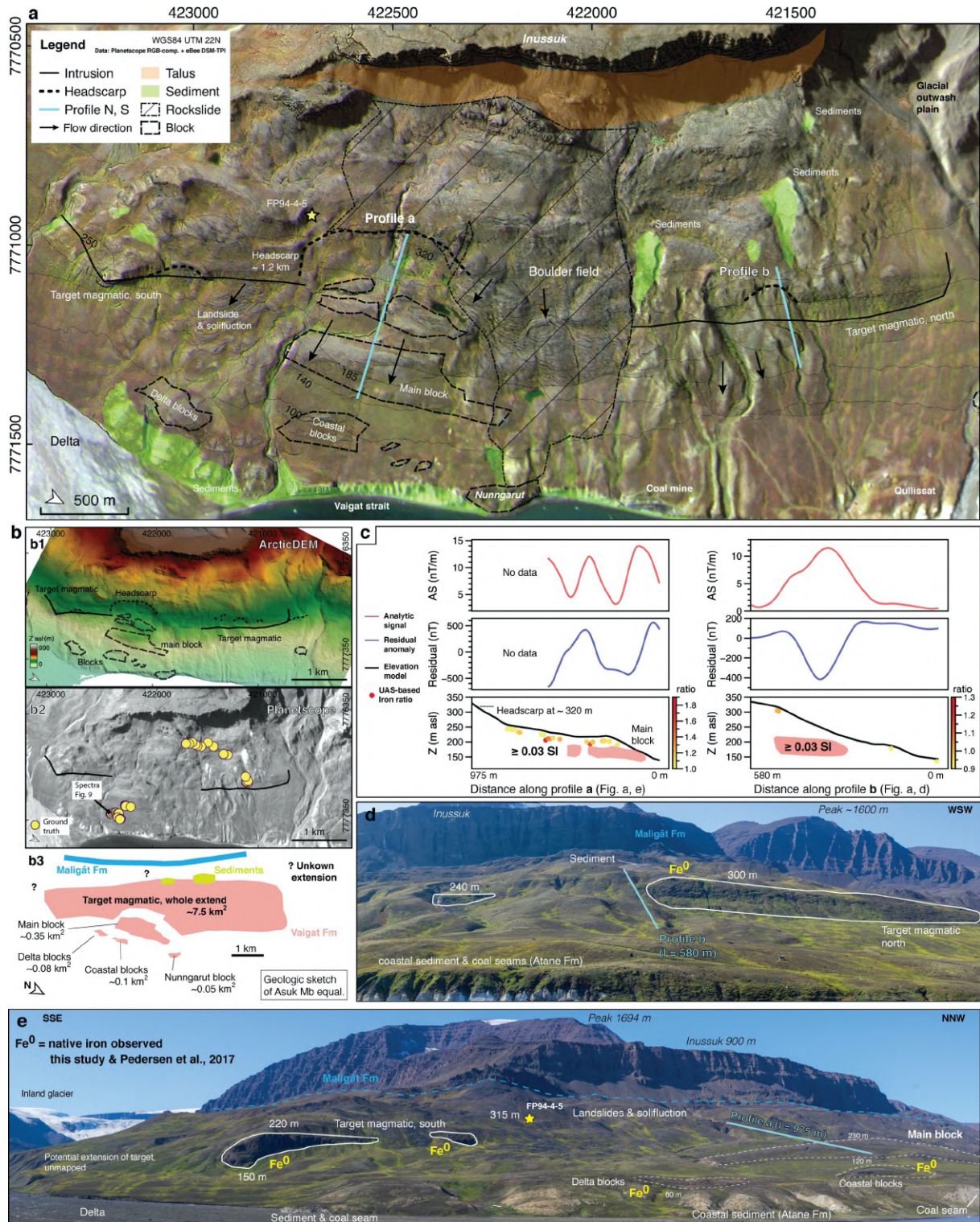


Figure 5.13 Integrated interpretation. (a) RGB-composite plot from a PlanetScope (PS) image that is merged with semi-transparent TPI-image of a eBee DSM to increase image contrast. Landslide features are marked as dashed lines with thin lines for larger blocks and thick lines for the main landslide scarp. Talus below the Inussuk and block fields are the source for numerous boulders in the whole area. Mapped sediments reach up till the foot of the Inussuk cliff. (b) Overview maps illustrate area relations: b1: ArcticDEM at 2 m GSD with interpreted blocks, b2: PS greyscale with ground truth locations (spectroscopy and susceptibility) b3: Sketch showing the assumed extent of the target magmatic body (only the part covered with UAS data are shown). (c) Two schematic cross-sections in west-east direction are shown together with the magnetic anomaly and the analytical signal from the drone-borne magnetic, and iron ratios extracted from the drone-borne multi-spectral. The locations of these cross-sections are sketched in (a). (d–e) Coast-side views onto the magmatic outcrops in the (d) northern and (e) southern part of the study area.

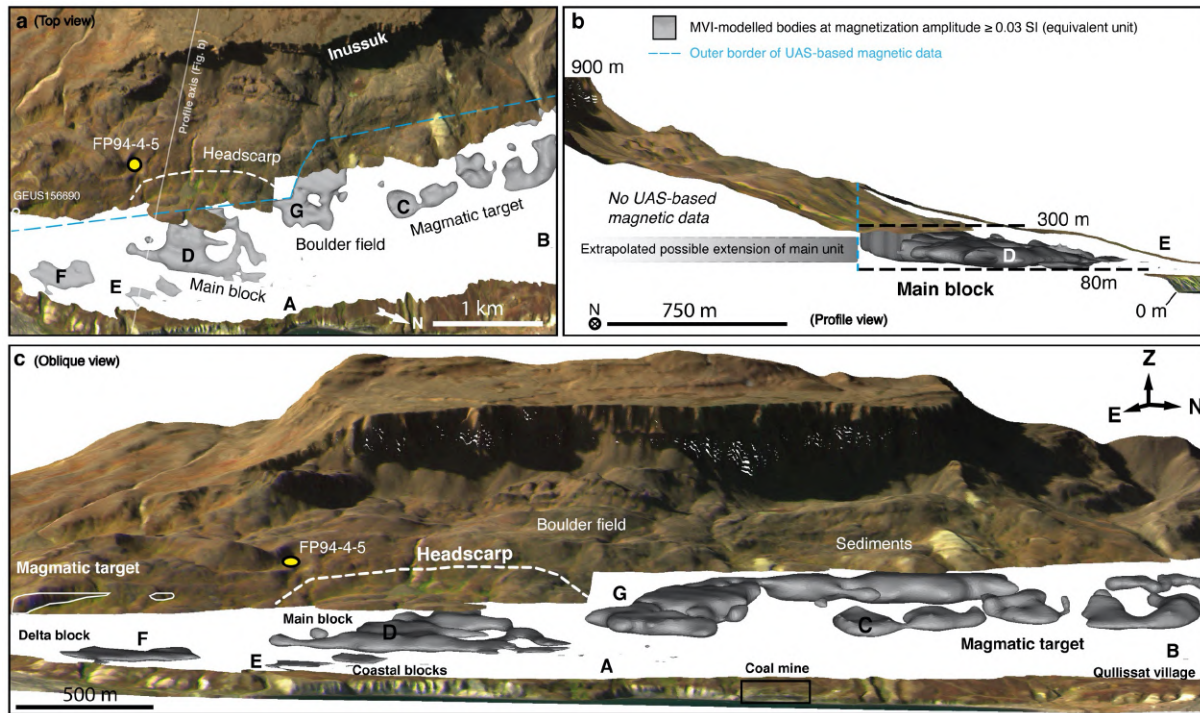


Figure 5.14 Combined plots of surface topography (PlanetScope mosaic fused with ArcticDEM) and larger magnetization amplitudes (> 0.03 SI) in the subsurface from the MVI. (a) Top view of survey area. (b) Side view cross-section facing north. Dashed lines indicate the maximum extension of the modelled bodies. (c) Oblique view from the east. In all views, the surface model is partly removed for areas where the magmatic body is present (compare with Figure 5.12a).

A 3D representation in Figure 5.14 integrates the 3D-modelled magmatics with surface topography and the identified anomalies. Table 5.1 presents the magnetic anomalies from Figure 5.4 and Figure 5.7. Results from the constrained MVI with standard magnetic filtering and topographic investigations allows the assumption that the magnetic anomalies predominantly originate from a magmatic body of a flat, non-specific shape, which is in accord with photogrammetric modelling and surface observations. Inversion results further propose that no further magnetic intrusions are present immediately underneath the target magmatic body and there are plausible explanations for the deviating anomalies A and B. Anomaly A is located in the central part that is affected by mass movements and may be associated with a fragment of the body that slid downward (see Section 5.3.3), but the anomaly B is located within the Qullissat village and may be associated with a human made construction built on a solid rock foundation.

The obtained range of magnetic values (up to 0.1–0.15 SI) of the first constrained inversion, where only the sediments were considered as non-magnetic, are in the same range of magnetizations as observed in the borehole FP94-4-5 (Figure 5.10d, around 0.12 SI). Our magnetization values obtained in the second inversion run (up to 0.4–0.6 SI) are unreasonably high to represent the values from the petrophysical measurements. In addition, alignments of

some larger anomalies in N–S to NNS–SSE (Figure 5.7d–i) directions as observed in the first run appear geologically more reasonable than these very complex patterns observed in this second run (Figure F8.10 in Appendix F3), since such oriented anomalies could be representative for the flow pattern of the intrusion (or lava flow). Accordingly, we assume that the results of this second run are less meaningful than from the previous run, although the target misfit was reached and, hence, it is a theoretical solution. This means that a magnetization pointing only into directions parallel or antiparallel to the regional field may not well enough represent the real magnetization distribution. This is an interesting and partly unexpected result, since there are components in the remanent magnetization that are not oriented towards the direction of the palaeomagnetic field.

Magnetic features C and D are attributed to the non-slipped target magmatic. Both anomalies strike towards northern direction. We assume that the so-called main block was fully or partly detached from the target magmatic and slipped towards the coast. It was accompanied by smaller blocks, described as E and F. Some slender features in the magnetics, orthogonal to the shore and close to the former coal mine could be mining shafts at shallow depths (see also Figure 5.13a, bottom right). The most obvious magnetic feature H is related to the central boulder field with debris streams that covers several square kilometres inside the survey area.

The appearance of anomalies having both positive and negative z-components are supporting the assumption that the remanent magnetization was created at a period of reverse polarization. Dominating induced, and remanent magnetization would result in different orientations of the z-component, since inclinations of both the remanent and induced magnetizations are close to 90° (Riisager and Abrahamsen, 1999, 2000).

5.4.3 Linking landslide features to the exploration target

Following a common landslide classification (Hung et al., 2014, 2014), the slope failure of uniformly composed mafic rocks created a translational block slide that moved one large block and smaller block fields in our survey area (Figure 5.13). This head escarpment can be identified clearly in the UAS-based DSM and expresses a concave rupture surface (Figure 5.13b, c). Larger rotated blocks at the central Nunngarut location, 3 km south of Qullissat (Figure 5.13a), was defined in former investigations as part of the known Mg-rich andesite intrusion associated with the Asuk Mb (Pedersen et al., 2017). It has a similar geochemical composition as compared to the Nunngarut block at sea level, adjacent to the coal mine. It also shows a distinct magnetic anomaly in the form of dipoles in the residual magnetic anomaly and appears strongly magnetized in the AS (Figure 5.4c).

We identified mature meltwater stream patterns that incise along and between the rotated blocks that separate buried landslide features in the southern part (Figure 5.13b, d). We assume that those streams formed energetically beneficial in-between the fissures and faults of the larger blocks and today, they outline the block area.

Our rock samples from delta-blocks and from the northern target magmatic are similar in microscopic observations (Figure 5.11), having a spatial distance of about 3.5 km. At the coastal block location, a magnetic low coincides with a small landslide block. The northern intrusion is partly covered by flowing quaternary debris, affecting both the magnetics and the multispectral data. To improve interpretation, a UAS-based DSM helped to investigate outcrops smaller than 3 m which showed small blocks, the blockslide and outcrops of the magmatic target. The influence of such small features highlights how beneficial UAS-based magnetics are in rugged terrain.

Imperative for the interpretation was the magnetic UAS data. The ground magnetics show the negative residual anomalies of the target in some areas, however the much larger spatial coverage of the UAS magnetics created the necessary frame to interpret the data and extract the landslipped blocks. The depth extends of the coal mine is not known, therefore any magnetic anomalies close to the shore might be related to abandoned coal shafts.

Considering all information layers combined (remote sensing, legacy data, surface, and laboratory observations), the morphology and structure of the target magmatics points to an intrusive lava flow which interacted with graphite-bearing sediments and mudstone. Investigating the centre of the Asuk eruption period, further north near the Kuunganguaq, is suggested. The eruption site of Asuk (Figure 5.1) and its feeders have not been found yet, but are assumed to be located between the coastal Asuk locality and Kuunganguaq valley (Pedersen et al., 2017), at about 50 km NW. There, the potential to identify a feeder structure is given. Lastly, results of this study carefully suggest that the Qullissat area is less feasible to host any viable mineralization.

Erosion, faulting, subsidence and uplift shaped the structure of the Nuussuaq Basin. Off-shore seismic line data was acquired and used to investigate structural control of the Cretaceous sediment basin and on-shore the basalt, and to map petroleum prospectivity. The mapped included NNE–SSW striking faulting, of which most are dated of pre-flood basalt origin, but were reactivated later during seafloor spreading of the Baffin bay in Eocene and after. The coastal occurrence of block slides and basalt morphology is controlled by reactivated faulting (Chalmers et al., 1998, 1999; Marcussen et al., 2001).

5.4.4 Evaluation and recommendation

A far-reaching goal was to better understand what sources (e.g., native iron, magnetite, and sulphides) cause observed anomalies in the geophysical data. However, properly addressing this aspect requires detailed petrophysical and mineralogical analysis, which has not been fully done yet. Therefore, it was only generally discussed in this contribution.

Shadows were removed during pre-processing, but remaining pixels with unusual low values cannot be ruled out. In addition, the band at 790 nm of the Sequoia camera is particularly affected by the low incidental radiation of dark volcanic rocks, and therefore the band ratios can be biased. An extended spectral range in the visible or short-wave infrared, next to an improved SNR, would increase spectral signature confidence. The diurnal solar variation at high latitude should be considered carefully in regard to radiometric quality (Assmann et al., 2019). But clearly, we show the time efficiency and safety of this large-scaled UAS survey. We recommend UAS-based experiments with multispectral cameras with more spectral bands and higher radiometric resolution.

5.5 Conclusion

Our results indicate an alternative evolution regarding the nature of the mineralized intrusive body and Qullissat. Our main findings are briefly summarized below:

- We suggest that along the whole coastal area south of Qullissat up till a delta plain, an invasive lava flow that consists of at least two flow impulses occurred during C26r, and is chemically similar to the Asuk member of the Vaigat Fm.
- By using UAS, mineralized horizons under cover are mappable in higher detail than in a combined ground and airborne survey. We discovered at least three major zones of mass movement with blocks that are under cover or only surfacing at shallow depth, an observation that was missed based on surface observations alone.
- Based on the modelled geometry of the intrusive, with MVI data, the assumption that the geometry and extent of the target volcanic body is likely an invasive lava flow and henceforth less promising to host an economic deposit.
- We incorporated the remanence in magnetic modelling for this area, since it is uncertain if a simplified assumption of a magnetization along the regional field direction properly approximates this basaltic geology where strongly varying magnetization directions are observed in rock samples.

- Feeder structures in the area could not be traced. We demonstrate the advantage of an integrated approach using UAS mapping, MVI and selected field observations. Integrated multispectral and magnetic UAS-based mapping in similarly complex areas improves scale and resolution for drill targeting and reduces time effort and required sampling material.

Acknowledgements: We thank Bluejay Mining PLC for their support during the preparation and conduction of the field work. In particular, we thank Bo Moller Stensgaard, Hans Jensen and Klaus for extensive logistic support. We thank Radaí Oy, especially Lauri Maalissma and Ari Saartenoiija for the UAS magnetics measurements. We thank GEUS for preparation of the field campaign and shipping. Lotte Larsen, Asger Pedersen and Ethan Barnes are gratefully thanked for the fruitful geologic discussions and additional interpretation. The Team Erzlabor at HZDR-HIF and Kai Bachmann are thanked for sample preparation and X-BSE image analysis, respectively. MULSEDRO's field campaign was conducted under scientific survey licence (VU-00158-2019) within mineral exploration licence MEL 2018-16 from Blue Jay Mining Plc. MULSEDRO was funded as an EIT Raw Materials (project ID 16193) by the European Union organization EIT.

Author Contributions: Conceptualization, R.J., B.H., R.Z., M.K.; processing: R.J., M.P., B.H., H.S. analysis MSI: R.J.; analysis Mag: R.J., B.H.; investigation: R.J., R.Z., B.H., S.L.; ground work: R.J., R.Z., B.H., H.S.; resources: R.G., B.H., H.S.; software: M.P., B.H., R.J.; validation: R.J., S.L.; visualization: R.J., B.H., E.V.; Writing—original draft: R.J., B.H., E.V., M.P.; writing—review and editing: B.H., E.V., M.K., R.Z., R.G.; supervision: R.G., B.H.; All authors have read and agreed to the published version of the manuscript.

Funding: The research work was funded through the European Union and the EIT Raw Materials project “MULSEDRO” (grant id: 16193).

Conflicts of Interest: The authors declare no conflict of interest.

Data assets:

- Supplemental data, including 3D .dfx files, photos and spectra, <https://doi.org/10.5281/zenodo.5592747>
- Supplement 2, eBee UAV Orthomosaic and DEM, <https://doi.org/10.5281/zenodo.6643571>
- 3D model for exploration at Qullissat, Disko Island, Greenland, <https://skfb.ly/psyZK>

References

- Airo, M.-L., and Sääuvori, H., 2013, Petrophysical characteristics of Finnish bedrock.: Geological Survey of Finland Report of Investigation Report of Investigation 205, 35 p.
- Assmann, J.J., Kerby, J.T., Cunliffe, A.M., and Myers-Smith, I.H., 2019, Vegetation monitoring using multispectral sensors — best practices and lessons learned from high latitudes: *Journal of Unmanned Vehicle Systems*, v. 7, p. 54–75, doi:10.1139/juvs-2018-0018.
- Athavale, R.N., and Sharma, P.V., 1975, Paleomagnetic Results on Early Tertiary Lava Flows from West Greenland and their bearing on the Evolution History of the Baffin Bay–Labrador Sea Region: *Canadian Journal of Earth Sciences*, v. 12, p. 1–18, doi:10.1139/e75-001.
- Austin, J., and Crawford, B., 2019, Remanent magnetization mapping: A tool for greenfields magmatic Ni-Cu-PGE exploration undercover: Part 1: *Ore Geology Reviews*, v. 107, p. 457–475, doi:<https://doi.org/10.1016/j.oregeorev.2019.03.008>.

- Austin, J.R., Schmidt, P.W., and Foss, C.A., 2013, Magnetic modeling of iron oxide copper-gold mineralization constrained by 3D multiscale integration of petrophysical and geochemical data: Cloncurry District, Australia: *Interpretation*, v. 1, p. T63–T84.
- Barnes, S.J., Cruden, A.R., Arndt, N., and Saumur, B.M., 2016, The mineral system approach applied to magmatic Ni–Cu–PGE sulphide deposits: *Ore Geology Reviews*, v. 76, p. 296–316, doi:<https://doi.org/10.1016/j.oregeorev.2015.06.012>.
- Bird, J.M., and Weathers, M.S., 1977, Native iron occurrences of Disko island, Greenland: *The Journal of Geology*, v. 85, p. 359–371.
- Bonow, J.M., Japsen, P., Lidmar-Bergström, K., Chalmers, J.A., and Pedersen, A.K., 2006, Cenozoic uplift of Nuussuaq and Disko, West Greenland—elevated erosion surfaces as uplift markers of a passive margin: *Geomorphology*, v. 80, p. 325–337.
- Booyesen, R., Zimmermann, R., Lorenz, S., Gloaguen, R., Nex, P.A.M., Andreani, L., and Möckel, R., 2019, Towards multiscale and multisource remote sensing mineral exploration using RPAS: A case study in the Lofdal Carbonatite-Hosted REE Deposit, Namibia: *Remote Sensing*, v. 11, doi:10.3390/rs11212500.
- Calou, P., and Munsch, M., 2020, Airborne Magnetic Surveying with a Drone and Determination of the Total Magnetization of a Dipole: *IEEE Transactions on Magnetics*, v. 56, doi:10.1109/TMAG.2020.2986988.
- Cande, S.C., and Kent, D.V., 1995, Revised calibration of the geomagnetic polarity timescale for the Late Cretaceous and Cenozoic: *Journal of Geophysical Research: Solid Earth*, v. 100, p. 6093–6095, doi:10.1029/94JB03098.
- Chalmers, J.A., Pulvertaft, T.C.R., Marcussen, C., and Pedersen, A.K., 1999, New insight into the structure of the Nuussuaq Basin, central West Greenland: *Marine and Petroleum Geology*, v. 16, p. 197–211, doi:10.1016/S0264-8172(98)00077-4.
- Chalmers, J.A., Pulvertaft, T.C.R., Marcussen, C., and Pedersen, A.K., 1998, New structure maps over the Nuussuaq Basin, central West Greenland: *GEUS Bulletin*, v. 27, p. 18–27, doi:10.34194/ggub.v180.5081.
- Clark, D., 1997, Magnetic petrophysics and magnetic petrology: Aids to geological interpretation of magnetic surveys: *AGSO journal of Australian geology & geophysics*, v. 17, p. 83–104.
- Clark, D.A., 2014, Methods for determining remanent and total magnetisations of magnetic sources—a review: *Exploration Geophysics*, v. 45, p. 271–304.
- Crowley, J.K., Williams, D.E., Hammarstrom, J.M., Piatak, N., Chou, I.-M., and Mars, J.C., 2003, Spectral reflectance properties (0.4–2.5 μm) of secondary Fe-oxide, Fe-hydroxide, and Fe-sulphate-hydrate minerals associated with sulphide-bearing mine wastes: *Geochemistry: Exploration, Environment, Analysis*, v. 3, p. 219–228, doi:10.1144/1467-7873/03-001.
- Cunningham, M., Samson, C., Wood, A., and Cook, I., 2018, Aeromagnetic Surveying with a Rotary-Wing Unmanned Aircraft System: A Case Study from a Zinc Deposit in Nash Creek, New Brunswick, Canada: *Pure and Applied Geophysics*, doi:10.1007/s00024-017-1736-2.
- Dahl-Jensen, T., Larsen, L.M., Pedersen, S.A.S., Pedersen, J., Jepsen, H.F., Pedersen, G., Nielsen, T., Pedersen, A.K., Von Platen-Hallermund, F., and Weng, W., 2004, Landslide and Tsunami 21 November 2000 in Paatuut, West Greenland: *Natural Hazards*, v. 31, p. 277–287, doi:10.1023/B:NHAZ.0000020264.70048.95.

- Dam, G., Pedersen, G.K., Sønderholm, M., Midtgaard, H.H., Larsen, L.M., Nøhr-Hansen, H., and Pedersen, A.K., 2009, Lithostratigraphy of the cretaceous-paleocene nuussuaq group, nuussuaq basin, west greenland: 1–171 p.
- Data, E., Donohue, J., and Legault, J., 2005, Geological report regarding the Quantec TITAN-24 distributed Array System Tensor-magnetotelluric survey over the Disko Project, Greenland, during 2004, on behalf of Vismand Exploration Inc.: GEUS report file Geological report 21888, 15 p.
- Dentith, M., and Mudge, S.T., 2014, Geophysics for the Mineral Exploration Geoscientist. (Ed.) Cambridge University Press:, doi:10.1007/s00126-014-0557-9.
- Dering, G.M., Micklethwaite, S., Thiele, S.T., Vollgger, S.A., and Cruden, A.R., 2019, Review of drones, photogrammetry and emerging sensor technology for the study of dykes: Best practises and future potential: Journal of Volcanology and Geothermal Research, v. 373, p. 148–166, doi:10.1016/j.jvolgeores.2019.01.018.
- Deutsch, E.R., and Kristjansson, L.G., 1974, Palaeomagnetism of Late Cretaceous-Tertiary Volcanics from Disko Island, West Greenland: Geophysical Journal of the Royal Astronomical Society, v. 39, p. 343–360, doi:10.1111/j.1365-246X.1974.tb05459.x.
- Ellis, R., de Wet, B., and Macleod, I., 2012, Inversion of Magnetic Data from Remanent and Induced Sources: ASEG Extended Abstracts, v. 2012, doi:10.1071/ASEG2012ab117.
- Flores, H., Lorenz, S., Jackisch, R., Tusa, L., Contreras, I.C., Zimmermann, R., and Gloaguen, R., 2021, UAS-Based Hyperspectral Environmental Monitoring of Acid Mine Drainage Affected Waters: Minerals, v. 11, doi:10.3390/min11020182.
- Gavazzi, B., Le Maire, P., Munsch, M., and Dechamp, A., 2016, Fluxgate vector magnetometers: A multisensor device for ground, UAV, and airborne magnetic surveys: The Leading Edge, v. 35, p. 795–797, doi:10.1190/tle35090795.1.
- Gunn, P.J., and Dentith, M.C., 1997, Magnetic responses associated with mineral deposits: AGSO journal of Australian geology & geophysics, v. 17, p. 145–158.
- Henderson, G., Schiener, E., Risum, J., Croxton, C., and Andersen, B., 1981, The west Greenland basin: Canadian Society of Petroleum Geologists, Memoir, v. 7, 399–428 p.
- Humlum, O., 1988, Rock glacier appearance level and rock glacier initiation line altitude: a methodological approach to the study of rock glaciers: Arctic & Alpine Research, v. 20, p. 160–178, doi:10.2307/1551495.
- Hungr, O., Leroueil, S., and Picarelli, L., 2014, The Varnes classification of landslide types, an update: Landslides, v. 11, p. 167–194.
- Hunt, G.R., and Ashley, R.P., 1979, Spectra of altered rocks in the visible and near infrared: Economic Geology, v. 74, p. 1613–1629, doi:10.2113/gsecongeo.74.7.1613.
- Isles, D.J., and Rankin, L.R., 2013, Geological interpretation of aeromagnetic data: Perth, Society of Exploration Geophysicists and Australian Society of Exploration, v. 1, 365 p.
- Jackisch, R. et al., 2020, Integrated geological and geophysical mapping of a carbonatite-hosting outcrop in Siilinjärvi, Finland, using unmanned aerial systems: Remote Sensing, v. 12, doi:10.3390/RS12182998.
- Jackisch, R., Madriz, Y., Zimmermann, R., Pirttijärvi, M., Saartenoja, A., Heincke, B.H., Salmirinne, H., Kujasalo, J.-P., Andreani, L., and Gloaguen, R., 2019, Drone-borne hyperspectral and magnetic data integration: Otanmäki Fe-Ti-V deposit in Finland: Remote Sensing, v. 11, doi:10.3390/rs11182084.

- Jakob, S., Zimmermann, R., and Gloaguen, R., 2017, The Need for Accurate Geometric and Radiometric Corrections of Drone-Borne Hyperspectral Data for Mineral Exploration: MEPHySTo-A Toolbox for Pre-Processing Drone-Borne Hyperspectral Data: *Remote Sensing*, v. 9, p. 88, doi:10.3390/rs9010088.
- James, M.R., Chandler, J.H., Eltner, A., Fraser, C., Miller, P.E., Mills, J.P., Noble, T., Robson, S., and Lane, S.N., 2019, Guidelines on the use of structure-from-motion photogrammetry in geomorphic research: *Earth Surface Processes and Landforms*, v. 2084, p. 2081–2084, doi:10.1002/esp.4637.
- James, M.R., and Robson, S., 2014, Mitigating systematic error in topographic models derived from UAV and ground-based image networks: *Earth Surface Processes and Landforms*, v. 39, p. 1413–1420.
- James, M.R., Robson, S., D'Oleire-Oltmanns, S., and Niethammer, U., 2016, Optimising UAV topographic surveys processed with structure-from-motion: Ground control quality, quantity and bundle adjustment: *Geomorphology*, doi:10.1016/j.geomorph.2016.11.021.
- Japsen, P., Green, P.F., and Chalmers, J.A., 2005, Separation of Palaeogene and Neogene uplift on Nuussuaq, West Greenland: *Journal of the Geological Society*, v. 162, p. 299–314.
- Keays, R.R., and Lightfoot, P.C., 2007, Siderophile and chalcophile metal variations in Tertiary picrites and basalts from West Greenland with implications for the sulphide saturation history of continental flood basalt magmas: *Mineralium Deposita*, v. 42, p. 319–336, doi:10.1007/s00126-006-0112-4.
- Kriegler, F.J., Malila, W.A., Nalepka, R.F., and Richardson, W., 1969, Preprocessing transformations and their effects on multispectral recognition: *Remote Sensing of Environment*, VI, p. 97.
- Larsen, L.M., and Pedersen, A.K., 2009, Petrology of the paleocene picrites and flood basalts on diskø and nuussuaq, West Greenland: *Journal of Petrology*, v. 50, p. 1667–1711, doi:10.1093/petrology/egp048.
- Larsen, L.M., Pedersen, A.K., Tegner, C., Duncan, R.A., Hald, N., and Larsen, J.G., 2016, Age of Tertiary volcanic rocks on the West Greenland continental margin: volcanic evolution and event correlation to other parts of the North Atlantic Igneous Province: *Geological Magazine*, v. 153, p. 487–511, doi:10.1017/S0016756815000515.
- Le Maire, P., Bertrand, L., Munsch, M., Diraison, M., and Géraud, Y., 2020, Aerial magnetic mapping with an unmanned aerial vehicle and a fluxgate magnetometer: a new method for rapid mapping and upscaling from the field to regional scale: *Geophysical Prospecting*, p. 1–13, doi:10.1111/1365-2478.12991.
- Li, Y., Sun, J., Li, S.-L., and Leão-Santos, M., 2021, A paradigm shift in magnetic data interpretation: Increased value through magnetization inversions: *The Leading Edge*, v. 40, p. 89–98, doi:10.1190/tle40020089.1.
- Lightfoot, P.C., Hawkesworth, C.J., Olshefsky, K., Green, T., Doherty, W., and Keays, R.R., 1997, Geochemistry of Tertiary tholeiites and picrites from Qeqertarsuaq (Disko Island) and Nuussuaq, West Greenland with implications for the mineral potential of comagmatic intrusions: *Contributions to Mineralogy and Petrology*, v. 128, p. 139–163, doi:10.1007/s004100050300.
- Liu, S., Hu, X., Zhang, H., Geng, M., and Zuo, B., 2017, 3D Magnetization Vector Inversion of Magnetic Data: Improving and Comparing Methods: *Pure and Applied Geophysics*, v. 174, p. 4421–4444, doi:10.1007/s00024-017-1654-3.

- MacLeod, I.N., and Ellis, R.G., 2013, Magnetic vector inversion, a simple approach to the challenge of varying direction of rock magnetization: Australian Society of Exploration Geophysicists, v. 1.
- MacLeod, I.N., and Ellis, R.G., 2016, Quantitative magnetization vector inversion: ASEG Extended Abstracts, v. 2016, p. 1–6.
- Malehmir, A., Dynesius, L., Paulusson, K., Paulusson, A., Johansson, H., Bastani, M., and Wedmark, M., 2017, The potential of rotary-wing UAV-based magnetic surveys for mineral exploration: A case study from central Sweden: , p. 552–557, doi:10.1190/tle36070552.1.
- Marcussen, C., Chalmers, J., Lykke-Andersen, H., Rasmussen, R., and Dahl-Jensen, T., 2001, Acquisition of high-resolution multichannel seismic data in the offshore part of the Nuussuaq Basin, central West Greenland: GEUS Bulletin, v. 189, p. 34–40, doi:10.34194/ggub.v189.5195.
- Miller, C.A., Schaefer, L.N., Kereszturi, G., and Fournier, D., 2020, Three-Dimensional Mapping of Mt. Ruapehu Volcano, New Zealand, From Aeromagnetic Data Inversion and Hyperspectral Imaging: Journal of Geophysical Research: Solid Earth, v. 125, p. 1–24, doi:10.1029/2019JB018247.
- Miller, H.G., and Singh, V., 1994, Potential field tilt—a new concept for location of potential field sources: Journal of Applied Geophysics, v. 32, p. 213–217, doi:10.1016/0926-9851(94)90022-1.
- Nabighian, M.N., 1972, The Analytic Signal Of Two-Dimensional Magnetic Bodies With Polygonal Cross-Section: Its Properties And Use For Automated Anomaly Interpretation: GEOPHYSICS, v. 37, p. 507–517, doi:10.1190/1.1440276.
- Nagata, T., Ishikawa, Y., Kinoshita, H., Kono, M., Syono, Y., and Fisher, R.M., 1970, Magnetic properties and natural remanent magnetization of lunar materials: Geochimica et Cosmochimica Acta Supplement, v. 1, p. 2325.
- Olshefsky, K., 1992, Falconbridge Limited - Report of 1991 Exploration Activities, West Greenland Tertiary Basalt Province for Prospecting License #156 and Exploration Concession #165: Geological Survey of Denmark and Greenland GEUS report file 21092, 149 p.
- Olshefsky, K., and Jerome, M., 1993, Falconbridge Limited - Report of 1992 Exploration Activities, West Greenland Tertiary Basalt Province for Prospecting License #156 and exploration licenses 02/91, 03/91, 04/91, 25/92: Geological Survey of Denmark and Greenland GEUS report file 21216, 300 p.
- Olshefsky, K., and Jerome, M., 1994, Falconbridge Limited - West Greenland Tertiary Basalt Province; Report of 1993 Exploration Activities for Prospecting License #156 and exploration licenses 02/91, 03/91: Geological Survey of Denmark and Greenland GEUS report file 21356, 333 p.
- Olshefsky, K., Jerome, M., and Graves, M., 1995, Falconbridge Limited A/S - West Greenland Tertiary Basalt Province; Report of 1994 Exploration Activities for Prospecting License 06/94 and exploration licenses 02/91 & 03/91: Geological Survey of Denmark and Greenland GEUS report file 21410, 326 p.
- Parshin, A., Grebenkin, N., Morozov, V., and Shikalenko, F., 2018, Research Note: First results of a low-altitude unmanned aircraft system gamma survey by comparison with the terrestrial and aerial gamma survey data: Geophysical Prospecting, v. 66, p. 1433–1438, doi:10.1111/1365-2478.12650.

- Pauly, H., 1958, Igdlukúnguaq nickeliferous pyrrhotite: Bulletin of the Geological Survey of Greenland, v. 17, p. 169.
- Pedersen, A., 1977, Iron-bearing and related volcanic rocks in the area between Gieseckes Dal and Hammers Dal, north-west Disko: Rapp Gronlands Geol Unders, v. 81, p. 5–14.
- Pedersen, A.K., 1985, Lithostratigraphy of the Tertiary Vaigat Formation on Disko, central West Greenland: Rapp. - Gronl. Geol. Unders.,
- Pedersen, A.K., Larsen, L.M., and Pedersen, G.K., 2017, Lithostratigraphy , geology and geochemistry of the volcanic rocks of the Vaigat Formation on Disko and Nuussuaq , Paleocene of West Greenland: GEUS Bulletin, v. 39, p. 244, doi:<https://doi.org/10.34194/geusb.v39.4354>.
- Pedersen, A.K., Larsen, L.M., and Pedersen, G.K., 2018, Lithostratigraphy, geology and geochemistry of the volcanic rocks of the Maligât formation and associated intrusions on disko and nuussuaq, paleocene of west greenland: Geological Survey of Denmark and Greenland Bulletin, v. 40, p. 239, doi:[10.34194/geusb.v40.4326](https://doi.org/10.34194/geusb.v40.4326).
- Pedersen, M., Weng, W.L., Keulen, N., and Kokfelt, T.F., 2013, A new seamless digital 1:500 000 scale geological map of Greenland: Geological Survey of Denmark and Greenland Bulletin, doi:[10.34194/geusb.v28.4727](https://doi.org/10.34194/geusb.v28.4727).
- Plouffe, A., Anderson, R.G., Gruenwald, W., Davis, W.J., Bednarski, J.M., and Paulen, R.C., 2011, Integrating ice-flow history, geochronology, geology, and geophysics to trace mineralized glacial erratics to their bedrock source: An example from south-central British Columbia: Canadian Journal of Earth Sciences, v. 48, p. 1113–1129.
- Porter, C. et al., 2018, ArcticDEM (National Science Foundation & National Science Foundation, Trans.); doi:[10.7910/DVN/OHHUKH](https://doi.org/10.7910/DVN/OHHUKH).
- Puranen, M., and Puranen, R., 1977, Apparatus for the measurement of magnetic susceptibility and its anisotropy.: Geological Survey of Finland Report of Investigation Report of Investigation 28, 46 p.
- Reeves, C., 2006, Aeromagnetic Surveys. Principles, Practice & Interpretation: Earthworks, p. 155, doi:[10.1007/BF01465543](https://doi.org/10.1007/BF01465543).
- Riisager, P., and Abrahamsen, N., 1999, Magnetostratigraphy of Palaeocene basalts from the Vaigat Formation of West Greenland: Geophysical Journal International, v. 137, p. 774–782, doi:[10.1046/j.1365-246X.1999.00830.x](https://doi.org/10.1046/j.1365-246X.1999.00830.x).
- Riisager, P., and Abrahamsen, N., 2000, Palaeointensity of West Greenland Palaeocene basalts: asymmetric intensity around the C27n–C26r transition: Physics of the Earth and Planetary Interiors, v. 118, p. 53–64, doi:[10.1016/S0031-9201\(99\)00125-9](https://doi.org/10.1016/S0031-9201(99)00125-9).
- Roest, W.R., Verhoef, J., and Pilkington, M., 1992, Magnetic interpretation using the 3-D analytic signal: GEOPHYSICS, v. 57, p. 116–125, doi:[10.1190/1.1443174](https://doi.org/10.1190/1.1443174).
- Rosa, D., Stensgaard, B.M., and Sørensen, L.L., 2013, Magmatic nickel potential in Greenland: Danmarks og Grønlands Geologiske Undersøgelse Rapport, v. 2013/57, p. 134.
- Rowan, L.C., and Mars, J.C., 2003, Lithologic mapping in the Mountain Pass, California area using Advanced Spaceborne Thermal Emission and Reflection Radiometer (ASTER) data: Remote Sensing of Environment, v. 84, p. 350–366.
- Rowan, L.C., Mars, J.C., and Simpson, C.J., 2005, Lithologic mapping of the Mordor, NT, Australia ultramafic complex by using the Advanced Spaceborne Thermal Emission and Reflection Radiometer (ASTER): Remote sensing of Environment, v. 99, p. 105–126.

- Salehi, S., Rogge, D., Rivard, B., Heincke, B.H., and Fensholt, R., 2017, Modeling and assessment of wavelength displacements of characteristic absorption features of common rock forming minerals encrusted by lichens: *Remote Sensing of Environment*, v. 199, p. 78–92, doi:10.1016/j.rse.2017.06.044.
- Sørensen, L.L., Stensgaard, B.M., Thrane, K., Rosa, D., and Kalvig, P., 2013, Sediment-hosted zinc potential in Greenland Reporting the mineral resource assessment workshop 29 November - 1 December 2011: , p. 184.
- Svennevig, K., 2019, Preliminary landslide mapping in Greenland: *Geological Survey of Denmark and Greenland Bulletin*, v. 43, p. 1–5, doi:10.34194/GEUSB-201943-02-07.
- Thorning, L., and Stemp, R.W., 1998, Airborne geophysical surveys in central West Greenland and central East Greenland in 1997: *GEUS Bulletin*, v. 66, p. 63–66, doi:10.34194/ggub.v180.5087.
- Ulf-Møller, F., 1990, Formation of native iron in sediment-contaminated magma: I. A case study of the Hanekammen Complex on Disko Island, West Greenland: *Geochimica et Cosmochimica Acta*, v. 54, p. 57–70, doi:10.1016/0016-7037(90)90195-Q.
- Ulf-Møller, F., 1977, Native iron bearing intrusions of the Hammersdal complex, North-West Disko: *Gronlands Geologiske Undersogelse Rapport*, v. 81, p. 15–33.
- Walter, C., Braun, A., and Fotopoulos, G., 2020, High-resolution unmanned aerial vehicle aeromagnetic surveys for mineral exploration targets: *Geophysical Prospecting*, v. 68, p. 334–349, doi:10.1111/1365-2478.12914.
- Weiss, A.D., 2001, Topographic position and landforms analysis, *in* Poster presentation: ESRI International User Conference, p. 1, <http://mfkp.org/INRMM/article/13930813>.

VI

Chapter 6 – Discussion

In this section, I address issues that were only briefly or not discussed in the presented research manuscripts and provide recommendations of data acquisition, processing and integration, as well as hyperspectral image assessment and examine selected external factors that influence UAS-based surveying.

Discussion

The following subchapters include a discussion on spatial, spectral and integration issues which I encountered during the work in my thesis. I provide an evaluation of area and resolution in qualitative form. Further, I show instances of UAS-based images compared to satellite data and ground examples to accentuate application differences. UAS-based surveying can provide high-resolution results. Depending on the required spatial or spectral resolution and survey area, either fixed-wing, helidrones or multicopter UAS were selected in the presented case studies.

6.1 Acquisition

6.1.1 Spatial footprints and survey efficiency

A survey area comparison between the three main UAS types is useful to frame the survey footprints as provided in this thesis (Figure 6.1). First, a UAS survey footprint is simply the covered surface area per flight, campaign, or case study. Measuring and reporting the area covered by UAS makes studies comparable and provides a first orientation of the preferable UAS drone. The literature review illustrates the scales at which the relevant drone types, multicopter and fixed-wing are usually used and includes our survey footprints. It shows that multicopter operations are between 0.01–1 km², and fixed-wing surveys between 1–100 km².

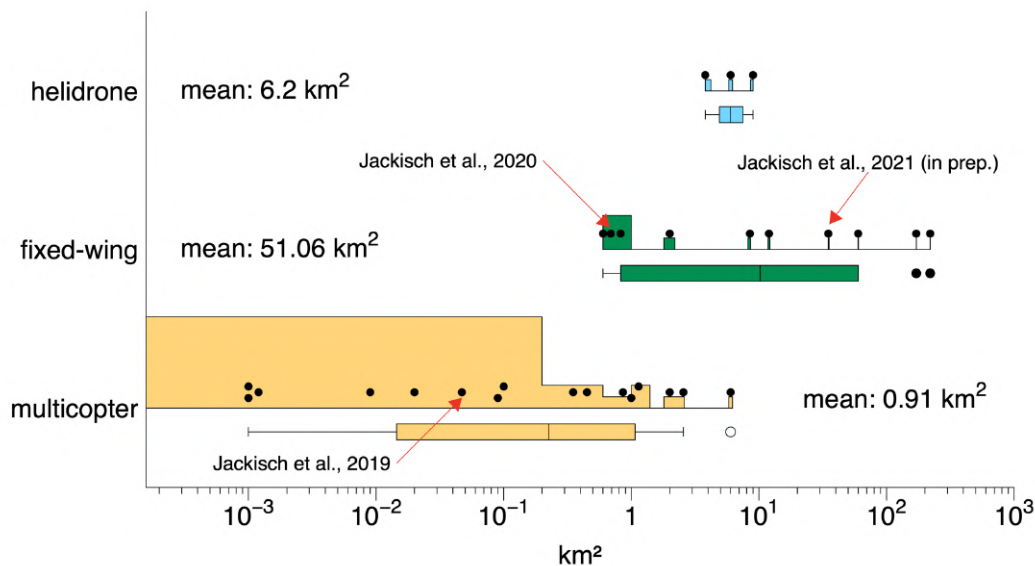


Figure 6.1 Distribution of survey area that was retrieved from available literature ($n = 29$; largely magnetic survey, section 1.2.2) and own surveys, categorized into 3 UAS groups. Boxplots plotted below pseudo-histogram, and mean survey area given per drone type. The interquartile range represents a good approximation of practical UAS survey scales.

A projection for UAS-based magnetic and hyperspectral survey footprints, in data points per m², illustrates the spatial prominence of magnetic fixed-wing survey compared to multicopter

and ground survey, based on data from this thesis (Figure 6.2). The survey footprint is an important aspect to evaluate for UAS data, as it makes the results transferable to future projects. At the presented scale, mine operators are inclined to use daily inspections and light-weight drones with RGB cameras to monitor extraction progress, blast points and tailing dams (Park and Choi, 2020). As seen in Greenland (case study C), the worth of airborne hyperspectral and satellite data rests in large-scaled, scarcely explored regions. Furthermore, satellite image products can support UAS-based image data, effectively, if they are available at useful spatial or spectral resolution, have sufficient radiometric quality and come at reasonable cost.



Figure 6.2 Spatial footprints of magnetic and hyperspectral UAS-based surveys from this work in true scale. The colour-coding represents the data point density per m^2 , calculated from clipped data points along the flight lines or the image pixel, including the spectral dimensions for the images and the XYZ dimensions for fluxgate magnetometers. Therefore, the actual survey data structure inherently differs between spectral imagery and magnetics. HSI = hyperspectral; mag = magnetics. The data from Greenland includes two HSI mosaics from Qullissat and Illukunnguaq (Duan et al., 2020).

In magnetic data acquisition, the distance between the flight lines and the sampling density along the line defines subsequent grid resolution. One factor for effective surveying using fixed-

wing UAS is the turning-space at the end of a survey line. In case study 2 with small line spacings, every third line was flown consecutively, while two adjacent lines were skipped to fly smooth turns with minute roll angles. That extends flight endurance and enables increased safety, but stretches the covered flight areal beyond the survey area. Multicopter magnetics can fly point-precise sweep patterns, applied in magnetic survey (Reeves, 2006), where no line turnings are flown. This is advantageous in small confined spaces, for example in open pits, near steep walls, or when there is no flight permission for adjacent land. For the first case study, the fixed-wing UAS flew dense sweep patterns.

The survey areas had a flat topography with consistent tree height at 15–30 m, bordering the outcrop area. Such situations provide some challenge to the UAS and the pilot. During the final case study in Greenland, the steep topography and high slopes forced flight lines that were executed in parallel to the main geologic strike. A decreased lateral magnetic susceptibility contrast, that is not advantageous for mapping and modelling, cannot be excluded from the data (Figure 5.4). An RGB photogrammetric survey was not included, favouring an MSI-UAS survey due to the constrained time budget. It is suggested for follow-up surveys. Further, in Greenland, the relevant ground truth magnetics cover a sum length of 27.96 km line kilometres and were measured in around 4 field days with intermissions. A total of 216 km UAS-magnetic lines were flown in about 3.7 hours (sum without technical intermissions) at 40 m line distance, which is significantly faster than our ground surveying at 50 m and 100 m spacing, respectively. The total area surveyed in Greenland was 35.8 km², that includes 8,979 single MSI frames and 82,932 magnetic data points.

To deduce performance indicators from the acquired UAS survey data in this thesis, a comparison of survey area against time-unit (Figure 6.3) illustrates that the size of a target area had a major impact on the selected UAS type (multicopter or fixed-wing) and spatial footprint (Figure 6.2). Most surveys were completed in under 100 minutes flight time. This time excludes several battery change times for multicopter. For large survey areas between 0.5–20 km² only fixed-wings were used, due to their higher flight efficiency (Figure 6.3a). A comparison of surveyed area per time unit, versus image resolution shows that fixed-wing and multicopter performance can be comparable. The advantage of multicopter hyperspectral imaging is high spectral and spatial resolution for moderately sized targets with about < 0.1 km² (Figure 6.3a). Eventually, the efficiency of image spectroscopy is highly case-specific and depends on spectral range, detectable signatures, required resolution, among others.

An assessment of the three magnetic data acquisition methods (ground, multicopter, fixed-wing) is more straightforward and shows a progressive advantage in surveyed area per unit

time, from ground survey over multicopter towards fixed-wing application. Multicopter magnetics are on par with ground survey in line spacing, but around 5–10 times faster. Fixed-wing magnetic surveys are again faster than multicopter, but can only be included at less line spacing within this example (Figure 6.3b).

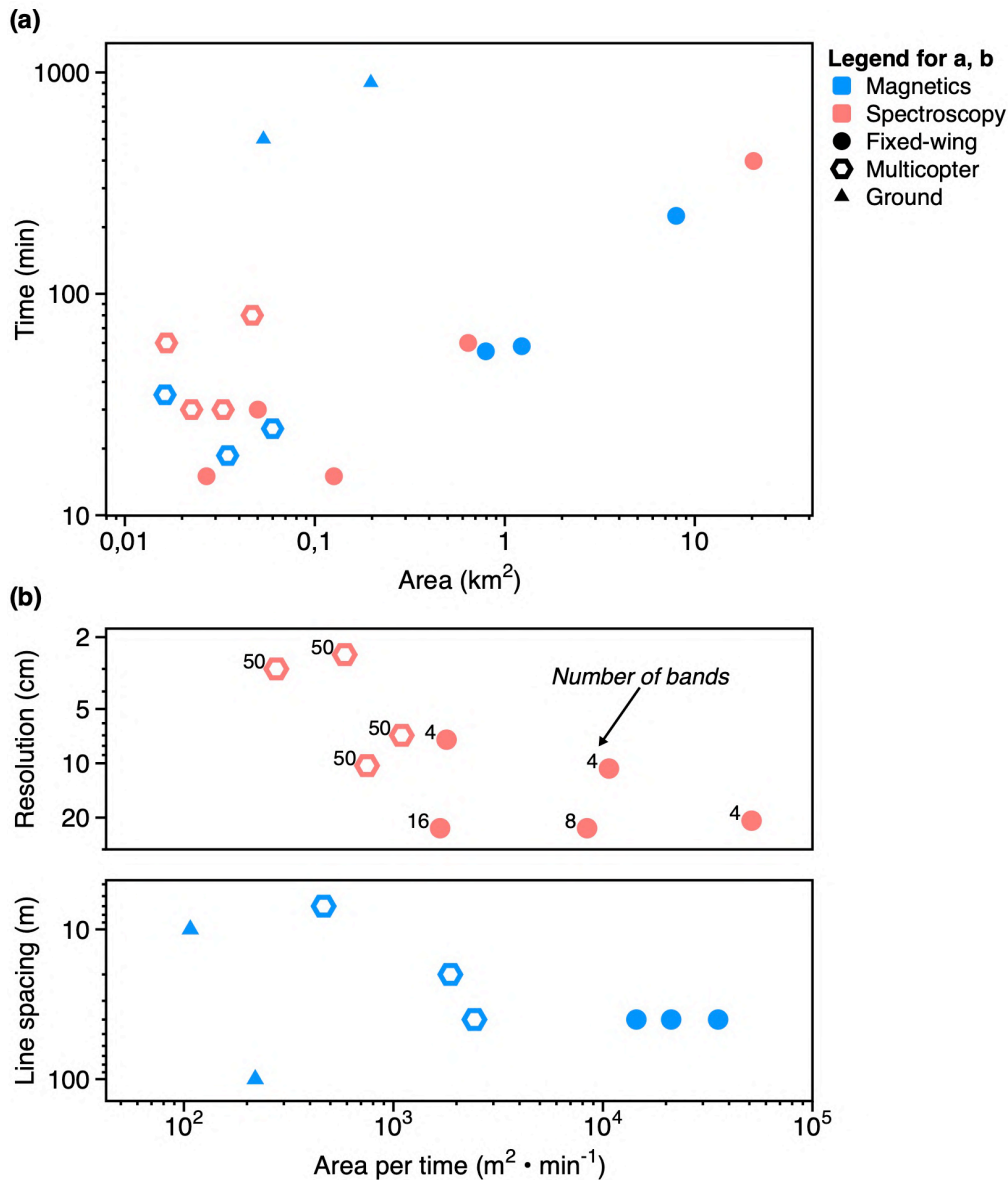


Figure 6.3 Plots of UAS performance (space, time, resolution) with survey data from the case studies. (a) Total surface area versus survey time, with a fitted exponential function and a 95 % confidence (conf.) interval. (b) The upper plot shows calculated survey area per time unit (x-axis) versus pixel resolution of image spectroscopy (y-axis), the lower plot shows magnetic flight line spacing (y-axis). Data includes only spectroscopy and magnetics.

6.1.2 Ground sampling

This work includes a variety of direct surface data for reference and validation of the spectral images and magnetics. The necessary ground sampling during field data acquisition demanded the largest time budget proportion per survey day. In sum for the three main field sites, 51 spectra from Otanmäki (Figure 3.10c), 336 ground spectra for the three trenches in Siilinjärvi

(Figure 4.5) and 204 spectra at Qullissat were collected (Figure 5.9). Several hundred ground-based susceptibility measurements were taken at all study sites combined. However, the ground susceptibility approach is a first-order approximation of magnetic rock properties, and cannot replace laboratory measurements. The decision on whether a sample is required was based on field conditions, experience and own personal safety. In-situ spectroscopy has the advantage of being directly comparable to UAS-based image spectra and handheld samples serve in subsequent laboratory analysis and as archive.

In case study 2, the field work of three days followed the legacy exploration trenches for magnetic susceptibility conducted by the Otanmäki mine company. The three acquired sample lines of our study included pXRF scans for chemical surface characterization and surficial magnetic susceptibility. A Pearson correlation between XRF-measured iron oxide and magnetic susceptibility and iron absorption compared between ground, and HSI image spectroscopy provided satisfying agreement (Pearson r of 0.83, resp. 0.80, Figure 3.15). Those results illustrate the capability of UAS to measure iron-alteration of low reflective intrusive magmatic rocks.

The acquisition workflow per outcrop in Siilinjärvi followed a sharp time schedule and was coordinated with mine safety. The ground sampling density differed significantly, which is attributed to the reduced time budget and existing transportation means in the mine. In summary, trench 1 was over-sampled, trench 2 sampled at 50 %, and trench 3 was probed along an oval-spaced sampling path with an under-represented central area. A DSM (Figure 4.6d) illustrates elevation differences of ~30 m and steep slope gradients in the third trench. We picked the training and validation points for the supervised classifications based on our ground data, and received a grand mean of 93.5 % for the reported overall accuracy. Furthermore, the high sampling density contributed to the experimental validation of UAS-based REE detection with HSI spectroscopy (Booyesen et al., 2020).

For Greenland, the survey conditions and time budget required a straightforward sampling approach. Additional probe material from outcrops increased carry weight and each requires necessity evaluation. Detours are not taken, therefore, the actual sampling route of a two-person ground team covered only a fraction of the potential survey area. However, the area is covered seamlessly by UAS at a kilometre scale (Figure 5.2), showing the efficiency of UAS in that scenario.

6.1.3 Solar elevation and survey window

The position of the sun is a crucial factor that affects the acquisition of UAS-based MSI/HSI data. As stated, we assume that the ground targets in this work are Lambertian, or diffuse reflectors (Palmer, 2003), that is the at-sensor radiance is independent of the viewing angle. Secondly, we assume that radiometric and geometric image corrections were applied beforehand (Jakob et al., 2017). When the solar position is known, the horizontal shadow length can be calculated with a simple equation:

$$L = \frac{h}{\tan \alpha} \quad (6.1)$$

where **L** is the shadow length, **h** is the object height and **α** is the angle between the horizon (a horizontal plane) and the sun (solar elevation). **L** and **h** share the same unit and **α** can be obtained from various references or online platforms (e.g., <https://planetcalc.com/318/>; <https://www.esrl.noaa.gov/gmd/grad/solcalc/azel.html>; last accessed 30.11.2020). We can calculate the shadow heights of an imaginary object ($h = 10$ m) for three main locations relevant to this work: Freiberg (50° N), Siilinjärvi (63° N) and Qullissat (70° N), a cast shadow length of 14 m, 17 m and ~20 m is calculated (05.08.2019, 12:00:00 CET). That shows the high demand on survey planning to include intensive topographic shadow for flight planning at high latitude. This was the case in the Finland surveys, but the locally flatter topography mitigated this issue.

Another aspect was monthly survey time windows. In Greenland, although the days are abundant with daylight during summer, the actual optical survey time windows that will deliver promising data might be limited. A related issue has been investigated at the Nunngarut Peninsula, West Greenland. Atmospheric corrections were conducted for VNIR-SWIR outcrop scans. The authors remarked that topographic corrections require careful application, and suggested that poorly illuminated areas and pronounced shadow zones should be masked, or at least interpreted with great care (Lorenz et al., 2018).

Solar elevation and atmosphere affect all satellite images taken at arctic and sub-arctic latitude. For example, the Landsat 8 user guide recommends being careful with all image products taken above 65° north or south, due to uncertainty in the processing quality (Young et al., 2017). Reasons identified here are high cloud cover, low solar angle and arid, water-saturated or snow-dominated areas. Daily updated satellite archive data (<https://worldview.earthdata.nasa.gov/>, last accessed 05.01.2021) illustrates the development of clouds and ice on Disko Island (Figure 6.4) with images captured by the MODIS Terra and Aqua satellites. A successful exploration campaign using UAS relies on clear view conditions. For the field campaign in this work, a

survey window opened around the 24.06.2019 and lasted for 77 days till around 09.09.2019, when snowfall increased. Practically, that window is shorter because $< 0^{\circ}\text{C}$ air temperatures and continuous near-coast cloud packets obstruct safe flight conditions for aircraft and UAS alike. Furthermore, UAS-battery lifetime is highly influenced by temperature-influenced capacity fluctuations, risking the operation. An endurance drop rate of 25 % or more for lithium-ion batteries is reported during low temperatures, and increased awareness is advised for air temperatures $< 20^{\circ}\text{C}$ (Chauhan et al., 2019). Our field results show that topographic, weather and light conditions can and will inhibit exploration campaigns, mainly when using UAS-based spectral imaging and structure from motion photogrammetric products. Furthermore, magnetic surveying is affected by UAS flight by adverse view conditions and low temperatures.

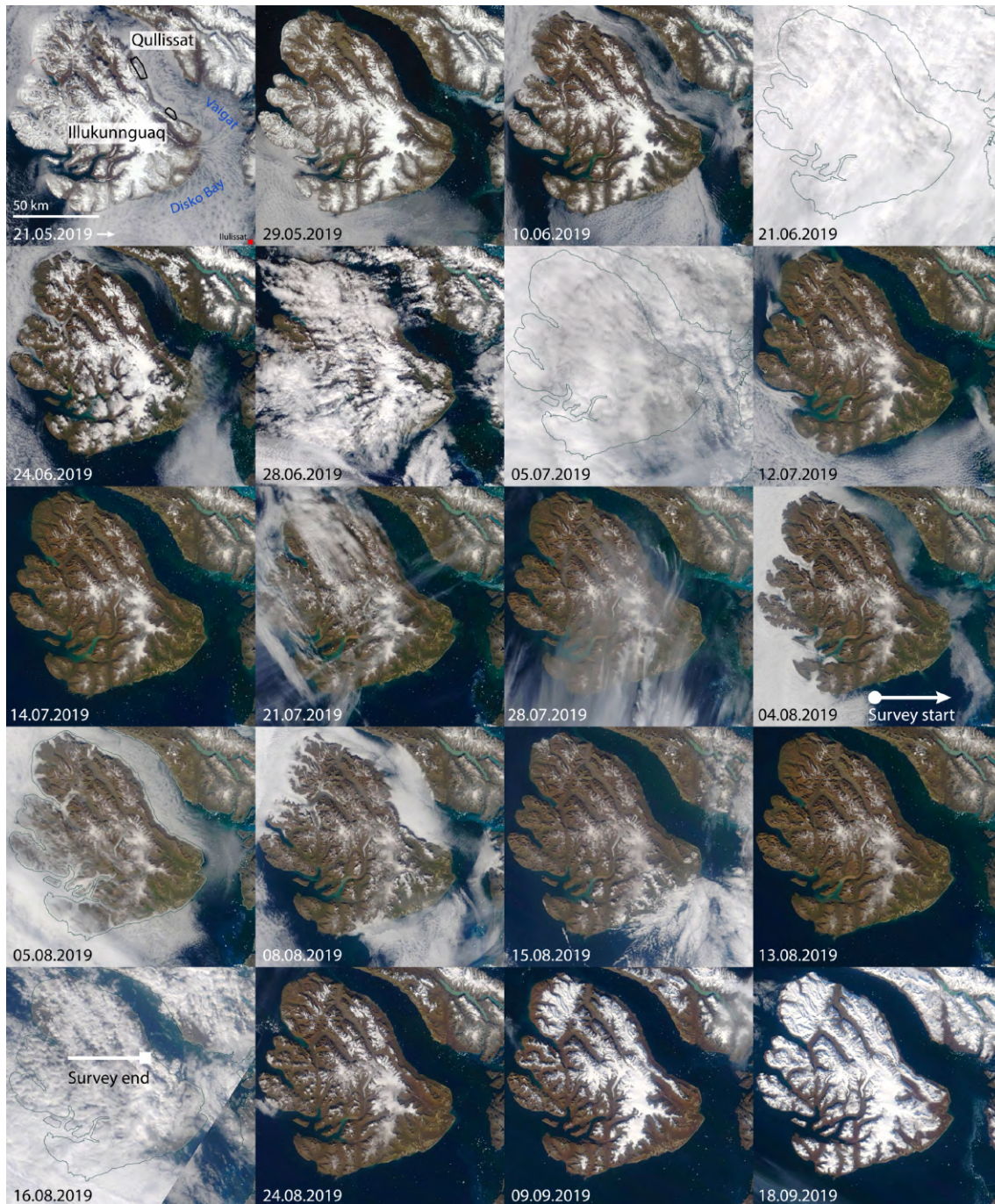


Figure 6.4 Displayed is a time series of Terra MODIS satellite images, showing the complete Disko Island and the southern part of Nuussuaq peninsula. Around the survey areas along the north coast, snow, and ice cloud the ROIs till the 24.06.2019, thereafter a survey window opened that lasted until early September 2019. The year was documented as an Arctic record warm year (Sasgen et al., 2020).

6.1.4 Magnetic data acquisition recommendation

The data acquisition strategies in this thesis were developed before and during the conduction of the first two case studies. Technical developments, adjustments, and tunings were necessary especially to integrate the Dronemag fluxgate magnetometer with the multicopter. It is recommended to increase sensor-drone distance as far as possible (Jirigalatu et al., 2021). We further showed that a fixed-wing UAS can survey areas around 10–20 times faster than one

person with a ground magnetometer. Acquired coverage ranged between 0.05–1 km² (case study A, B). In Otanmäki, we acquired magnetic data at three survey elevation levels (15 m, 40 m, 65 m; Figure 3.11) for subsequent comparison with ground magnetics and quality control. If possible, magnetic UAS-based surveys should cover identical plots in at least two elevation levels. Moreover, partial coverage can be sufficient. This increases quality control, reduces signal ambiguity and benefits joint modelling, respectively inversion (Le Maire et al., 2020). Magnetic noise protocols should be delivered for quality assessment. As seen in case study 3, a steep topography enforces partially higher flight altitude with potentially negative effects on the measured magnetic signal of geologic anomalies.

6.1.5 Image acquisition recommendation

Acquisition of high-resolution photogrammetric RGB data proved to be essential and supported subsequent data processing, 3D integration and interpretation. We found the application of GCPs to correct RGB photogrammetric data as most useful. Our examined data rely on ground calibration targets and sample evaluation. Therefore, I commend the straightforward integration of GCPs in the acquisition part. All data points geolocated by GPS in this thesis contain a certain positioning error. The existing real-time kinematic and post-processing kinematic solutions can increase the standard GPS accuracies by a magnitude (Tomaščík et al., 2019), if such services are available. Although high navigational precision is advised for the vulnerable polar regions, the use of GNSS augmentation services is not yet fully established in the polar (drone-user) community. Poor vertical position accuracy, ionospheric scintillation and base station lack are among the reasons (Sheridan, 2020). Furthermore, the use of low-cost calibration panels is advised as best measure to spectral calibrate image data. It is recommended to GPS-mark the panel location for larger survey areas, and to capture several images of the same panel cluster, and the beginning and end of a flight.

Case study 3 was conducted under the challenging topographic conditions. A clear suggestion is that multi/hyperspectral UAS surveying should have priority scheduling in a Nordic campaign (Assmann et al., 2019), and start at the same time each day. Surveys with less light dependency should follow in schedule, i.e., magnetics. In remote and unpopulated areas, the conduction of beyond visual line of sight UAS survey is beneficial to cover the area more efficiently. In remote and unpopulated areas, the conduction of beyond visual line of sight UAS survey is beneficial to cover the area more efficiently. Acquisition was completed under analogous climatic and atmospheric conditions at the three sites. As mentioned, shadows caused by undulating relief, low solar angles, lichen, and debris are part of each acquired data set and

were addressed in processing. In case study 1, up to 30 % of all optical data is covered by lichen and debris. In such cases, the acquisition of multi-source data improved interpretation and reduced ambiguity.

6.2 Processing

6.2.1 Hyperspectral reliability

Atmospheric conditions are a major factor that influence the fidelity of hyperspectral data. During several occasions of the HSI surveys in this thesis, the weather conditions allowed only limited visibility, approximately less than 3 kilometres of view distance and a cloud ceiling below 1000 metres. Those flight conditions would be deemed risky from an aircraft pilot perspective, but less so for UAS use. For hyperspectral flights that last 15–30 minutes, a change of the atmospheric composition is less likely, but cloud cover can change. That means a sudden modification of the total reflectance per scene. Therefore, absolute scene comparison becomes more complicated. To minimize the effect of illumination change, evenly illuminated regions could be interpreted as separate images or a radiometric correction using an irradiance sensor could be used. But experiences with data from the Greenland surveys showed that the eBee Plus irradiance sensor not increase the spectral image quality.

All hyperspectral data sets in this work were pre-processed from raw data to radiance with the Rikola hyperspectral imager software (version 2.0, SENOPS, former Rikola Ltd., 2016). Radiometric and geometric corrections followed the workflows outlined by Jakob et al., 2017. The conversion from at-sensor-radiance to reflectance (Karpouzli and Malthus, 2003) is required for spectral comparison with reference material spectra. For the conversion, we used cost-effective, store-available PVC panels with an average reflectivity of ~98 % for white, ~20 % for grey and ~5 % for black shade. The UAS-based reference panel scans are usually conducted shortly after UAS take-off. The panel spectra are digitized and cross-referenced with an optical-quality PTFE panel (Spectralon[®]) in the laboratory. During stable atmospheric conditions, the practise of reference panels is considered a highly accurate approach (Aasen et al., 2018). Another error source is surface alterations of the panel itself. Therefore, proper panel handling, transportation and routine cleaning of the surface is self-evident. Dust transported by winds and abbreviations from former field days accumulate on the surface and contribute to mixed spectral response.

To systematically investigate the general spectral characteristics, I obtained ten grey panel radiance values from our different study sites (Figure 6.5a). Starting from mid-2016 till the last MULSEDRO field campaign of late 2019, all at-sensor radiance values from an ROI covering

the grey panel are plotted for comparison (Figure 6.5b). A drawback of this approach is that the panels were replaced by similar versions, due to their abbreviation during field work. At first glance, the measured panel spectra appear similar but the distribution of variance and net offset are seen in the violin distribution plots (Figure 6.5c). Violin plots can be considered as a combined box- and kernel density plot that show the entire distribution, especially when various data peaks are expected. High radiance with multiple peaks illustrate sunny conditions and the dented areas correspond to the known sensor shift. Standard deviations are aggregated around $0.5\text{--}1.5 \text{ mW}\cdot\text{nm}^{-1}\cdot\text{sr}^{-1}\cdot\text{m}^{-2}$ and the histogram fits to a stretched exponential distribution (Figure 6.5d). Importantly, the signal-noise-ratio (SNR), shown as function per band mean, increases from 504–639 nm, drops for about 30 % between 639–671 nm, then decreases below the initial level towards 900 nm.

There is less SNR variation in the NIR region, indicating a stability of band ratios used with this camera (e.g., in Litov; see Jackisch et al., 2018). The average SNR per campaign survey is changing (Figure 6.5f). The Rikola band range between $\sim 550\text{--}671$ nm is susceptible to this systematic error and spectral analysis at that range should be treated carefully. However, further external noise sources, such as air moisture, camera temperature, warm-up times, panel quality and further could not be evaluated under field conditions.

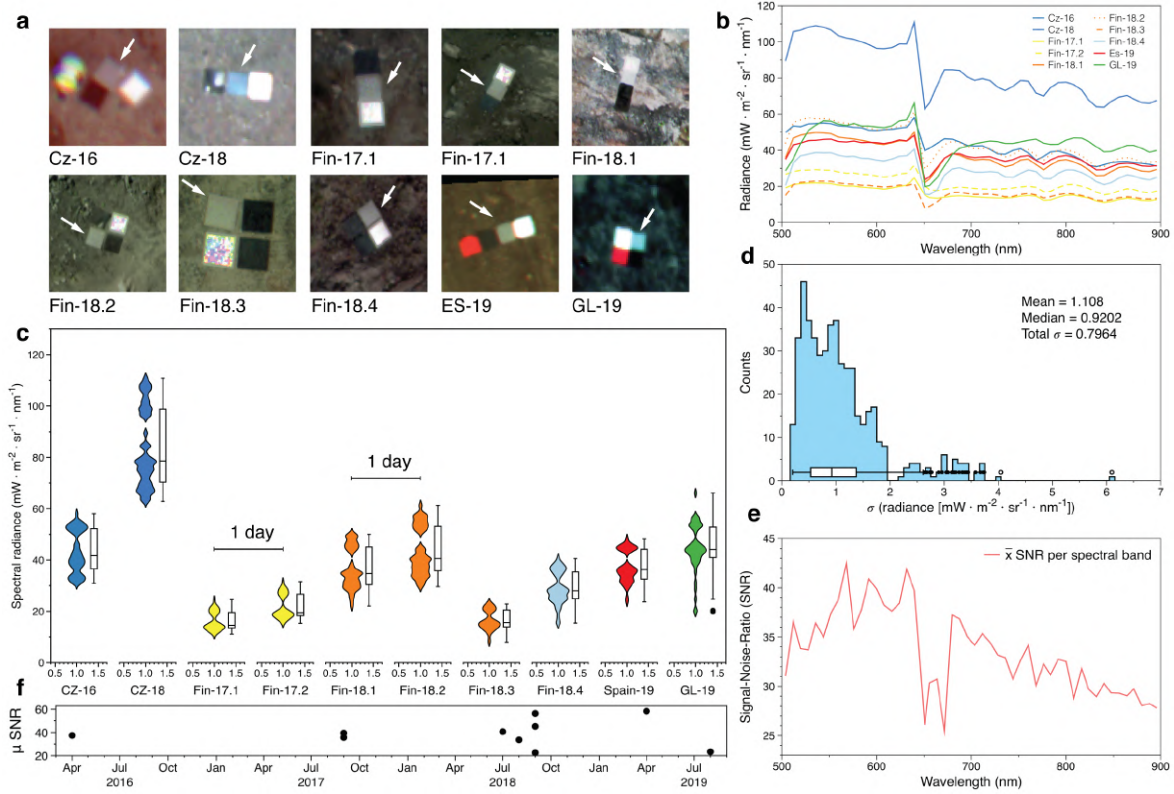


Figure 6.5 Radiance distribution of each calibration panel per HSI campaign. (a) RGB composite images show the black, grey, white and an unused red calibration panel (bands 17, 7, 1). (b) Mean radiance plotted per campaign. (c) Violin density distribution and aligned boxplot illustrate the radiance variation per grey panel. Different integration times and solar azimuth influences at-sensor radiance. (d) Histogram of standard deviations for all bands and campaigns show signal deviations. (e) Signal-to-noise-ratio calculated per band, shows a signal decrease towards the NIR spectrum, and a sharp SNR drop between 639–671 nm, caused by the sensor shift. (f) Mean SNR value computed per campaign.

At instances where the pilot was manually controlling the UAS, we could acquire several images of a panel group (Figure 6.6a). To evaluate the accuracy of HSI data, I retrieved a pair of overlapping images including the same panels. The georeferencing was improved manually in QGIS to obtain a high-precise pixel overlap for the panels. I placed sampling points inside a rectangular polygon-layer of both panels, using the random point creation function in QGIS. A mean radiance distribution is plotted and shows a nearly similar spectrum (Figure 6.6b), with a RMSE of $0.23 \text{ mW} \cdot \text{nm}^{-1} \cdot \text{sr}^{-1} \cdot \text{m}^{-2}$ (0.38 % mean deviation). I extended the statistical analysis of the sampling points further in RStudio (RStudio version 1.2, the R team, 2019) with a linear regression (Montgomery et al., 2012) to compare selected bands per sampled reference pixels (Figure 6.6c). The averaged sum of regression residuals from those sampling points of $-2.24 \cdot 10^{-17}$ is near-zero. The linear regression plots between the two panels (Figure 6.6c) show a satisfying correlation in wavelength ranges that have a high SNR (Figure 6.5e).

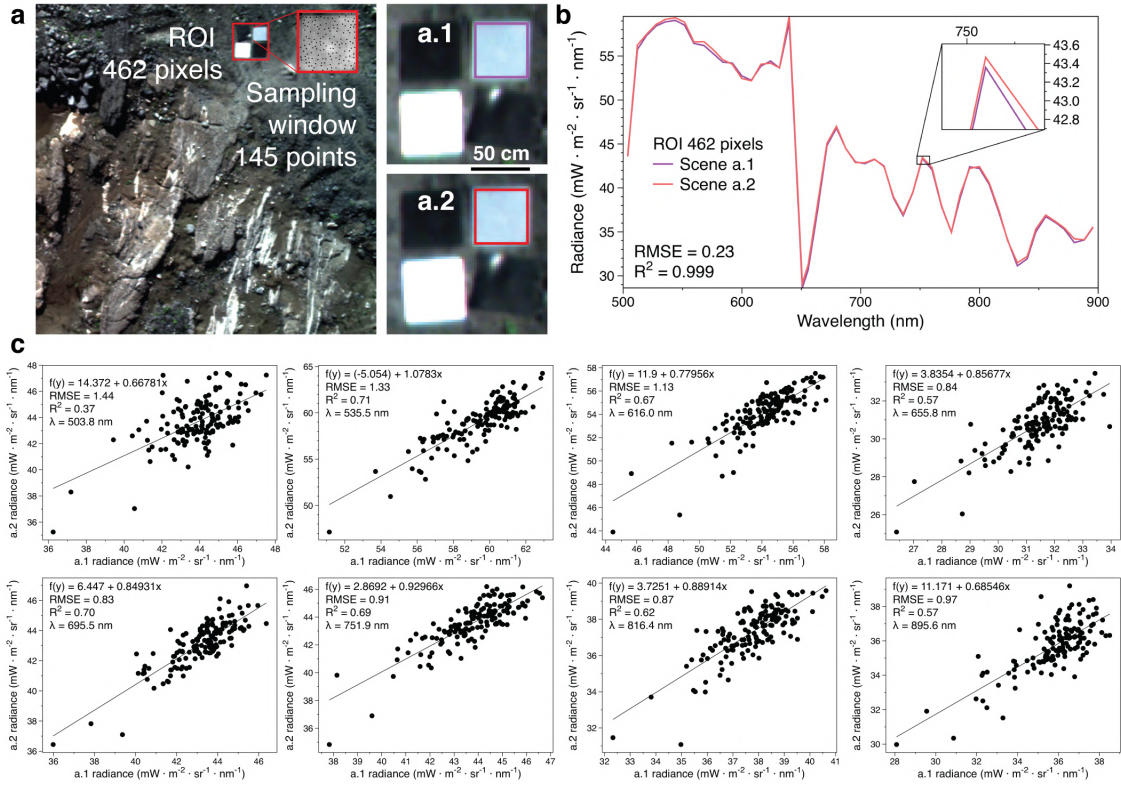


Figure 6.6 Comparison of two Rikola HSI scenes (a) over the same target at Siilinjärvi, rare sunny conditions. Scenes taken successively during the UAS flight at trench 2 with an integration time of 10 ms. (b) Plotted radiance spectra as mean extracted from the grey panels of scenes a.1 and a.2. (c) Scatter plots of the 145 sample points at eight selected bands of panels a.1 & a.2, plotted with the linear regression response equation, the RMSE in radiance units, the R^2 and the corresponding band wavelength.

6.2.2 Narrow spectral absorption features detected by HSI methods

Good efforts were made recently in the hyperspectral detection of narrow, REE-related absorption features (Turner et al., 2014; Boesche et al., 2015). Their characteristic absorption minima at narrow widths, e.g., between 800–830 nm for Nd^{3+} and Dy^{3+} , were detected with the Rikola camera in artificial and natural samples (Figure 6.7; Booyesen et al., 2019; Lorenz et al., 2019). Siilinjärvi data gave the opportunity to test the actual challenges in mapping REE-features at different sampling conditions (Figure 6.7a, b). As reported, the carbonatite-glimmerite is enriched with apatite that contains REEs (O'Brien et al., 2015). The main obstacle for REE mapping was capturing a low-noise HSI frame under suitable atmospheric conditions with adapted HSI camera settings. Our successful field tests proved that UAS-based hyperspectral data can detect REEs. Based on experience, we adapted the scene integration time according to the daily sunlight conditions. We used 10 ms integration time for sunny to light-overcast conditions. During strongly overcast skylight (grey, low ceiling), we used 30 ms with 50 bands standard setting. For the HSI mosaics acquired during low-ceiling clouds, a spectral identification of REE occurrence in the minor carbonatite lenses was futile. Testing supervised and unsupervised classifications only lead to a mixture of the similarly reflective carbonatite

lenses with the feldspar, due to their high spectral similarity. Hence, the identified carbonatite veins were mapped manually in a GIS environment for the larger hyperspectral mosaic (Figure 6.10i).

Camera sampling interval and spectral shift were examined under laboratory settings (Figure 6.7c) to better understand limits given by the sensor. We detected a spectral shift for the minimum sampling interval at 1 nm and the standard interval of 8 nm, using known peaks of irradiated light from a fluorescent lamp. Hg-related emission lines do occur at 546 nm and 611 nm for this setting, and an offset between 3–7 nm was seen. This offset artefact is known since our early investigation of the camera and has been described before (Pekkala et al., 2019). It can be resolved by a factory re-calibration or using the aforementioned emission lines of a well-characterized light source. Careful calibration and registration of HSI images has been studied in detail in former publications regarding frame-based HSI sensors (Honkavaara et al., 2013; de Oliveira et al., 2016; Tommaselli et al., 2018). Those studies were mainly focusing on the geometric image properties and were tested within vegetation and forestry research.

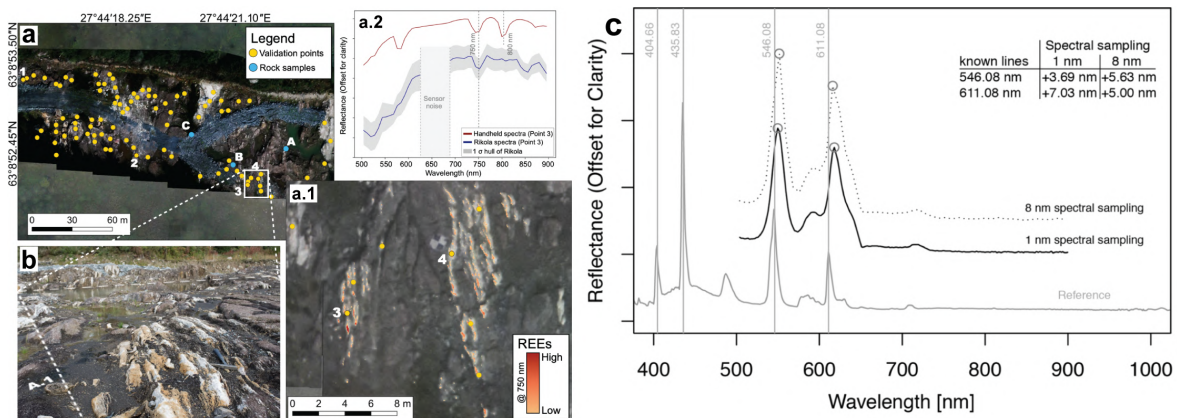


Figure 6.7 Example for detectable, narrow spectral absorptions caused by REE minerals found in apatite crystals. Figures modified after Booyesen et al. (2020). (a) Hyperspectral image mosaic, as seen in Figure 4.6 and 4.7. Yellow points display GPS-tagged spectral, validations points, blue points are rock samples. (a.1) Sub-figure showing a detailed view of absorption minima at 750 nm, indicating REE occurrence in the spectrum. Darker red represents higher light absorption, which is associated with higher REE abundance. (b) Northward showing field photograph over the HSI scene (Image courtesy Moritz Kirsch). (c) Investigation of spectral sampling intervals (1 nm, 8 nm) and its response signal to a known spectral feature. Here, the identified emission lines, of a fluorescent Hg-vapour lamp, were used for reference in a laboratory setting.

6.2.3 Processing suggestions

The acquired image spectroscopy data was processed using recommended routines (Jakob et al., 2017; Jackisch et al., 2018) and processing chains. Magnetic data processing was implemented following geophysical airborne and satellite data processing routines. The joint processing of multicopter-based magnetics (Madriz, 2019) resulted in gridded magnetic data products with proper data and heading corrections. Obtaining metadata from UAS flight

controllers (compass, inertial measurement unit) is required for further quality control and error analysis, e.g., direction offsets in x, y, z (see also Appendix F1). Adaptions for each case study were required for UAS-based targeting of mineral resources, in regard to scale and resolution. We recommend the use of a moderate number of spectral bands for a tuneable hyperspectral camera, depending on the targeted spectroscopic-mineralogic features. The broad iron feature absorption (700–900 nm) was fully resolved by UAS in hyperspectral data and evident in UAS multispectral images. Narrow REE absorption bands were evident within 50 spectral bands with 5–8 nm spectral sampling in 2–3 cm GSD (Booyesen et al., 2020). Our data suggests that more bands do not increase the spectral fidelity, when used in UAS-based surveying. For the spectral detection of narrow absorption features, a sufficient SNR ratio is important (Figure 6.5b). Furthermore, important is the integration time of HSI scanning. Both under- and over-exposure are serious noise sources. Therefore, integration time intervals should be tested before each field campaign.

6.2.4 Improving degraded image data

Optical images were subject to impeding weather conditions and mismatch of data resolutions among different data sets. Target outcrops were partially covered by vegetation (shrubs, lichen), dust, debris and further. We mitigated those issues by using masking, dimensionality reductions (MNF), feature extractions (OTVCA) and data fusion (see Chapter 4.2.2). Pixel masking was always necessary to create image products prepared for classification. Issues during processing of the large-scaled optical images in case study 3 were edge effects and illumination gradients, which could only be processed partially in a satisfying manner. But this data provides opportunity to apply corrective measures based on machine learning or inversion methods. A regression between extracted spectral characteristics of several similar HSI scenes including reference panels could be used to derive further correction factors, and thus increase the spectral reliability.

6.3 Integration

6.3.1 Integrating magnetics

The magnetic data of case study 2 comprises UAS-based fixed wing and public data. Magnetic susceptibilities were measured in the laboratory for a limited number of samples. Ground truth was provided from the exploration trenches, outcrops in the forested area were not accessible (Figure 6.8a). For the geology under cover, we defined the subsurface boundaries based on filtered and transformed magnetic products and forward modelling. Magnetic flight lines

(Figure 6.8b) and the gridded magnetic surface (Figure 6.8c) illustrate the gaps between the scanned area. The gridded magnetic data appears as a coarse image, and the space between flight lines is populated with interpolated values. We used the minimum curvature algorithm which creates quite smooth surfaces between data points (Smith and Wessel, 1990). Here lies a great opportunity to integrate UAS-based spectral and RGB data for an uninterrupted geological interpretation. Although, the ambiguous source depth of the geophysical signal complicates direct integration. The available public orthophotos are shown for completeness in good resolution (0.5 m) but were outdated during writing (pre-2017; Figure 6.8d). In our presented case studies, we acquired the data in only a handful of UAS field survey days. Planning, especially for magnetic line distribution and acquisition is critical and should only be compromised if flight safety would be compromised. Magnetic flight line distance should be sufficiently narrow, but target areas should not be dissected in overly small parts. Magnetic coverage should include a surplus of coverage outside the target area, to reduce integration issues and edge effects.

The mapped geologic subsurface structure as inferred from magnetic filtering and gridding Figure 4.10c) is influenced by the chosen flight line distance, which again is defined by topography and UAS endurance. Based on aeromagnetic surveying, the ratio between flight altitude and line spacing is often set between $1:2.5 \pm 1.5$. Those values depend largely on the required geological resolution and the survey budget (Reeves, 2006; Coyle et al., 2014). Favourable for detailed survey tasks are small line spacings that reduce the influence of line orientation on gridded magnetic maps (Isles and Rankin, 2013). The flight line distance also determines the detail at which a model can satisfy the resolution needed for inversion or forward modelling in accurate mapping, e.g., at a scale of $\sim 1:1000$. The Nyquist-Shannon-Whitaker sampling theorem, applied for geologic forward modelling indicates a minimum body resolution of 60 m based on the flight line spacing of 30 m in Siilinjärvi. Hence, the area between the trenches is resolved coarser and I set the geologic labels more conservatively as for visible geology. I show that difference for comparison in our data (Figure 6.10h & Figure 6.10i). A feasible integration of orthomosaics and magnetic grids depends on their resolutions. From the two smaller trenches 1 and 2, the fixed-wing magnetics provided less additional information on the visible surface geology (Figure 6.8a). I suggest a reduced feasibility of fixed-wing magnetics at outcrop size below 200 m, therefore a densely flown multicopter survey is suggested.

Magnetic UAS-fixed wing data points, with an average point distance of 2.5 m along the flight line (Figure 6.10h) records magnetic contrast. Regarding the magnetic response of the covered

dyke, a decrease in the TMI is recorded, and also for the surrounding carbonatite which is in assembly with glimmerite and contains trace amounts of magnetite. An interpolated raster grid of the flight lines was produced, using the minimum curvature gridding (Smith and Wessel, 1990). The original flight line distance of 30 m was upscaled to a 15 m grid for improved resolution contrast (Figure 6.10h). Caution is advised when the interpolated magnetic data is further used for geologic forward modelling. The chosen size of the model bodies should be relating to the flight line distance. Forward modelling in case study 2 was highly influenced by preliminary considerations of the RGB, and hyperspectral mosaics. Lastly, the structural modelling along the test pit provided sufficient structural constraints to build a plausible forward model (Figure 4.12).

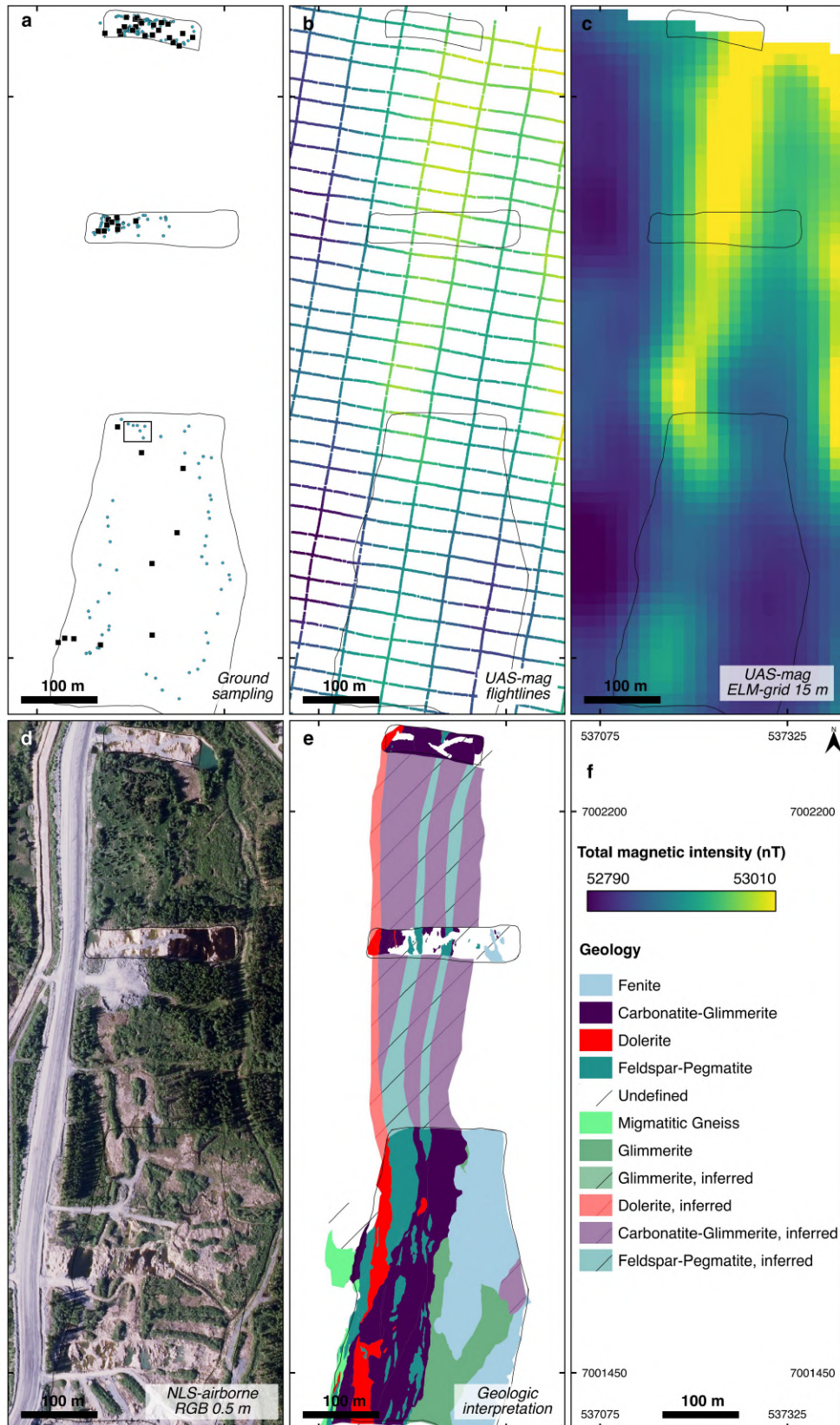


Figure 6.8 Sampling points, magnetics, and geology at Jaakonlampi. (a) Ground truth sampling for point spectroscopy (dot symbols) and rock grab sampling (square symbols). (b) UAS-based total magnetic field along flight lines, colour-coded. (c) Minimum curvature grid of equivalent layer magnetics, plotted at 15 m. (d) Publicly available RGB orthoimages at 0.5 m GSD. (e) Published UAS-based mapping (Jackisch et al., 2020). (f) Magnetic scale for subfigures b, c and geologic legend for e.

6.3.2 Spatial and spectral integration

Space-borne images with weekly location revisit can close survey gaps that were not covered using UAS. I selected Sentinel-2 satellite data (Drusch et al., 2012) as an example which is often used in remote sensing geology (Mielke et al., 2014; van der Meer et al., 2018). The Sentinel-2 multispectral instrument collects reflected light in a swath width of 290 km. The sensor covers 13 channels in the VNIR-SWIR range with a ground pixel resolution between 10–60 m depending on the channel. Area re-examining times between 2–10 days are possible, depending on position, latitude, and cloud coverage (sentinel.esa.int/web/sentinel/missions/sentinel-2; last accessed 19.12.2020). The high-resolution bands (10 m) are located in the VIS-NIR range, the medium-resolution (20 m) are in the NIR-SWIR and targeted for surface material characterization. Streamlined access via the ESA Sentinel hub provides access for unrestricted satellite data (scihub.copernicus.eu; last accessed 30.11.2020). I use those two remote sensing resources for comparison alongside our generated UAS-based image products at case study 2. For Sentinel S2A, scene S2A_MSIL2A_20180828T094031_N0208_R036_T35VNL in reflectance, including atmospheric and radiometric corrections (solar angle of $\sim 36^\circ$) was selected for comparison. For PlanetScope, scene 20180829_090335_0f4e (solar angle 34.8°) was acquired. All data products are cloud-free over the target area. An example is the PlanetScope satellites (Planet Team, 2017) that provide access to high-spatial resolution 4-band VIS–NIR images at 3.0–4.1 m GSD, delivered by satellite clusters (orbit at 475 km above surface). Image frames measure $24 \text{ km} \times 8 \text{ km}$, respectively $\times 16 \text{ km}$ (Planet Team, 2020). The daily revisit times provide images which are useful for geologic problems, such as detection of small structural features i.e., lineaments, texture patterns related to exploration.

Details in spatial and spectral resolution of integrated data at target scale are used to examine a sampled feldspar-rich pegmatite in detail. This unit is part of a larger dyke system and exhibits high surface reflectance but no diagnostic features in the VNIR, and it is non-magnetic. A reflectance spectrum of a reference point is provided by the handheld spectrometer PSR3500 and compared with a UAS-based HIS spectrum and a Sentinel-2A spectrum (Figure 6.9 and Figure 6.10i). The Sentinel-2A spectrum generally matches with the reference spectrum, but significantly deviates between 600–800 nm. Similarly, the UAS spectrum matches the ground spectrum between 500–700 nm but fluctuates beyond 800 nm. In this example the spectral signature of the material in the image pixel appears to be a mixture of geology, vegetation and cast shadow from the neighbouring unit. The spectral range, the number of bands and their

positions substantially differ. Atmospheric conditions during different acquisition times influenced the spectra.

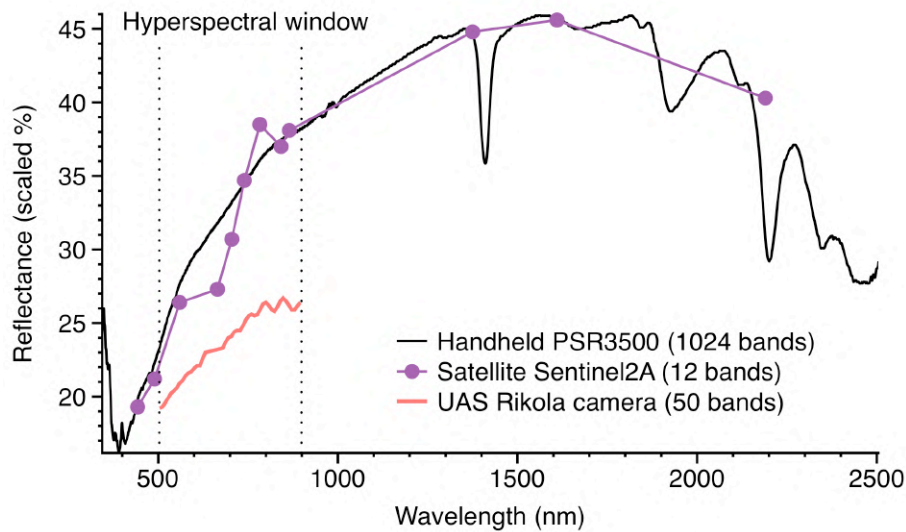


Figure 6.9 Spectral comparison of a PSR3500-handheld spectrum (350–2500 nm), satellite (normalized to PSR3500 reflectance) and UAS-based spectrum (Rikola HIS camera). The handheld spectrum point is a single measurement. Sentinel-2A presents one pixel at 20 m GSD and the UAS spectrum is the mean of a 6 m by 6 m area because atmospheric conditions were poor (Point visible in Figure 6.10i).

The target body has a maximum width of 15 m in the displayed section. Sentinel-2 data (Figure 6.10a) does resolve the bodies extending in 1–2 pixels. For PlanetScope data, 26 pixels capture the body with a 1 pixel rim of adjacent carbonatite-glimmerite (Figure 6.10b). The UAS-based image products, however, preserve the shape, geometry, and texture at the highest (1:100) scale (Figure 6.10c–g). Shadows, centimetre-sized carbonatite lenses and the reflectance/calibration panels are clearly visible.

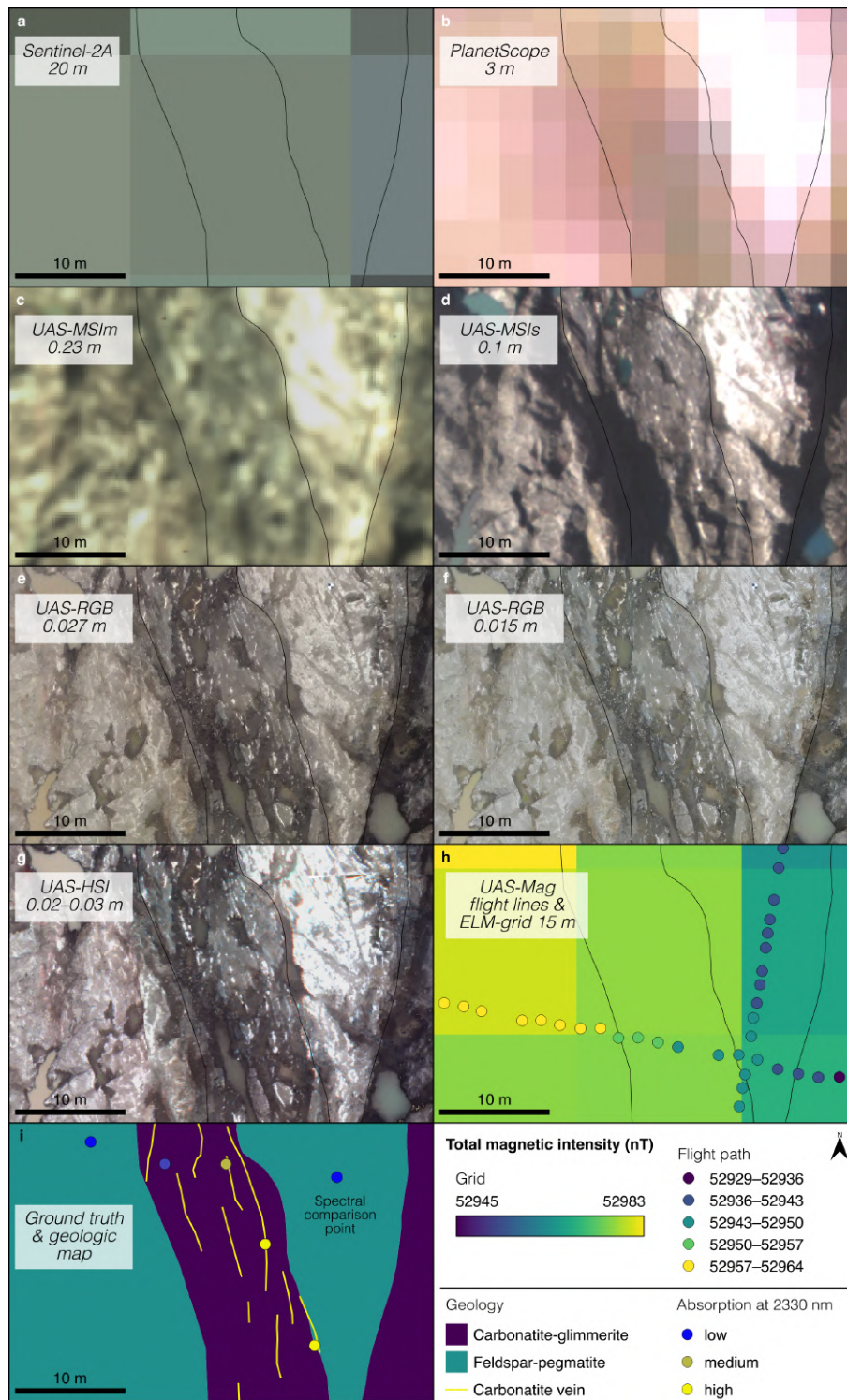


Figure 6.10 High-contrast resolution comparison for different sensors illustrates target resolution. Images in true-colour with band wavelength in brackets. (a) Sentinel-2A (665 nm, 560 nm, 490 nm) (b) PlanetScope (630 nm, 545 nm, 485 nm) (c) UAS-MSI 'msCam' (640 nm, 540 nm, 435 nm) (d) UAS-MSI Sequoia (735 nm, 660 nm, 550 nm) (e) UAS-RGB SODA (f) UAS-eBee S.O.D.A. (g) UAS-HSI Rikola (651 nm, 552 nm, 504 nm) (h) Fixed-wing UAS magnetic points over the gridded data (i) Spectroscopic ground truth points show feature depth at 2330 nm and mapped geologic features.

6.3.3 The value of integrated public geologic and satellite data

The access to publicly available geologic maps, digital surface models and satellite imagery was crucial to all case studies. As mentioned before, in countries with strong incentive to develop mineral exploration, there are data access portals that provide geological and geophysical maps at different scales. Geologic surveys provide sub-meter scaled airborne RGB and NIR orthoimages, Lidar-based point clouds and DSM data. An improved data sharing between geological surveys, mining industry and the public is essential to strengthen partnerships and knowledge transfer (Ali et al., 2017). Practical examples are the Government of Greenland, GEUS, and the National Land survey of Finland and GTK. The Greenland portal (greenmin.gl; last accessed 10.11.2020) is an open-access platform that shares data relevant for mineral exploration of Greenland. Similarly, the National Geological Database of Finland (<https://www.gtk.fi/en/services/data-sets-and-online-services-geo-fi/national-geological-database/>; last accessed 10.11.2020) provided geophysical and geological datasets for the direct comparison and interpretation of data products found in this thesis.

For the Otanmäki survey, we used a geologic reference map (Figure 3.2) for guidance on how to design the UAS-survey line headings. To achieve a high magnetic contrast, we set the main flight direction perpendicular to the magnetic orebody (Figure 3.5), with $\sim 10^\circ$ deviation to the ground survey lines. The resulting total magnetic anomaly maps are in good agreement with the local geology and ground-based magnetic measurements (Figure 3.12). A legacy map (Figure 6.11) from the Otanmäki site was compiled from several map sheets that consolidate magnetic surveys of numerous field campaigns, dating back years (personal communication Jouko Jylänki, Otanmäki mine Oy, 05.09.2018). The map features a high level of detail and shows the subterranean tunnel layout of the Fe-Ti-V mine site. The legacy map comparison (Figure 6.11a) illustrates the high efficiency at which UAS can acquire magnetic data. The fixed-wing UAS magnetic survey (Figure 6.11b) was conducted in about one hour.

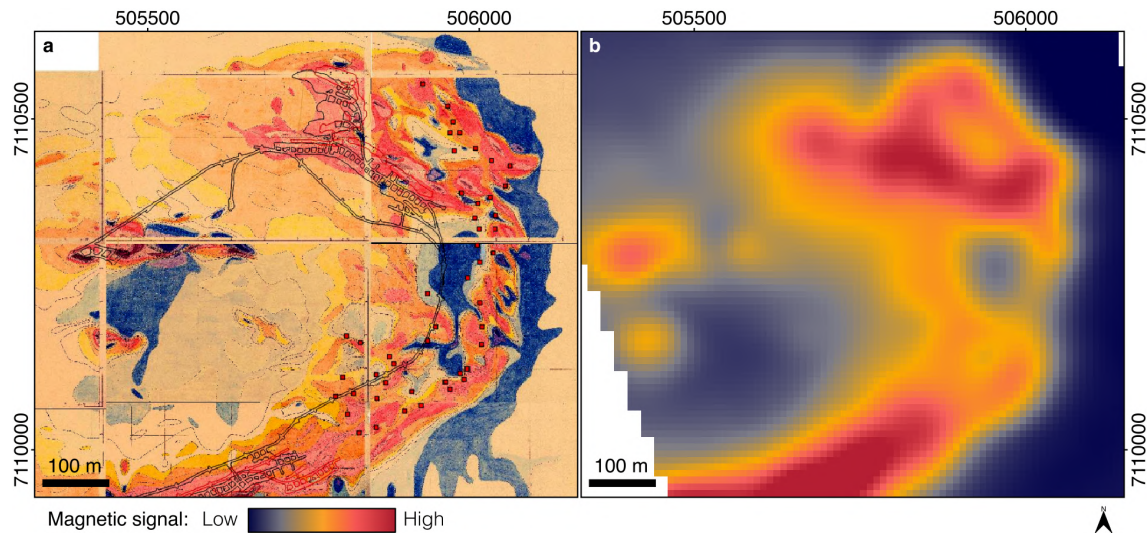


Figure 6.11 Comparison of legacy (a) ground magnetic mapping and (b) fixed-wing UAS-based magnetic surveying of the Otanmäki mine site gridded at 15 m pixel size. The colour scale of the UAS data was based according to the given RGB-colour values from the legacy map (ETRS89 / UTM 35 N).

The value of UAS-based geologic mapping is also demonstrated in the surface-subsurface mapping for the Siilinjärvi outcrops. The classified data and follow-up mapping clearly show that the carbonatite orebody (Figure 4.2) is offset, when compared with the official mapping data. A major infill drilling program, conducted by Yara Oy in 2015–2016, confirms that. Again, the value of UAS-based data could be harvested to update available mapping products. Substantial for an accurate result was an implicit understanding of the known geology of the area and a comparison with legacy data. There is room for interpretation in the presented geologic map. User bias and expert-driven presumptions play as much a role in the final product as the inherent sensor limitations. I compare the interpreted geology of the Jaakonlampi trenches with recent satellite data (PlanetScope maps of 2018 and 2020) highlights the improved survey capabilities and resolution of UAS-based mapping at that scale (Figure 6.12). The indicated pegmatite intrusions (grey dykes in geologic map Figure 6.12b, c) show an offset of 2–5 pixel or 6–30 m comparison. Different interpreters create different geologic maps and models, based on knowledge, experience, and time. This epistemic uncertainty leads to a variability that might be expressed in statistical measures such as a probability distribution for geological-structural characteristics per model (Heim et al., 2019). This is not the focus of this thesis, yet validation of remote sensing (Loew et al., 2017) and geologic modelling are highly discussed research topics (Wellmann and Caumon, 2018).

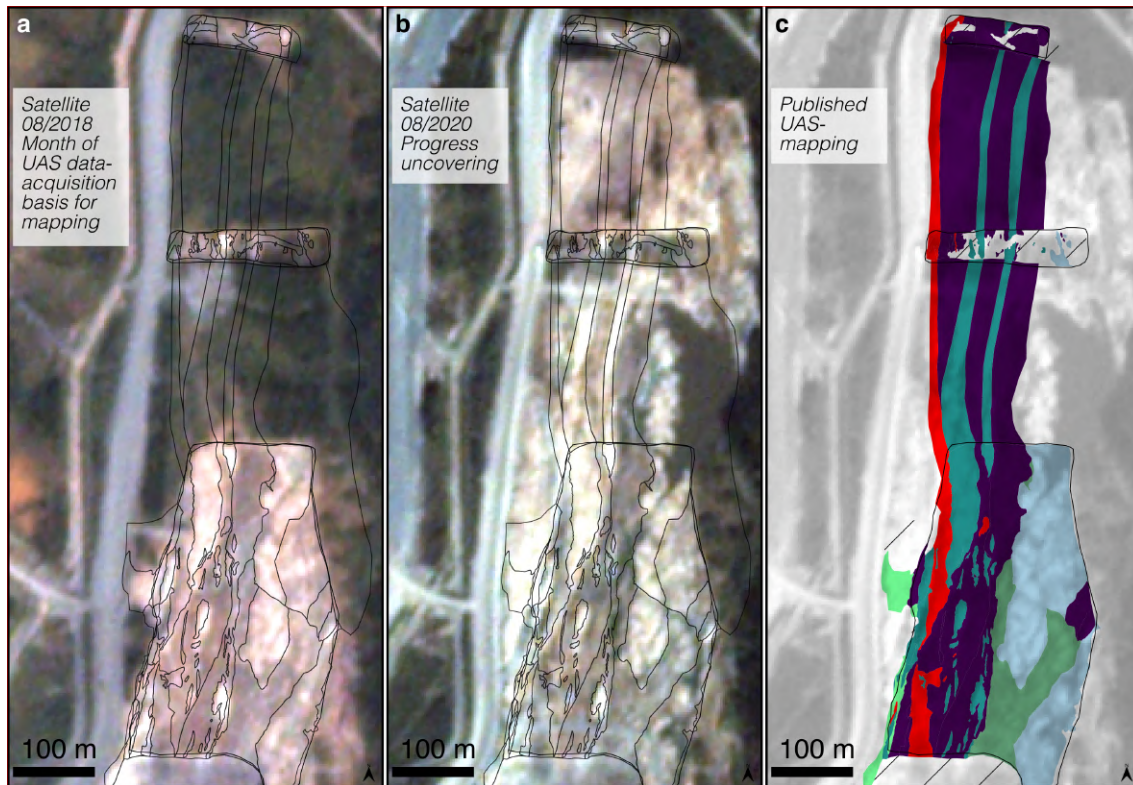


Figure 6.12 Two publicly available PlanetScope (PS) satellite images at 3 m GSD (RGB bands 630 nm, 545 nm, 485 nm) are compared with the conducted UAS survey of 2018, Siilinjärvi. (a) PS image from 31.08.2018 with geologic outlines based on published UAS mapping. (b) PS image (31.08.2020) showing revealed geology along the formerly covered parts between the three trenches. (c) The mapped geologic bodies with legend shown in Figure 6.8f.

6.3.4 Recommendations for integration

The integrated magnetic data added information with geological-structural relevance in all case studies. A challenge in case study 2 was the indirect targeting, but possible from the magnetic contrast associated with magnetic minerals within the carbonatite. A feasible integration strategy was developed based on the data in case study 2. This approach was derived by using the potential of 3D-SfM-MVS data, hyperspectral classification and magnetic subsurface mapping for 3D-forward modelling of an orebody. Integrated field- and UAS-survey data resulted in a geologic outcrop model that covers 0.69 km² and its volume in depth roughly occupies 0.02 km³.

The combination of RGB and multispectral imaging provides the highest cost-benefit for surface mapping, in terms of covered area versus spatial resolution. It is recommended to use fixed-wing data when high spatial resolution, cover and time efficiency are required. Multicopter HSI surveying is recommended for specific surface targets whose detection and quantification requires high spectral resolution and quality. HSI are advantageous to identify specific spectral signatures but a generally higher application effort is noted. Integrated HSI

data was used in a subsequent study that demonstrates how spatially constrained, machine-learning based feature extraction methods can increase classification quality of geologic materials (Lorenz et al., 2021). In case study 3, one major obstacle is the abundance of cast shadow that blocks larger parts of the Qullissat survey area. The Greenland campaign incorporated the experiences made during the first two case studies.

A promising addition to abundant geophysical interpretation is magnetic vector-based inversion of potential field data (Chapter V), that integrates magnetic field direction in modelling and can be helpful to recover structural constraints faster than user-based forward modelling. Sections of missing surface image data can be substituted with high-resolution satellite imagery (PlanetScope, WorldView).

References

- Aasen, H., Honkavaara, E., Lucieer, A., and Zarco-Tejada, P.J., 2018, Quantitative remote sensing at ultra-high resolution with UAV spectroscopy: A review of sensor technology, measurement procedures, and data correction workflows: *Remote Sensing*, v. 10, p. 1–42, doi:10.3390/rs10071091.
- Ali, S.H. et al., 2017, Mineral supply for sustainable development requires resource governance: *Nature*, v. 543, p. 367–372, doi:10.1038/nature21359.
- Assmann, J.J., Kerby, J.T., Cunliffe, A.M., and Myers-Smith, I.H., 2019, Vegetation monitoring using multispectral sensors — best practices and lessons learned from high latitudes: *Journal of Unmanned Vehicle Systems*, v. 7, p. 54–75, doi:10.1139/juvs-2018-0018.
- Boesche, N.K., Rogass, C., Lubitz, C., Brell, M., Herrmann, S., Mielke, C., Tonn, S., Appelt, O., Altenberger, U., and Kaufmann, H., 2015, Hyperspectral REE (Rare Earth Element) Mapping of Outcrops—Applications for Neodymium Detection: *Remote Sensing*, v. 7, doi:10.3390/rs70505160.
- Booyesen, R., Jackisch, R., Lorenz, S., Zimmermann, R., Kirsch, M., Nex, P.A.M., and Gloaguen, R., 2020, Detection of REEs with lightweight UAV-based hyperspectral imaging: *Scientific Reports*, v. 10, doi:10.1038/s41598-020-74422-0.
- Booyesen, R., Zimmermann, R., Lorenz, S., Gloaguen, R., Nex, P.A.M., Andreani, L., and Möckel, R., 2019, Towards multiscale and multisource remote sensing mineral exploration using RPAS: A case study in the Lofdal Carbonatite-Hosted REE Deposit, Namibia: *Remote Sensing*, v. 11, doi:10.3390/rs11212500.
- Chauhan, D., Unnikrishnan, A., and Figliozzi, M., 2019, Maximum coverage capacitated facility location problem with range constrained drones: *Transportation Research Part C: Emerging Technologies*, v. 99, p. 1–18.
- Coyle, M., Dumont, R., Keating, P., Kiss, F., and Miles, W., 2014, Geological Survey of Canada aeromagnetic surveys: Design, quality assurance, and data dissemination:
- Drusch, M. et al., 2012, Sentinel-2: ESA's Optical High-Resolution Mission for GMES Operational Services: *Remote Sensing of Environment*, v. 120, p. 25–36, doi:https://doi.org/10.1016/j.rse.2011.11.026.

- Duan, P., Lai, J., Ghamisi, P., Kang, X., Jackisch, R., Kang, J., and Gloaguen, R., 2020, Component Decomposition-Based Hyperspectral Resolution Enhancement for Mineral Mapping: *Remote Sensing*, v. 12, doi:10.3390/rs12182903.
- Heim, E., Virgo, S., de la Varga, M., and Wellmann, F., 2019, Is it possible to capture epistemic uncertainty in geological models?, *in* EGU General Assembly Conference Abstracts, EGU General Assembly Conference Abstracts, p. 17448.
- Honkavaara, E., Saari, H., Kaivosoja, J., Pölönen, I., Hakala, T., Litkey, P., Mäkynen, J., and Pesonen, L., 2013, Processing and Assessment of Spectrometric, Stereoscopic Imagery Collected Using a Lightweight UAV Spectral Camera for Precision Agriculture: *Remote Sensing*, v. 5, doi:10.3390/rs5105006.
- Isles, D.J., and Rankin, L.R., 2013, Geological interpretation of aeromagnetic data: *Society of Exploration Geophysicists and Australian Society of Exploration*, v. 1, 365 p.
- Jackisch, R., Lorenz, S., Zimmermann, R., Möckel, R., and Gloaguen, R., 2018, Drone-borne hyperspectral monitoring of acid mine drainage: An example from the Sokolov lignite district: *Remote Sensing*, v. 10, doi:10.3390/rs10030385.
- Jackisch, R., Madriz, Y., Zimmermann, R., Pirttijärvi, M., Saartenoja, A., Heincke, B.H., Salmirinne, H., Kujasalo, J.-P., Andreani, L., and Gloaguen, R., 2019, Drone-borne hyperspectral and magnetic data integration: Otanmäki Fe-Ti-V deposit in Finland: *Remote Sensing*, v. 11, doi:10.3390/rs11182084.
- Jakob, S., Zimmermann, R., and Gloaguen, R., 2017, The Need for Accurate Geometric and Radiometric Corrections of Drone-Borne Hyperspectral Data for Mineral Exploration: *MEPhySTo-A Toolbox for Pre-Processing Drone-Borne Hyperspectral Data: Remote Sensing*, v. 9, p. 88, doi:10.3390/rs9010088.
- Jirigalatu, J., Krishna, V., da Silva, E., and Døssing, A., 2021, Experiments on magnetic interference for a portable airborne magnetometry system using a hybrid unmanned aerial vehicle (UAV): *Geoscientific Instrumentation, Methods and Data Systems*, v. 10, p. 25–34, doi:10.5194/gi-10-25-2021.
- Karpouzli, E., and Malthus, T., 2003, The empirical line method for the atmospheric correction of IKONOS imagery: *International Journal of Remote Sensing*, doi:10.1080/0143116021000026779.
- Le Maire, P., Bertrand, L., Munsch, M., Diraison, M., and Géraud, Y., 2020, Aerial magnetic mapping with an unmanned aerial vehicle and a fluxgate magnetometer: a new method for rapid mapping and upscaling from the field to regional scale: *Geophysical Prospecting*, p. 1–13, doi:10.1111/1365-2478.12991.
- Loew, A. et al., 2017, Validation practices for satellite-based Earth observation data across communities: *Reviews of Geophysics*, v. 55, p. 779–817, doi:https://doi.org/10.1002/2017RG000562.
- Lorenz, S., Beyer, J., Fuchs, M., Seidel, P., Turner, D., Heitmann, J., and Gloaguen, R., 2019, The Potential of Reflectance and Laser Induced Luminescence Spectroscopy for Near-Field Rare Earth Element Detection in Mineral Exploration: *Remote Sensing*, v. 11, doi:10.3390/rs11010021.
- Lorenz, S., Ghamisi, P., Kirsch, M., Jackisch, R., Rasti, B., and Gloaguen, R., 2021, Feature extraction for hyperspectral mineral domain mapping: A test of conventional and innovative methods: *Remote Sensing of Environment*, v. 252, p. 112129, doi:https://doi.org/10.1016/j.rse.2020.112129.

- Lorenz, S., Salehi, S., Kirsch, M., Zimmermann, R., Unger, G., Vest Sørensen, E., and Gloaguen, R., 2018, Radiometric Correction and 3D Integration of Long-Range Ground-Based Hyperspectral Imagery for Mineral Exploration of Vertical Outcrops: *Remote Sensing*, v. 10, doi:10.3390/rs10020176.
- Madriz, Y., 2019, Drone-borne geophysics: magnetic survey for mineral exploration [unpublished MSc thesis]: TU Freiberg, 88 p.
- van der Meer, F., Kopačková, V., Koucká, L., van der Werff, H.M.A., van Ruitenbeek, F.J.A., and Bakker, W.H., 2018, Wavelength feature mapping as a proxy to mineral chemistry for investigating geologic systems: An example from the Rodalquilar epithermal system: *International Journal of Applied Earth Observation and Geoinformation*, v. 64, p. 237–248, doi:10.1016/j.jag.2017.09.008.
- Mielke, C., Boesche, N.K., Rogass, C., Kaufmann, H., Gauert, C., and de Wit, M., 2014, Spaceborne mine waste mineralogy monitoring in South Africa, applications for modern push-broom missions: Hyperion/OLI and EnMAP/Sentinel-2: *Remote Sensing*, v. 6, p. 6790–6816, doi:10.3390/rs6086790.
- Montgomery, D.C., Peck, E.A., and Vining, G.G., 2012, *Introduction to Linear Regression Analysis*: Wiley.
- O'Brien, H., Heilimo, E., and Heino, P., 2015, The Archean Siilinjärvi Carbonatite Complex: Mineral Deposits of Finland, p. 327–343, doi:10.1016/B978-0-12-410438-9.00013-3.
- de Oliveira, R.A., Tommaselli, A.M.G., and Honkavaara, E., 2016, Geometric Calibration of a Hyperspectral Frame Camera: Photogrammetric Record, v. 31, p. 325–347, doi:10.1111/phor.12153.
- Palmer, J.M., 2003, Radiometry and photometry FAQ: University of Arizona, 14 p.
- Park, S., and Choi, Y., 2020, Applications of unmanned aerial vehicles in mining from exploration to reclamation: A review: *Minerals*, v. 10, p. 1–32, doi:10.3390/min10080663.
- Pekkala, O., Pulli, T., Kokka, A., and Ikonen, E., 2019, Setup for characterising the spectral responsivity of Fabry–Pérot-interferometer-based hyperspectral cameras: *Metrologia*, v. 56, p. 65005, doi:10.1088/1681-7575/ab3fd1.
- Planet Team, 2017, Planet Application Program Interface: In Space for Life on Earth.: planet.com, <https://api.planet.com> (accessed November 2020).
- Planet Team, 2020, Planet Imagery Product Specifications: Planet Labs Inc., 97 p.
- Reeves, C., 2006, *Aeromagnetic Surveys. Principles, Practice & Interpretation*: Earthworks, p. 155, doi:10.1007/BF01465543.
- Sasgen, I., Wouters, B., Gardner, A.S., King, M.D., Tedesco, M., Landerer, F.W., Dahle, C., Save, H., and Fettweis, X., 2020, Return to rapid ice loss in Greenland and record loss in 2019 detected by the GRACE-FO satellites: *Communications Earth & Environment*, v. 1, p. 1–8.
- Sheridan, I., 2020, Drones and global navigation satellite systems: Current evidence from polar scientists: *Royal Society Open Science*, v. 7, doi:10.1098/rsos.191494.
- Smith, W.H.F., and Wessel, P., 1990a, Gridding with continuous curvature splines in tension: *Geophysics*, v. 55, p. 293–305.
- Tomašík, J., Mokroš, M., Surový, P., Grznárová, A., and Merganič, J., 2019, UAV RTK/PPK Method—An Optimal Solution for Mapping Inaccessible Forested Areas? *Remote Sensing*, v. 11, p. 721, doi:10.3390/rs11060721.

- Tommaselli, A.M.G., Santos, L.D., De Oliveira, R.A., and Honkavaara, E., 2018, Refining the geometric calibration of a hiperspectral frame camera with preliminary bands coregistration, *in* International Geoscience and Remote Sensing Symposium (IGARSS), v. 2018-July, p. 6468–6471, doi:10.1109/IGARSS.2018.8519058.
- Turner, D.J., Rivard, B., and Groat, L.A., 2014, Visible and short-wave infrared reflectance spectroscopy of REE fluorocarbonates: *American Mineralogist*, v. 99, p. 1335–1346.
- Wellmann, F., and Caumon, G., 2018, 3-D Structural geological models: Concepts, methods, and uncertainties: Elsevier Inc., v. 59, 1–121 p., doi:10.1016/bs.agph.2018.09.001.
- Young, N.E., Anderson, R.S., Chignell, S.M., Vorster, A.G., Lawrence, R., and Evangelista, P.H., 2017, A survival guide to Landsat preprocessing: *Ecology*, doi:10.1002/ecy.1730.

VII

Chapter 7 – Conclusions and Outlook

In the final chapter of this thesis, I reassess the objectives and provide a general conclusion. I offer recommendations for additional research in UAS-based spectroscopic and magnetic data integration, and an outlook of recently developed UAS-based sensor applications with relevance to mineral exploration.

7.1 Summary and general recommendations

The purpose of this thesis has been to explore the potential of multi-sensor UAS-based mineral exploration with a cohesive survey approach using optical and magnetic UAS-based methods. My principal methodology included three case studies where UAS surveying was applied on geologic targets in subarctic to arctic regions. Our case studies gave the opportunity to test our UAS-based approach within different geological environments.

We adapted each survey workflow according to the external conditions and target characteristics, such as ambiguous magnetic anomaly sources and varied spectral proxies. The research was conducted in terrain with flat and rugged topography, outcropping or concealed targets and often low light conditions. With those conditions, the aim of this thesis was to evaluate the applicability of UAS-based multi-sensor data in different exploration settings. The aim was achieved based on results from successful data acquisition, processing, and integration.

The presented works highlight the advantage of UAS as a practical, light-weight, fast and comfortably deployable geoscientific tool. Integrated UAS-based surface and sub-surface data were used to create digital outcrop models for precise geologic mapping and interpretation. High-resolution surface imagery and subsurface information from magnetics are fused and jointly interpreted. By using UAS, petrophysical-mineralogical proxies under cover are mappable in a higher spatial detail and comprehensiveness than possible in an exclusive ground or airborne survey. The ground survey is a crucial part of this thesis and is necessary for validation. UAS-based imaging is generally recommended augmenting ground surveying. We show that multi-sensor UAS-based data integration supports decision-makers. The following points recapitulate the main thoughts:

- The reviewed literature suggests that UAS-based image spectroscopy and magnetic applications are reaching mature levels and provide significant potential for technology and application development. Research that integrates UAS-based multi-sensor surveying is infrequent in mineral exploration. High costs, lack of successful case studies and user barriers are mainly responsible.
- Integrated multispectral and magnetic UAS-based mapping in complex areas improves detection rate and spatial resolution of targets and reduces time, effort and required sampling material. The sampling resolution of UAS magnetics does not surpass ground survey, but the covered area per time-unit is exceedingly higher. The developed data integration workflows stand as a holistic concept and can be applied for the most different

targets. A combination of UAS technology with RGB, multi- and hyperspectral cameras and fluxgate magnetometers is advantageous and created the basis for integrated modelling.

- A straightforward resource estimation was conducted for an iron ore deposit at Otanmäki, by integrating magnetics, image spectroscopy-based indices and 2D structural interpretation. Photogrammetric 3D-modelling and hyperspectral classifications were applied for a carbonatite intrusion at Siilinjärvi to capture a complete exploration section. UAS-based data provided the link between 2D mapping and 3D modelling. UAS-based magnetics close the gap between ground magnetics and aeromagnetics. Magnetic forward modelling in Siilinjärvi and magnetic vector inversion in Disko Island was used to create plausible 3D models, down to depths of several hundred meters. In Greenland, modelling was supported by photogrammetric surface models that can reduce time effort and uncertainty. Undifferentiated landslide blocks could be identified and surveyed in high detail at Disko Island. Remanent magnetization effects could be identified and incorporated into a magnetic vector inversion.
- The prototype of a multispectral camera for rapid fixed-wing surveying was developed and tested at the outcrops of Siilinjärvi. More testing will include the simultaneous acquisition of magnetic and multispectral data at expanded areal coverage.
- Image classification and machine learning-based feature extraction methods characterized surfaces to map lithologies and structures. Image spectroscopy needs to consider atmospheric conditions, expected solar elevation and pre-existing ground truth. If circumstances during surveying are complex, the use of image data fusion approaches with dimensionality reduction methods for supervised classification of spectroscopic imagery is recommended. Those methods can be computational demanding, time intensive and, thus, their use needs to be evaluated against the true requirements of a survey. The key is an understanding of the expected geologic patterns, which are derived from preliminary field surveying using UAS images, existing geologic maps, or satellite and airborne data.
- The acquisition of high-detailed RGB data was indispensable in this work and is recommended as an auxiliary data product. Photogrammetric orthomosaics, point clouds and elevation models are invaluable for processing, correction, fusion, and interpretation with other surface data. RGB sensors and photogrammetric processing software are the most affordable from the tools presented in this thesis.
- The establishment and presentation of UAS-based multi, and hyperspectral imaging workflows contributes to their normalization along the implemented RGB photogrammetric methods. An increase of available tools for less invasive, data-driven mineral exploration

and mining will follow. In the same notion, the application of inversion methods, such as the MVI (Chapter V), for magnetic data can be highly beneficial for geometric and structural problems and complex magnetization patterns. UAS imaging techniques will be used further in automatic mining procedures, where geophysical and spectral methods become state-of-the-art.

I suggest that UAS surveying supports ground-based operations in areas up to 50 km², inferred from the conjunct experience of this thesis, and become a valuable alternative to time-consuming ground surveying. In conclusion, this work solidifies the UAS as multi-sensor platform is placed between ground survey and manned airborne, respectively satellite survey for mineral exploration.

7.2 Further research directions for UAS-based sensors

There are promising approaches that provide innovative aspects towards material and structural mapping, next to the sensor technology I presented in this thesis. In this section, I give a selection of UAS-based sensors that exist as technology demonstrator or application and potentially guide future directions of mineral exploration. To identify other minerals and different molecule groups than shown in this work, e.g., sheet silicates, the use of an extended spectral range, i.e., SWIR, is feasible. Currently, that range requires a push-broom line scanner. Due to differences in camera architecture, optical pathways and sensor materials that require active cooling, those cameras have an increased payload of several kilograms. Research examples are abundant in vegetation analysis (Horstrand et al., 2019; Arroyo-Mora et al., 2021). Image processing pipelines for those cameras exist and would require only little adaptation to shift from phenotyping to mineral mapping. Future developments could use nanomaterials (e.g., graphene; Goossens et al., 2017), to reduce detector size and energy consumption.

UAS-based thermal imaging in the MWIR or LWIR range are used to detect thermal gradients for example in powerline inspection (Nguyen et al., 2018) or in volcanology to detect gas plumes, measure dome morphology and further (Thiele et al., 2017; James et al., 2020). A UAS-based thermal camera with the ability to acquire a quantized LWIR spectrum could extend the suite of targetable lithologies with rock-forming minerals (quartz, feldspars, pyroxene, see also Booyesen et al., 2020). A way of obtaining UAS-based VNIR-SWIR spectra without image context is using a point spectrometer. This application was effectively used for land-cover classification (Natesan et al., 2018), and is practicable to acquire point-based identifications of mineral-specific absorption features.

The former measurement concepts use passive light sources. A recent proof-of-concept study employed a UAS-based laser to stimulate and perceive material-specific fluorescence of surface targets. The authors suggested geochemical distinction of rocks, fossils, and biomass (Kaye and Pittman, 2020). The more common light detection and ranging (LiDAR) systems are used on UAS for a multitude of applications. Structural and topographical mapping of outcrops and under vegetation, or riverbed surveying are just a few examples of the possible applications of active, laser-based systems (Wallace et al., 2012; Tong et al., 2015). However, LiDAR usually provides only geometric information and comes at high payloads in multiple kilogram ranges. Future developments in that field are aiming to include multiple wavelengths (i.e., multispectral LiDAR, see Kaasalainen and Malkamäki (2020)). An alternative development aims to miniaturize lightweight LiDAR and was recently introduced for handheld devices (Abdullah, 2021) with high potential for UAS.

Related to UAS-based passive magnetics, but active, are electromagnetics (EM), very low frequency (VLF) methods, and time domain electromagnetics (TDEM). Such technology would create opportunities to extend the geological target range (e.g., clays, sulphides, groundwater, saline intrusions) detectable with UAS. EM and VLF UAS-based systems have been approached by using heavy-duty helidrones (Eröss et al., 2013; Altdorff et al., 2014) that operate with high payloads (> 25 kg), which limits their ease-of-use in the field. However, lightweight multicopter UAS using EM and TDEM have been introduced recently and can survey several line kilometres using the combination of a UAS-towed loop system with a ground-based electromagnetic transmitter long-cable (Parshin et al., 2021a). Practical and market-ready devices need to overcome limitations of payloads, range, and energy supply.

Effectively used are also UAS-based passive radiometric systems. For example, radiometric UAS-based sensors can measure radioactivity in minimal target distance and without the human operator. This reduces unwanted exposure to any hazardous material and maintains operator safety (MacFarlane et al., 2014; Van Der Veeke et al., 2018). Technology demonstrators for exploration have successfully proven the applicability of measuring radioactive sources by UAS (Parshin et al., 2018, 2021b). The radiometric method has similar limitations to magnetics and electromagnetics (non-unique signal, distance to target) but used successfully in exploration (Telford et al., 1990).

Another active system is ground penetrating radar (GPR) which was established on UAS (Altdorff et al., 2014; Ludeno et al., 2017). Such systems have proven the feasibility to detect soil moisture, buried dielectric and metallic targets, and other hidden structures (García-Fernandez et al., 2018; Wu et al., 2019). A promising approach of UAS-based GPR is the safe

detection of UXO and landmines in former and active conflict regions (Colorado et al., 2017). Further targets are buried geological or archaeological structures.

I presented different modern sensor examples. However, the technical prowess towards the platform itself will progress further. The planners of future cities already include UAS for delivery of services and products (Alsamhi et al., 2019). Technological advancements at UAS platform level will benefit exploration efforts. Intelligent UAS swarm technology will improve the service quality in most aspects (Chen et al., 2019). With improved standards in payload, endurance, safety and redundancy, airspace awareness and extended autonomy, drones will become standard tools in geoscience and take new frontiers of earth observation.

References

- Abdullah, Q., 2021, Top Geospatial Trends to Watch in 2021: Photogrammetric Engineering & Remote Sensing, v. 87, p. 149–151.
- Altdorff, D., Schliffke, N., Riedel, M., Schmidt, V., van der Kruk, J., Vereecken, H., Stoll, J., and Becken, M., 2014, UAV-borne electromagnetic induction and ground-penetrating radar measurements: a feasibility test: *Water Resour Res*, v. 42, p. W11403.
- Arroyo-Mora, J.P., Kalacska, M., Løke, T., Schläpfer, D., Coops, N.C., Lucanus, O., and Leblanc, G., 2021, Assessing the impact of illumination on UAV pushbroom hyperspectral imagery collected under various cloud cover conditions: *Remote Sensing of Environment*, v. 258, p. 112396, doi:10.1016/j.rse.2021.112396.
- Booyesen, R., Gloaguen, R., Lorenz, S., Zimmermann, R., and Nex, P.A.M., 2020, *Geological Remote Sensing*: Elsevier Inc., 1–14 p., doi:10.1016/b978-0-12-409548-9.12127-x.
- Colorado, J., Perez, M., Mondragon, I., Mendez, D., Parra, C., Devia, C., Martinez-Moritz, J., and Neira, L., 2017, An integrated aerial system for landmine detection: SDR-based Ground Penetrating Radar onboard an autonomous drone: *Advanced Robotics*, v. 31, p. 791–808, doi:10.1080/01691864.2017.1351393.
- Eröss, R., Stoll, J.B., Bergers, R., and Tezkan, B., 2013, Three-component VLF using an unmanned aerial system as sensor platform: *First Break*, v. 31.
- García-Fernandez, M., Y. Álvarez López, A. Arboleya Arboleya, B. González Valdés, Y. Rodríguez Vaquero, F. Las-Heras Andrés, and A. Pino García, 2018, Synthetic Aperture Radar Imaging System for Landmine Detection Using a Ground Penetrating Radar on Board a Unmanned Aerial Vehicle: *IEEE Access*, v. 6, p. 45100–45112, doi:10.1109/ACCESS.2018.2863572.
- Goossens, S. et al., 2017, Broadband image sensor array based on graphene–CMOS integration: *Nature Photonics*, v. 11, p. 366–371, doi:10.1038/nphoton.2017.75.
- Horstrand, P., Guerra, R., Rodriguez, A., Diaz, M., Lopez, S., and Lopez, J.F., 2019, A UAV Platform Based on a Hyperspectral Sensor for Image Capturing and On-Board Processing: *IEEE Access*, v. 7, p. 66919–66938, doi:10.1109/ACCESS.2019.2913957.
- James, M. et al., 2020, Volcanological applications of unoccupied aircraft systems (UAS): Developments, strategies, and future challenges: *Volcanica*, p. 67–114, doi:10.30909/vol.03.01.67114.

- Kaasalainen, S., and Malkamäki, T., 2020, Potential of active multispectral lidar for detecting low reflectance targets: *Optics Express*, v. 28, p. 1408–1416, doi:10.1364/OE.379491.
- Kaye, T.G., and Pittman, M., 2020, Fluorescence-based detection of field targets using an autonomous unmanned aerial vehicle system: *Methods in Ecology and Evolution*, v. 11, p. 890–898, doi:10.1111/2041-210X.13402.
- Ludeno, G., I. Catapano, G. Gennarelli, F. Soldovieri, A. R. Vetrella, A. Renga, and G. Fasano, 2017, A micro-UAV-borne system for radar imaging: A feasibility study, *in* 2017 9th International Workshop on Advanced Ground Penetrating Radar (IWAGPR), p. 1–4, doi:10.1109/IWAGPR.2017.7996034.
- MacFarlane, J.W., Payton, O.D., Keatley, A.C., Scott, G.P.T., Pullin, H., Crane, R.A., Smilion, M., Popescu, I., Curlea, V., and Scott, T.B., 2014, Lightweight aerial vehicles for monitoring, assessment and mapping of radiation anomalies: *Journal of Environmental Radioactivity*, v. 136, p. 127–130, doi:10.1016/j.jenvrad.2014.05.008.
- Natesan, S., Armenakis, C., Benari, G., and Lee, R., 2018, Use of UAV-Borne Spectrometer for Land Cover Classification: *Drones*, v. 2, doi:10.3390/drones2020016.
- Nguyen, V.N., Jenssen, R., and Roverso, D., 2018, Automatic autonomous vision-based power line inspection: A review of current status and the potential role of deep learning: *International Journal of Electrical Power & Energy Systems*, v. 99, p. 107–120, doi:10.1016/j.ijepes.2017.12.016.
- Parshin, A., Bashkeev, A., Davidenko, Y., Persova, M., Iakovlev, S., Bukhalov, S., Grebenkin, N., and Tokareva, M., 2021a, Lightweight Unmanned Aerial System for Time-Domain Electromagnetic Prospecting—The Next Stage in Applied UAV-Geophysics: *Applied Sciences*, v. 11, doi:10.3390/app11052060.
- Parshin, A., Grebenkin, N., Morozov, V., and Shikalenko, F., 2018, Research Note: First results of a low-altitude unmanned aircraft system gamma survey by comparison with the terrestrial and aerial gamma survey data: *Geophysical Prospecting*, v. 66, p. 1433–1438, doi:10.1111/1365-2478.12650.
- Parshin, A., Morozov, V., Snegirev, N., Valkova, E., and Shikalenko, F., 2021b, Advantages of Gamma-Radiometric and Spectrometric Low-Altitude Geophysical Surveys by Unmanned Aerial Systems with Small Scintillation Detectors: *Applied Sciences*, v. 11, doi:10.3390/app11052247.
- S. H. Alsamhi, O. Ma, M. S. Ansari, and F. A. Almalki, 2019, Survey on Collaborative Smart Drones and Internet of Things for Improving Smartness of Smart Cities: *IEEE Access*, v. 7, p. 128125–128152, doi:10.1109/ACCESS.2019.2934998.
- Telford, W.M., Geldart, L.P., and Sheriff, R.E., 1990, *Applied Geophysics*: 770 p.
- Thiele, S.T., Varley, N., and James, M.R., 2017, Thermal photogrammetric imaging: A new technique for monitoring dome eruptions: *Journal of Volcanology and Geothermal Research*, v. 337, p. 140–145, doi:10.1016/j.jvolgeores.2017.03.022.
- Tong, X. et al., 2015, Integration of UAV-Based Photogrammetry and Terrestrial Laser Scanning for the Three-Dimensional Mapping and Monitoring of Open-Pit Mine Areas: *Remote Sensing*, v. 7, doi:10.3390/rs70606635.
- Van Der Veeke, S., Koomans, R.L., Van Egmond, F.M., and Limburg, J., 2018, A drone as platform for airborne gamma-ray surveys to characterize soil and monitor contaminations, *in* 24th European Meeting of Environmental and Engineering Geophysics, doi:10.3997/2214-4609.201802510.

- W. Chen, B. Liu, H. Huang, S. Guo, and Z. Zheng, 2019, When UAV Swarm Meets Edge-Cloud Computing: The QoS Perspective: *IEEE Network*, v. 33, p. 36–43, doi:10.1109/MNET.2019.1800222.
- Wallace, L., Lucieer, A., Watson, C., and Turner, D., 2012, Development of a UAV-LiDAR System with Application to Forest Inventory: *Remote Sensing*, v. 4, doi:10.3390/rs4061519.
- Wu, K., Rodriguez, G.A., Zajc, M., Jacquemin, E., Clément, M., De Coster, A., and Lambot, S., 2019, A new drone-borne GPR for soil moisture mapping: *Remote Sensing of Environment*, v. 235, p. 111456, doi:10.1016/j.rse.2019.111456.

Appendix

Appendix A

The literature database SCOPUS (www.scopus.com, last accessed 06.11.2020) was used to produce a representative bibliography of UAS-based mineral exploration. Results were produced via the title-abstract-keyword search. The following keyword-based search with their Boolean connection

(uav OR drone OR uas OR rpas OR unmanned) AND geology

resulted in 449 entries. After a brief examination, those entries seemed to drift away well to far from the target topic. A refined search strategy using the following keyword-based search

(uav OR uavs OR drone OR uas OR rpas) AND geology OR geologic OR mineral AND exploration OR magnetic OR hyperspectral OR multispectral OR spectroscopy OR mining OR photogrammetry OR geomorphology

Based on that search inquiry, 307 items were found. Manual inspection showed several missing manuscripts focusing on UAS magnetics, so a second search query and manual search was added

(uav OR uavs OR drone OR uas OR rpas) AND fluxgate

producing 23 items.

Then, the titles were merged and screened manually to remove items focusing on forest, cropland, agriculture, and biomass. Further inspection produced 287 documents from 2006–2021, which are indexed and relate to UASs, geology, remote sensing, geophysics along with others. Items were screened for duplicates, with a remaining of 277 files. Those items were extracted as spreadsheet that contains bibliographic data, abstracts, index keywords from authors and given by the database and importantly, citations by other documents.

During the work of this thesis, a library of articles, conference papers and technical reports focusing on UAS-based magnetics were collected, which are overlapping with the SCOPUS database. Those documents form a sub-library outside the available body of literature from SCOPUS, where 55 articles are found in SCOPUS and 12 were collected externally. This library of 67 documents is processed subsequently in detail for qualitative and quantitative information, such as theme, used UAV and type of magnetometer.

The VOS software is employed to chart a thematic map for the relatively new field of UASs application in mineral exploration. Visualisation of similarities (VOS) is a mapping technique that focuses on displaying bibliographic data in so-called bibliometric network maps. The

software is useful to illustrate for example the connection, occurrence, co-occurrence of citations, keywords, authors, and other bibliographic metrics, especially for large databases, e.g., > 100 items. Keyword-based nodes reflect relationships of research fields, mainly technologically in a map. Node distance and number of links play an important role in the interpretation of relationship strength among items.

I focus on the co-occurrence of keywords to map the topic field for the past 15 years based on literary keywords. I choose author-based and index-based keywords to create a co-occurrence network map (van Eck and Waltman, 2014). Citations among documents produced maps without any interpretative value, presumably because this research field is not adequately matured yet.

Here, co-occurrence is calculated based on the number of documents in which the terms appear together, and each co-occurrence network link has the same weight (Van Eck and Waltman, 2019). Author-based keywords are provided by the respective study authors and reflect what authors consider to be relevant in their work. Indexed keywords are provided by the literature database. Some keywords are neglected by authors, and some indexed keywords are controlled by quite broad concepts or ideas of a topic.

Some SCOPUS keywords are ambiguous and produce results which do not fit the search scope, which required manual clear-out. Keywords such as “antenna” and “target drone” are not suitable in the geoscientific scope and were omitted. After several mapping iterations, a minimum of 9 occurrences per keyword was found the most meaningful to map the semantic research landscape. The top five keywords are: UAV, remote sensing, geology, photogrammetry, surveying. After thorough inspection, the following keywords were removed: ‘forestry, antennas, aircraft detection, optical radar, china’. Multi-sensor or sensor fusion as terms were picked up only very limited.

The resulting keyword co-occurrence network map contains: 56 items, 4 main clusters and 908 links. The strength of a network link that pairs items represents the number of publications in which the two terms appear. For a clearer overview, the link strength is set to three occurrences (Figure A8.1).

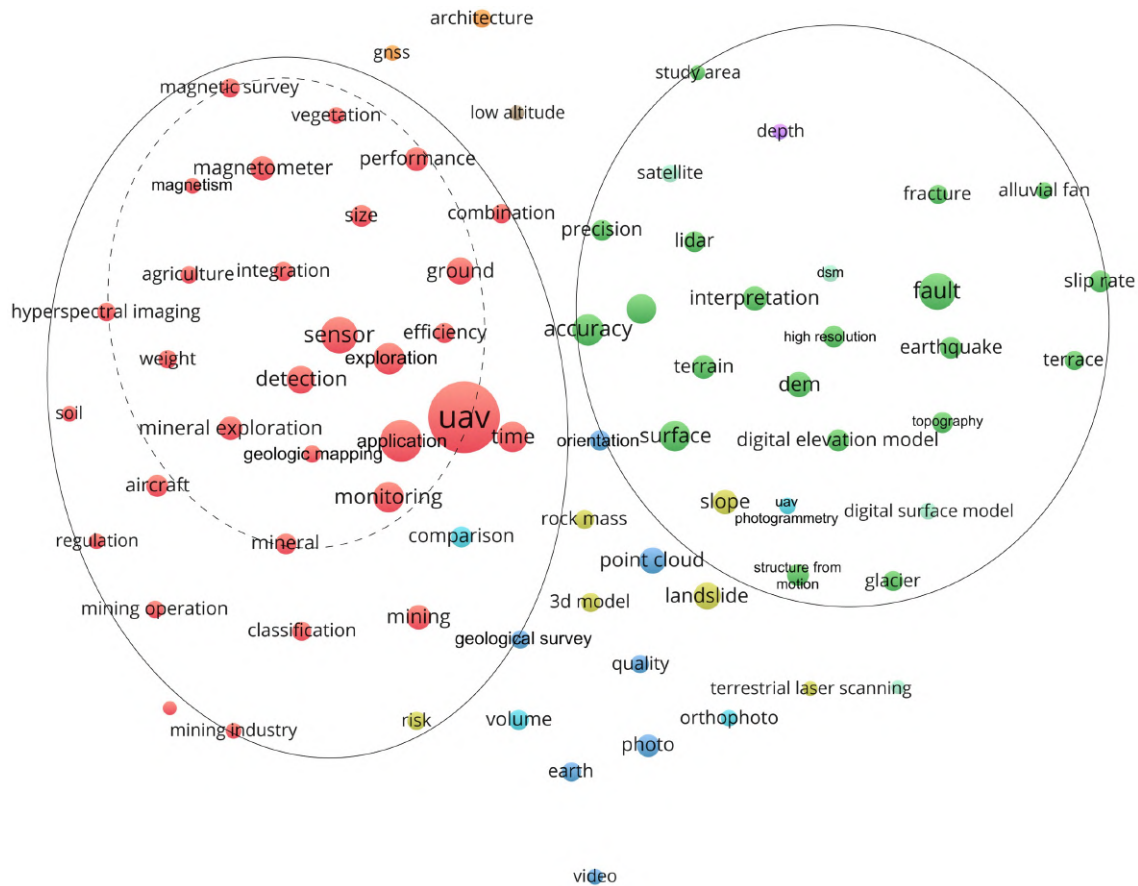


Figure A8.1 Co-occurrence network based on abstract and title keywords. 76 items, 9 clusters. Word linkage not shown for increased readability.

From the available literature review of UAS use, all of them apply magnetics. From the total, 44 % use multicopters and 25 % use fixed-wings, which are the two drone types applied in this thesis (Figure A8.2). The remaining studies used helidrones, airships or multiple types. Thematically, 32 % of these studies focused primarily on developing the technology for magnetic survey (e.g., Samson et al., 2010; Tezkan et al., 2011; Stoll and Moritz, 2013). About 29 % reports on mineral exploration and 14 % on geologic mapping. Further categories are unexploded ordnance (UXO), archaeology, oil and gas, and general reviews. It seems natural that the first civilian-sector reports on UAS magnetics were applied in the geosciences, especially for geophysical mineral exploration, mining and oil & gas (Anderson and Pita, 2005). Japanese research groups followed with developments of fixed-wings for polar science (Funaki and Hirasawa, 2008; Funaki et al., 2014) and helidrones for volcanology (Kaneko et al., 2011; Koyama et al., 2013).

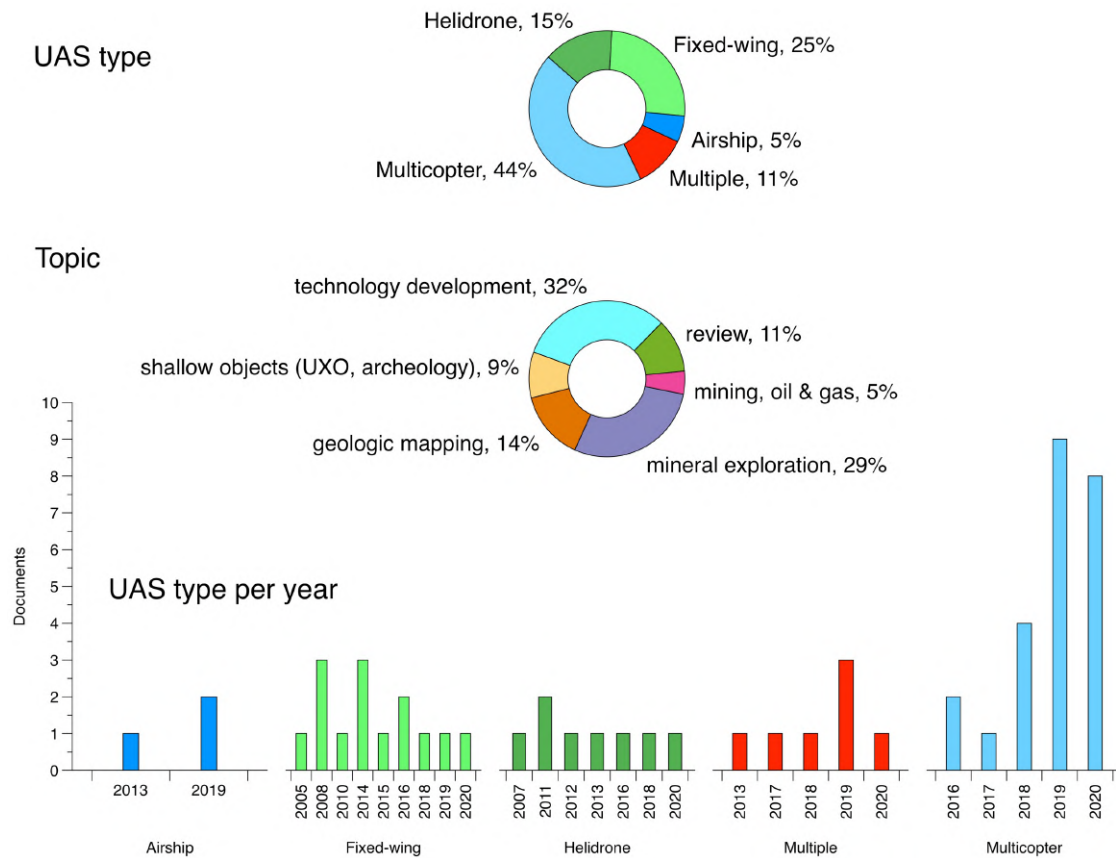


Figure A8.2 An overview of reported UAS types, research topics and the documented UAS-type per publication year that apply magnetic sensing.

UAS type per publication year reveals a growing trend to use multicopter. They are small, light-weight and mobile and provide accessible work flows at a low entry level, speaking from my own experience during this thesis. Early developments of heavy helidrones are highly complex, fulfil technical and payload criteria, but their practical applicability is limited, as the take-off weight can for example be between 84 kg (Koyama et al., 2013) to 640 kg (Li et al., 2014).

Appendix B

Magnetic components

Laplace's equation for a potential field V in Cartesian coordinates for the sum rate change of a field gradient is given as (Blakely, 1995):

$$\nabla^2 V = \frac{\partial^2 V}{\partial x^2} + \frac{\partial^2 V}{\partial y^2} + \frac{\partial^2 V}{\partial z^2} = 0 \quad (8.1)$$

Vector representations after Figure 2.7 (Kearey and Brooks, 1991):

$$B_h = B \cos I \quad (8.2)$$

$$B_z = B \sin I = B_h \tan I \quad (8.3)$$

$$B_x = B_h \cos D \quad (8.4)$$

$$B_y = B_h \sin D \quad (8.5)$$

The **upward continuation** of a magnetic grid $\Delta T(x, y, z_0)$ between the elevation from plane z_0 to Δz ($\Delta z > 0$) in Fourier integral terms is (Henderson and Zietz, 1949; Blakely, 1995):

$$\Delta T(x, y, z_0 - \Delta z) = \frac{\Delta z}{2\pi} \int_{-\infty}^{\infty} \int_{-\infty}^{\infty} \frac{\Delta T(x', y', z_0)}{[\Delta z^2 + (x' - x)^2 + (y' - y)^2]^{\frac{3}{2}}} dx' dy' \quad (8.6)$$

The amplitude of the **analytic signal** AS (Nabighian, 1972; Debeglia and Corpel, 1997) of a magnetic field anomaly M in spectral domain is defined as:

$$|AS(x, y)| = \sqrt{\left(\frac{\partial M}{\partial x}\right)^2 + \left(\frac{\partial M}{\partial y}\right)^2 + \left(\frac{\partial M}{\partial z}\right)^2} \quad (8.7)$$

Appendix C

Apatite-bearing rock samples from Siilinjärvi were catalogued, cut and prepared for thin section analysis (Figure C8.3a). A computer tomography (CT) scan was acquired for a small rock slab of carbonatite (Figure C8.3b). The CT scanner (XRE CoreTOM, Tescan Orsay) creates a 3D model based on X-ray attenuation which strength depends on the electron density of the minerals. This 3D image shows density contrast and is used here to identify the distribution of REE-bearing minerals in-between the apatite crystals, in pathways, cracks and pores. Originally, the experiment was thought to identify iron-bearing minerals, i.e., the magnetite and further ferrimagnetic minerals that largely cause the magnetic anomaly measured in Siilinjärvi. However, the density contrast between iron- and REE phases was not clearly distinguishable for this scan. Further efforts and CT scanning of smaller samples would be necessary for further insights on the magnetite-formation. As non-invasive material identification procedure, the CT has its advantages. Especially volumetric differences would be detectable (Godinho et al., 2019).

More sample preparation is required for back-scattered electron (BSE) imaging of 2D surfaces (Figure C8.3c). The prepared and finely polished carbonatite sample was scanned with BSE, so that electron dispersive X-ray spectroscopy can be performed to detect grains of up $\sim 1\ \mu\text{m}$ (hwww.hzdr.de/db/Cms?pNid=177, last accessed 06.01.2021). Again, the certain identification and quantification of surficial REE occurrence was possible, based on their high electron density. An identification of iron-phase is possible partly, but remains challenging (Bachmann et al., 2017).

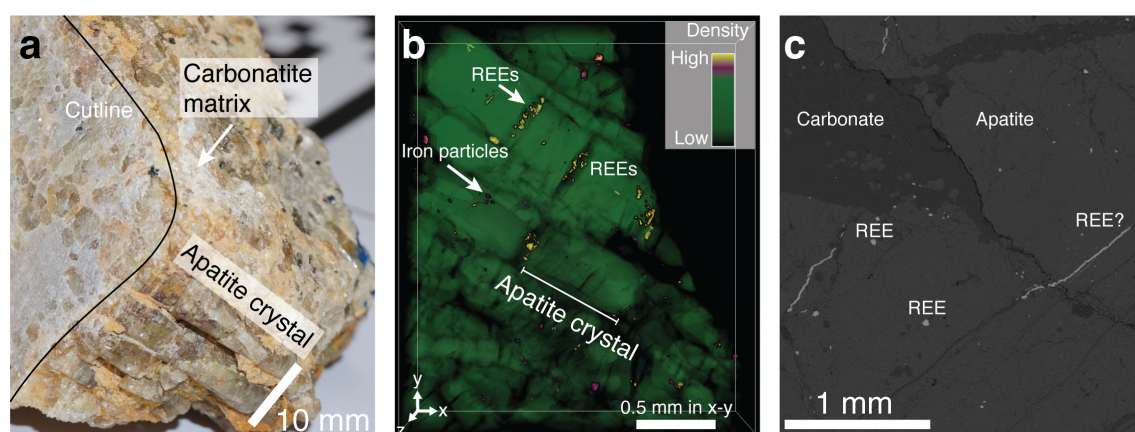


Figure C8.3 (a) Photograph of an apatite-bearing carbonatite sample from Siilinjärvi, trench 1, sample FI18RJA21b (b) CT-scanned 3D-volume model of a sub-part from the sample FI18RJA21b. (c) 2D-BSE greyscale image of a polished thin section sample, sample FI17GU10, a similar apatite-bearing carbonatite.

Appendix D

Technical specification of survey and camera systems

Table D2 Properties of test trenches, information for the UAS surveys, and further details of the HSI mapping, as we only surveyed the exposed trench rocks by HSIs. Altitude in m above sea level. The last column refers to the input layers used in the OTVCA for supervised image classification. GSD = ground sampling distance.

Outcrop / Method	Coordinates	Dimension x-y	Survey condition	Used bands / Integration time	Flights / Coverage	GSD	Altitude	OTVCA layers
Method (<i>Hyperspectral only</i>)								
Trench 1	63.147N, 27.738E	130 × 36 m	sunny, windless	50 / 10 ms	1 / 5,500 m ²	2.7 cm	40 m	HSI
Trench 2	63.145N, 27.738E	200 × 40 m	sunny, windless	50 / 10 ms	1 / 3,050 m ²	2.3 cm	30 m	HSI
Trench 3	63.141N, 27.738E	220 × 400 m	low clouds, breeze	50 / 30 ms	3 / 38,200 m ²	3.4 cm	50 m	HSI, MSI, RGB
Multi-spectral	63.143N, 27.738E	450 × 1,430 m	sunny, windless	4 / automatic	1 / 0.649 km ²	10.5 cm	100 m	–
RGB	63.143N, 27.738E	540 × 1,290 m	low clouds, breeze	3 / automatic	2 / 0.623 km ²	2.7 (1.5) cm	100 m / 70 m	–
Magnetic	63.143N, 27.738E	620 × 1,100 m	sunny, windless	–	1 / 0.695 km ²	30 m*	40 m	–

* 15 m after interpolation.

Technical details for the used multi- and hyperspectral cameras are provided in Table D3.

Table D3. Technical specifications of used cameras,

Sensor	Senop Rikola	Parrot Sequoia	senseFly S.O.D.A.
Dynamic range	12 bits	10 bits	–
Horizontal field of view	36.5°	70.6°	90°
Vertical field of view	23.5°	52.6°	60°
Focal length	9 mm	4 mm	2.8–11
Mass	720 g	135 g (with sunshine sensor)	111 g
Frame rate	30 Hz	1 Hz	0.3 Hz
Spectral resolution	8 nm	40 nm (10 nm)	–

Training and validation points

Training and validation samples used for the supervised image classification used a cross-referencing support vector machine algorithm. The final classification maps are used to approximate the geologic contacts which were indifferentiable in RGB orthophotos. Additionally, the carbonatite classification is possible, mainly for trenches 1 and 2, represented by the higher amount of training and validation pixels. The labels for the test and training points were determined with the handheld spectrometer. Each spectral signal was measured with a Spectral Evolution PSR-3500. A spectral resolution of 3.5 nm (1.5 nm sampling interval) in the visible and near-infrared (VNIR) range and 7 nm (2.5 nm sampling interval) in the SWIR range is provided, using a contact probe. Each spectral record consists of 10 individual measurements taken consecutively and averaged. To convert radiance to reflectance, we use a PTFE panel (Zenith Polymer with >99 % reflectance VNIR; >95 % reflectance SWIR).

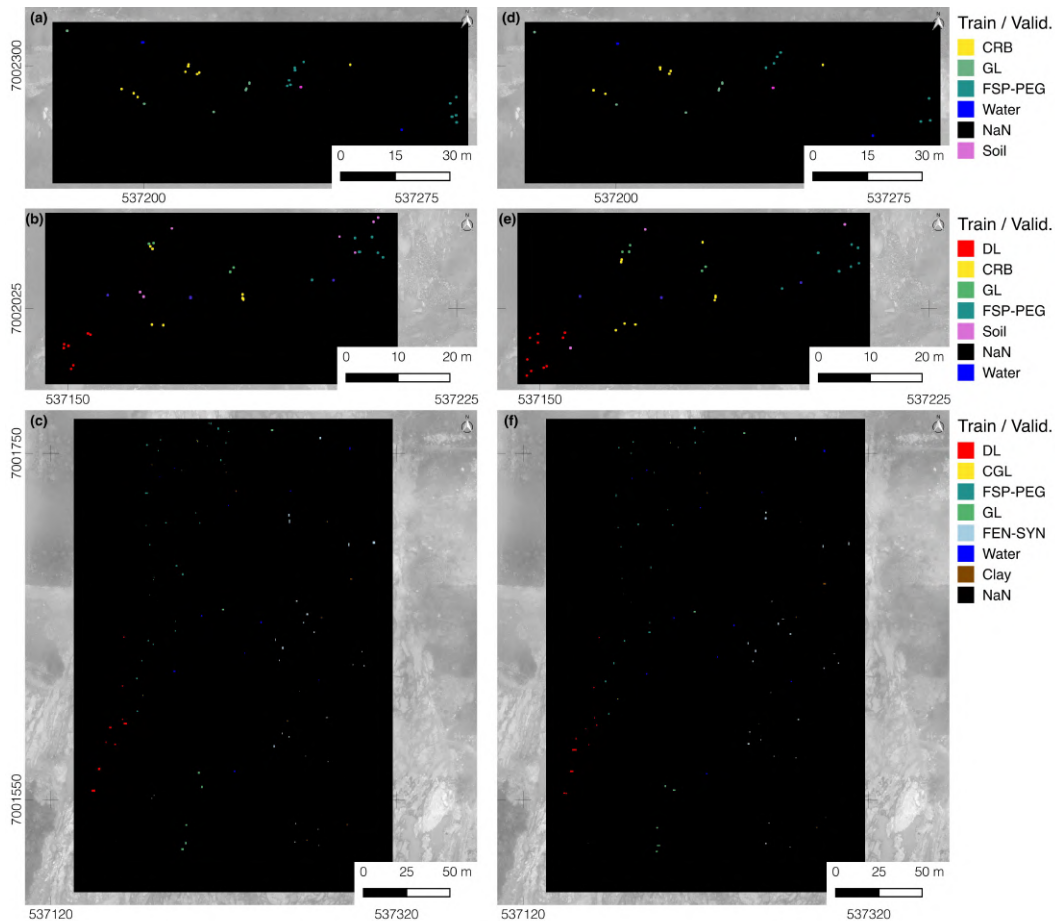


Figure D8.4 Training and validation for support vector machine classification in column-wise order. (a) Training samples trench 1. (b) Training samples trench 2. (c) Training samples trench 3. (d) Validation samples trench 1. (e) Validation samples trench 2. (f) Validation samples trench 3. CRB = Carbonatite; GL = Glimmerite; CGL = Carbonatite-glimmerite; FSP-PEG = Feldspar-pegmatite; NaN = Not a number; DL = Dolerite; FEN-SYN = Fenite-syenite.

Appendix

Table D4 Confusion matrix trench 1. Indef./NaN = black pixel.

Predicted \ Truth	Carbonatite	Glimmerite	Feldspar–Pegmatite	Water	Indef.	Soil
Carbonatite	123	0	17	0	0	7
Glimmerite	0	120	0	0	0	0
Feldspar–Pegmatite	4	0	172	0	0	0
Water	0	0	0	63	0	0
Indef./Nan	0	0	0	0	42	0
Soil	0	0	2	0	0	87

Table D5 Confusion matrix trench 2. We observe that the differentiation between the water and soil pixels is ambiguous, however, both classes were rejected from the geological interpretation.

Predicted \ Truth	Dolerite	Carbonatite	Glimmerite	Feldspar–Pegmatite	Soil	Indef./Nan	Water
Dolerite	83	0	0	0	0	0	0
Carbonatite	0	147	0	6	0	0	0
Glimmerite	0	4	80	0	0	0	0
Feldspar–Pegmatite	0	8	0	124	0	0	0
Soil	0	0	1	0	50	0	0
Indef./Nan	0	0	0	0	0	32	0
Water	0	0	0	0	48	0	90

Table D6 Confusion matrix trench 3.

Predicted \ Truth	Dolerite	Glimmerite–Carbonatite	Feldspar–Pegmatite	Glimmerite	Fenite–Syenite	Water	Soil	Indef./Nan
Dolerite	649	0	0	15	0	0	0	0
Glimmerite–Carbonatite	0	34	11	0	0	0	0	0
Feldspar–Pegmatite	31	0	1,141	0	80	0	0	0
Glimmerite	8	0	13	650	0	0	2	0
Fenite–Syenite	17	6	39	0	1,296	0	0	0
Water	0	0	0	0	0	532	0	0
Soil	2	0	0	0	2	0	353	0
Indef./Nan	0	0	0	0	0	0	0	4

Forward-modelled blocks in cross-section view

Profile plots across the DSM and the underlying modelled carbonatite–glimmerite bodies are shown. Note the increasing length scale. Corresponding magnetic profiles are shown in Figure 4.8 in the manuscript. Here, the calculated magnetic response per profile is plotted on the UAS-

measured TMI signal. Due to the ambiguous nature of geophysical forward models, all available constraints were employed to create the model bodies. Starting parameters for each profile are given by the user. We iterated 20 sessions with various starting parameters for magnetic susceptibility, as well as position and depth of initial body geometry. We assumed tabular body shapes. Strike direction, dip, and length of each body were estimated based on UAS-RGB, hyperspectral and structural data. For example, the depth of the body for profile 4 (S4) seems to be overestimated, and constrained possible susceptibility. This corresponds with the magnetic low of profile 4, directly above a shear zone. Even with an apparent good model fit, an interpretation is complicated. As stated above, shear stress could have decreased the amount of magnetic minerals. For profile S1, a gap between two carbonatite bodies exists, caused by the absence of magnetic rock material, caused by an observed feldspar–pegmatite intrusion. Data of a comprehensive exploration drill campaign would solidify further interpretations.

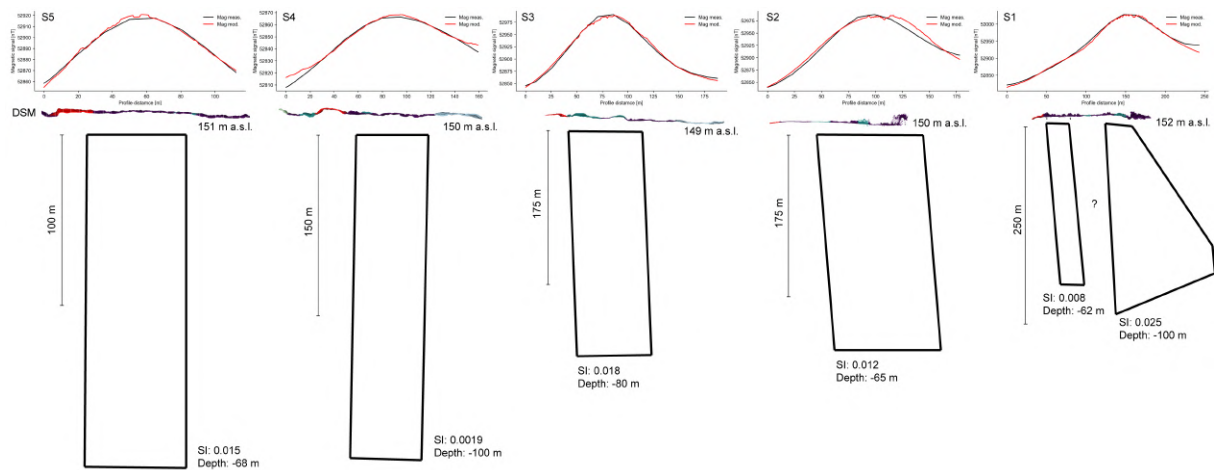


Figure D8.5 Cross-section profile plots across the DSM and the underlying, modelled tabular carbonatite–glimmerite bodies.

Microscopy

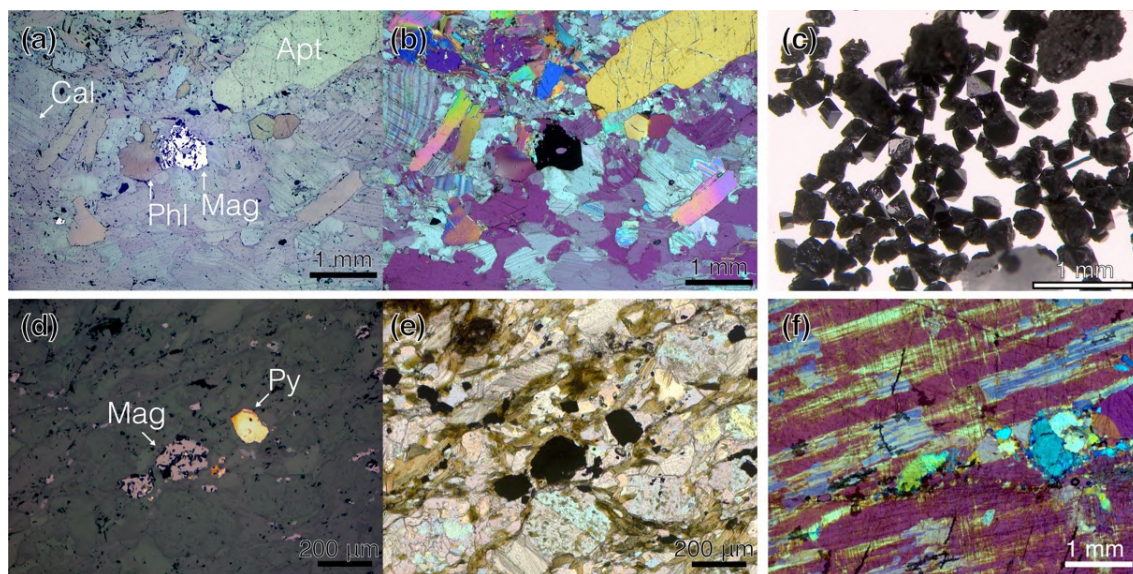


Figure D8.6 Optical microscopy (with the Zeiss Axio Imager M2m with Axiocam MRc 5 imaging module) conducted for thin sections of representative samples; Cal = calcite; Phl = phlogopite; Apt = apatite; Mag = magnetite; Py = pyrite. (a) Carbonatite–glimmerite, reflected light. (b) Carbonatite–glimmerite, transmitted light, crossed nicols. (c) Magnetite (subhedral–euhedral), reflected light. (d) Carbonatite–glimmerite, reflected light. (e) Carbonatite–glimmerite, transmitted light, parallel nicols. (f) Feldspar–pegmatite, transmitted light, crossed nicols.

X-ray diffraction plots

Magnetic susceptibility, detecting magnetite signature, among others, is measured with a Bartington MS2 magnetic susceptibility system (Bartington Instruments, Witney, Oxon, United Kingdom). A mass fraction of material per sample was crushed to a fine powder (<0.1 mm grain size), weighed to 10.00 g and its susceptibility was measured with the sample tray holder of the MS2 system. The values are augmented with additional susceptibility values taken from the literature for those lithologies without available rock specimens.

XRD is conducted with the PANalytical Empyrean diffractometer with cobalt as the X-ray source and equipped with a PIXcel 3D Medipix detector. The main targets are mineral content, including detection and quantification of magnetic minerals. X-ray diffraction patterns for two selected samples are shown in Figure D7 and Figure D8.

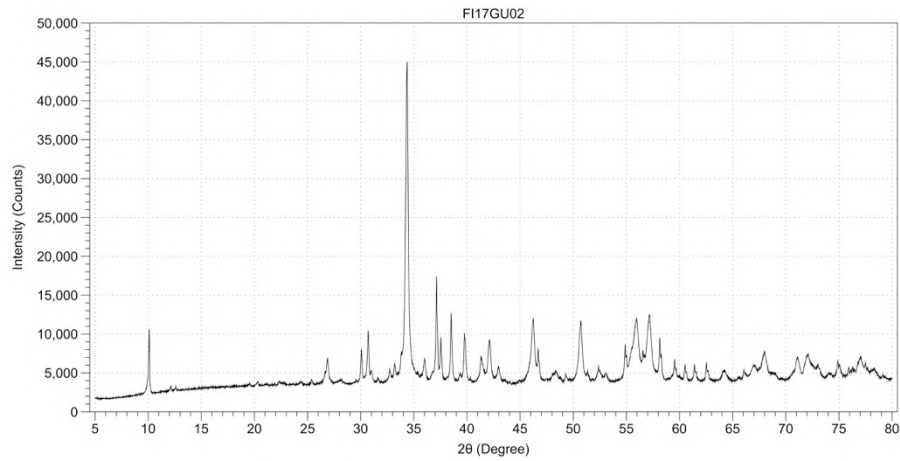


Figure D8.7. X-ray diffraction pattern for the carbonatite sample.

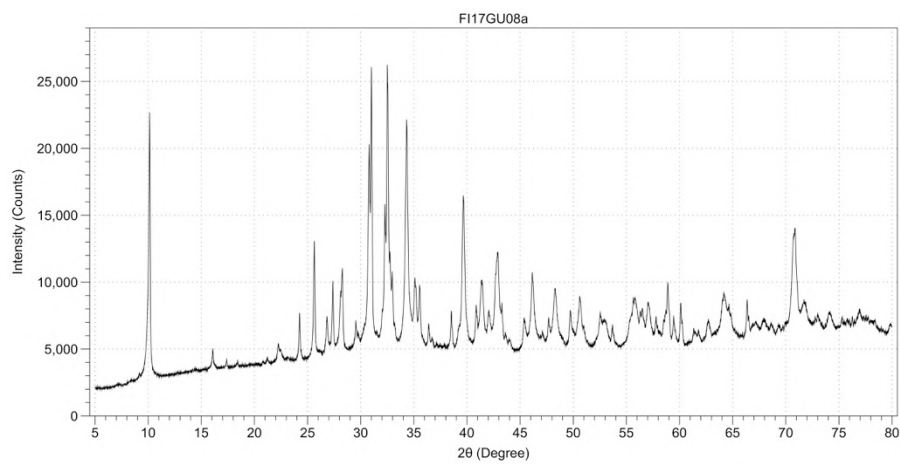


Figure D8.8. X-ray diffraction pattern for the dolerite sample.

Table D7 Mineral abundance from a carbonatite–glimmerite zone (GU02) and a dolerite dyke (GU08a) sample is listed below, with the mineral content in weight % (wt.%).

Mineral (wt.%)	Carbonatite (and glimmerite)	Dolerite
Coordinates: UTM zone 35N	537156E, 7002020N	537124E, 7001475N
Calcite	59.6	16.6
Magnetite	1.8	2.4
Pyrite	—	2.0
Actinolite	3.7	—
Ankerite	4.1	—
Albite	—	37.4
Annite	9.8	—
Apatite	21.0	—
Biotite	—	29.7
K-Feldspar	—	4.8
Quartz	—	7.2

Appendix E

A severe flight error was logged with the DJI Mavic during an RGB outcrop survey on Disko Island (13.08.2019). The flight controller announced two warning messages: *large yaw error* and *magnetic interference error* with the recommendation to land immediately. To investigate if those interferences are related to the local geology with strong magnetic gradients and inverse magnetisations, the VD of fixed-wing TMI is compared with the recorded error positions. The magnetic compass of the DJI Mavic is a microelectronic magnetometer. Both compass yaw and interference warnings appeared near or atop the magmatic outcrop with native iron occurrence. It is probable that the local magnetic gradient affected the UAS compass, signifying the instrument's sensitivity. A similar phenomenon occurred during the Otanmäki HSI survey, where the multicopter yaw was influenced by the locally strong magnetic gradients.

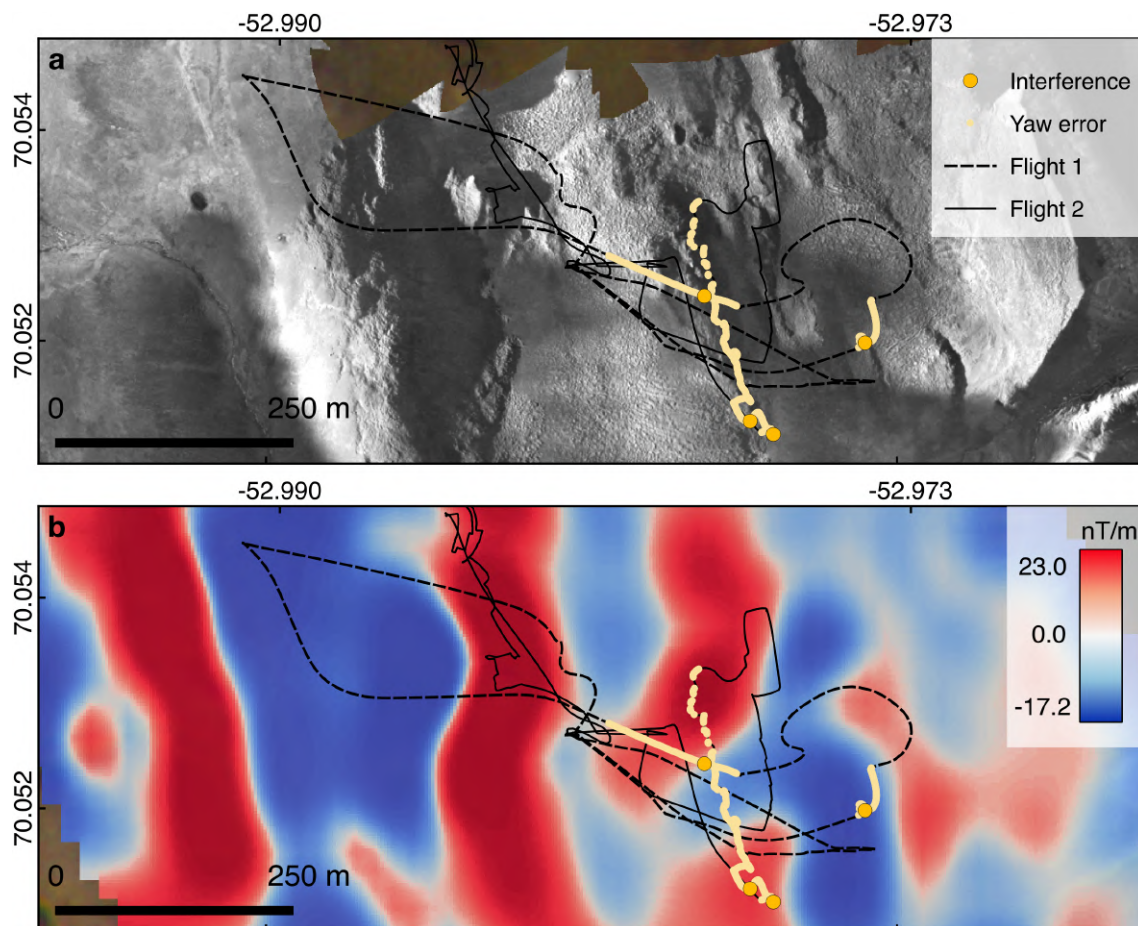


Figure E8.9 Flight lines and error points logged by DJI Mavic and plotted with supporting UAS-based surface data of local outcrops at the Qullissat delta (Chapter 5, anomaly “E”). (a) Interference and yaw error shown on eBee MSI mosaic. (b) Vertical derivative (1VD) of total magnetics from fixed-wing UAS.

Appendix F

F1 Flight control and processing of UAS borne magnetic data

Flight performance is controlled by live-link software via telemetry. A GSM-based tracker device allows locating the UAS in case of lost telemetry signal. A magnetic and barometric base station, which is placed near to the mobile telemetry/control station, measures the time variant part of the magnetic field (three-component fluxgate magnetometer) and the barometric pressure.

In the post-processing of the data, the magnetic field (and optionally the barometric altitude) measured by the moving UAS platform are corrected by the variations measured at the base station. For these surveys, the dedicated base station magnetometer was not available, and a replacement UAS magnetometer was used for the base. The basic data processing (Table F1) utilized the Radaipro software (version 2.0, Radaipro Oy, Oulu, Finland). After these basic processing steps, 1) data were checked visually and invalid or unnecessary points (e.g., spikes and flights between the home base and the survey area) were removed, 2) base station correction was applied to the magnetic total field data, 3) separate flights were combined and data outside the survey area were taken out (with 25 m margins), 4) a low-pass filter with a cut-off wavelength of ~18 meters was applied, 5) a ELM was conducted and finally 6) the IGRF core field was removed.

In the ELM method, first a deterministic inversion is used to find a simple susceptibility model, whose synthetic response fits the measured magnetic total field. In a second step, the obtained susceptibility model is used to compute the total magnetic intensity at a constant elevation level on an even grid. Here, the susceptibility model is composed of a single layer of three-dimensional magnetized cells.

The ELM method reduces the effects of varying flight altitude and uneven sampling of the data points, high frequency noise and artefacts provided that their wavelength is short compared to the size of the elements used in the layer model. ELM is used also to level the datasets and make the heading correction.

The ELM was applied to the fully pre-processed total field data. Horizontal size of the elements was $40\text{ m} \times 40\text{ m}$ and their vertical height was 111 m. Depth to the top of the model was 2 m and the top of the model followed the terrain topography. The total number of elements was $148 \times 64 = 9,472$, and the total number of (decimated) data points was 12,531 (15.10 %).

Table F1 General processing steps of UAS fixed-wing magnetics.

1. Remove dummy values
2. Computation of barometric height (relative altitude) from pressure data.
3. Computation of rectangular X and Y map coordinates (UTM 22W).
4. Computation of running profile distance coordinates and azimuth/heading angles
5. Application of fluxgate calibration parameters (derived from a separate calibration measurement).
6. Computation of the raw and (orientation) corrected magnetic total field.

F2 Multispectral surveys

We used Agisoft Metashape (version 1.6.2, Agisoft, St. Petersburg, Russia) to process multispectral data, creates digital surface models as raster and 3D point clouds, and multispectral orthomosaics from each flight area, and the complete flight area in one image.

For spectral calibration, three images with different image acquisition settings (i.e., different integration time to adjust for varying illumination strengths) were taken from a ground reference target (AirnovTM VIS-NIR greyscale panel). These calibration images are automatically detected in Agisoft Metashape or selected manually. Our selected settings in the image alignment step are: alignment accuracy in high; pair selection with reference; adaptive camera model fitting is activated.

After each step, the points were filtered with gradual selection repeatedly, and the option “optimize camera” was applied each time to reduced spatial errors (see 3D remote sensing lab at SLU Umeå, Sweden, <http://www.rslab.se/agisoft-photoscan-pro>, last accessed 04.03.2021). After the correction steps were applied, the sparse points were used to create a dense point cloud, using the “high quality” settings in the creation dialogue. From the dense cloud, we exported the elevation model and the 3D point cloud (reference standard WGS84 UTM 22N, EPSG 32622).

F3 Magnetic vector inversion with constrained the magnetization directions

It appears as a reasonable assumption that the remanent magnetization in the magmatic body has roughly the direction of the palaeomagnetic field, when the body formed, since no tectonic processes with major rotations have taken place after the formation of the basalt. However, this must be considered with some care, since the central part of the investigation area has been affected by slope instabilities and may some rotational movements are associated with them.

Referring to Riisager and Abrahamson (1999, 2000; see Section 5.1.3), the palaeomagnetic field direction of the Asuk Mb can be estimated with an inclination and declination of -80.7° and 228.1° , respectively. The current Earth magnetic field direction (IGRF) at Qullissat had during the field campaign an inclination of 81° and a declination of -31.5° resulting in an angle of $\sim 168.3^\circ$ between the two fields.

Accordingly, it was assumed that the induced and the remanent magnetization are approximately parallel or antiparallel in most locations. We considered these main magnetization directions in the magmatic units by keeping the components perpendicular to the Earth magnetic field small. This was achieved by modifying the weights \mathbf{w}_0 (basalts) of $\Phi_{M,Ref}$ and having non-zero weights of 0.125 in the direction perpendicular to the current Earth magnetic field such that zero-weights only remained in the direction of the Earth magnetic field for the basalts and the magmatic body. Since the weights had to be expressed in the coordinate system used for the model ($x = \text{East}$, $y = \text{North}$, $z = \text{height}$), a rotation was applied onto the weighting factors resulting in $\mathbf{w}_{0,p}(\text{Basalts}) = (0.124, 0.123, 0.0196)$. Rather small weights were selected with 0.125, since there is a higher uncertainty with the assumed magnetization direction.

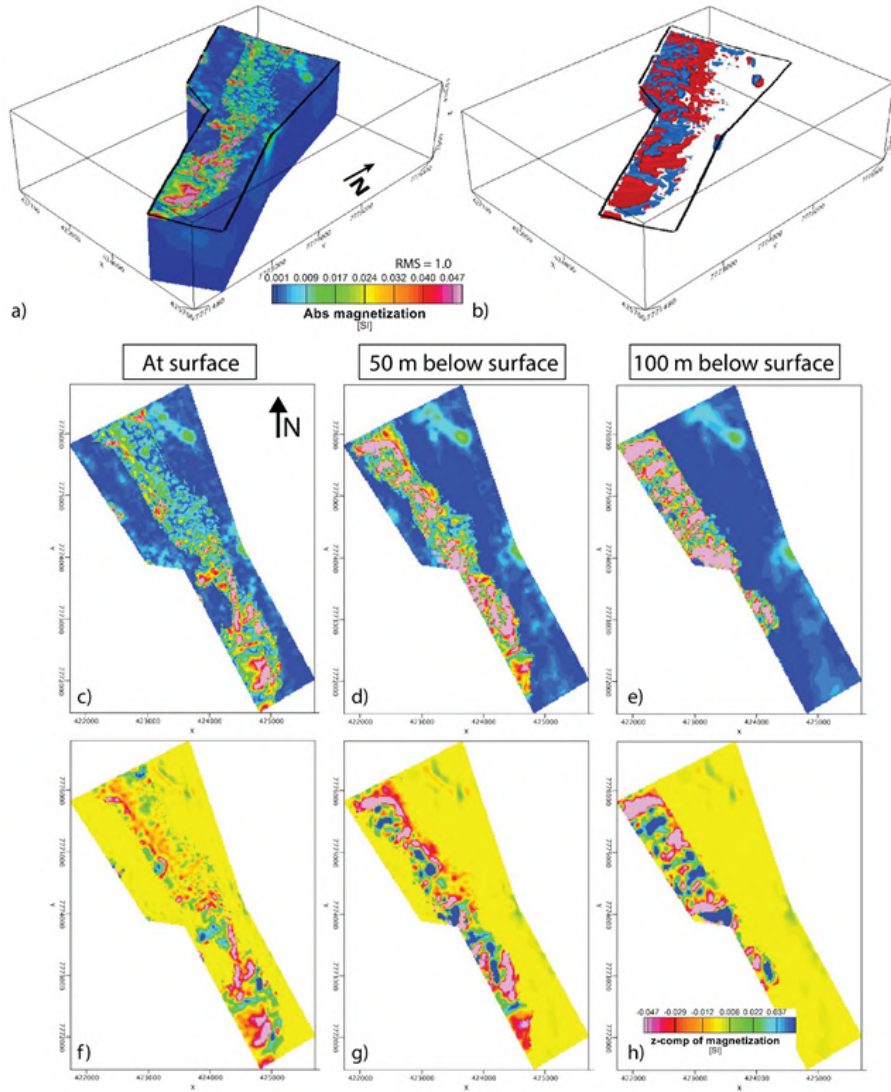


Figure F8.10 Results from the inversion model, where in addition the direction of the magnetization in the magmatic units is constrained towards the direction of the regional magnetic field. (a) The final magnetization distribution is presented as absolute values of the magnetization vectors. (b) Only cells with absolute magnetization values > 0.01 SI are shown as isosurfaces. Blue and red colours are associated with locations, where the z-component of the magnetization points out of the ground (z-component is positive) and into the ground (z-component is negative), respectively. The remaining figures show the magnetization along the surface (c and f), and at depths of 50 m (d and g) and 100 m (e and h) below the surface, respectively. In (c) to (e) and (f) to (h), the absolute value and the z-components of the magnetization are presented, respectively.

Results of this test are presented in Figure F8.10. As for the former inversion test, in which only the sediment units were constrained, higher magnetization values are accumulated in cells associated with the magmatic units and both positive and negative anomalies appear. The only anomalies located outside this volume are again the anomalies A and B. In contrast to the former inversion run, the x- and y-components have rather small values within areas assigned to the magmatic units (see Figure F8.11 as an example) such that almost the whole magnetization is associated with the z-component. In addition, the absolute magnetization values are generally higher, but are usually not > 0.4 SI (maximum value is 0.6 SI), and general orientations in an

N–S to NNW–SSE direction are less pronounced (Figure F8.10) than in the former test but anomalies are more scattered and generally more small-scaled.

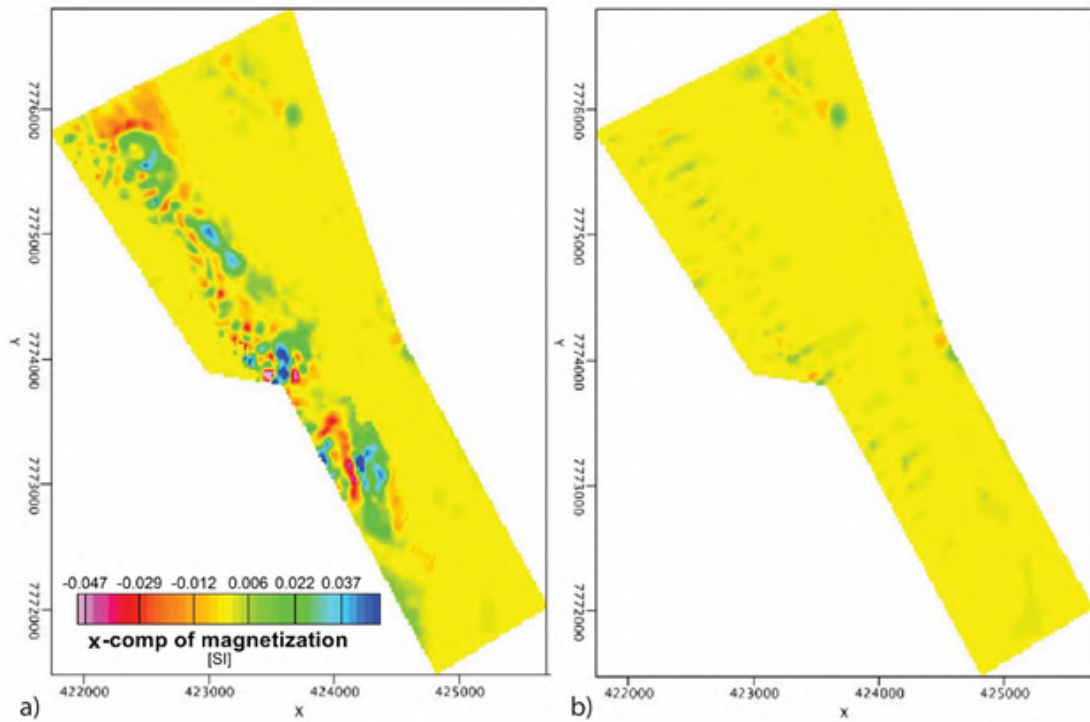


Figure F8.11 The x-components of the magnetization 50 m below the surface are shown for the two constrained inversion tests. In (a) cells associated with sediment units were constrained towards a non-magnetic reference model, but in (b) in addition the direction of the magnetization in the magmatic units is constrained towards the direction of the regional magnetic field.

Appendix G

Development of a multispectral camera for fixed-wing UAS

This section provides an overview of the light-weight camera aimed for fixed-wing UAS use. We designed, constructed and tested a prototype multispectral system as the final technical contribution of MULSEDRO (Heincke et al., 2019) within this thesis. Unfortunately, planned tests with the Tholeg multicopter in Freiberg were postponed indefinitely, due to the pandemic in 2020. The designed camera systems aims to scan geologic outcrops in mine sites, exploration greenfield and remediation areas. Rapidly acquired MSI data can increase survey opportunities and data abundance for mine planners and in remediation procedures. As introduced in *Chapter 2.2.3 Development of a fixed-wing-based multispectral camera*, airborne and satellite-based spectral data often lack the resolution to map land cover changes in sub-meter resolution. Either that resolution level is needed, or the data is compromised by the atmosphere or lack of imagery (Padró et al., 2019). An alternative, cost-effective mapping solution is to use light-weighted UAS with a short preparation phase to support surveying operations flexibly and repeatedly. UAS-based camera systems are abundant on the market and tests with fixed-wing UAS have been conducted (Laliberte et al., 2011; Aasen et al., 2018; Kim et al., 2019).

We designed a system based on an existing camera body frame, and we selected available image filters. We choose components such that the spectral range, spectral and spatial resolution as well as scene overlap and data quality would be suitable for geological mineral mapping. A general challenge for cameras is the high velocity of fixed-wing drones ($10\text{--}30\text{ m}\cdot\text{s}^{-1}$) because short exposure times are needed to obtain sufficient image overlap. Most cameras systems either do not fit technical UAS requirements or only provide a limited set of multispectral bands (e.g., Parrot eBee Sequoia 4 bands, Sal-Engineering Eoptis MAIA camera 9 bands). Furthermore, the data logging hardware to store or transmit images during the flight adds additional weight and energy consumption.

Our experience with the Sequoia camera (Parrot, 2017) and the eBee UAS justified to choose the Radai Oy Albatros as fixed-wing platform. Image processing and photogrammetric workflows for the Sequoia camera are implemented with standard industry software. Radiance-to-reflectance calibration using the empirical line regression method or the one-point calibration is known to provide suitable results (Tu et al., 2018). An evaluation of performance metrics for the radiometric calibration is recommended (Poncet et al., 2019).

The Albatros UAS fulfils the criteria of (1) capability to starting without heavy lift-up equipment and land on unconsolidated ground, (2) allows survey of large areas and (3) has

stable and steady aerodynamic properties. Landing of fixed-wing planes often need to be conducted under confined spatial conditions in forests, open pit mines, on tailing surfaces and rock slopes. Flight behaviour should be smooth to guarantee straightforwardly processable image data. In addition, the rather sensitive camera equipment should be cushioned inside the UAS fuselage to enable damage protection during rough landings.

First in-flight camera tests

Preliminary camera setup tests were done in 2018, with the Rikola camera in flight mode in order to evaluate the potential of frame-based images acquired in a fixed-wing UAS scenario. Fixed-wing planes and UAS have to maintain a certain flight velocity to create sufficient uplift. To simulate a fixed-wing flight, the Aibot hexacopter with the Rikola camera was flown at constant speed over a crop field near Freiberg. The camera was set for continuous image acquisition (2 seconds per image). The camera image sequence was programmed with 50 bands and a full wavelength range from 504–900 nm. Flight speed was programmed for $3.5 \text{ m}\cdot\text{s}^{-1}$ above ground, which was consequently higher with headwinds during test flights. Velocity is quite high considering the usual operation procedure of stop-scan-go flights. Nominal flight height was set to 25 m above ground. The integration time per band was set for 20 ms (1 second for 1 hyperspectral image cube). Based on previous flight campaigns, an integration time of 20 ms allows the camera to scan an image at high spectral quality. The resulting singly image bands in high offset from each other, which solidifies the image acquisition in this setup as not feasible (Figure G8.12).

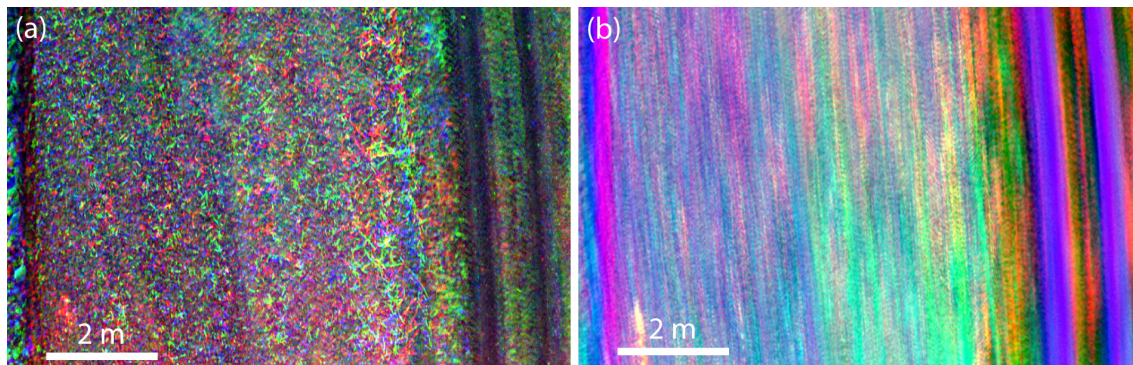


Figure G8.12 Field test of hyperspectral image acquisition during constant and rapid multicopter flight creates a blur effect. (a) Single RGB 640 nm, 550 nm, 503 nm Rikola. Intensive false colours appear where green vegetation and dark soil is expected. (b) Principal components calculated for 50 bands and shown for bands 3, 2, 1, increasing the smearing effect, where clear surface features are not visible.

The msCam development

Here, the integration of the multispectral camera system, henceforth referred to as ‘msCam’ from Spectral Devices Inc. (London, Ontario, Canada) is described. We aimed to integrate the msCam into the fixed-wing plane Radai Oy Albatros, that is successfully used for magnetic surveys. Doing so would create a multi-sensor UAS system that can collect magnetic and multispectral data simultaneously. This would be time-efficient and provide consistent multi-parameter data information for interpretation.

The UAS fuselage was augmented to fit with already existing magnetic surveying equipment (magnetometer, datalogger, accessories) and extended by the msCam camera and its datalogger. The UAS hull was modified to fulfil msCam requirements, such as stiff fasteners, a suitable hatch for the camera lens and vibration damping material around the camera. Technical details are found in Table G8.8.

Table G8.8. Technical parameters of msCam system.

Parameter	Value
Camera dimension	56 × 50 × 52 mm
MS mirror sledge dimension	180 × 62 × 62 mm
Sensor size	25.6 × 25.6 mm
Pixels per frame	256 × 256
Total mass of system	480 g
Centre wavelength VIS (nm)	435, 470, 505, 540, 575, 610, 645, 680
Centre wavelength NIR (nm)	720, 760, 800, 840, 860, 900, 940, 980
FWHM VIS/NIR (nm)	10/7
Shutter/ exposure time minimum	Global/0.1 ms
Sensor type/size	CMOSIS CMV4000 CMOS / 2.54 × 2.54 cm
Lens properties	NMV-25M, 25 mm, f/1.4, focal length 25 mm
Transfer rate camera to SBC1	5 Gbit/s
Total costs	22,230 USD (~18,500 Euro)

Integration of the msCam

Several conditions needed to be fulfilled for this system to achieve image qualities that allow reliable geological interpretation from data acquired in drone surveys. Each camera is mounted on a specifically designed mirror sledge with an aluminium harness. This sledge holds a tilted mirror that guides light from the surveyed surface to the camera placed inside the UAS fuselage. The fixed-wing was calibrated, and plane aviation controls were tuned with a new setup in regard to its changed centre of gravity.

The multispectral image filters are based on the Bayer-matrix pixel separation (de Oliveira et al., 2016). This allows the camera to simultaneously take 8 bands simultaneously per image

frame. Hence, to make use of the total available wavelength range, two cameras with complementary wavelength ranges were required. Since the space within the fuselage is too small to place both cameras, survey areas have to be flown twice — one time with each camera implemented — to acquire data in the full spectral range. To create a 16-band multispectral image mosaic, the resulting multispectral image mosaics are stacked in a consecutive processing step. The created image data stream needs temporal storage and therefore an additional processing and storage unit (SBC-1) was implemented.

Each camera in the mirror sledge frame (Figure G8.13c) and placed inside the UAS fuselage is facing nadir at 90°. The MS mirror construction is an optical path system designed to hold the msCam in a position comparable to a periscope. This construction keeps the msCam stable inside the fuselage and adds protection to lens and camera.



Figure G8.13 Different views depicting the msCam system. Black bar represents 5 cm. (a) Camera body with open sensor array (orange) and C-mount lens mount, often used in machine vision applications. (b) Example image of camera and lens in front view. (c) Rendered 3D view of msCam mirror sledge illustrated from (Spectral Devices Inc., 2018).

The mirrors (angled 45°) guide the incoming light from the reflected surface through the lens onto the sensor. Two mirrors for two cameras are used, one for the VIS camera, one for the NIR camera. An optical flat was used to measure the surface accuracy. Surface flatness is a technical term that describes the tolerance of surfaces for planarity and smoothness (e.g., Fritz, 1984; test glasses with flat surface). The VIS mirror surface consists of enhanced, brushed aluminium with a surface flatness of $\lambda/4-6$ and a reflectivity of approximately 95 % between 400–700 nm. The λ describes a wavelength in the VNIR used to measure the accuracy in the optical laboratory. The NIR mirror's surface consists of protected gold with a surface flatness of $\lambda/4-6$ and a reflectivity of > 95 % from 700–1600 nm (Spectral Devices Inc., 2019).

Image processing workflow

Data processing involves the same workflow for the two cameras resulting in two point clouds that are merged to achieve a full 16-band image. Recommendations of the camera manufacturer

to use and optimize the created images were integrated to achieve usable images (Spectral Devices 2019).

The advised workflow starts with transferring images from the SBC-1 memory to a PC with Agisoft Photoscan/Metashape, to perform structure-from-motion stereo-photogrammetry (Westoby et al., 2012). Image processing of multispectral images basically involves vignetting correction, lens distortion correction, band registration, and radiometric correction. Optimal results for sparse point cloud generation are achieved with ‘very high’ settings where the images are up-sampled before point matching. For visually identified control points, the marker point accuracy was set to 1 m for most uncertain marker coordinates. Manual filtering of the sparse cloud as well as gradual filter methods were applied before dense cloud creation. Then, manual filtering of the dense cloud for obvious outliers (e.g., points outside the model space) was done. The product is a multispectral image mosaic in arbitrary units (digital number, DN). An empirical line calibration was used for radiometric calibration with field targets or known target spectra of the scene. The final result is a georeferenced orthophoto, a digital elevation model and a 3D point cloud of the scene.

System test and geologic field tests

Before flight tests with the equipment were conducted, the image quality of the camera was evaluated under controlled conditions near the head office of Radai Oy in Oulu, early 2019 under sunny weather conditions. Fast roll, turns, and shaking were simulated to investigate how movement influences the image quality in terms of blurring, noise and image content. Only small blurring effects were discovered during visual inspection of fast-moving image sequences, conducted by shaking the camera, rotating it along one axis from between a 180-degree field of view, and running a straight line to simulate a moving platform imaging sequence (Figure G8.14).

(a) stationary chaotic shaking



(b) stationary sweep rotation right to left



(c) straight line run



Figure G8.14 Ground imaging performance test of msCam for capturing during rapid movements to simulate a fixed-wing UAS flight using 20 ms image integration time. (a) Chaotic shaking movement from a stationary point at pitch and roll axis. (b) Rotary sweep at the yaw-axis in a high angular change of $\sim 300^\circ/\text{s}$. (c) Moving camera test along a straight line at velocity of $\sim 6 \text{ m/s}$.

For a geological evaluation, twenty geologic samples of different rocks and minerals were provided by the Geological Survey of Finland (Geologian tutkimuskeskus (GTK)) for test scans with the cameras (Figure G8.15). The setup of this scanning experiment is shown with different sensor–target distances (1 m, 7.5 m, 15 m) were evaluated, but since the test rock specimen were only provided at some centimetres in diameter, realistic distances to simulate a UAS flight were not available.

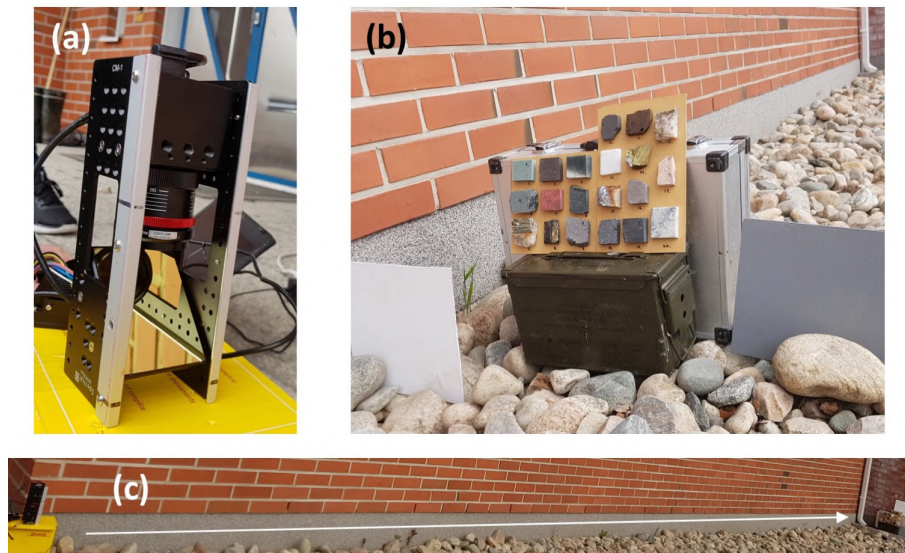


Figure G8.15 Setup for field test scans with the msCam near the Radai Oy office in Oulu. Rock samples are scanned that were provided by GTK. (a) The VIS camera was faced towards the rock samples. (b) The small mineral samples are scanned together. (c) Distance to target was extended for ~15 m from the camera, the background walls are from the Radai office building.

Captured images of the VIS camera and the result of a fast, unsupervised clustering approach to evaluate the image quality in terms of separability and resolution. Again, the empirical line calibration with a white and grey reflectance panel was applied to calibrate the images. The results are promising, since different lithologies are distinguishable. The iron-bearing minerals goethite and hematite are grouped in one class (Figure G8.16).

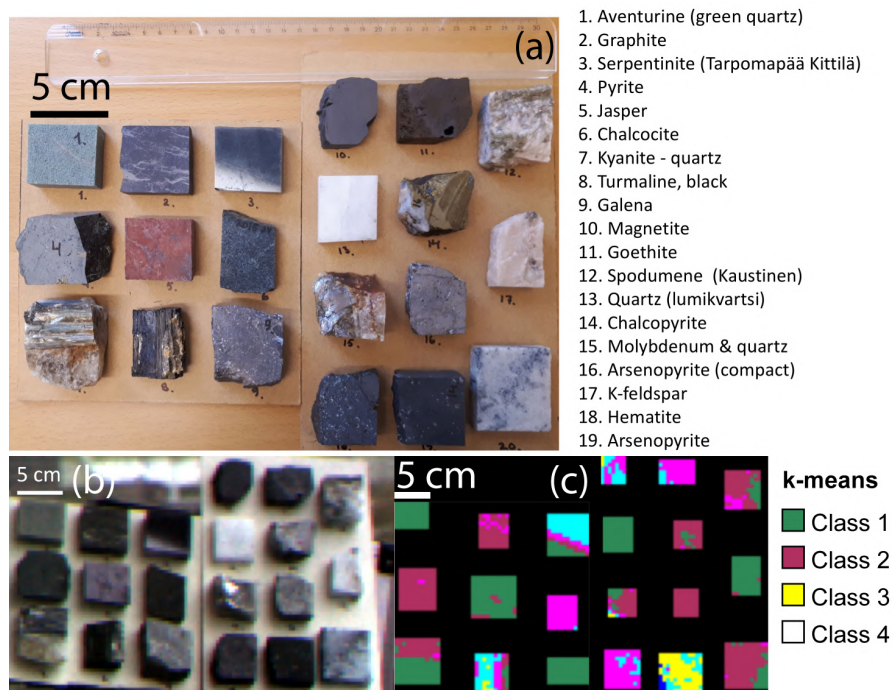


Figure G8.16 Geologic test samples (a) Rock samples provided by Heikki Salmirinne and GTK. Samples were polished and fixed on a board for spectral scanning. Mineral names are plotted in the side. (b) Resulting RGB image and (c) unsupervised image clustering from the VIS camera data. Different colours indicate different mineral classes.

Field test on an active mine site in Finland

First UAS-based test surveys were done at Ahmosuon aerodrome near Oulu (not further shown) and in the phosphate mine of Siilinjärvi in Central Finland (Chapter IV provides a complete field study of the area). The data were collected on the premise of Yara across a test outcrop, where the hard rock geology is associated with rocks from an Archean carbonatite-glimmerite complex that intruded into granite-gneiss (O'Brien et al., 2015). The approximate flight line lengths were 1400 m during the Siilinjärvi flights, with a mean line spacing of 40 m and a median altitude of 120 m. During the test, the crew faced challenging weather conditions with higher winds and changing light conditions, which means tuning of the image integration time was required and not every image frame could be retrieved and used for image mosaicking. Between 2500–3907 images could be recovered per flight, based on 4000 target images. Missing images were not saved due to an internal memory bottleneck. The goal of sustaining a realistic high sampling frequency between 1–2 Hz, where each flight lasted 35–40 minutes, was achieved (Figure G8.17).

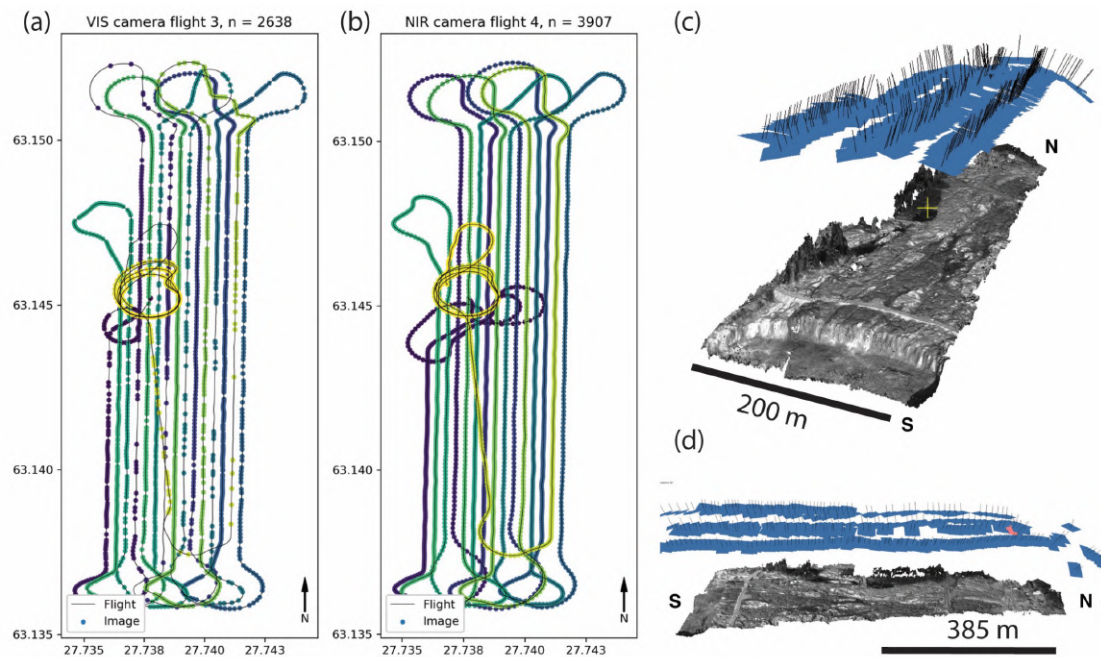


Figure G8.17 Examples of recovered flight lines and image positions from the msCam survey in Siilinjärvi. Images for (a) VIS camera image positions indicated by dots, based on the time stamp of each image. Colour-code according to time stamp, with blue at start, light-green marking the survey end. (b) NIR camera image positions shown as dots. (c) 3D views from NE–SW and (d) E–W cross-view directions onto the surveyed outcrop. The reconstructed surface from the 3D dense point cloud is shown in grey, build from the computed dense point cloud. Blue rectangles and black arrows illustrate reconstructed camera position and image view vectors of each camera. Coordinates in degree latitude, longitude WGS84.

A python script was used to extract the image time stamp from each image ID tag. The time stamp was transformed to a time series frame and matched with the time stamp from the Pixhawk UAS mission log file, in order to retrieve the actual image position and roll, pitch and yaw positions. Data synchronization by time had to be made with care, because of an offset between image and log file timestamp, due to a time zone difference (3h) and also differing system clock times deviating by some seconds. A precise time synchronization for both camera and Pixhawk flight controller and automatic image GPS stamp is developed with a future data logger.

I used existing reference data to retrieve cameras positions, as highlighted in blue rectangles above the dense point cloud (Figure G8.17c–d). Using GNSS-measured ground control points (GCP) is a suitable tool to decrease absolute image position errors and improve the quality and reliability of the digital surface model. Because the illumination conditions were quite low during the test flights, an increase in the brightness by 400 % and 750 % in Agisoft Photoscan for the VIS images and for the NIR images, respectively, was necessary. A larger correction percentage was chosen for the NIR dataset, since the overall recalled radiance was considerably lower during that flight.

Results of the Siilinjärvi field test

The resulting VIS camera mosaics with a ground sampling distance (GSD) of 23 cm (Figure G8.18). A comparison with a market competitor camera (Parrot S.O.D.A. flown on eBee UAS in 2018, Jackisch et al., 2020) shows that the msCam reaches comparable image quality, but has the advantage of 8 (respectively 16) image bands to get more refined spectral information from the surface. The created MNF mosaic of the VIS data shows acceptably little noise up to the 4th variance band.

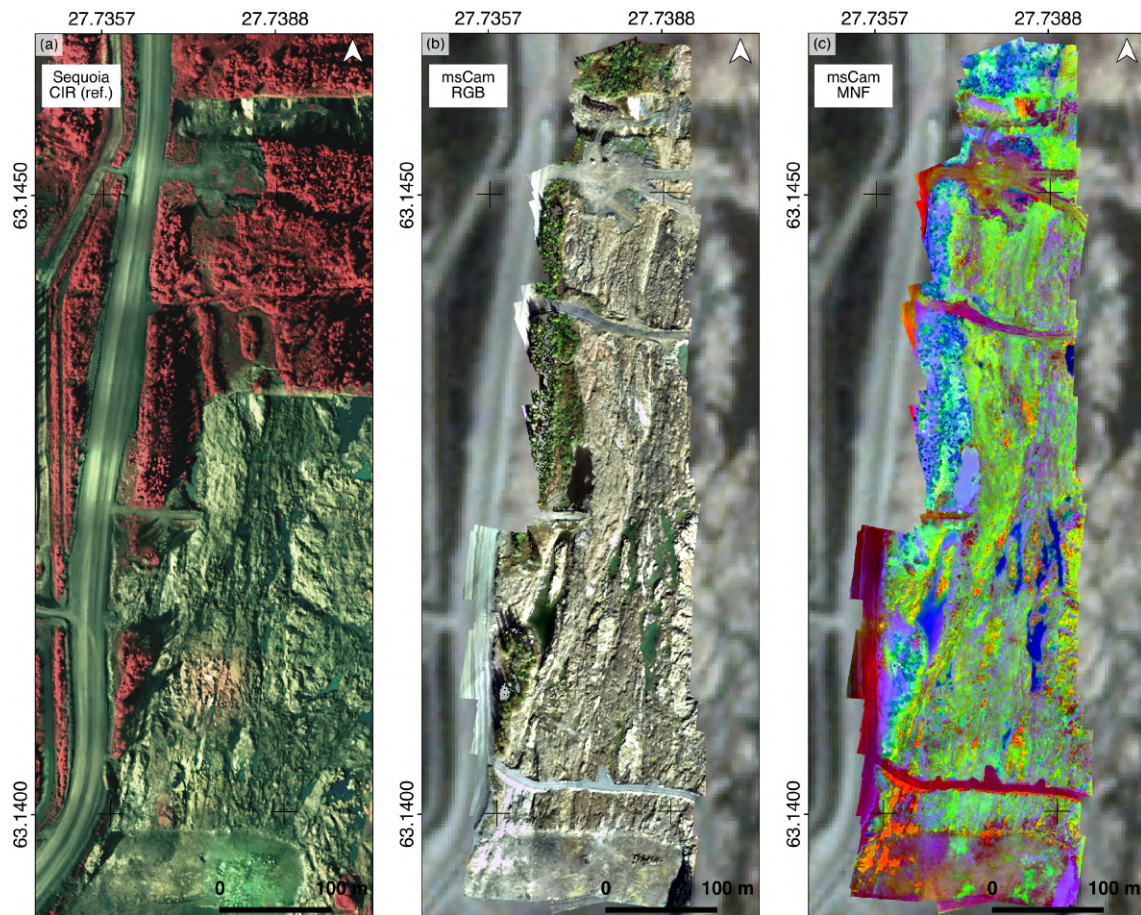


Figure G8.18 Comparing the commercial UAS eBee Sequoia with msCam. (a) The multispectral eBee orthophoto obtained from the survey 2018 serves as reference. (b) RGB orthophoto obtained from VIS camera data. (c) Minimum noise fraction bands 3,2,1 from the VIS camera data, illustrating that the signal-to-noise ratio is satisfying for qualitative geologic interpretation.

The retrieved DSM (Figure G8.19) shows the reconstructed surface compared with the associated digital elevation model of the former survey. The outcropping rock surface, water, vegetation, and mining infrastructure are outlined clear and sharp. Overlapping multispectral mosaic featuring 16 bands, where the image datasets from both cameras are combined also shows a decrease of the recovered surface area because of the overcast sky during the NIR camera flight (Figure G8.20). Furthermore, the NIR region towards 800–900 nm degrades in its sensitivity towards electromagnetic radiation, meaning that those images are generally under-illuminated. In summary, results show that the msCams have the capability to create high-quality multispectral image mosaics and other imaging products from fast-moving platforms. Resulting GSD was 22.9 cm for the mosaic.

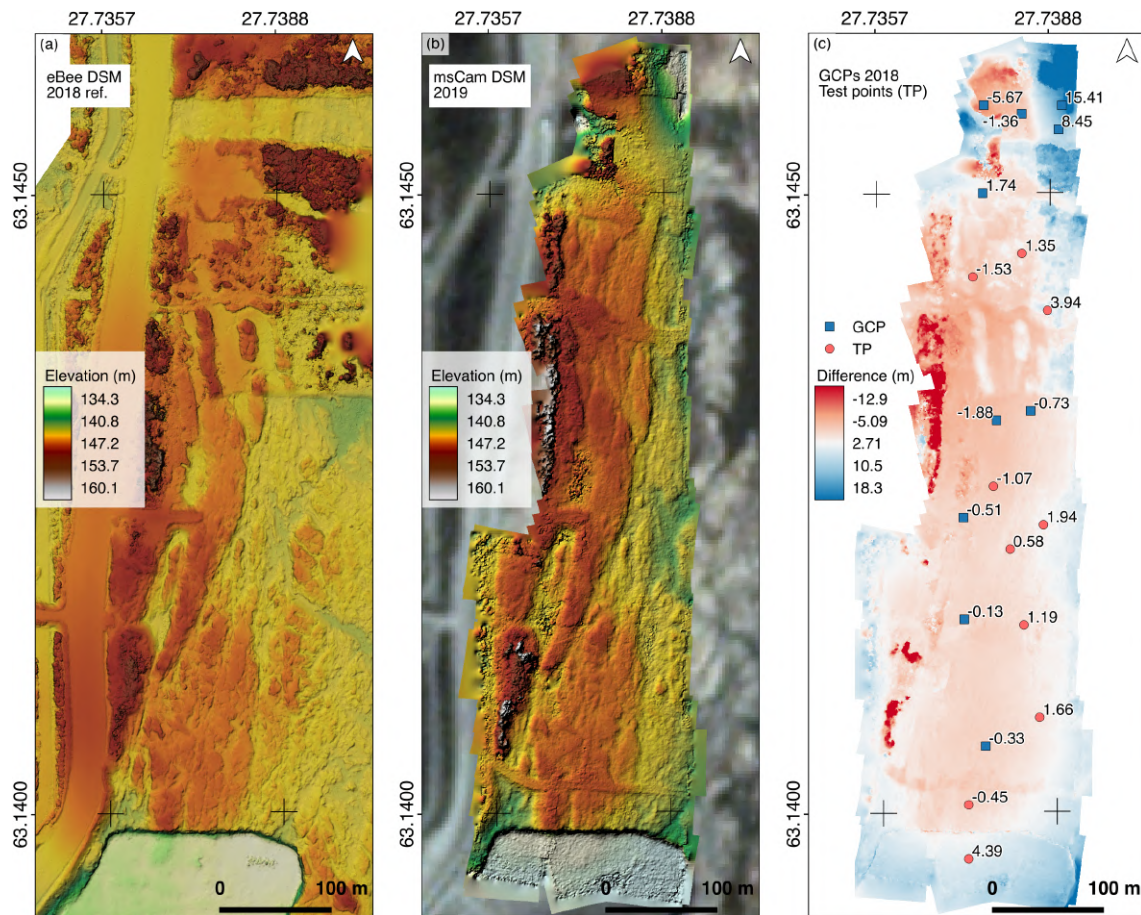


Figure G8.19 Comparison of reference with msCam DSM (a) Reference DSM and (b) digital elevation model of the test outcrop obtained from the VIS camera data, shown as total elevation asl. (c) Elevation difference calculated between the 2018 eBee DSM (reference) and the recent msCam DSM. Squared symbols show 2018 GCP's and test points (TP) are randomly set along the trench. Note that though the outcrop face changed between the trenches, the central area remained fairly similar, and TP were chosen from those unchanged areas.

Statistical information of processing for automatic image matching and error values of GCPs compared with actual elevation values (Figure 4.6) reveal a total reconstruction error between 1.98 and 4.2 m, for NIR and VIS msCam, respectively. A mean elevation error of 1.35 m, compared to the reference DSM is satisfactory (Figure G8.19c). Those values are acceptable, given the fact that the camera resolution is quite low (65,536 pixels) and GPS tagging was not working during the image acquisition. Further works include synchronization of the on-board UAS GPS with the msCam. Then, for each multispectral frame a GPS tag will be available along the flight track, which is expected to increase the reconstruction accuracy and removes tedious manual GCP-tagging from the processing workflow.

Table G8.9 Processing metrics as generated from Agisoft Photoscan and error statistics for msCam VIS DSM compared to 2018 eBee UAS-DSM.

Parameter	msCam VIS	msCam NIR
Report metrics		
Resolution	22.9 cm	22.3 cm
Cameras	2528	1328
RMS reprojection error	0.22	0.26
GCP	20	27
XY error (m)	2.31	1.83
Z error (m)	3.51	0.76
Total error (m)	4.20	1.98
Comparison reference GCP (2018) vs VIS-DSM test points (n=20)		
Mean error (m)	1.35	
Median error (m)	0.22	
Std. Dev. (m)	4.25	
min, max (m)	-5.67, 15.41	

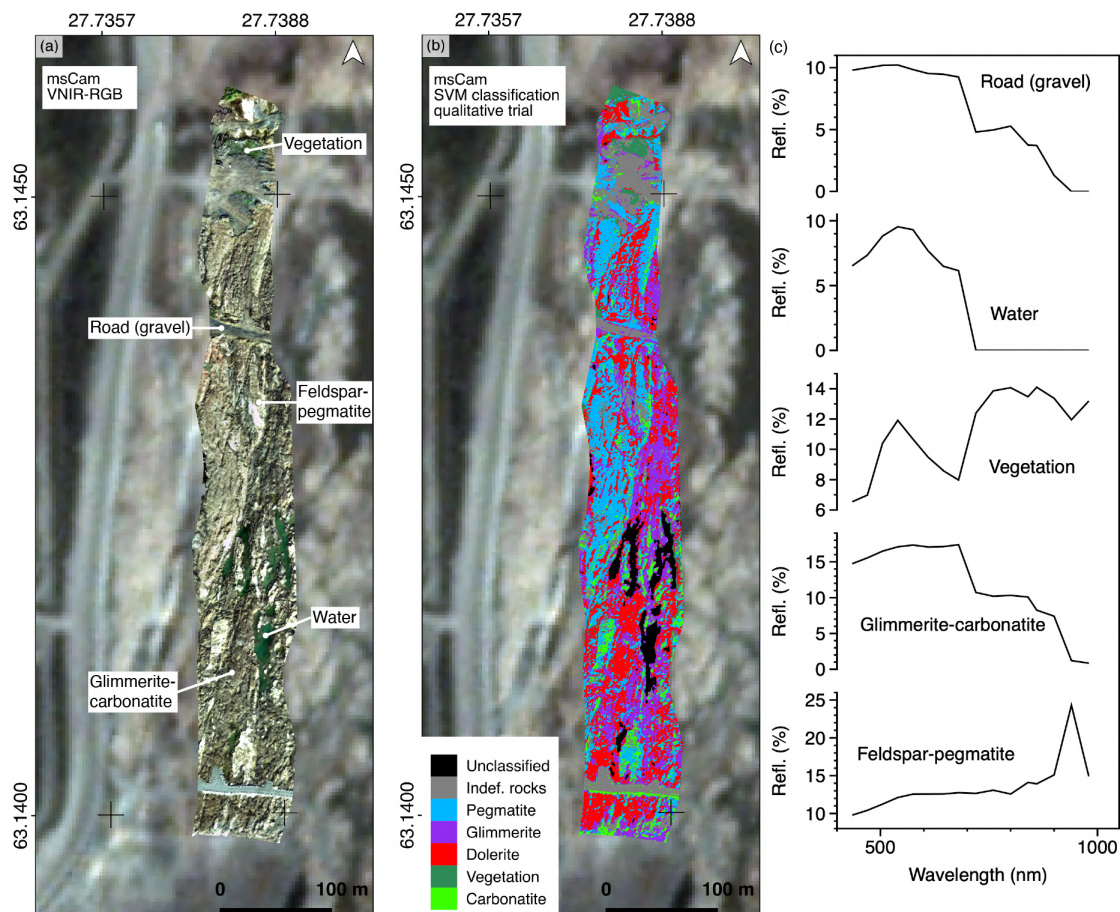


Figure G8.20 msCam VIS-NIR mosaic image and product from a combination of two flights with two cameras. (a) True-colour RGB obtained from the fused image mosaic containing 16 bands. (b) Qualitative trial classification using the implemented support vector machine (SVM) classifier in ENVI (Harris Geospatial) showing a promising distinction of surface classes. (c) Extracted image point spectra from five principal surface features, locations plotted in panel in reflectance (refl.).

Discussion and conclusion for msCam as UAS-based geologic imaging system

The msCAMs were selected such that a limited spatial resolution was traded favouring a higher spectral resolution to explore the added benefit of an evenly spaced spectral response along the possible electromagnetic spectrum. Its mirrors are a source of additional spectral distortion, but they allow to place the sensitive optical components inside the fuselage for protection. The high image frame rate enables the system to capture large numbers of images, when flight operations are performed with high speed.

The 8, respectively 16 bands allow a discrimination of the spectrally rather similar dark rocks. A fast, supervised classification done for seven classes on the VIS-NIR data allows a visual but qualitative surface discrimination (Figure G8.20b).

The derived DSM from the multispectral images provides additional value for lithological and structural mapping. With the magnetic system, this setup is a rather unique integrated multispectral and geophysical UAS survey solution. Listed characteristics of the tested camera solution are:

- Opportunities:
 - High endurance and spatial coverage for hourly flight intervals
 - Light weight and small size, fitted in ultra-light fixed-wing UAS with protected camera during landings
 - Affordable for relatively low costs (~ 20,000 US\$, prototype development, working hours not included, market price expected to be lower)
 - Camera operation per wireless connection possible
 - Rapid image capturing allows for sufficient image overlap in flight direction at high velocity
 - A large outcrop could be mapped in 30 minutes, with an extended survey potential of several km²
 - 8 resp. 16 bands allow a discrimination of outcropping rocks with supervised and unsupervised classifications
 - Derived digital elevation model from multispectral images create additional value for lithological and structural mapping
- Challenges:
 - Spatial resolution restricted in favour of spectral resolution
 - Radiometric sensitivity requires further investigation
 - Mirror with lens is additional noise source, e.g., spectral distortion
 - Fragile nature of the mirror-camera construction
 - Used consumer-grade single-frequency GPS receivers lack in accuracy; RTK or PPK recommended

Test results indicate that the system was working very well and the quality of imaging products was very high. At an operational flight altitude of 70 m, the camera shutter speed was fast enough (0.5 seconds) for having sufficient image overlaps and sharp images with 22.9 cm GSD were taken. Several parallel survey lines were flown that resulted in a 16-channel image mosaic that allowed characterizing main lithology in the test outcrop area. A quantitative and statistical evaluation of the image spectra and the classification accuracy could not be achieved with the current data set. Therefore, future tests should include a survey with different multispectral and hyperspectral cameras from different UAS at the same day and target area, including ground spectra.

Integrated drone technology would be accessible permanently for exploration & mining companies in LDCs, therefore reduce the need to rent services of the few international exploration providers, given a certain spatial scale at deposit or camp scale.

References

- Aasen, H., Honkavaara, E., Lucieer, A., and Zarco-Tejada, P.J., 2018, Quantitative remote sensing at ultra-high resolution with UAV spectroscopy: A review of sensor technology, measurement procedures, and data correction workflows: *Remote Sensing*, v. 10, p. 1–42, doi:10.3390/rs10071091.
- Anderson, D.E., and Pita, A.C., 2005, Geophysical surveying with GeoRange™ UAV: Collection of Technical Papers - InfoTech at Aerospace: Advancing Contemporary Aerospace Technologies and Their Integration, v. 1, p. 471–483, doi:10.2514/6.2005-6952.
- Bachmann, K., Frenzel, M., Krause, J., and Gutzmer, J., 2017, Advanced Identification and Quantification of In-Bearing Minerals by Scanning Electron Microscope-Based Image Analysis: *Microscopy and Microanalysis*, v. 23, p. 527–537, doi:DOI: 10.1017/S1431927617000460.
- Blakely, R.J., 1995, *Potential Theory in Gravity and Magnetic Applications*, doi:10.1017/cbo9780511549816.
- Debeglia, N., and Corpel, J., 1997, Automatic 3-D interpretation of potential field data using analytic signal derivatives: *Geophysics*, v. 62, p. 87–96.
- van Eck, N.J., and Waltman, L., 2014, Measuring Scholarly Impact: 285–320 p., doi:10.1007/978-3-319-10377-8.
- Van Eck, N.J., and Waltman, L., 2019, VOSviewer Manual version 1.6.10: CWTS Meaningful metrics.
- Fritz, B.S., 1984, Absolute calibration of an optical flat: *Optical Engineering*, v. 23, p. 234379.
- Funaki, M., Higashino, S.I., Sakanaka, S., Iwata, N., Nakamura, N., Hirasawa, N., Obara, N., and Kuwabara, M., 2014, Small unmanned aerial vehicles for aeromagnetic surveys and their flights in the South Shetland Islands, Antarctica: *Polar Science*, v. 8, p. 342–356, doi:10.1016/j.polar.2014.07.001.

- Funaki, M., and Hirasawa, N., 2008, Outline of a small unmanned aerial vehicle (Ant-Plane) designed for Antarctic research: *Polar Science*, v. 2, p. 129–142, doi:10.1016/j.polar.2008.05.002.
- Godinho, J.R.A., Kern, M., Renno, A.D., and Gutzmer, J., 2019, Volume quantification in interphase voxels of ore minerals using 3D imaging: *Minerals Engineering*, v. 144, p. 106016, doi:https://doi.org/10.1016/j.mineng.2019.106016.
- Heincke, B. et al., 2019, Developing multi-sensor drones for geological mapping and mineral exploration: setup and first results from the MULSEDRO project: *Geological Survey of Denmark and Greenland Bulletin*, v. 43, p. 2–6, doi:10.34194/geusb-201943-03-02.
- Henderson, R.G., and Zietz, I., 1949, The upward continuation of anomalies in total magnetic intensity fields: *Geophysics*, v. 14, p. 517–534.
- Kaneko, T., Koyama, T., Yasuda, A., Takeo, M., Yanagisawa, T., Kajiwar, K., and Honda, Y., 2011, Low-altitude remote sensing of volcanoes using an unmanned autonomous helicopter: an example of aeromagnetic observation at Izu-Oshima volcano, Japan: *International Journal of Remote Sensing*, v. 32, p. 1491–1504, doi:10.1080/01431160903559770.
- Kearey, P., and Brooks, M., 1991, An introduction to geophysical exploration. 2nd edition: An introduction to geophysical exploration. 2nd edition,.
- Kim, J., Kim, S., Ju, C., and Son, H. Il, 2019, Unmanned Aerial Vehicles in Agriculture: A Review of Perspective of Platform, Control, and Applications: *IEEE Access*, v. 7, p. 105100–105115, doi:10.1109/access.2019.2932119.
- Koyama, T., Kaneko, T., Ohminato, T., Yanagisawa, T., Watanabe, A., and Takeo, M., 2013, An aeromagnetic survey of Shinmoe-dake volcano, Kirishima, Japan, after the 2011 eruption using an unmanned autonomous helicopter: *Earth, Planets and Space*, v. 65, p. 657–666, doi:10.5047/eps.2013.03.005.
- Laliberte, A.S., Goforth, M.A., Steele, C.M., and Rango, A., 2011, Multispectral remote sensing from unmanned aircraft: Image processing workflows and applications for rangeland environments: *Remote Sensing*, v. 3, p. 2529–2551, doi:10.3390/rs3112529.
- Li, W.J., Qin, X.W., and Gan, X.P., 2014, The IGGE UAV Aero Magnetic and Radiometric Survey System, *in* Near Surface Geoscience 2014 - 20th European Meeting of Environmental and Engineering Geophysics, European Association of Geoscientists & Engineers, v. 2014, p. 1–5, doi:https://doi.org/10.3997/2214-4609.20141981.
- Nabighian, M.N., 1972, The Analytic Signal Of Two-Dimensional Magnetic Bodies With Polygonal Cross-Section: Its Properties And Use For Automated Anomaly Interpretation: *GEOPHYSICS*, v. 37, p. 507–517, doi:10.1190/1.1440276.
- O’Brien, H., Heilimo, E., and Heino, P., 2015, The Archean Siilinjärvi Carbonatite Complex: Mineral Deposits of Finland, p. 327–343, doi:10.1016/B978-0-12-410438-9.00013-3.
- de Oliveira, R.A., Tommaselli, A.M.G., and Honkavaara, E., 2016, Geometric Calibration of a Hyperspectral Frame Camera: Photogrammetric Record, v. 31, p. 325–347, doi:10.1111/phor.12153.
- Padró, J., Carabassa, V., Balagué, J., Brotons, L., Alcañiz, J.M., and Pons, X., 2019, Science of the Total Environment Monitoring opencast mine restorations using Unmanned Aerial System (UAS) imagery: *Science of the Total Environment*, v. 657, p. 1602–1614, doi:10.1016/j.scitotenv.2018.12.156.
-

- Parrot, 2017, How to register images from Sequoia single-band cameras: Application note SEQ-AN-03, 1 p.
- Poncet, A.M., Knappenberger, T., Brodbeck, C., Fogle, M., Shaw, J.N., and Ortiz, B. V., 2019, Multispectral UAS data accuracy for different radiometric calibration methods: *Remote Sensing*, v. 11, p. 1–22, doi:10.3390/rs11161917.
- Samson, C., Straznicky, P., Laliberté, J., Caron, R., Ferguson, S., and Archer, R., 2010, Designing and Building an Unmanned Aircraft System for Aeromagnetic Surveying: SEG Technical Program Expanded Abstracts 2010, p. 1167–1171, doi:10.1190/1.3513051.
- Spectral Devices Inc., 2018, Technical Document - Manual for msCAM ver. 008: Technical document #54, p. 37.
- Spectral Devices Inc., 2019, User Manual - msMirror ver. 001: , p. 9.
- Stoll, J., and Moritz, D., 2013, Unmanned aircraft systems for rapid near surface geophysical measurements, *in* 75th EAGE Conference and Exhibition Incorporating SPE EUROPEC 2013, doi:10.3997/2214-4609.20131212.
- Tezkan, B., Stoll, J.B., Bergers, R., and Großbach, H., 2011, Unmanned aircraft system proves itself as a geophysical measuring platform for aeromagnetic surveys: *First Break*, v. 29, p. 103–105.
- Tu, Y.-H., Phinn, S., Johansen, K., and Robson, A., 2018, Assessing Radiometric Correction Approaches for Multi-Spectral UAS Imagery for Horticultural Applications: *Remote Sensing*, v. 10, doi:10.3390/rs10111684.